Study of χ_c production in pA interactions at HERA-B

Yuriy Pylypchenko
Department of Physics
University of Oslo

Thesis submitted in partial fulfillment of the requirements
for the degree Doctor Scientarium

November 2004

Acknowledgments

I would like to express my sincere gratitude and appreciation to my adviser, Associated Professor Farid Ould-Saada, for his expert and thoughtful guidance, immense patience, encouragement and support at all levels. I am also really grateful to Professor Torleiv Buran, my co-adviser, for encouragement and invaluable advices. Many thanks also to Professor Lars Bugge for reading this dissertation and offering constructive comments.

I would next like to thank to Norwegian Research Council and Elementary Particle Physics Analysis Project for providing me with the unique opportunity to discover Norway and to work in the HERA-B experiment.

My special thanks to all members of HERA-B Charmonium working group for providing a highly competent and skilled environment with good companionship and fruitful discussions. I also appreciate all the members of HERA-B collaboration for keeping the experiment and providing good data.

I would also like to express my appreciation to all members of the EPF group at Oslo University for creative and friendly atmosphere full of encouragement and inspiration. Andreas Christensen deserves to be mentioned specially for his great assistance in my initial adaptation. Also, special thanks to Sigve Haug, Børge Kile Gjelsten, Torkjell Huse, Heidi Sandaker, Samir Ferrag and Kjell Martin Danielsen.

Finally, I would like to thank my parents for their life-long love and support. Without them, this work could not have been completed.

Contents

List of Figures

List of Tables

Chapter 1

Introduction

Charmonium is the bound state of charmed quark and its antiquark. In November 1974 it was discovered in two experiments independently, one at the Brookhaven National Laboratory (BNL) [1] and the other at the Stanford Linear Accelerator (SLAC) [2]. The BNL group named this new particle J, while the scientist at SLAC chose Ψ. It is known now as J/Ψ, one of the lightest of charmonium system.

The discovery of charmonium, known among physicists as November Revolution, was perhaps the biggest event in particle physics. Rather than opening up new fields, it had the effect of picking out one model above all others. Of all the competing models available in 1974 only Quantum Chromodynamics (QCD) and the electroweak theory, with the addition of the charm quark, accounted for all the data. This event turned the vast majority of particle physicists into believers of the Standard Model (SM) of particle physics.

Since that time charmonium still plays an important role in the physics programs in existing and coming experiments. Studies of charmonium production are relevant to CP-violation in B system, to top-quark mass measurements and even to discovering new physics. In high energy heavy-ion collisions, it is important to identify a clear signature of the expected occurrence of a phase transition to a quark-gluon plasma (QGP). One of the possible probes is J/Ψ which decays to lepton pairs with a clear peak in the di-lepton invariant mass spectrum [3].

Moreover, on its own charmonium attracts a lot of attention. Precision measurements of the bound $c\bar{c}$ system, i.e. masses, widths, energy splitting, production cross-sections and their ratios, are important inputs to test the limit of perturbative QCD and the order of magnitude of relativistic and radiative corrections.

The production of charmonium involves two distinct scales, the mass of the c quark, m_c, and the relative velocity of the heavy quarks, v, with a hierarchy

$$m_c \gg m_c v \gg m_c v^2 \sim \Lambda_{QCD}.$$

Because the mass of the heavy quark is relatively larger than the QCD scale, the creation of heavy quark pair is a short-distance process on scales of the order of $1/m_c$ or smaller, which can be calculated reliably in perturbation theory. The non-perturbative processes involve

long-distance scales of order of the charmonium size $1/(m_c v)$ or larger. It is thus intuitive to expect that long-distance and short-distance physics in charmonium production can be separated such that binding effects factorize into non-perturbative parameters.

There exist three theoretical models that have been developed to describe charmonium production, which are based on different assumptions about the factorization. These are the Color-Singlet Model (CSM) [4], Non-relativistic QCD (NRQCD) [5, 6, 7] and Color Evaporation Model (CEM) [8].

According to CSM the $c\bar{c}$ pair has to be produced during the short-distance interaction in a color-singlet state, with the same spin and angular momentum quantum numbers of the charmonium state we are interested in. A single non-perturbative parameter accounts for the hadronization of the $c\bar{c}$ pair into the physical charmonium state.

In NRQCD, perturbative factorization is retained by allowing the charmonium production and decay to take place via intermediate $c\bar{c}$ states with quantum numbers (color, spin, angular momentum) different than those of the physical charmonium state which is being produced. Non-perturbative transition probabilities from color-singlet and color-octet intermediate states to the charmonium are related to the NRQCD non-perturbative parameters, so-called long-distance matrix elements. Their relative importance can be evaluated using their scaling properties with respect to the small relative velocity in the center-of-mass frame of the two heavy quarks. One of the most important consequences of the NRQCD factorization is the prediction that the value of the matrix elements does not depend on the details of the production process, so that parameters extracted from a given experiment can be used in different ones.

The CEM assumes the universality of charmonium hadronization through soft gluon emission. According to the model, charmonium production is strictly factorized in the production of the intermediate $c\bar{c}$ pairs which hadronize to a charmonium state through the emission of one of more soft gluons. It is assumed that the hadronization does not affect the kinematics of the parent $c\bar{c}$ so that only a single universal factor is necessary for each state. Because this factors are constant, the differential and integrated charmonium production rates are proportional to each other and independent of projectile, target and interaction energy.

Despite large experimental and theoretical efforts the range of applicability of different theoretical approaches is still object to debate, as is the quantitative verification of the factorization [9]. In this situation more precise measurements performed in wide energy range and covering various production processes are mandatory in order to resolve present ambiguities.

Among a large variety of production processes in fixed-target and collider experiments, which provide a good possibility to test different theoretical approaches, investigations of relative production of different charmonium states look especially attractive, as most of the uncertainties are expected to cancel in the ratio.

In this thesis we present a study of the production of charmonium χ_c[1] states in collisions of 920 GeV protons with nuclear targets. We report on the studies of the fraction

[1]Here and further on in the thesis we use the notation χ_c to indicate the sum of the χ_{c1} and χ_{c2} states.

of J/Ψ produced via $\chi_c \to \gamma J/\Psi$ radiative decays, R_{χ_c}, and the relative production cross-section of χ_{c1} and χ_{c2} states, $\sigma_{\chi_{c1}}/\sigma_{\chi_{c2}}$. The analysis is based on the data collected with the HERA-B detector [10] at DESY during the period from October 2002 to March 2003, which amounts to about 300,000 J/Ψ reconstructed in di-muon and in di-electron channels in the x_F range $-0.35 \lesssim x_F \lesssim 0.15$.

A precise measurement of R_{χ_c} allows to specify the value of the ratio in the given kinematical range, assisting thus in quantifying the relative importance of different processes in the production of charmonium. Moreover, a study of the differential distribution of R_{χ_c} and its dependence on the atomic number of the target is a step forward in distinguishing between the CEM and NRQCD, as the two models provide different predictions about χ_c and J/Ψ nuclear effects. It is also an aid in understanding the J/Ψ nuclear suppression, which is important for the interpretation of heavy-ion data.

A measurement of the ratio $\sigma_{\chi_{c1}}/\sigma_{\chi_{c2}}$ is another test of the relative contribution of color-singlet and color-octet mechanisms in the production of charmonium. Only three measurements were performed in fixed-target experiments [11, 12] before. Therefore, the estimation of $\sigma_{\chi_{c1}}/\sigma_{\chi_{c2}}$ at $\sqrt{s} = 41.6\ GeV$ in a nice possibility to improve the existing experimental statistics. Beside that, it may be useful to understand the polarization of χ_c and J/Ψ which are considered as crucial tests of the NRQCD approach to charmonium production [13].

A brief theoretical overview of charmonium production is given in chapter 2. It is followed by the description of the HERA-B spectrometer, presented in chapter 3. In chapter 4, we discuss the reconstruction of the J/Ψ leptonic decays, determined by examining the invariant mass of two leptons of opposite charges. We describe the analysis chain leading to a clean sample of events containing a J/Ψ, including a comparison between J/Ψ differential distributions obtained with carbon and tungsten targets. Succeeding chapter 5 presents the description of the search for $\chi_c \to \gamma J/\Psi$ radiative decays. The reconstruction of the photon is done by measuring the energy released in the electromagnetic calorimeter. Chapter 6, then, provides the details related to the measurement of the fraction of J/Ψ particles produced via χ_c decays in pA collisions, summarizing the results given in chapters 4 and 5. The following chapter, chapter 7, illuminates the analysis leading to the measurement of the integrated $\sigma_{\chi_{c1}}/\sigma_{\chi_{c2}}$ ratio. The distinctive feature of the analysis is the reconstruction of χ_c's photon, which proceeds using the pair conversions processes. The final chapter, chapter 8, accommodates a summary of the results as well as conclusions.

Chapter 2

Charmonium production

2.1 Prelude

2.1.1 Symmetries and Conservation Laws

Symmetries, i.e regularities in the behavior of a physical system, are of great importance in high energy physics, as they often express fundamental properties of forces and can be used to deduce information about particles and their interaction. Symmetries reflect intrinsic properties of objects and of the space to which they belong. They are closely related to conservation laws and to the concept of invariance. A symmetry S is the set of invariances under the transformation given by S or, equivalently, when the Hamiltonian of the system H is invariant

$$SHS^{\dagger} = H$$

The set of all symmetry transformations of a system generates an algebraic structure of a group, which is the symmetry group of the system.

The different symmetries are usually classified as *discrete symmetries* and *continuous symmetries*. In the first case the parameters can take just discrete values. In particle physics the most relevant symmetries of this type are the transformations of parity, P, charge conjugation, C, and time reversal, T. They have proved very useful in telling us, among other, which particle reaction are possible with a given force and which are not. In the second case the parameters take continuous values. This kind of symmetries can be of two types

- space-time symmetries, which reflect intrinsic properties of the space the system belongs to (e.g. translation, rotational invariance);
- internal symmetries, which act on internal quantum numbers of the system and reflect its intrinsic properties (e.g. $SU(2)_L$ weak isospin symmetry etc.).

There are two distinct classes of internal symmetries: global symmetries and local (gauge) symmetries. The continuous parameters of the transformation of global symmetries are independent of the space-time coordinates while those of gauge symmetries

do depend on the position in space-time. If the Hamiltonian (or the Lagrangian) of a physical system has a global symmetry, there must be a current and an associated charge that are conserved. Gauge invariance requires the existence of gauge bosons which carry interactions between particles. This is a very important aspect of particle physics and has a crucial role in the Standard Model, fixing the interaction between particles. It is now believed that all forces in nature obey a form of gauge symmetry.

2.1.2 Standard Model

All known particle physics phenomena are well described within the Standard Model (SM), the current theory of elementary particles and their fundamental interactions. Under elementary particles we understand the constituents of matter with no known substructure down to the present scale of our observation ($\sim 10^{-19} cm$). The elementary particles are of two types: fermions, which are the basic building blocks of matter, and bosons, which are intermediate interaction particles. The fermions (Table 2.1) are divided into leptons and quarks. The known leptons are: the electron, e^-, the muon, μ^- and the tauon, τ^-; as well as the corresponding neutrinos ν_e, ν_μ and ν_τ. The known quarks are of six different flavours: u, d, s, c, b and t.

Table 2.1: *Fermions*

Leptons, spin = 1/2			**Quarks**, spin = 1/2		
Flavor	Mass, GeV/c^2	Electric charge	Flavor	Mass, GeV/c^2	Electric charge
ν_e	$< 7 \times 10^{-9}$	0	u (up)	0.005	2/3
e	0.000511	-1	d (down)	0.01	$-1/3$
ν_μ	< 0.0003	0	c (charm)	1.5	2/3
μ	0.106	-1	s (strange)	0.2	$-1/3$
ν_τ	< 0.03	0	t (top)	174	2/3
τ	1.7771	-1	b (bottom)	4.7	$-1/3$

In SM the interactions between two particles are described in terms of the exchange of bosons (Table 2.2) which couple to the conserved charges. The strength of the interaction is described by an effective constant, called *coupling constant*, which is a function of the energy transfer, Q^2, during the interaction. From a theoretical point of view the SM is a quantum field theory that is based on a gauge symmetry $SU(3)_c \times SU(2)_L \times U(1)_Y$. Gauge invariance plays a fundamental role in the theoretical treatment of the dynamical processes in SM and is used to deduce the detailed forms of the interactions. The gauge group

Table 2.2: *Bosons*

Interaction	Particle	Mass, GeV/c^2	Electric charge
Electromagnetic	γ (photon)	0	0
Weak	$W^{\pm}$	80.22	± 1
	Z^0	91.19	0
Strong	$\mathcal{G}$ (gluon)	0	0

of SM includes the symmetry group of strong interactions, $SU(3)_c$, and the symmetry group of unified electromagnetic and weak interactions, electroweak interaction, $SU(2)_L \times U(1)_Y$, comprising weak isospin $SU(2)_L$ symmetry group and weak hypercharge $U(1)_Y$ symmetry group. The symmetry group of electromagnetic force appears as a subgroup of the electroweak symmetry group.

The electroweak interaction is carried by three $W^{\pm}$, W^0 bosons for the $SU(2)_L$ sector, universally coupled with the strength g, and the neutral boson B^0 for the $U(1)$ sector, with coupling g'. The corresponding physical states are $W^{\pm}$ carrying weak charged current and γ, Z^0 carrying electromagnetic and weak neutral currents. The latter are mixtures of the W^0 and B^0 states. $W^{\pm}$ and Z^0 are massive particles, while the photon appears to be massless. The masses of the gauge bosons are generated due to spontaneous symmetry breaking of $SU(2)_L \times U(1)_Y$ symmetry through the *Higgs Mechanism*. The relations between the generators of the electroweak symmetry group and the physical particles are the following

$$W^{\pm} = \frac{1}{\sqrt{2}} \left(W^1 \mp i W^2 \right)$$

$$\begin{pmatrix} Z^0 \\ \gamma \end{pmatrix} = \begin{pmatrix} \cos\theta_W & \sin\theta_W \\ -\sin\theta_W & \cos\theta_W \end{pmatrix} \begin{pmatrix} W^0 \\ B^0 \end{pmatrix}$$

where θ_W is the weak mixing angle. The relation among the quantum numbers associated to the various conserved charges in the electroweak interactions is given by

$$Q = T_3 + \frac{Y}{2}$$

Here Q is the electric charge, T_3 is 3^d component of the weak isospin and Y is the weak hypercharge.

The various coupling constants that occur in electroweak interactions are related. Based on gauge invariance, the relation between g and g' is expressed in terms of unification condition

$$e = g \sin\theta_W = g' \cos\theta_W, \quad \cos\theta_W = M_W/M_Z$$

which relates the strength of weak and electromagnetic interactions to the $W^{\pm}$ and Z^0 masses, and anomaly conditions

$$\sum_l Q_l + 3 \sum_q Q_q = 0,$$

which, in contrast, relate the electric charges Q_l and Q_q of the leptons l and quarks q. The sum extends over all leptons l and all quark flavours $q = u, s, c, s, t, b$.

The quarks and leptons are organized in three families with identical properties except for mass. The particle content in each family is:

$$\begin{array}{ll} 1^{st} \text{ family:} & \begin{pmatrix} \nu_e \\ e^- \end{pmatrix}_L,\ e^-_R,\ \begin{pmatrix} u \\ d \end{pmatrix}_L,\ u_R,\ d_R \\ 2^{nd} \text{ family:} & \begin{pmatrix} \nu_\mu \\ \mu^- \end{pmatrix}_L,\ \mu^-_R,\ \begin{pmatrix} c \\ s \end{pmatrix}_L,\ c_R,\ s_R \\ 3^{rd} \text{ family:} & \begin{pmatrix} \nu_\tau \\ \tau^- \end{pmatrix}_L,\ \tau^-_R,\ \begin{pmatrix} t \\ b \end{pmatrix}_L,\ t_R,\ b_R \end{array}$$

and the corresponding antiparticles. Due to the spin structure of the weak interaction, which manifest itself in the parity, P, and charge conjugation, C, violation [1], the fermions are divided into left-handed and right-handed and transform as weak isodoublets or weak isosinglets respectively. The transitions within the quark isospin doublet is only approximate due to the phenomenon of quark mixing, which reflects the fact that the quark mass eigenstates are not the same as the weak eigenstates. Convincing evidences of existing neutrino oscillations [14], which is a consequence of neutrino masses and mixing, imply that the transition within the lepton isospin doublet is also an approximation. The quark mixing is often parametrized by a 3×3 unitary matrix V − Cabbibo-Kobayashi-Maskawa (CKM) matrix − operating on the charge -1/3 quark mass eigenstates (d, s and b):

$$\begin{pmatrix} d' \\ s' \\ b' \end{pmatrix} = \begin{pmatrix} V_{ud} & V_{us} & V_{ub} \\ V_{cd} & V_{cs} & V_{cb} \\ V_{td} & V_{ts} & V_{tb} \end{pmatrix} \begin{pmatrix} d \\ s \\ b \end{pmatrix}.$$

Any matrix element describing a weak process includes CKM factors[2] as well as terms related to the quark wavefunction. The values of individual matrix elements can, in principle, all be determined in weak decays of the relevant quarks, or, in some cases from deep inelastic neutrino scattering. The mixing formalism within three quark families accommodates the explanation of experimentally observed violation of combined CP-parity. The HERA-B experiment, in fact, was originally designed to study the phenomenon of CP violation in the B^0 system [10].

The quantum numbers for the fermions of the first family are collected in Tables 2.3 and 2.4. The fermions of the second and third family have the same quantum numbers as the corresponding fermions of the first family.

Unlike the leptons, the quarks have an additional quantum number, the color. They can exist in three different color states and generally are denoted as q_j, $j = 1, 2, 3$. The color charges act as the sources of the strong interaction. This idea is implemented in Quantum Chromodynamics (QCD), the gauge theory of strong interactions based on the gauge symmetry of the $SU(3)_c$ group. QCD emerged as a mathematically consistent

[1] However the combined parity, CPT is respected in the weak interaction

[2] The complex conjugate of CKM factors for antiparticles

Table 2.3: *Lepton quantum numbers.*

Lepton	T	T_3	Q	Y
ν_L	$\frac{1}{2}$	$\frac{1}{2}$	0	-1
e_L	$\frac{1}{2}$	$-\frac{1}{2}$	-1	-1
e_R	0	0	-1	-2

Table 2.4: *Quark quantum numbers.*

Quark	T	T_3	Q	Y
u_L	$\frac{1}{2}$	$\frac{1}{2}$	$\frac{2}{3}$	$\frac{1}{3}$
d_L	$\frac{1}{2}$	$-\frac{1}{2}$	$-\frac{1}{3}$	$\frac{1}{3}$
u_R	0	0	$\frac{2}{3}$	$\frac{4}{3}$
d_R	0	0	$-\frac{1}{3}$	$-\frac{2}{3}$

theory in the 1970s, and nowadays is regarded as one of the cornerstones of the Standard Model.

The strong interaction is carried by gluons. They carry color and anti-color simultaneously. According to the $SU(3)_c$, nine (3×3) color combinations form two multiplets of states: a singlet and an octet. The octet states form the basis from which all other color states may be constructed. They correspond to an octet of gluons.

The gauge transformation in the strong sector can be written

$$q(x) \rightarrow Uq(x) \equiv \exp\left[i\alpha_a(x)T_a\right] q(x), \tag{2.1}$$

were U is an arbitrary 3×3 unitary matrix which is shown parametrized by its general form. A set of U forms a gauge group. In (2.1) a summation over all repeated indices a is implied. T_a with $a = 1, ..., 8$ are set of linearly independent traceless 3×3 matrices, and α_a are the group parameters. The group is non-Abelian, since not all of the generators T_a commute with each other. In general

$$[T_a, T_b] = if_{abc}T_c \neq 0 \tag{2.2}$$

where f_{abc} are real constants called structure constants of the group. The structure of QCD is inferred by requiring gauge invariance. The QCD Lagrangian is given by

$$\mathcal{L}_{QCD} = \sum_{q=1}^{6} \bar{q}(x)(i\gamma^\mu \partial_\mu - m_q)q(x) - \alpha_s(\bar{q}(x)\gamma^\mu T_a q(x))G^a_\mu - \frac{1}{4}G^a_{\mu\nu}G^{\mu\nu}_a \tag{2.3}$$

where α_s is the strong coupling constant and the gluon field strength tensor $G^a_{\mu\nu}$ is given by

$$G^a_{\mu\nu} = \partial_\mu G^a_\nu - \partial_\nu G^a_\mu - \alpha_s f_{abc} G^b_\mu G^c_\nu \tag{2.4}$$

with the gluon field G^a_μ transforming under local phase transformation as

$$G^a_\mu \rightarrow G^a_\mu + \frac{1}{\alpha_s}\partial_\mu \alpha_a - f_{abc}\alpha_b G^c_\mu. \tag{2.5}$$

It is very informative to rewrite the Lagrangian (2.3) in schematic form

$$\mathcal{L} = \bar{q}q + G^2 + \alpha_s \bar{q}qG + \alpha_s G^3 + \alpha_s^2 G^4. \tag{2.6}$$

The first two terms in (2.6) describe the free propagation of quarks and gluons. The interactions among the quark and gluons are contained in the term

$$\alpha_s \bar{q}qG.$$

By their exchange the eight gluons mediate the interaction between not only the quarks but also the gluons themselves. The gluon self-interaction is reflected in the last two terms in (2.6), which contain three-gluon and four-gluon interactions. The fact that gluons themselves carry color charge and, accordingly, can interact between each other, result in the specific dependency of QCD coupling on momentum Q^2 transfered in interaction. At large energy scales, i.e. large Q^2 and corresponding small separation between interacting particles, the coupling constant α_s is small and quarks inside hadrons can be considered as free particles which are not bound by the color force. This very important feature of the strong force is called *asymptotic freedom*. Asymptotic freedom is the key for using perturbation approach in QCD. The predictions based on perturbative calculations can be compared to the experimentally observed cross-sections for quark or gluon production. Firts-order perturbative calculations in QCD yields:

$$\alpha_s(Q^2) = \frac{12\pi}{(33 - 2n_f) \cdot \ln(Q^2/\Lambda^2)}. \tag{2.7}$$

Here n_f is the number of quark flavors. Λ is a free parameter determined from experiment. At small momentum transfers, however, α_s is large and perturbative approach becomes inaccurate. In this regime, the dynamics of QCD is dominated by the non-perturbative phenomenon known as *confinement*. It is due to the fact that the color forces increase with the distance between strongly interacting particles. Because of that effect only states with zero total color, *color-singlets*, can exist as physical bound states, hadrons. In that sense Λ can be seen as marking the boundary between the quarks and gluons being asymptotically free where the perturbative theory is applicable (i.e. $\alpha_s \gg 1$ which is satisfied for $Q^2 \gg \Lambda^2 \approx 0.06(GeV/c^2)$) and the quarks and gluons confined inside colorless hadrons, where non-perturbative phenomena dominate.

The extent to which QCD has successfully accounted for the strong interactions processes, such as hadronic jets and heavy quark production observed in different experiments, is one of the triumphs of modern particle physics. However, many areas need further development. Increasingly the study of QCD also has an "engineering" aspect. In order to exploit the potential of high-energy colliders to study other physics, especially

at the machines with circulating hadron beams, one needs a quantitative understanding of QCD.

According to QCD matter becomes "simple" at high energy density in the matter. The hadrons and hadronic resonances from which the matter is constituted at moderate densities turn into a weakly interacting system of quarks and gluons, the quark-gluon plasma (QGP), at high densities, e.g. high temperatures. Such a new state of matter may appear whenever the energy density in the matter exceeds that inside a hadron. Nowadays there are big effort to detect QGP in heavy-ion collisions. The observation of the QGP would mean an experimental confirmation of the above ideas of the structure of strongly interacting matter. The detection of deconfined quarks and gluons would give the possibility to simulate the state of universe at the very early stage of its history.

2.1.3 Hadron classification

Hadrons are composite particles bound together by the color interactions. They consist of quarks and gluons, conventionally separated into valence quarks and sea of quark and gluons. Hadrons are classified according to which valence quark is thought to compose them. This classification in terms of valence quarks provides a useful and accurate description of most known strongly interacting particles. The simplest physically allowed color-singlet states one can form from quarks and antiquarks are generally of the form

$\|q\ \overline{q}\rangle$	meson
$\|q\ q\ q\rangle$	baryon
$\|\overline{q}\ \overline{q}\ \overline{q}\rangle$	antibaryon

There might exist other color-singlet sates, referred to as exotic and hybrid particles as well as glueballs. Exotic baryons are thought to comprise more than three quarks (or anti-quarks) odd in number. Exotic mesons must contain more than one valence $q\bar{q}$ pair. Hybrid hadrons are considered to embed a gluon in addition to valence quarks, whereas glueballs contain no valence quarks at all, being composed solely of gluons. Recently there have been some evidences for states composed of four quarks and one anti-quark $\Theta^+(uudd\overline{s})$ [15], $\Xi^{--}(dsds\bar{u})$ [16] and $\Xi^0(dsus\bar{d})$ [16] as well as for a state consisting of two valence quark-antiquark pairs $X(3872)$ [17, 18].

Most known mesons are reasonably described as quark-antiquark bound states. The complete spectrum of $q\ \overline{q}$ states is determined by quark quantum numbers. Since quarks have spin $s = \frac{1}{2}$, the $|q\ \overline{q}\rangle$ pair can have total spin $s_{q\overline{q}} = 0$ or 1. The $|q\ \overline{q}\rangle$ orbital angular momentum $L_{q\overline{q}}$ can take on any integer value; combining these L and s $q\overline{q}$ angular momenta gives the allowed total angular momentum $J_{q\overline{q}}$. The allowed values are $J = L$ (for $s = 0$) and $J = L + 1, L, L - 1$ (for $s = 1$). Using spectroscopic notation meson quark model assignments may be specified as $^{2s+1}L_J$, where, instead of numerical value of L, it is conventional to write $S, P, D, F, ...$ for $L = 0, 1, 2, 3, ...$ As an example, the J/Ψ meson is an $^3S_1$ state with the spin $s = 1$, angular momentum $L = 0$ and total angular momentum $J = 1$.

Spatial parity P and charge-conjugation parity C are conserved in strong interactions. In $q\overline{q}$ states these quantum numbers are $P = (-1)^{L+1}$ and $C = (-1)^{L+s}$. A state's J^{PC} follows directly from these relations; for example the state $^3S_1$ corresponding to the J/Ψ meson has $J^{PC} = 1^{--}$.

2.2 The $c\bar{c}$ bound system

Experimental and theoretical investigation of $c\bar{c}$ bound states, generally called charmonium, have been very important in establishing QCD as a true theory of strong interactions. The properties of charmonium states have been found in qualitative and in some cases quantitative agreement with theoretical expectations based on QCD. Nevertheless, since many important non-perturbative problems are still not solved, one may expect that the closer look at the properties and production of charmonium states will help in elucidating the interplay between perturbative and non-perturbative effects in QCD. This is why the experimental results on charmonium production always attract a lot of interest and attention.

Moreover, charmonium is considered as a possible signature in search for quark-gluon plasma (QGP). However its usefulness is under question as long as the charmonium production process is not fully understood. The measurements and theoretical predictions are not in good agreement with each other. Although the recent calculations suggest several ways to explain the situation precise measurements are needed in order to resolve the existing uncertainties and figure out the right model.

2.2.1 Mass spectrum

Most of the known charmonium states were found at e^+e^- colliders, which form only $J^{PC} = 1^{--}$ states in s-channel: $e^+e^- \to \gamma \to c\bar{c}$. The remaining states in the 1P multiplet and $^1S_0$ spin-singlets $\eta_c(2980)$ and $\eta_c(3594)$ [19, 20] were found in radiative transitions from 1S and 2S vector states. The single exception is the $h_c(3526)$ particle observed in $p\overline{p}$ collisions [21]. However like in the $\eta_c(3594)$ case the existence of $h_c(3526)$ needs further experimental confirmation.

All charmonium states with masses below the kinematic threshold of $D\bar{D}$[3] production (dissociation threshold) are summarized in Table 2.5 and Fig 2.1. Charmonium states which lie above that threshold are broad resonances which decay into pairs of charmed particles involving the creation of light quark-antiquark pair, in contrast to the states below the open charm threshold, which cannot decay into charmed particles because of energy conservation ($M_{c\bar{c}} < 2m_D$).

The low-lying states of charmonium decay eventually via quark antiquark annihilation into gluons. However radiation transitions between different states are also possible since their lifetime is long enough for electromagnetic transitions between various excitations

[3] D being the lightest charmed meson: $D^0 = c\bar{u}$, $\bar{D}^0 = \bar{c}u$, $D^+ = c\bar{d}$, $D^- = \bar{c}d$, and $m_D \approx 1.870 GeV/c^2$ [20].

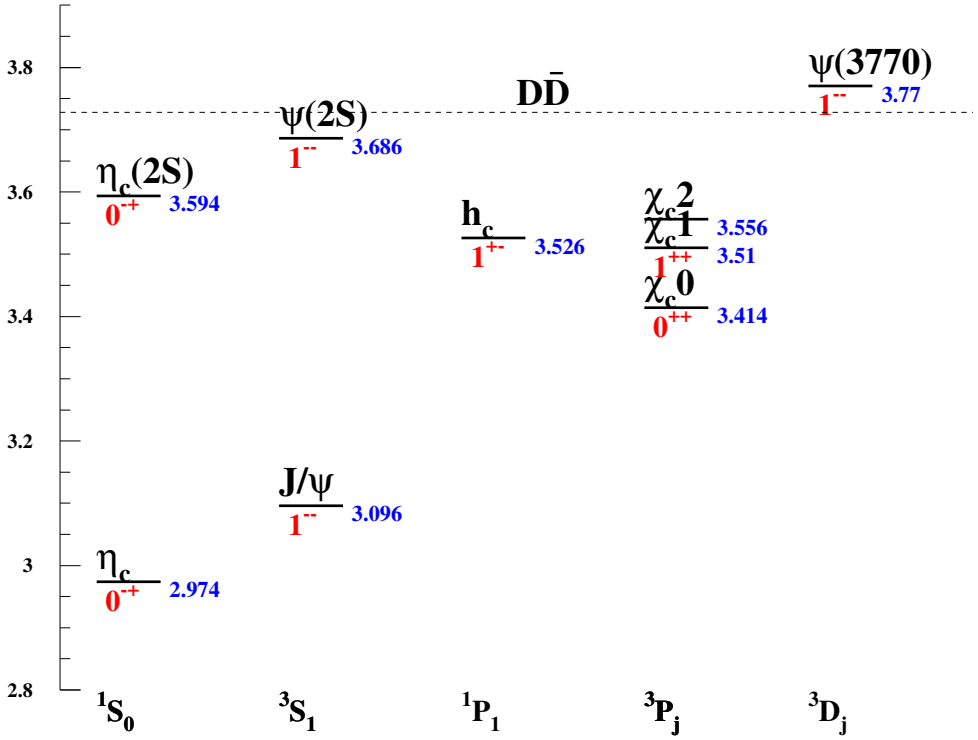

Figure 2.1: *Charmonium spectrum. The states below the dissociation threshold plus* $\Psi(3770)$*, the first state of* ${}^3D_J$ *multiplet, are shown. The vertical axis shows the masses in* GeV/c^2 *while horizontal axis presents the corresponding quantum numbers.*

to occur. The electromagnetic transitions compete with transitions mediated by the emission of soft gluons. The latter materialize as light hadrons. Another possibility to disintegrate is via leptonic decay, which is used by many experiments, including HERA-B, to reconstruct $J/\Psi$and $\Psi(2S)$ particles. Properties of these bound states and their decays are good testing grounds for QCD in both the non-perturbative and perturbative regimes.

2.2.2 Potential model

The distinctive phenomenological feature of the charmonium system is that, for many purposes, it is well described by the quark potential model, in which the heavy quark and antiquark are bound by a instantaneous (static) potential.

The low-lying $c\bar{c}$ states are essentially non-relativistic systems because of heavy mass of the c quark, e.g. $M_{J/\Psi=c\bar{c}} \approx 3.1 GeV/c^2$ where $m_c \approx 1.5 GeV/c^2$. Under such circumstances, the observed mass spectrum of charmonium states is well understood in simple non-relativistic treatment. In the center-of-mass frame of the $c\bar{c}$ pair, neglecting spin-dependent effects, the Schrödinger equation is

$$-\frac{1}{2\mu}\nabla^2\psi(\vec{x}) + V(r)\psi(\vec{x}) = E\psi(\vec{x}) \tag{2.8}$$

Table 2.5: *Known charmonium states under $D\overline{D}$ dissociation threshold [20].*

State	Mass (MeV/c^2)	Width (MeV/c^2)	e^+e^-, $\mu^+\mu^-$ decays and γ transitions
$\eta_c(1S)$ (1^3S_0) $J^{PC}=0^{-+}$	2979.6 ± 1.2	$17.3^{+2.7}_{-2.5}$	
J/Ψ (1^3S_1) $J^{PC}=1^{--}$	3096.92 ± 0.01	0.091 ± 0.003	$e^+e^-(5.93 \pm 0.10)\%$ $\mu^+\mu^-(5.88 \pm 0.10)\%$ $\gamma\eta_c(1S), (1.3 \pm 0.4)\%$
$\Psi(2S)$ (2^3S_1) $J^{PC}=1^{--}$, also called Ψ'	3686.09 ± 0.03	0.277 ± 0.022	$e^+e^-, (7.55 \pm 0.31) \times 10^{-3}$, $\mu^+\mu^-, (7.3 \pm 0.8) \times 10^{-3}$ $\gamma\chi_{c0}(1P), (8.6 \pm 0.7)\%$ $\gamma\chi_{c1}(1P), (8.4 \pm 0.8)\%$ $\gamma\chi_{c2}(1P), (6.4 \pm 0.6)\%$ $\gamma\eta_c(1S), (2.8 \pm 0.6) \times 10^{-3}$
χ_{c0} (1^3P_0) $J^{PC}=0^{++}$	3415.2 ± 0.3	10.2 ± 0.9	$\gamma J/\Psi(1S), (1.18 \pm 0.14)\%$
χ_{c1} (1^3P_1) $J^{PC}=1^{++}$	3510.6 ± 0.1	0.91 ± 0.13	$\gamma J/\Psi(1S), (31.6 \pm 3.3)\%$
χ_{c2} (1^3P_2) $J^{PC}=2^{++}$	3556.3 ± 0.1	2.11 ± 0.16	$\gamma J/\Psi(1S), (20.2 \pm 1.7)\%$
h_c (1^1P_1) $J^{PC}=?^{??}$	3526.21 ± 0.25	< 1.1 (at CL 90 %)	
$\eta_c(2S)$ (2^3S_0) $J^{PC}=0^{-+}$	3654 ± 10	< 55	

where $r = |\vec{x}|$ is the distance between the quarks, $\mu = m_c/2$ is their reduced mass (m_c is the c quark mass), and ψ is the wave function of the $c\bar{c}$ bound state. The mass

$$M_{c\bar{c}} = 2m_c + E(m_c, V) \tag{2.9}$$

depends only on the principal quantum number n and the orbital quantum number l, for a given potential $V(r)$. The potential $V(r)$ is inferred from the charmonium spectrum and the properties of the strong forces [22]. In particular it can be determined as

$$V(r) \approx \begin{cases} -\frac{\alpha_s(r)}{r}, & r \to 0 \\ k^2 r, & r \to \infty \end{cases} \tag{2.10}$$

$V(r)$ behaves like a Coulomb potential at small distances between quarks, but rises linearly at large values of r as dictated by asymptotic freedom and confinement, respectively. The mass of the observed states and the decay width, which is sensitive to the short-distance part of the potential of $c\bar{c}$ bound state, are usually used to test the potential model in question.

There are variety of phenomenological models for the potential, which may have different ways of treatment of the short and long distance limits with respect to the static potential. Moreover, they may include relativistic corrections and higher order corrections in perturbative expansion to the short distance limit. They all, with the proper

choice of c-quark mass, give a satisfactory description of the experimentally observed mass spectrum of charmonium states [23].

2.3 Kinematical observables

For a $c\bar{c}$ bound state formed from two colliding nucleons with four-momenta p_1 and p_2 the energy in their center-of-mass system (c.m.s.) is given by

$$\sqrt{s} = \sqrt{(p_1 + p_2)^2} \tag{2.11}$$

Since the nucleons are composite objects we can try to describe the interaction as a collision between two elementary constituents, partons, which carry longitudinal momentum fractions x_1 and x_2 respectively. Provided we can transform to a frame where the energy of both nucleons is large, we can neglect the transverse momentum and mass of the partons. The heavy object created by the two partons then has an invariant mass

$$M = \sqrt{\hat{s}} = \sqrt{x_1 x_2 s} \tag{2.12}$$

Differential cross-sections are usually described in terms of the momentum coordinates parallel and perpendicular to $\vec{p}_1 - \vec{p}_2$ direction. A common choice in fixed-target collisions are the transverse momentum p_T and the Feynman-x variable x_F [24],

$$\begin{aligned} p_T &= \sqrt{p_x^2 + p_y^2} \\ x_F &= \frac{p_z}{p_z^{max}} \approx \frac{2p_z}{\sqrt{s}} \end{aligned} \tag{2.13}$$

where p_z is calculated in the c.m.s. frame of the proton-nucleon collision and p_z^{max} is its maximum value in this frame. The center-of-mass frame is defined as if the projectile proton is colliding with a stationary nucleon inside the nucleus. In the parton picture x_F is related to the parton momentum fractions by

$$x_F = x_1 - x_2 \tag{2.14}$$

An alternative to the longitudinal momentum is the rapidity, defined as

$$y = \frac{1}{2} \log \left(\frac{E + p_z}{E - p_z} \right), \tag{2.15}$$

where E is the energy of the hadron. Under the Lorentz transformation along the z-axis, the rapidity transforms like $y \rightarrow y - tanh^{-1}\beta$, such that the shape of the rapidity distribution is independent of the reference frame. If $m \ll |\vec{p}|$ the rapidity is approximately equal to the pseudorapidity given by

$$\eta = -\log \left[\tan \left(\frac{\theta}{2} \right) \right], \tag{2.16}$$

where θ is the angle between the particle momentum vector and the z-axis.

2.4 Charmonium production cross-section

There are several momentum scales that play important roles in the dynamics in a charmonium state [25]. The most important scales are:

- Mass of the charmed quark, m_c:
  it sets the overall scale of the rest energy of the bound state and, also, provides the short-distance scale, $1/m_c$, at which the production of $c\bar{c}$ pair takes place.

- Quark relative momentum in the meson rest frame, $m_c v$:
  the formation of the charmonium state takes place over distances that are of order $m_c v$ in the charmonium rest frame and the size of the bound state is inverse to the momentum $m_c v$.

- Quark kinetic energy scale, $m_c v^2$:
  this is the scale of binding energies.

- The energy scale Λ_{QCD} (the same as Λ in (2.7)):
  it is associated with the non-perturbative effects involving gluons and light quarks. It determines the long range behavior of the potential between the quark and anti-quark, which is approximately linear, with the coefficient of $(k \approx 450MeV)^2$. This can be used as an estimate for the non-perturbative scale: $\Lambda_{QCD} \approx 450MeV$ [5]

Assuming the non-relativistic nature of the $c\bar{c}$ bound states with the relative quark velocities $v \ll c$, one can treat the processes associated with different energy scales m_c, $m_c v$ and $m_c v^2$ separately:

$$\Lambda_{QCD}^2 \sim (m_c v^2)^2 \ll (m_c v)^2 \ll m_c^2 \tag{2.17}$$

Calculations based on quark potential model indicate that the average value of v^2 is about 0.25 for the charmonium system [25], which means that the assumption (2.17) is reasonably good in our case. Under such circumstances, the cross-section for producing

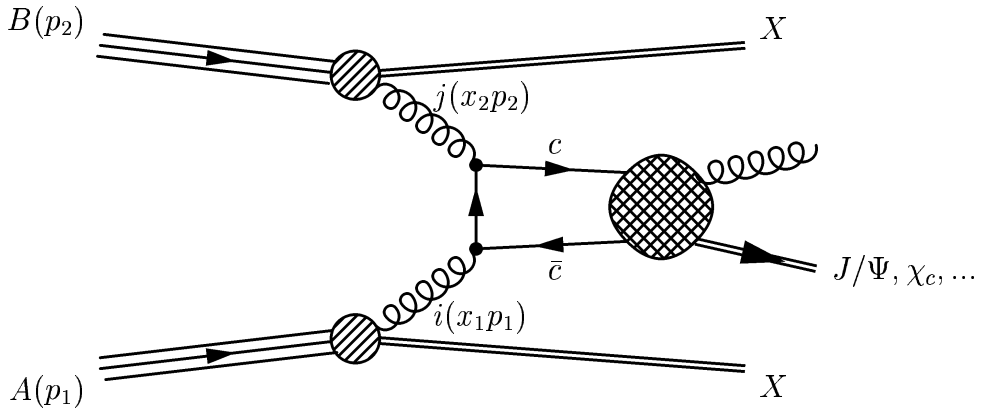

Figure 2.2: Schematic view of charmonium production in hadronic collision

a charmonium states $\mathcal{CH}$ is usually written in a factorized form, that is the effects at the energy scale m_c are separated from those at the lower energy scales $m_c v$, $m_c v^2$ and Λ_{QCD}. In other words, the cross-section is written as a sum of terms, each of which factors into a short-distance part ($\sim 1/m_c$ or smaller), which can be calculated in QCD perturbation theory, multiplied by long-distance coefficients ($\sim 1/(m_c v)$ or larger) associated with the non-perturbative effects (Fig. 2.2):

$$\sigma_{\mathcal{CH}} = \sum_{i,j} \int \underbrace{dx_1 dx_2 f_{i/A} f_{j/B}}_{\Lambda_{QCD}} \times \underbrace{\hat{\sigma}[ij \to (c\bar{c}[n] + X')]}_{m_c} \times \underbrace{O[c\bar{c} \to \mathcal{CH}]}_{m_c v} + \mathcal{O}(\frac{\Lambda_{QCD}}{m_c^2}) \quad (2.18)$$

Here i, j represent the interacting partons (gluons, light quarks and antiquarks) and the functions $f_{i/A} = f_{i/A}(x_1, \mu_F^2)$ and $f_{j/B} = f_{j/B}(x_2, \mu_F^2)$ are their number densities, the parton distribution function (PDF) evaluated at the momentum fraction x_1 and x_2 and factorization scale μ_F. The calculation of PDF cannot be achieved from first principles in perturbation theory. However their dependence on factorization scale can be calculated perturbatively [26].

The cross-section $\hat{\sigma}$ of the hard scattering process describes the transition from the initial partons i and j with momentum fractions x_1 and x_2 to a $c\bar{c}$ pair in quantum state n and possibly other gluons and quarks (X'). It can be calculated as a perturbation series in α_s, where the strong coupling constant is evaluated at the renormalization scale μ_R. At leading order three processes contribute to the $c\bar{c}$ production (Fig. 2.3).

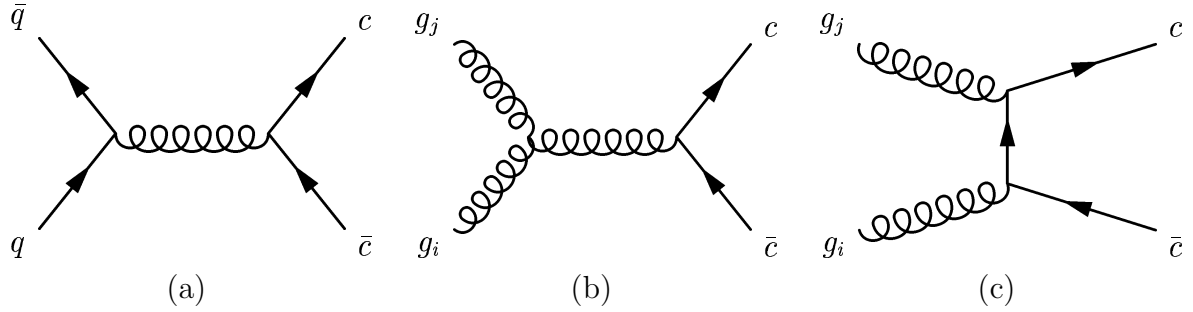

Figure 2.3: Leading order diagrams for heavy-quark production.

In general, the hard-scattering cross-section should be considered as a function of two scales, factorization scale μ_F and renormalization scale μ_R: $\hat{\sigma} = \hat{\sigma}(\mu_F, \mu_R)$.

Since the short distance cross-sections depend upon the helicity of the partons, the spin of the $c\bar{c}[n]$ state can be preferentially aligned with respect to the relative momentum of the nucleons [7, 27]. Information about the spin alignment which for charmonium is usually called polarization is revealed by the angular distribution of the decay products, which, in HERA-B, are the two leptons in case of the decay of J/Ψ, and photon and J/Ψ in case of χ_c decays. Usually the angular distribution is expressed in terms of the polar angle of the positive lepton and photon in the rest frame of the J/Ψ and χ_c resonances, respectively. There are two conventional choices for the coordinates in this frame, namely either with the z-axis parallel to the projectile momentum vector or parallel

to the bisection of the projectile momentum vector and (minus) the target momentum vector The prediction for the polarization depends on the choice of the reference frame, but at small p_T (as in fixed-target experiments) the difference is small enough that most authors do not mention it. After integration over the azimuthal angle, the differential cross-section can be written as [7]

$$\frac{d\sigma}{dcos\theta} \propto 1 + \lambda cos^2\theta \tag{2.19}$$

where $\lambda = 1$ ($\lambda = 0$) corresponds to complete transverse (longitudinal) polarization.

The angular dependency of charmonium states plays an important role in the discussion of the production mechanism. The different models for charmonium production, which are discussed in the following section, supply with rather different predictions. This makes the experimental studies of the polarization of charmonium states to be a sensitive and attractive test of theoretical calculations. The comparison of the predictions and the present experimental results are discussed later in section 2.6.

2.5 Charmonium formation

Because of the relatively large c-quark mass, $c\bar{c}$ production is perturbatively calculable, as it is pointed out in the previous section. However, the subsequent transition from $c\bar{c}$ pairs to physical charmonium state $\mathcal{CH}$ introduces non-perturbative effects, presenting a particular challenge to theoretical calculation. If the factorization assumption (2.18) is valid, this long-distance process can be treated in theoretical calculation as universal parameters, $O[c\bar{c} \to \mathcal{CH}]$ in (2.18).

There exist three theoretical models that have been developed to describe charmonium formation, which are based on different assumptions about the factorization [9, 28]. These are the Color-Singlet Model (CSM) [4], Non-Relativistic QCD (NRQCD) [5, 6, 7] and the Color Evaporation Model (CEM) [8, 29].

2.5.1 Color evaporation model

According to color evaporation model (CEM), the production cross-section of bound states is strictly factorized in the production of $c\bar{c}$ pair and its subsequent evolution into a charmonium state. The perturbatively calculated total partonic cross-section into free charmed quarks is equal to the sum of all the cross-sections of all charm hadrons (*duality argument*). Correspondingly, all the information on the non-perturbative transition of the $c\bar{c}$ pair to the heavy quarkonium $\mathcal{CH}$ of quantum numbers J^{PC} is contained in "fudge factors" $F_{nJ^{PC}}$ that a priori may depend on all quantum numbers ($w = x_F, p_T, ...$):

$$\frac{d\sigma[\mathcal{CH}(nJ^{PC})](s,w)}{dw} = F_{nJ^{PC}} \frac{d\hat{\sigma}[c\bar{c}](s,w)}{dw} \tag{2.20}$$

$\hat{\sigma}[c\bar{c}]$ is the total cross-section of heavy-quark production calculated by integrating over the $c\bar{c}$ pair mass M from $2m_c$ to $2m_D$. For example, in hadronic collisions at high energy

$$\begin{aligned}\hat{\sigma}[c\bar{c}](s) = \; & \int_{4m_c^2}^{4m_D^2} d\hat{s} \int dx_1 dx_2 f_{i/A}(x_1, M^2) \\ & \times f_{j/B}(x_2, M^2) \hat{\sigma}[ij \to c\bar{c}X](\hat{s}) \delta(\hat{s} - x_1 x_2 s),\end{aligned} \tag{2.21}$$

where the relation between M and $\hat{s}$ is specified by (2.12). Note that $\hat{\sigma}[c\bar{c}]$ is the spin-summed cross-section and that the heavy-quark pair can be both in a color-singlet and a color-octet state. The $c\bar{c}$ configuration arranges itself into a definite outgoing charmonium state by interacting with the collision-induced color field ("color evaporation"). A big fraction of the sub-threshold cross-section $\hat{\sigma}[c\bar{c}]$, however, goes into open charm production. The additional energy needed to produce charmed hadrons is obtained (in general non-perturbatively) from the color field in the interaction region. The yield of all charmonium states below the $D\bar{D}$ threshold is, thus, only a part of the total sub-threshold cross-section [8].

Neither the division of $\hat{\sigma}[c\bar{c}]$ into open charm and charmonium nor the relative charmonium production rates are specified by the generalized color evaporation model. Hence its essential prediction is that the dynamics of charmonium production is that of $\hat{\sigma}[c\bar{c}]$, i.e. the energy dependence, x_F - and p_T -distributions of $\mathcal{CH}$ are identical to those of the free $c\bar{c}$ pair. In particular, ratios of different charmonium production cross-sections should be energy-, x_F -, and p_T -independent. In other words, the non-perturbative factors $F_{nJ^{PC}}$ should be universal constants whose values may, however, depend on the heavy-quark mass.

2.5.2 Color-singlet model

In the color-singlet model (CSM), the dominant production mechanism of a charmonium state $\mathcal{CH}$ is assumed to be the one in which it is produced at short distances in a color-singlet $c\bar{c}$ state with the correct quantum numbers. Hence the cross-section is given by the factorized form:

$$\frac{d\sigma[\mathcal{CH}(nJ^{PC})](s,w)}{dw} = F_{nL} \frac{d\sigma[c\bar{c}(n^{2S+1}L_J, \underline{1})](s,w)}{dw}, \tag{2.22}$$

where $\underline{1}$ underline the color-singlet nature of the $c\bar{c}$ pair. The non-perturbative probability F_{nL} for the $c\bar{c}$ pair to form the bound state $\mathcal{CH}$ is given in a calculable way in terms of the radial wave function $R_{nL}^{(L)}(0)$ of non-relativistic Schrödinger equation for $c\bar{c}$ bound state or its derivatives

$$F_{nL} \propto \frac{\left| R_{nL}^{(L)}(0) \right|^2}{M_{\mathcal{CH}}^{3+2L}} \tag{2.23}$$

and can either be calculated using a potential from potential model or extracted from the $\mathcal{CH}$ decay widths.

If the relevant momentum scale Q^2 is of the order of the heavy quark mass, the dominant cross-section is given by (2.22). The production mechanism in hadronic collisions via

leading order is represented on Fig. 2.5(a). At large scale Q^2 however, the short-distance production becomes suppressed by a factor m_c^2/Q^2 with respect to production via fragmentation. Similarly, fragmentation processes start to dominate at high-p_T (Fig. 2.5(b)) [9, 28]. In this case, important contributions arise from gluon fragmentation

$$\frac{d\sigma[\mathcal{CH}+X](s,p_T)}{dp_T} = \int_0^1 dz \frac{d\hat{\sigma}[g(p_T/z)+X](s,p_T,\mu)}{dp_T} D_{g\to\mathcal{CH}}(z,\mu,m) \tag{2.24}$$

The fragmentation functions $D_{i\to\mathcal{CH}}(z;\mu;m)$ specify the probability for partons i (gluons, light and heavy quarks) to hadronize into the hadron $\mathcal{CH}$ as a function of its longitudinal momentum fraction relative to i: $z = p_l^{\mathcal{CH}}/p_l^i$. The fragmentation functions at the input scale m_c, $D^{(0)}_{i\to\mathcal{CH}}(z)$ can be calculated as series in $\alpha_s(m_c)$ by assuming that they take the same factorized form as (2.22). For example, the lowest-order diagrams that contribute to gluon fragmentation into J/Ψ are $g \to c\bar{c}(^3S_1;\underline{1})gg$, so that

$$D^{(0)}_{i\to\mathcal{CH}}(z) = \left(\frac{\alpha_s(m_c)}{m_c}\right)^3 |R_{1S}(0)|^2 f(z) + O(\alpha_s^4) \tag{2.25}$$

where $R_{1S}(0)$ is the radial wave function of J/Ψ and $f(z)$ is a calculable function.

In contrast to S-wave fragmentation functions, the color-singlet contributions to fragmentation functions into χ_{cJ} state are, however, singular. For example, the process $g \to c\bar{c}(^3P_J,\underline{1}) + g$ diverges logarithmically (analogically $c \to c\bar{c}(^3P_J,\underline{1}) + c$)

$$D^{(0)}_{i\to\chi_J}(z) = \frac{\alpha_s^2(m_c)}{9\pi} \frac{\left|R'_\chi(0)\right|^2}{m_c^5} \mathcal{F}(\ln\frac{m_c}{\epsilon_0}), \tag{2.26}$$

where $R'_\chi(0)$ is the derivative of the radial wave function of χ_{cJ} charmonium state. The presence of the infrared divergence clearly spoils the factorization assumption of the color-singlet model. An additional non-perturbative parameter has to be introduced in order to still separate the long- and short-distance contributions [9, 28]. In (2.26) infrared divergence, associated with the soft limit of the final-state gluon, has been made explicit by the introduction of a lower cutoff ϵ_0 on the gluon energy in the quarkonium rest frame. But even with the introduced cutoff, the color-singlet model still encounters difficulties to reproduce the high-p_T prompt charmonium production measured by CDF experiment [34]. By including fragmentation mechanisms the theoretical predictions for prompt J/Ψ production can be brought to rough agreement with the data, relating remaining discrepancy to theoretical uncertainties in the P-wave fragmentation. However, this conclusion of a rather successful description of J/Ψ production relies on the postulation of a very large $g \to \chi_{cJ}(1P)$ fragmentation contribution where the χ_{cJ} subsequently decays into J/Ψ. There is no such contribution for Ψ'. Therefore, the prediction of its production rate falls far below the data, casting doubts [4] on the correctness of the picture of the J/Ψ production.

[4]The ad hoc introduction of (not-yet) observed charmonium states above the $D\bar{D}$ threshold such as higher P-wave or D-wave states appears quite questionable [28]. Only with very optimistic production rates and branching fractions into Ψ' can one account for the observed rate for prompt Ψ' to J/Ψ production [31]

It is clear that a generalization of the naive factorization a la (2.22,2.25) is necessary for the description of charmonium production.

2.5.3 Non-relativistic QCD

The two previous sections discussed two extreme scenarios to describe production cross-sections and decay rates of charmonium. In CEM (2.20), no constraints are imposed on the color and angular momentum states of the $c\bar{c}$ pair. Non-perturbative QCD effects, mediating the transition to the color-singlet hadronic state $\mathcal{CH}(J^{PC})$ containing the $c\bar{c}$ pair, are assumed to be universal and negligible for the dynamics of $\mathcal{CH}$ ($\sqrt{s}$, p_T, etc.) dependence. The normalization factors for the various states are not predictable. Nevertheless, once being fixed phenomenologically, the model rather successfully fits the data.

The factorization assumption (2.22) of CSM, on the other hand, says that all non-perturbative effects are contained in a single term that can be expressed as the non-relativistic wave function of the bound state. In turn, relative production rates of different quarkonium states can be predicted. Moreover, different states may have different dynamical dependences since only specific short-distance cross-sections contribute to each state. However, the color-singlet model fails in two respects. First, predictions for S-wave states often are way off, and second logarithmic infrared divergences spoil the factorization in the case of P-wave. This failure of the color-singlet model can be traced back to that of the underlying quark potential model. Relativistic corrections, which realize in the velocity power counting rules, are essential for a description that is both consistent for P-wave states and successful for S-wave states.

In the approach of non-relativistic quantum chromodynamics (NRQCD) the cross-section (2.18) is organized in powers of v^2, the average velocity of the heavy (anti-)quark in the meson rest frame. The long-distance factors generated by the expansion can be identified as long-distance matrix elements $\langle O^{\mathcal{CH}}[n]\rangle$:

$$\langle O^{\mathcal{CH}}[n]\rangle = \sum_{X,\lambda} \langle 0|\chi^+ \mathcal{K}_n \psi|\mathcal{CH}(\lambda) + X\rangle\langle \mathcal{CH}(\lambda) + X|\psi^+ \mathcal{K}'_n \chi|0\rangle. \tag{2.27}$$

Here the sum is over the charmonium polarization λ and any number of light hadrons X in the final state. The ψ and χ are two-component spinor fields describing the heavy quark and antiquark, respectively. The factors $\mathcal{K}_n$ and $\mathcal{K}'_n$ can contain products of color and spin matrices as well as covariant derivatives [9]. The color and angular momentum quantum numbers of the intermediate $c\bar{c}$ pair need not be equal to those of the physical charmonium $\mathcal{CH}$. Soft gluons with energy of order $m_c v$ can be emitted before the formation of the bound state $\mathcal{CH}$, and change the color and spin of the pair. The effects of these soft gluons are included in the long-distance matrix elements $\langle O^{\mathcal{CH}}[n]\rangle$. In the framework of NRQCD both short-distance and long-distance coefficients in the expression (2.18) depend on the factorization scale μ_F. The factorization scale plays the role of an infrared cutoff in the short-distance term and an ultraviolet cutoff for long-distance matrix elements. The μ_F-dependence of the short-distance coefficient cancels with the μ_F-dependence of long-

distance matrix elements, removing, thus, the problem of infrared divergences encountered in (2.26) [28].

The matrix elements have to be calculated using non-perturbative methods or determined from experimental data. Since the coefficients $\hat{\sigma}$ are calculated as perturbation series in $\alpha_s(m_c)$, eq. (2.18) is really a double expansion in $\alpha_s(m_c)$ and v^2. For charmonium, the two expansion parameters are not independent: $v \approx \alpha_s(m_c v) > \alpha_s(m_c)$ [28]. Hence corrections of order v^n must not be neglected compared to those of order $\alpha_s^n(m_c)$. Which terms in (2.18) actually contribute to the production of a quarkonium $|\mathcal{CH}\rangle$ depends on both the $\alpha_s(m_c)$ expansion of $d\hat{\sigma}$ and the v^2 expansion of the matrix elements. The magnitude of various non-perturbative transition probabilities is determined using power counting rules [25]. They depend upon the relative size of three different energy scales (2.17). The power counting rules for the long-distance matrix elements $\langle O^{\mathcal{CH}}[n]\rangle$ in (2.18) can be derived by considering the Fock state decomposition of a charmonium state $\mathcal{CH}$ [9, 28],

$$|\mathcal{CH}\rangle = \psi_{c\bar{c}}^{\mathcal{CH}}|c\bar{c}\rangle + \psi_{c\bar{c}g}^{\mathcal{CH}}|c\bar{c}g\rangle + ... \tag{2.28}$$

The $c\bar{c}$ pair can be in either a color-singlet or a color-octet state with spin $S = 0, 1$ and angular momentum $L = 0, 1, 2, ...$ The dominant component $|c\bar{c}\rangle$ comprises a quark pair in a color-singlet state and with angular momentum quantum numbers ${}^{2S+1}L_J$ that are consistent with the quantum numbers of the charmonium. The higher Fock states, such as $|c\bar{c}g\rangle$, contain dynamical gluons or light quarks. All higher Fock states have probabilities suppressed by powers of v in comparison to $|c\bar{c}\rangle$.

The NRQCD formalism implies that color-octet processes associated with higher Fock state components of the charmonium wave function must contribute to the cross-section. $c\bar{c}$ pairs that are produced at short distances in color-octet state can evolve into a physical charmonium through radiation of soft gluons at late times in the production process, when the quark pair has already expanded to the charmonium size.

In this way NRQCD factorization approach provides a natural solution to the problem of infrared divergences encountered in (2.26). According to the NRQCD power counting rules, two terms contribute to the production cross-section of the P-wave states at leading order in the velocity expansion. For χ_{cJ} production one has

$$\begin{aligned} d\sigma(\chi_{cJ} + X) \propto \quad & d\hat{\sigma}(c\bar{c}[1,^3P_J] + X)\langle O^{\chi_{cJ}}[1,^3P_J]\rangle + \\ & d\hat{\sigma}(c\bar{c}[8,^3S_1] + X)\langle O^{\chi_{cJ}}[8,^3S_1]\rangle + \mathcal{O}(v^2). \end{aligned} \tag{2.29}$$

The matrix element $\langle O^{\chi_{cJ}}[1,^3P_J]\rangle$ can be related to the derivative of the radial wave function at the origin, and the first term in equation (2.29) corresponds to the expression of CSM. The second term represents the contribution of the color-octet mechanism: the short distance factor is the cross-section for producing $c\bar{c}$ pair in a color-octet ${}^3S_1$ state, and the corresponding long-distance matrix element $\langle O^{\chi_{cJ}}[8,^3S_1]\rangle$ describes the probability of such a $c\bar{c}[8,^3S_1]$ pair to form a χ_{cJ} state of charmonium. According to the NRQCD power counting rules, the $\langle O^{\chi_{cJ}}[1,^3P_J]\rangle$ and $\langle O^{\chi_{cJ}}[8,^3S_1]\rangle$ matrix elements scale with the same power of velocity $\sim v^5$ and must both be included in a consistent theoretical

description. Other terms in the general factorization formula are suppressed by relative order of v^2 or more. The infrared divergences in color-singlet short-distance cross-section $d\hat{\sigma}(c\bar{c}[1,3_J^P]+X)$ at the next-to-leading order is canceled by a matching infrared singularity from the radiative corrections to the color-octet matrix element $\langle O^{\chi_{cJ}}[8,^3S_1]\rangle$.

color-octet processes are necessary for a consistent description of P-wave charmonium, but they can be even more important phenomenologically for the S-wave states like J/Ψ and Ψ'. In the non-relativistic limit $v \to 0$, the NRQCD description of S-wave charmonium production reduces to the color-singlet processes. However, color-octet contribution can become significant, and even dominant, if the short-distance cross-section for producing $c\bar{c}$ in a color-octet state is enhanced. The experimental studies of J/Ψ and Ψ' direct production show that the simple treatment in the framework of color-singlet processes is not sufficient to reproduce the phenomenology. At the same time the inclusion of the color-octet mechanism in the consideration removes that discrepancy (see Fig. 2.4).

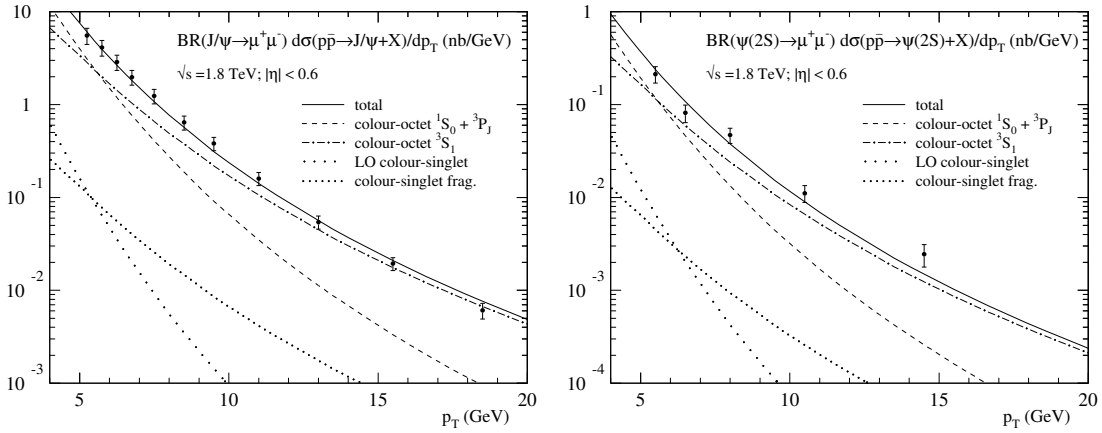

Figure 2.4: *Experimental data of direct J/Ψ (left) and Ψ' (right) production measured at CDF [30]. The lines show the theoretical predictions based on color-octet and/or color-singlet mechanisms [9]. The plot is taken from reference [9].*

2.5.4 Production in hadronic interactions.

The J/Ψ and Ψ' production in hadron-hadron collisions via leading order in color-singlet mechanism is represented in Fig. 2.5(a). At large transverse momentum, the two internal quark propagators are off-shell by $\sim p_T^2$ so that the parton differential cross section scales like $d\sigma/dp_T^2 \sim 1/p_T^8$, as indicated in the figure. On the other hand, when $p_T \gg 2m_c$ the charmonium mass can be considered small and the inclusive charmonium cross-section scales like any other single-particle inclusive cross-section $\sim 1/p_T^4$. The dominant production mechanism for charmonium at sufficiently large values of p_T must, thus, proceed via fragmentation, the production of a parton with large p_T which subsequently decays into charmonium and other partons [9]. A typical fragmentation contribution for color-singlet production of J/Ψ is shown in Fig 2.5(b). While the fragmentation contributions are

(a) leading order color-singlet: $g + g \to c\bar{c}[^3S_1^{(1)}] + g$

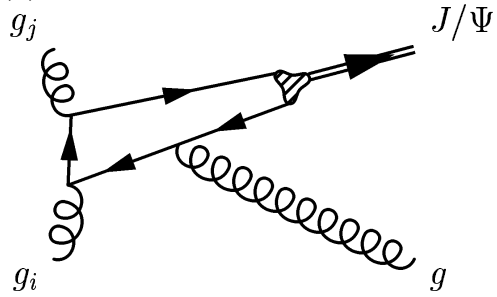

$+...$ $\sim \alpha_s^3 \frac{(2m_c)^4}{p_T^8}$

(b) color-singlet fragmentation: $g + g \to \left[c\bar{c}[^3S_1^{(1)}] + gg\right] + g$

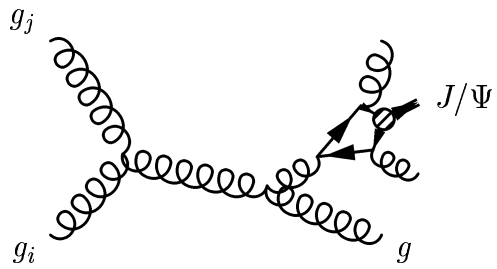

$+...$ $\sim \alpha_s^5 \frac{1}{p_T^4}$

(c) color-octet fragmentation: $g + g \to c\bar{c}[^3S_1^{(8)}] + g$

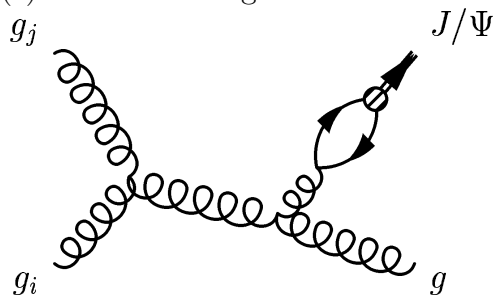

$+...$ $\sim \alpha_s^3 \frac{1}{p_T^4} v^4$

(d) color-octet t-channel gluon exchange: $g + g \to c\bar{c}[^3S_0^{(8)}, ^3P_J^{(8)}] + g$

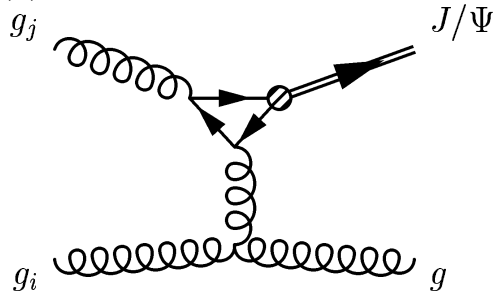

$+...$ $\sim \alpha_s^3 \frac{(2m_c)^2}{p_T^6} v^4$

Figure 2.5: *Generic diagrams for J/Ψ and Ψ' production in hadron-hadron collisions through color-singlet and color-octet processes.*

of higher order in α_s compared to the fusion process in Fig 2.5(a), they are enhanced by a power $p_T^4/(2m_c)^4$ at large p_T and can, thus, overtake the fusion contribution at $p_T \gg 2m_c$. When the color-singlet (Fig. 2.5(b)) and color-octet (Fig. 2.5(c)) fragmentations are included, the p_T dependence of theoretical predictions comes to agreement with the measurements at Tevatron [30]. In is now believed that the gluon fragmentation into color-octet ${}^3S_1$ charmed quark pairs, shown in Fig. 2.5(c), is the dominant source of J/Ψ and $\Psi^{'}$ at large p_T. At moderate p_T, i.e. $p_T \sim 2m_c$, the importance of the $c\bar{c}[\underline{8},{}^1S_0]$ and $c\bar{c}[\underline{8},{}^3P_J]$ contributions follows from the dominance of t-channel gluon exchange, shown in Fig. 2.5(d), which is forbidden in the leading-order color-singlet cross-section.

In fixed-target interactions the spin and color state that can be produced at order α_s^2 are as follows:

$$\begin{aligned} gg \to c\bar{c}[n]: \quad & n = {}^1S_0^{(1,8)},\ {}^3P_{0,2}^{(1,8)},\ {}^1P_1^{(8)},\ D-waves, ... \\ q\bar{q} \to c\bar{c}[n]: \quad & n = {}^3S_1^{(8)},\ D-waves, ... \end{aligned} \tag{2.30}$$

At relatively high energies ($4m_c^2/s \ll 1$), the production cross-sections are dominated by gluon-gluon fusion. Consequently, the P-wave feed-down incorporated for J/Ψ is entirely color-singlet at the leading order [25]. Consequently, at energies where $q\bar{q}$ annihilation is irrelevant, $\sigma_{\chi_{c1}}/\sigma_{\chi_{c2}} = \mathcal{O}\left(\frac{\alpha_s}{\pi}\right) \sim 0.05$, which is rather small compared to data [11, 12]. However, the addition of relativistic corrections in the velocity expansion that scale as v^4 makes the χ_{c1} production cross-section an order of magnitude larger and $\sigma_{\chi_{c1}}/\sigma_{\chi_{c2}} \sim 0.3$ [25], which agrees with the measurements in pA collisions [11, 12]. Thus, color-octet contributions are important components for a consistent description of the charmonium production in fixed-target experiments.

2.6 Nuclear effects

The target nucleon in HERA-B is part of a nucleus. Consequently, one must consider modifications to the bare nucleon-nucleon cross-section. The dependence of particle production on the atomic mass number A is conventionally parameterized by a power law [31]:

$$\sigma_{pA} = \sigma_{pN} A^{\alpha}, \tag{2.31}$$

where σ_{pA} and σ_{pN} are the particle production cross-sections in proton-nucleus and proton-nucleon interactions, respectively. In the absence of nuclear effects, charmonium production is expected to follow a linear dependence with larger A. However, measurements of the total cross-section of J/Ψ performed at various combinations of projectile and target, which are summarized in [31], show a small nuclear suppression. The experimental values of α vary in the range $0.85 - 0.96$. In addition, the data show that the shape of the differential cross-sections depends on A. The differential distributions usually are parameterized in terms of x_F and p_T. The average p_T of a charmonium state increases with the atomic number of target material, which is usually called p_T broadening, whereas the average x_F shifts to smaller values with A.

These observations of nuclear dependence of charmonium production can be explained by a variety of processes, which may affect initial and final stages of the production process. It makes sense to distinguish between initial state effects, which influence the creation of the heavy quark pair,

- *nuclear shadowing*,
- *initial state energy loss*,
- *intrinsic charm*

and final state effects, which affect the evolution of the $c\bar{c}$ quark pair into a bound state,

- *nuclear absorption*,
- *absorption by co-moving secondaries*
- *final state energy loss*.

When the incoming partons carry small fraction of the incoming proton momentum, shadowing of the sea quarks and gluons in the nucleus may lead to a change in the initial parton densities. This effect becomes more important with increasing beam energies, where smaller momentum fractions are probed. Elastic initial-state scattering of the partons in the projectile as they break through the target can influence x_F and p_T distribution of the charmonium state. A $c\bar{c}$ component in the projectile wave function could imply a different nuclear dependence for this component with respect to the normal production processes at large x_F.

Once a $c\bar{c}$ pair is produced, it may be absorbed by the nucleons in the target and/or interact with secondary particles produced in the collision and co-moving with the pair. There is a connection between final state effects and the charmonium production model, since colored states are expected to have a different nuclear absorption cross-section than singlet states [31, 32].

The interest in nuclear effects in charmonium production comes mainly from their importance as a probe of deconfinement in heavy ion collisions [3]. It is assumed that in the nuclear environment the main source of $c\bar{c}$ dissociation are soft gluons. In a deconfined medium the average momentum of such gluons is a few times higher than in normal confined matter. Consequently, one expects a sharp increase of nuclear suppression of Ψ production if a deconfined medium is created. Such an effect has recently been reported by the NA50 Collaboration [33]. Since extra-ordinary claims require extra-ordinary evidence, a full understanding of the normal charmonium production mechanisms in nucleus-nucleus collisions is essential, before any conclusions on the existence of a deconfined medium can be made.

2.7 Experimental tests

As already mentioned, the CSM prediction calculated at lowest order in α_s fails when confronted with experimental data, as measured in $p\bar{p}$ [30, 34] and pA [11, 12] collisions. When the color-singlet fragmentation is included, the discrepancy decreases by more than an order of magnitude, but it still falls significantly below the experimental points. experimental results [9, 25] (see also Fig. 2.4). On the other hand, color-octet mechanisms have to be included in a theoretically consistent description of χ_c production. While the disagreement between the CSM predictions and experimental results [34] is less dramatic than in the case of S-wave states of charmonium, the inclusion of the ${}^3S_1$ color-octet process (2.29) significantly improves the theoretical predictions (Fig 2.6).

Charmonium production was also investigated in $e^+e^- \to J/\Psi X$. The data obtained at LEP [35] favor the NRQCD predictions over those of the CSM. The J/Ψ total cross-sections measured in $e^+e^- \to J/\Psi X$ at BaBar [36] and Belle [53] also seem to favor NRQCD although being incompatible with each other. The measurement done by Belle collaboration [37] showed that most of the produced J/Ψ's are accompanied by an additional $c\bar{c}$ pair: $\frac{\sigma(e^+e^-\to J/\Psi c\bar{c})}{\sigma(e^+e^-\to J/\Psi X)} \approx 0.59$, while predictions based on perturbative QCD together with CSM estimate this ratio to be about 0.1 [38].

The NRQCD predictions deviate from photoproduction data [39] near large photon-momentum fractions, owing to the large color-octet contribution at the leading order of the calculations. The CSM calculations performed at the NLO level agree with the data over all momentum fractions, as well as with the data as a function of p_T. In the case of deep-inelastic scattering [40], the Q^2 and p_T dependencies are in agreement with NRQCD, but the results are more ambiguous for the dependence on the longitudinal momentum fraction. However, in the last two cases the measurements are sensitive to the intrinsic transverse momentum of the partons, which impairs the test of NRQCD predictions.

Being very encouraging, the existing results do not provide a conclusive test of NRQCD factorization. A good fit to the Tevatron and fixed-target data can be done by CEM, which like NRQCD allows color-octet production of $c\bar{c}$ pair.

The theoretical situation is, thus, far from being clear and demands more experimental

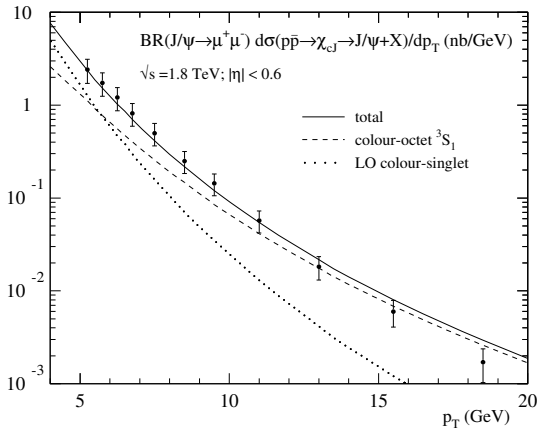

Figure 2.6: *Experimental data of χ_c production measured at CDF [34]. The lines show the theoretical predictions based on color-octet and/or color-singlet mechanisms [9]. The plot is taken from reference [9].*

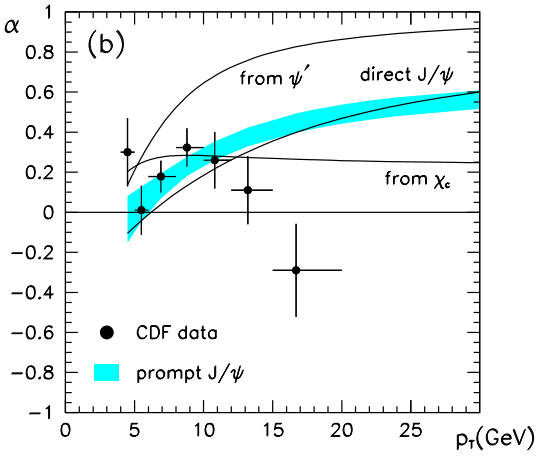

Figure 2.7: *Polar angle asymmetry α for prompt J/Ψ production in $p\bar{b} \rightarrow J/\Psi(\rightarrow \mu^+\mu^-) + X$ at Tevatron as a function of p_T. The experimental points are taken from [41] and theoretical predictions from [46].*

tests, which can be performed by studying

- polarization of charmonium states;
- nuclear suppression;
- relative cross-section of different states.

The polarization signature of J/Ψ and $\Psi^{'}$ production at large transverse momentum can be one of the most crucial tests of the NRQCD approach. The NRQCD approach incorporates the spin symmetry of QCD in the heavy quark limit, which implies transverse polarization of J/Ψ and $\Psi^{'}$ at large p_T [9]. In contrast, the CEM assumes unsuppressed gluon emission from $c\bar{c}$ pair during hadronization, which randomizes spin and color, and, consequently, predicts unpolarized charmonium.

CDF measurements [41] do not support the distinctive NRQCD prediction transverse polarization of J/Ψ (see Fig 2.7). The results from fixed-target experiments performed with incident pions [42, 43, 44, 45] and protons also do not show large effects. However, the polarization effect at fixed-target energies is not expected to be strong neither. For pion beams polarization is compatible with zero for both J/Ψ and Ψ'. Two measurements were done with incident protons: by E771 [47] and E866 [48] collaborations. The result from E771 shows a J/Ψ polarization compatible with zero. The E866 measurement comprises a much larger statistic but only for $x_F \in [0.2; 0.8]$ and with insufficient momentum resolution to separate J/Ψ and Ψ'. E866 measured $\lambda > 0$ for $x_F \in [0.2; 0.6]$ and $\lambda < 0$ for x_F in the range $[0.6; 0.8]$ (parameter λ is defined in (2.19)).

The J/Ψ polarization has been studied at BaBar [36] also. The measurements show no evidence of the transverse polarization, as a result of color-octet production mechanism. However it could be explained by the fact that the center-of-mass momentum is rather small and the polarization is not expected to be large in general.

The available experimental results indicate that either the present uncertainties in the determination of matrix elements, higher order QCD effects, feed-down from higher states could be crucial to describe the spin-dependence of charmonium cross-section or the predictions based on the NRQCD approach might not be able to accommodate the observed

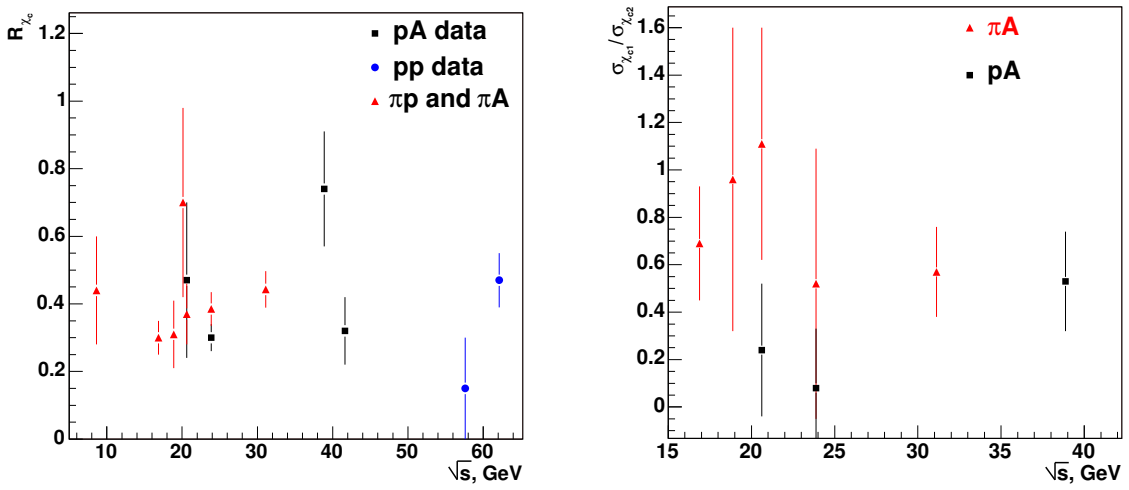

(a) (b)

Figure 2.8: *Experimental results on R_{χ_c} [49, 50, 51] (a) and $\sigma_{\chi c1}/\sigma_{\chi c2}$ [11, 12, 52] (b), obtained in pp, $p\bar{p}$, πA and pA collisions.*

results on charmonium polarization. On the other hand, the uncertainties assigned to both NRQCD predictions and experimental results are still too large to provide a clear proof or disproof of the NRQCD prediction.

Under such circumstances the experimental study of the relative production of χ_c charmonium states looks very attractive. Many uncertainties should cancel out in ratios of the cross-sections and, thus, increase the precision of the test. Moreover, the measurement of the fraction of J/Ψ produced via χ_c decays, R_{χ_c} is itself of great interest as far as many distinctive predictions for J/Ψ, like polarization and A-dependence are dependent on uncertainties related to the feed-down from χ_c states. Therefore, the measurement of χ_c production in proton-nucleus collisions can bring a considerable improvement in the understanding of the production mechanism.

2.8 Existing measurement of R_{χ_c} and $\sigma_{\chi c1}/\sigma_{\chi c2}$

Table 2.6 presents a summary of the previous experimental results on R_{χ_c} and $\sigma_{\chi c2}/\sigma_{\chi c1}$. The ratio R_{χ_c} is defined as

$$R_{\chi_c} = \frac{\sum_{i=1,2} \sigma_{\chi ci} Br(\chi_{ci} \to \gamma J/\Psi)}{\sigma(J/\Psi)},$$

where $\sigma_{\chi_{ci}}$ and $\sigma(J/\Psi)$ are the total production cross-sections for χ_{ci} and J/Ψ, respectively, including the feed-down from higher states; $Br(\chi_{ci} \to \gamma J/\Psi)$ is the branching ratio of the χ_{ci} radiative decay to J/Ψ. The prediction based on CSM and NRQCD as-

Table 2.6: *Experimental results on R_{χ_c} [49, 50, 51, 53, 54] and $\sigma_{\chi_{c1}}/\sigma_{\chi_{c2}}$ [11, 12, 52] obtained in experiments reffered in pp, $p\bar{p}$, πA, pA, e^+e^- and γA collisions.*

Experiment	Interaction	$\sqrt{s}$, GeV	R_{χ_c}	$\sigma_{\chi_{c1}}/\sigma_{\chi_{c2}}$
proton-nucleus collisions				
E610	pBe	19.4, 21.7	0.47 ± 0.23	0.24 ± 0.28
E705	pLi	23.8	0.30 ± 0.04	$0.08^{+0.25}_{-0.15}$
E771	pSi	38.8	0.74 ± 0.17	0.53 ± 0.21
HERA-B	pC, Ti	41.6	0.32 ± 0.10	–
pp and $p\bar{p}$ collisions				
R702	pp	52, 63	$0.15^{+0.10}_{0.15}$	–
ISR	pp	62	0.47 ± 0.08	–
CDF	$p\bar{p}$	1800	0.297 ± 0.059	1.04 ± 0.31*
πp and πA collisions				
IHEP140	$\pi^- p$	8.5	0.44 ± 0.16	–
WA11	$\pi^- Be$	16.8, 18.7	0.30 ± 0.05	0.69 ± 0.24
E610	$\pi^- Be$	18.9	0.31 ± 0.10	0.96 ± 0.64
E673	$\pi^- H_2, Be$	20.2	0.70 ± 0.28	–
E369	$\pi^- Be$	20.6	0.37 ± 0.09	1.11 ± 0.49 *
E705	$\pi^- Li$	23.8	0.37 ± 0.03	$0.52^{+0.57}_{-0.27}$ **
E705	$\pi^+ Li$	23.8	0.40 ± 0.04	–
E672/706	$\pi^- Be$	31.1	0.443 ± 0.054	0.57 ± 0.19
e^+e^- and γA collisions				
Belle	e^+e^-	10.6	< 0.18	–
NA14	γLi	13.0	< 0.08	–

* Obtained using the $\sigma_{\chi_{c2}}/\sigma_{\chi_{c1}}$ measurement.
** Average for π^- and π^+ data.

sume that the values of R_{χ_c} and $\sigma_{\chi_{c1}}/\sigma_{\chi_{c2}}$ depend on the c.m.s. energy in the collision [5]. CEM predicts flat dependency on $\sqrt{s}$, however the absolute values of the ratios are not specified. Moreover, according to the CEM predictions, there should be no difference for the results obtained with proton and pion beams. Results obtained with incident pion beam seem to support the ascending of R_{χ_c} with the c.m.s. energy in the interaction (Fig. 2.8(a)). However, at the present level of experimental uncertainties CEM cannot be excluded. The few experimental points obtained in pp and pA collisions are not enough to draw any conclusion. NRQCD prediction for R_{χ_c} ($\sigma_{\chi_{c1}}/\sigma_{\chi_{c2}}$) is about 0.3 (0.3), while the calculation based on CSM gives a value of about 0.7(0.08), for pN data [6]. CSM clearly overestimates the ratios. The observed discrepancies in absolute scale between the data and NRQCD prediction can be related to the uncertainty in the estimated value of long-

[5]The $\sigma_{\chi_{c1}}/\sigma_{\chi_{c2}}$ ratio obtained in fixed-target experiments should be approximately independent if the production through the $q\bar{q}$ annihilation channel can be neglected [25].

distance matrix elements. $\sigma_{\chi_{c1}}/\sigma_{\chi_{c2}}$ ratio, on the other hand, should not depend on this uncertainty. They simply cancel in the cross-section ratio. Therefore, the measurement of $\sigma_{\chi_{c1}}/\sigma_{\chi_{c2}}$ gives a better test of the prediction based on NRQCD. The experimental results obtained in interactions of pions and protons with nuclei are presented in Fig. 2.8(b). As in case of R_{χ_c}, experimental data do not exclude CEM, yet.

Chapter 3

The HERA-B Experiment

HERA-B is a fixed-target experiment operating at the HERA-ep storage ring at DESY. Charmonium and other heavy flavor states are produced in inelastic collisions by inserting wire targets into the halo of the 920 GeV proton beam circulating in HERA. The pN (N = p,n) c.m.s. energy is $\sqrt{s} = 41.6\ GeV$. The detector is a magnetic spectrometer emphasizing vertexing, tracking and particle identification, with a dedicated J/Ψ-trigger. The components of the HERA-B detector used for this analysis include a Silicon Strip Vertex Detector, honeycomb drift chambers and micro-strip gaseous chambers of the Tracking System, a large acceptance Magnet, a finely segmented "shashlik" Electromagnetic Calorimeter, and a Muon System consisting of wire chambers interleaved with iron shielding which detects muons with momenta larger than 5 GeV/c. The HERA-B detector allows an efficient reconstruction of particles with momenta larger than 1 GeV/c, including γ's and π^0's, within the acceptance. Two views (top and side) of the apparatus are shown in Fig. 3.1. The HERA-B coordinate system takes its origin at the target. The z-axis is directed along the proton beam, the y-axis points upward while the direction of the x-axis extends towards the center of the HERA ring. The HERA-B magnet provides a magnetic field integral of 2.2 $T \cdot m$. The main bending component of the inhomogeneous magnetic field is directed along the y axis. Accordingly, the coordinate planes of the detector coordinate system, zx and zy, are called *bending* and *non-bending* planes, respectively. In the following, we describe the main components relevant to the present analysis. A detailed description of the apparatus is given elsewhere [55].

3.1 Proton beam and HERA-B target system

Protons in the HERA-p beam are arranged in bunches separated by 96 ns. In total, there are 220 bunches. Only 180 of these are filled.

A group of 10 consecutive bunches form a train. The trains are arranged in three groups of six elements. One group corresponds to one PETRA fill (Fig. 3.2). The bunches are separated by one empty bunch within each group. The groups are spaced by 5 empty bunches. The last two bunches of each group are called *pilot bunches*. They are less populated and barely contribute to the rate. The last 15 bunches are left empty to

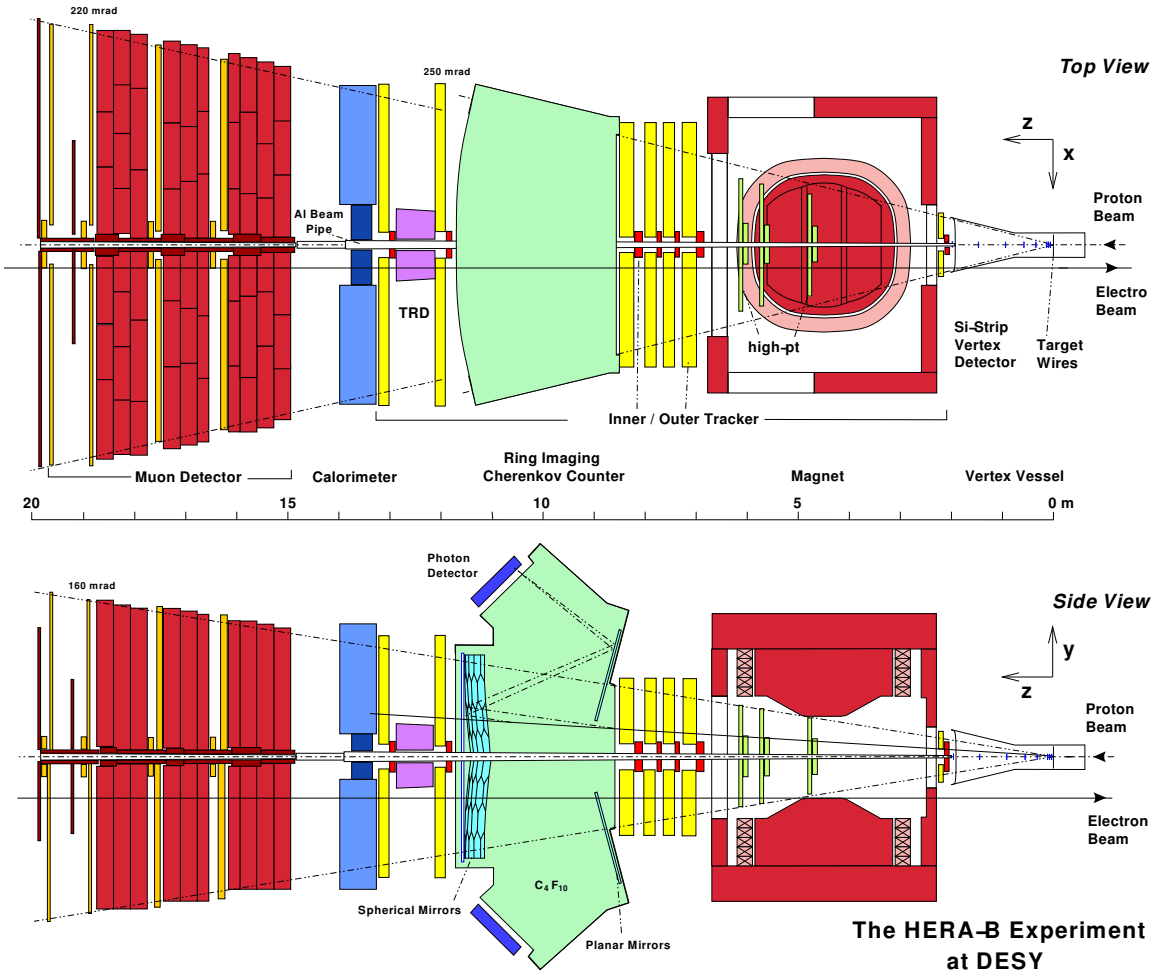

Figure 3.1: *The HERA-B spectrometer*

permit a safe beam dump.

Table 3.1: *HERA-B target set-up during data taking in 2002-2003. Here Al, C, W, Re, Ti and Pd denote aluminum, carbon, tungsten, rhenium, titanium and palladium, respectively.*

target	usage	material	shape
above1		Al	ribbon, $50\mu m \times 500\mu m$
below1	yes	C	ribbon, $100\mu m \times 500\mu m$
inner1[a]	yes	W / W+Re	round, $50\mu m$ diameter
outer1		Ti	round, $50\mu m$ diameter / round, $100\mu m$ diameter
above2		Pd	round, $50\mu m$ diameter
below2[b]	yes	Ti / W+Re	round, $50\mu m$ diameter / round, $50\mu m$ diameter
inner2	yes	C	ribbon, $100\mu m \times 500\mu m$
outer2[c]	yes	C / W	ribbon, $100\mu m \times 500\mu m$ / ribbon, $50\mu m \times 500\mu m$

[a]The change from W to W+Re was done on 06.02.2003
[b]The change of material was on 06.02.2003
[c]The change from C to W took place on 02.01.2003

The HERA-B target station houses 8 target wires which can be moved independently into the beam halo (Fig. 3.3). Their positions are steered such that the proton interaction rates are equalized for the targets in use [56]. The individual contribution of each wire is monitored with the help of charge integrators. The interaction rate is measured by a set of scintillator hodoscopes located behind the Ring Imaging Cherenkov Detector.

The analysis presented here is based on data collected at the end of 2002 and beginning of 2003. The analyzed data were taken with different wire materials (mainly Carbon (C) and Tungsten (W)) in single or double wire running mode. The proton-nucleus interaction rate was approximately 5MHz. Table 3.1 summarizes the target set-up during the data taking.

3.2 Vertex Detector System

The Vertex Detector System (VDS) of the HERA-B experiment is a forward micro-vertex detector integrated into the HERA proton storage ring. It provides high resolution tracking near the interaction point, which is necessary for precision measurement of vertices and impact parameters of particles.

The VDS comprises eight super-layers (SLs) of four quadrants (Fig. 3.4) arranged perpendicular to the beam axis. The quadrants of each super-layer are equipped with two double-sided silicon micro-strip detectors (64 in total) that provide four stereo views of $\pm 2.5^o$ and $90^o \pm 2.5^o$. The first seven super-layers are realized as a Roman pot system - 5 pots per quadrant. Together with the target wire stations, they are placed in a 2.6 m

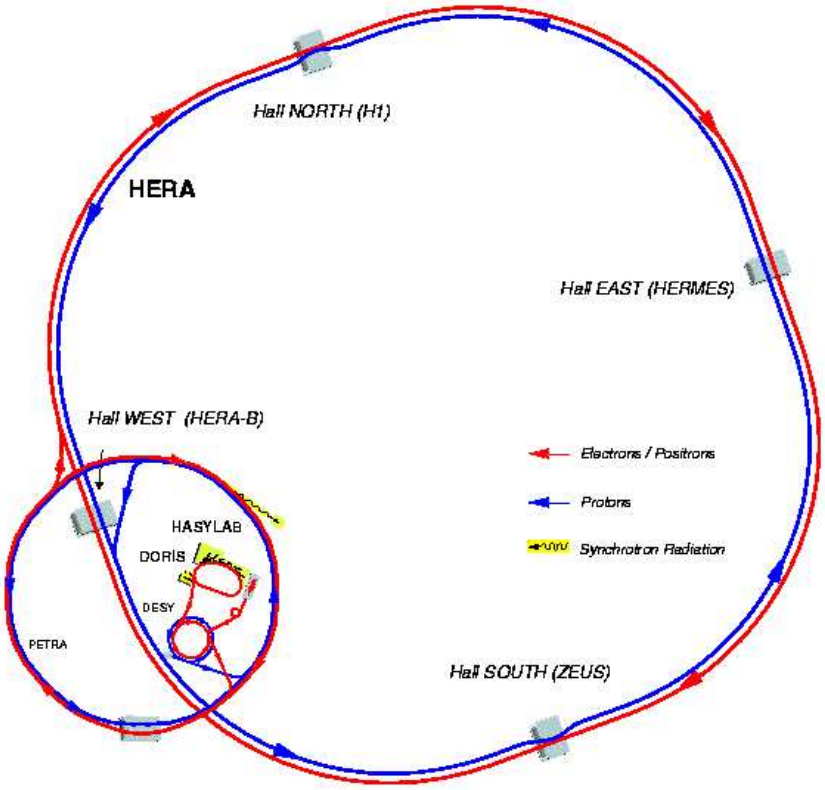

(a)

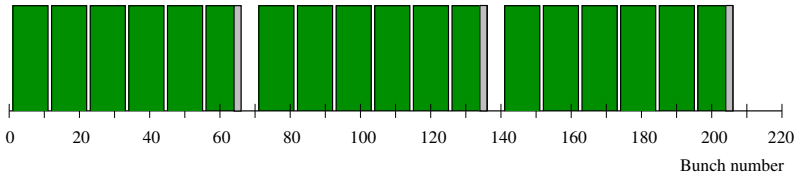

(b)

Figure 3.2: *HERA and HERA-p bunch structure: (a) The layout of HERA-ep storage ring, its pre-accelerators and experiments which used the facility. (b) Schematic view of the HERA-p bunch structure. Each filled rectangle corresponds to a train. Light filled strips at the end of each of three groups are the 6 pilot bunches.*

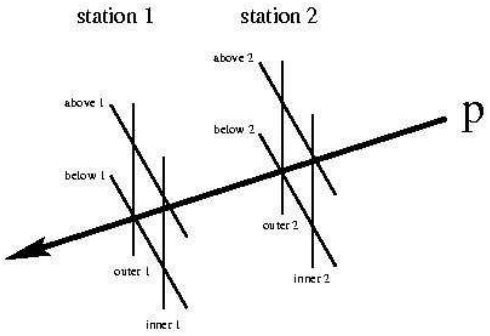

Figure 3.3: *Schematic view of the target configuration during the 2002-2003 data taking period*

long stainless steel ultra-high vacuum (UHV) vessel at 10^{-6} $mbar$ pressure. The detector modules are mounted at the end of the pots and separated from the vacuum of the beam pipe by 150 μm thick aluminum caps. The pots are movable in radial and lateral directions, which allows insertion and retraction in and out of the irradiated region. The nominal radial distance of the detectors to the beam is 10 mm. The 8^{th} super-layer is mounted stationary behind the 3 mm thick aluminum exit window of the UHV vessel, 2 m downstream the target. The system covers an angular range from 10 to 250 mrad.

The double-sided silicon strip sensors are made of 280 μm thick n-type material. The n-side strips are insulated with p^+ blocking implants or by a moderated p-spray layer. The active area of the sensors is 50×70 mm^2. The p- and n-sides have 1024 and 1280 readout strips, respectively, at a pitch of 50 μm.

The performance of the detector during the operation in 2002-2003 was close to design expectations, with a hit efficiency above 95 % and spatial resolutions of order 50 μm and 500 μm in transverse and longitudinal directions respectively [57]. A detailed description of the system can be found elsewhere [55, 58]

3.3 HERA-B Main Tracking System

The Tracking System, which provides with the spatial position of particles crossing the detector along 10 meters, comprises 7 super-layers. The system covers a polar angular range from 10 mrad up to 220 mrad (zx plane) and up to 160 mrad (zy plane).

Technologically, the tracking system is divided in two different parts, the Inner Tracker (ITR) and the Outer Tracker (OTR), which are described in the following subsections.

According to the functional purposes, the tracking system is stretched along the proton beam to provide the necessary information for tracking, momentum measurement and triggering:

- Superlayers, MS1 and MC1, belonging to Inner and Outer Tracker, respectively, are placed in the magnet entrance.

- The core of the tracking system is made of four superlayers MS10-13 of the ITR and

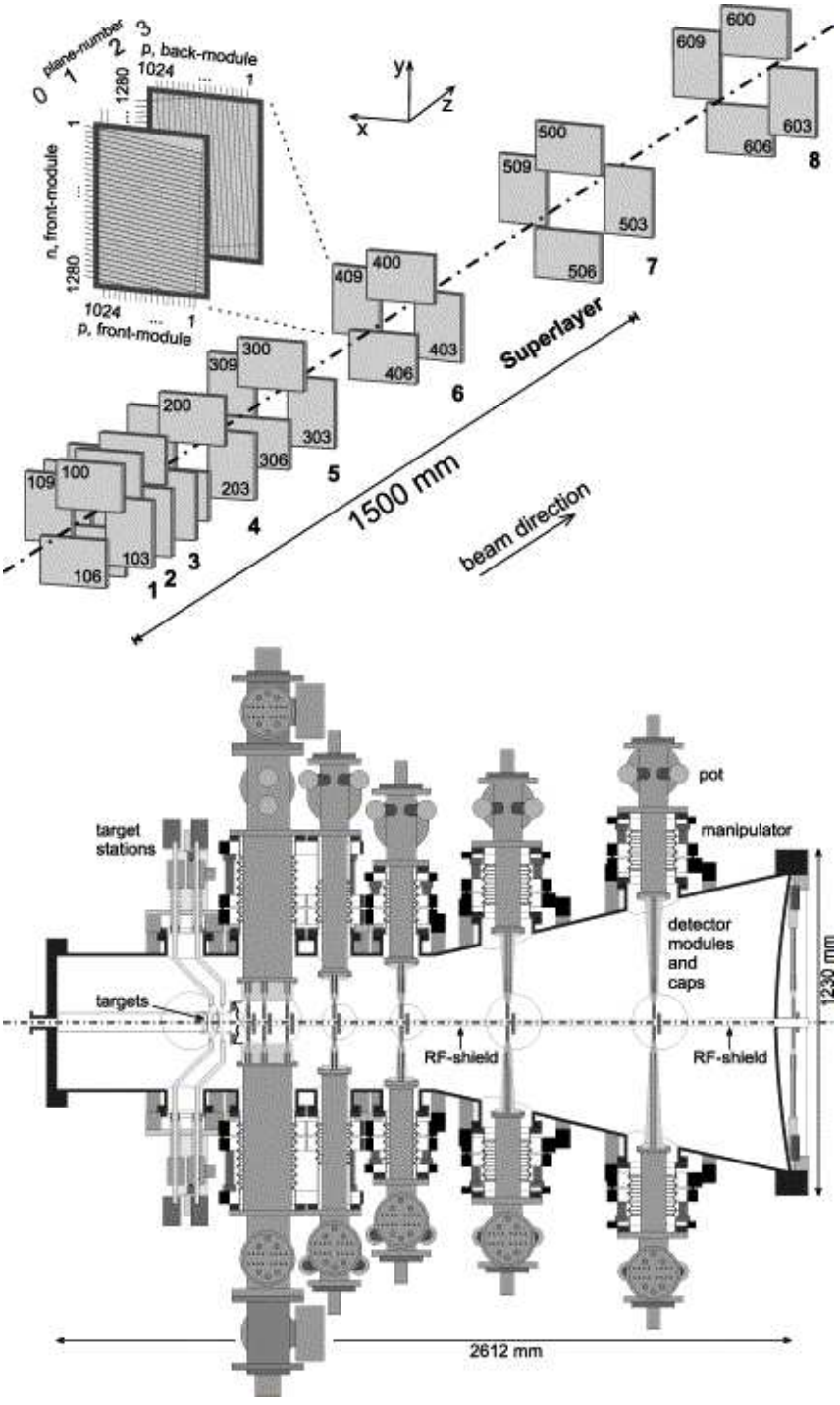

Figure 3.4: *The Vertex Detector System.*

four pattern recognition chambers PC1-4 of the OTR located between the magnet region and the Ring Imaging Cherenkov Detector (RICH).

- The two super-layers placed between the RICH and the Electromagnetic Calorimeter (ECAL) are supposed to provide with seeds to the candidates for the Trigger System and are named trigger chambers (TC1 and TC2) in case of the Outer Tracker and MS14,MS15 in case of the Inner Tracker.

Originally, additional super-layers, 3 for Inner Tracker (MS3,MS5,MS6) and 7 for Outer Tracker (MC2-MC8), were placed in the first half of the magnet. They were designed to perform tracking to VDS and for high efficiency reconstruction of $K_s^0 \to \pi^+\pi^-$ decay. The aim was to enhance the detection efficiency of $B^0 \to J/\Psi K_s^0$ decay, a mode HERA-B was originally designed for. However, during the 2001 shut-down they were removed in order to reduce the background for the trigger and, thus, better accomplish the new physical goals, mainly charmonium studies.

Another device, the High-Pt tracking system, was designed for fast tracking inside the magnet in order to identify hadrons with high transverse momentum at trigger level. Since this detector was not included in the common Data Acquisition system during the 2002-2003 running period, it is not discussed here.

The performance of the tracking system is evaluated upon two most important parameters of a tracking detector, which are the spatial resolution and the efficiency. The efficiency of the detector is the probability that a traversing particle is observed. The resolution determines how accurately the trajectory of the particle can be reconstructed and, therefore, the momentum resolution of the spectrometer can be determined.

3.3.1 Inner Tracker

To cope with high particle fluxes, the Inner Tracker (ITR), the region in radial distance from 5 cm up to 25 - 30 cm relative to the proton beam pipe, is instrumented with micro-strip gaseous chambers (MSGC).

The sensitive area of ITR (7.2 m^2) corresponds to 135,000 channels. The original design presented massive sparking in the electrodes under hadron irradiation and thus the 25×25 cm^2 MSGC was complemented with a gas-electron-multiplier (GEM) that allowed to reduce the cathode voltage while keeping the total multiplication factor.

The MSGC-GEM (Fig. 3.5) readout pitch is chosen to allow a spatial resolution of order $100\mu m$ in the zx plane and to keep the strip occupancy below 5 % level. There are two gas amplification steps. The first one, with gain factor of $15-100$, takes place at the GEM foil and the second one, with the gain factor of $200-1000$, at the MSGC wafer. The chambers are operated with a gas mixture of Ar/CO_2 with the proportion 70/30 %. The front-end readout is carried, similarly to VDS, by the HELIX128 chip [59].

During the 2002-2003 data taking period, the average hit efficiency was $80-90\%$ [60]. The presence of large fraction of dead channels and low efficiency of ITR stations made the system not suitable to be integrated in the trigger chain. Therefore, ITR played only a secondary role as tracking system.

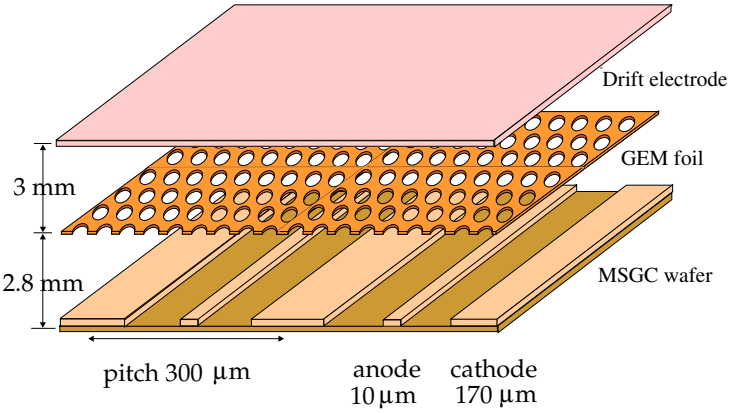

Figure 3.5: *Schematic view of GEM MSGC used for ITR.*

3.3.2 Outer Tracker

The Outer Tracker (OTR) provides coverage starting from about 25 cm from the beam pipe up to the whole aperture of the spectrometer, with the superlayers size from $0.6 \times 0.9m^2$ at the magnet entrance up to $6.5 \times 4.6m^2$ for the superlayer located in front of the Electromagnetic Calorimeter. Each super-layer is divided into two stations, the $+x$ and $-x$ halves, in order to allow lateral movement without interfering with proton and positron beam pipes traversing the detector at a distance of about 50 cm from each other (Fig. 3.6).

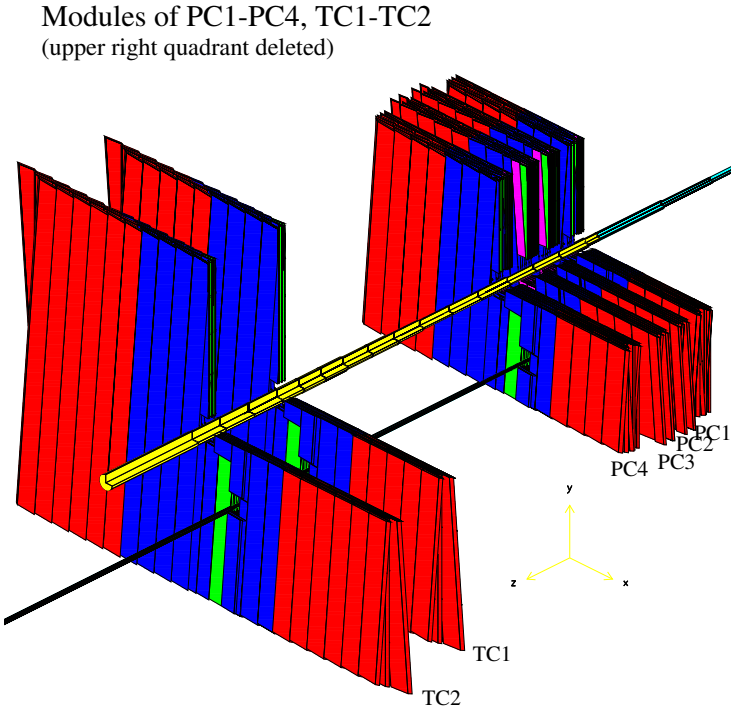

Figure 3.6: *3D view of OTR superlayers [61].*

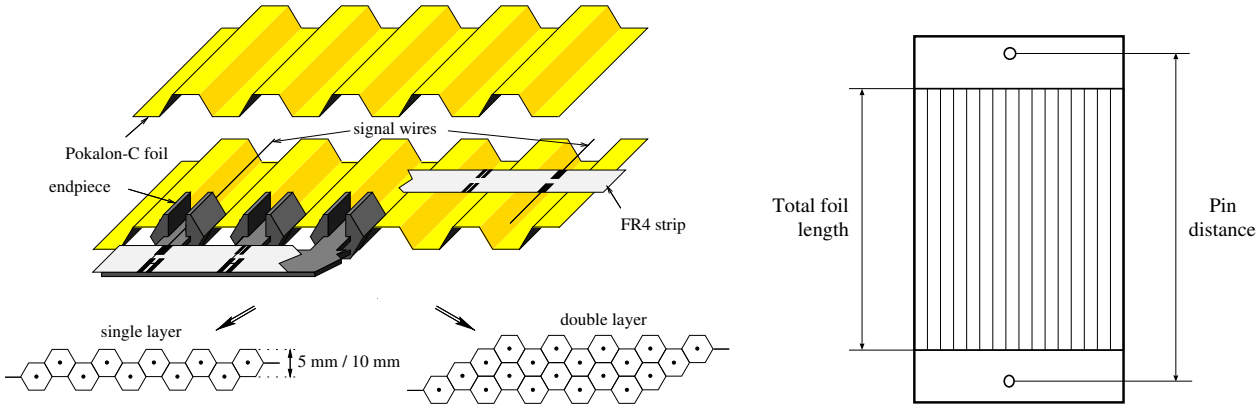

Figure 3.7: *Honeycomb modules for the Outer Tracker.*

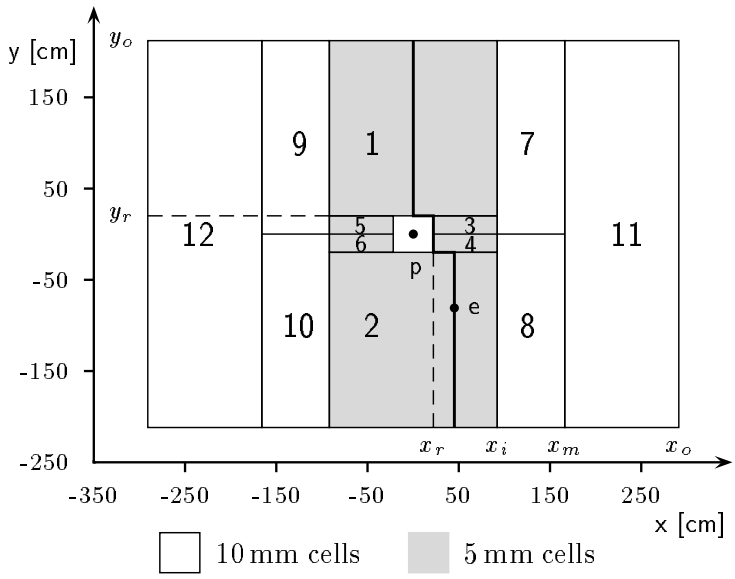

Figure 3.8: *Schematic view of superlayer sector structure in xy plane [61].*

The superlayers comprise measuring layers oriented at 0^o and $\pm 5^o$ with respect to the vertical direction. This allows measurements of tracks in tree different projections. That arrangement provides both the offline reconstruction and the trigger with measured space points. The layers are assembled from standard width modules of varying length. Modules consist of honeycomb drift tubes of up to 4.5 m length and are mounted inside a gas tight frame with the wires in the vertical direction. The construction and schematic view of the modules are presented in Fig. 3.7. A polycarbonate 75 μm thick foil is folded such that if staggered, it encloses hexagonal tubes. The foil has the required bulk conductivity to transport the ion current and is covered with a thin layer of copper and gold to provide sufficient surface conductivity. A gold-plated sense wire with diameter of 25 μm is positioned in the center of the tube and soldered onto non-conducting bromine-free FR4 strips glued across the cathode foils. Either two or four layers of tubes are

combined into single and double layer modules respectively. The four superlayers behind the magnet (PC1,PC4,TC1,TC2), used for triggering (Fig. 3.6), are realized as double layers (Fig. 3.7). This is done in order to ensure high trigger efficiency.

Each superlayer is logically segmented into 12 sectors of varying dimensions (Fig. 3.8), e.g smaller active areas near the beam pipe and larger active areas away from the beam. Depending on a sector, a wire pitch of cells is either 5 mm or 10 mm. The maximal size of the tube diameter is limited by the requirement that the drift time must be shorter than the period of bunch crossing, which is 96 ns. The minimal size is restricted by costs requirements.

In total, OTR comprises about 60,000 honeycomb drift tubes operating with $Ar/CF_4/CO_2$ gas mixture. The selected gas mixture in a volume ratio $Ar : CF_4 : CO_2 = 60 : 35 : 5$ is a relatively safe combination with respect to large drift velocity and large ionization density requirements as well as minimal aging effects.

During the 2002-2003 runs the OTR hit efficiency was at the level of 95% and 98% for 5 mm and 10 mm tubes, respectively. The track reconstruction efficieny was of order 97%. The resolution provided by the system was $370 - 400$ μm for the x-coordinate. [62].

3.4 The Electromagnetic Calorimeter

The main purpose of the Electromagnetic Calorimeter (ECAL) is to perform $e^{\pm}$, and γ detection and measurement, and to provide candidates to the First Level Trigger.

ECAL, placed at 13.5 m downstream the interaction region, is realized as a sampling calorimeter of "shashlik"-type modules. The size of quadratic module cells scales with the radial distance from the beam pipe in order to fit the particle flux gradient. This leads to the division of ECAL into *inner*, *middle* and *outer* radial parts with descending granularity (Fig. 3.9). The granularity is chosen in the way that electromagnetic shower develops in a 3×3 matrix of readout cells. The main parameters of ECAL are summarized in Table 3.2 [63] .

Table 3.2: *Parameters of the HERA-B electromagnetic calorimeter.*

	Inner part	Middle part	Outer part
outer size	156 cm $\times$ 89 cm	446 cm $\times$ 245 cm	624 cm $\times$ 468 cm
channels	2100	2128	1728
cell per module	5×5	2×2	1
absorber	W	Pb	Pb
volume ratio	$\frac{W}{Scintillator} = \frac{2}{1}$	$\frac{Pb}{Scintillator} = \frac{3}{6}$	$\frac{Pb}{Scintillator} = \frac{3}{6}$
Moliere radius	1.42 cm	4.15 cm	4.15 cm
cell size	2.24 cm $\times$ 2.24 cm	5.59 cm $\times$ 5.59 cm	11.18 cm $\times$ 11.18 cm
depth	13 $cm(23X_0)$	34 $cm(20X_0)$	34 $cm(20X_0)$

A photon or an electron with energy E deposits an energy E' in the calorimeter towers. The released energy produces a scintillation light L that is transformed into an electrical

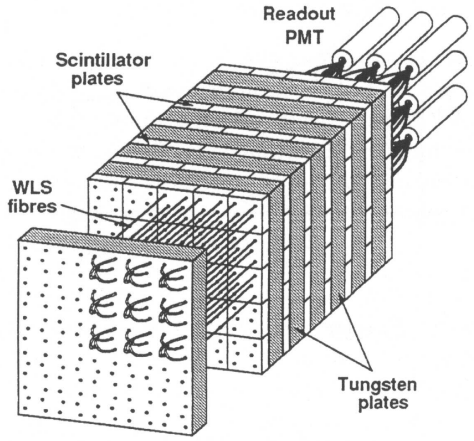

(a)

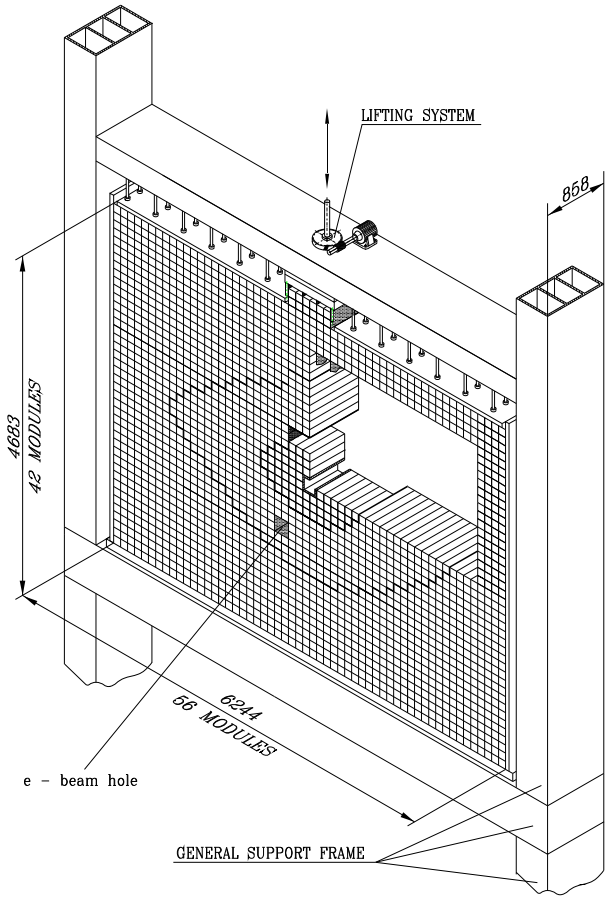

(b)

Figure 3.9: *The Electromagnetic Calorimeter: (a) Schematic view of a module from the inner part of ECAL. (b) Isometric view of the calorimeter; the inner, middle and outer parts are separated by the bold plotted lines; the numbers are given in mm.*

current $\mathcal{I}$ by the Photo-Multiplier readout Tubes (PMT). In front of each ECAL cell a Light Emitting Diode (LED) is placed that, properly pulsed, injects a fixed amount of light in the optical fibers of a readout cell and allows to test the readout cell stability of response with time. The electrical signal produced in PMTs travels through 40 m long coaxial cables and is fed into the input channel of the readout board. The initial energy is proportional to the charge Q of the electrical signal. The electrical current is converted to a digital information by a 12-bit ADC sampling at the HERA-B clock frequency. An absolute energy value is obtained from the converted signal by means of look up tables (LUT). All the factors that relate ADC output and the initial particle energy are absorbed in the calibration constant C. In addition, there is a shift to the given ADC output number, called *pedestal*, which is constant for the particular channel and varies from channel to channel. In the ideal case the pedestal distribution for the given channel follows the normal distribution with the width of 2-3 ADC channels, so that the value of pedestal is taken as the mean value of the corresponding Gaussian. The presence of noise correlation between electronic channels leads to uncompensated pedestal shifts, which, in turn, result in inaccuracies in energy determination. That fact should be taken into account in the analysis.

The estimation of the calibration constants C is based on the information provided by ECAL itself. It uses $\pi^0 \to \gamma\gamma$ signal, reconstructed in two-cluster invariant mass distribution

$$M_{\gamma_1\gamma_2} = \sqrt{2E_{\gamma_1}E_{\gamma_2}(1 - cos\theta_{12})}, \tag{3.1}$$

where E_{γ_1} and E_{γ_2} are the measured energies of the photons and θ_{12} is the decay opening angle. When the cells are not well calibrated the $M_{\gamma_1\gamma_2}$ is shifted with respect to the nominal mass of π^0:

$$\begin{aligned} M_{\pi^0} &= \sqrt{2C_1E_{\gamma_1}C_2E_{\gamma_2}(1 - cos\theta_{12})} \\ &= \sqrt{C_1C_2}M_{\gamma_1\gamma_2} \end{aligned} \tag{3.2}$$

The calibration factors are obtained forcing the peak to the π^0 nominal value. The procedure can be iterated until the calibration factors converge to unity [64]. By means of these techniques it is possible to calibrate all the channels in the ECAL up to 2% precision in the areas where a reasonable statistics is available and the background is tolerable. The calibration has proved to be stable with time by monitoring the π^0 and η reconstructed mass values.

Another way to calibrate the ECAL is to use the information from electrons originating from gamma conversions, e.g. to compare the cluster energy and position of the electrons in ECAL and the momenta measured in the tracking system. However, this method depends on the alignment of the detector. Such a fit leads to the energy and spatial resolutions presented in Table 3.3 for the middle part of the calorimeter.

Table 3.3: *ECAL performance [65]. The spatial resolution in zy coordinate plane is expected to be much better then that in zx plane, as electrons follow in zy plane essentially linear trajectories.*

$\delta E/E$	$\frac{9.8\%}{\sqrt{E}} \oplus 6.4 \oplus 0.0045 \cdot P$
δ_x	$\frac{1.1\%}{\sqrt{P}} \oplus 0.43$

3.5 The Muon Detector

The HERA-B muon system is located in the region from 15 to 20 m downstream the interaction point with angular coverage from 9 $mrad$ near the beam pipe up to 160 $mrad$ in bending and 250 $mrad$ in non-bending directions. The system consists of about 500 chambers with 30,000 readout channels. It is based on three different types of proportional chambers: tube, pad and pixel. It is segmented into four super-layers interleaved with iron-loaded concrete and steel shielding after the third and fourth super-layers (Fig. 3.10). The first two super-layers have three layers of tube chambers with 0^o and $\pm 20^o$ stereo angles. The 3d and 4th super-layers consist of one zero angle layer with pad chambers. Each of the super-layers is equipped with pixel chambers in the central region.

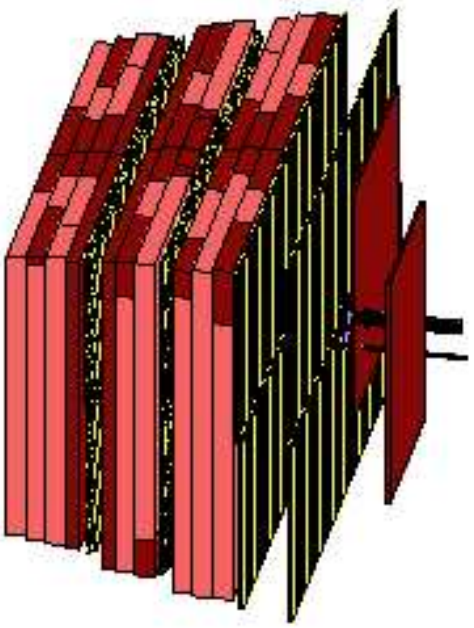

Figure 3.10: *Schematic view of the MUON system: superlayers interleaved with absorbers.*

The basic sensitive element of the tube chamber is a drift cell of size 14×12 mm^2 with a $45-\mu m$-diameter gold-plated tungsten wire. A typical chamber length is approximately 3 m.

The pixel detector placed at the innermost part of the system comprises a single layer of multi-wire proportional chamber. The cell of the pixel chamber has a quadratic form of size 9×9 mm^2. It is formed from one 25 μm thick gold-plated tungsten signal wire and four 500 μm thick potential wires made of copper. The length of the potential wires, which are oriented along the beam, is about 30 mm [66].

In order to decrease the number of readout channels and to optimize the spatial resolution, four signal wires are connected to one readout channel. For the first two super-layers, 2×2 readout channels are implemented. For the last two super-layers, 1 horizontal signal wire and 4 vertical signal wires are connected into one channel.

All types of chambers operate with fast Ar/CF_4-based gas mixtures. The readout is based on the ASD-08 amplifier shaper discriminator chip [66]. The track efficiency of the

system was of order $77 - 84$ % during the 2002-2003 data taking period [67], which is somewhat below the design specifications.

3.6 Ring Imaging Cherenkov Counter

The Ring Imaging Cerenkov Counter (RICH) was designed to identify charged particles over a wide range of momenta and in particular to distinguish kaons, pions and protons.

RICH is placed about 8.5 m downstream the interaction point and consists of:

- a radiator, where Cerenkov photons are produced by passing charged particles,
- a mirror which projects Cerenkov photons to form rings on the focal surface,
- a wire chamber as a position sensitive photon detector, that fits the focal surface and is capable of detecting photons with high efficiency and good resolution in two dimensions,
- a wire chamber read-out system.

The radiator gas, C_4F_{10}, is contained in a vessel made of stainless steel plates and equipped with 1 mm thick particle entrance and exit windows. The Cerenkov light exits the vessel trough 2 mm thick UV grade (fused quartz) Plexiglas windows, which serve also as entrance windows for the photon detectors. The choice of that particular radiator was dictated by requirement of low dispersion and low Cerenkov threshold, which is 2.7 GeV/c and 9.6 GeV/c for π's and K's, respectively, for a mean value of the refractive index ($n = 1.00137$ [68]). The Cerenkov angle corresponding to $\beta = 1$ particles amounts to 52.4 mrad [68]. The 2.5 m length of the gas radiator is enough to achieve detection of sufficient number of Cerenkov photons, of order 35 per ring.

The main imaging device is a spherical mirror placed inside the radiator vessel with the center of the sphere near the target and radius of curvature of 11.4 m. The mirror, a 6×4 m rectangular cutout from the sphere, consists of 80 full or partial hexagons made from 7 mm thick Pyrex glass and coated with 200 nm of aluminum and 30 nm of MgF_2 (See Fig 3.11). In order to place the focal surface outside the particle flux (± 160 $mrad$ in non-bending zy plane), the mirror is split horizontally and both halves are tilted by 9^o away from the beam-line. A set of two planar mirrors, made of float glass and composed of 18 rectangular elements each, translates the focal surface to the photon detector area above and below the radiator vessel (see Fig. 3.11). All 80 spherical and 36 planar mirrors are mounted on a rigid, low mass support structure inside the radiator volume and can be individually adjusted by stepper motors from the outside.

The photon detector consists of Hamamatsu multi-anode photomultiplier tubes (PMTs) [68]. The PMTs have outer dimension of $28 \times 28 mm^2$ with an active area of $18 \times 18 mm^2$. The two different versions of PMTs have 16 pads of 4.5×4.5 mm^2 each and 4 pads of 9×9 mm^2 each. The single photo-electron detection efficiency exceeds 98%.

Cerenkov light emitted by charged particles in the radiator volume is projected by focal and planar mirrors in a ring image on the photomultiplier plane. The detected

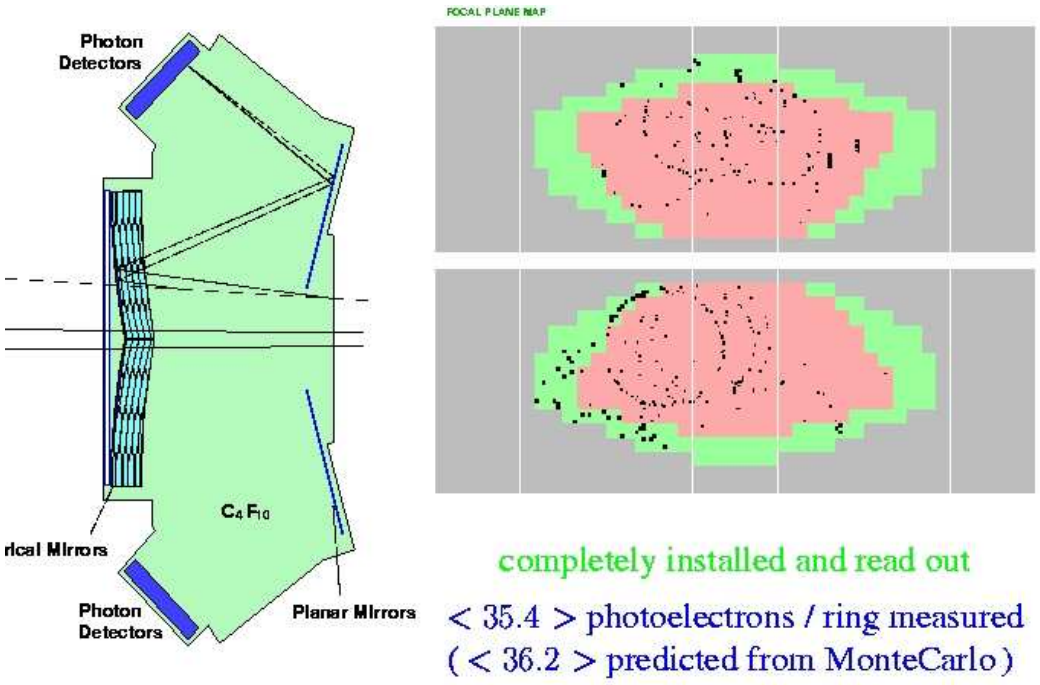

Figure 3.11: *Ring Image Cherenkov Detector.*

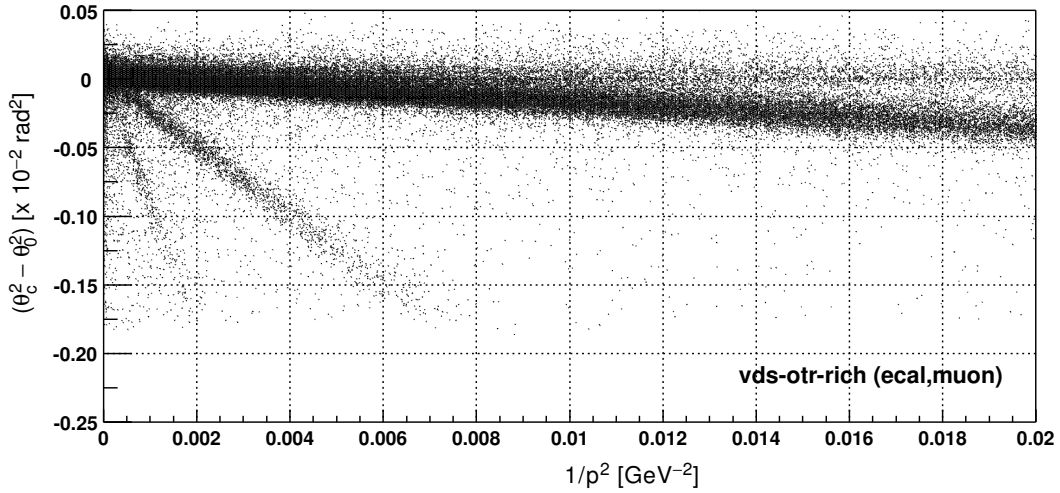

Figure 3.12: *RICH particle identification. The difference of squares of the measured and the maximal value of Cherenkov angle, $\theta_c^2 - \theta_0^2$ is plotted as a function of $1/p^2$ to find the particle identity through the association to a particular band which correspond to a stable charged particle. On the plot (from left counterclockwise) bands for protons, kaons, pions and electrons are clearly seen.*

rings provide information about the direction and velocity of the particle. The relation between the observed velocity and the momentum measured in the spectrometer is used for particle identification. Fig. 3.12 shows a distribution of the square of Cerenkov angle versus the square of inverse momentum. One can clearly see the bands corresponding to pions, kaons and protons.

The RICH system was operating at its design specifications. It provides a 4σ separation for electron-pion in the momentum range $3.4 - 15\ GeV/c$, for pion-kaon in the range $12 - 54\ GeV/c$, and for kaon-proton in the range $23 - 85\ GeV/c$.

3.7 The Trigger System

The main task of the multilevel trigger system is to find $J/\psi \to \mu^+\mu^-$ and $J/\psi \to e^+e^-$ decays. To minimize the processing time the First Level Trigger (FLT) is designed to consider only a small fraction of the event data. As events pass through the Second Level Trigger (SLT), they are either discarded or increasingly more event data and more processing time are devoted to them. The events accepted by the SLT are sent to the Fourth Level Trigger (4LT) which is a Linux PC farm of 200 CPUs in 100 dual PCs. There events are online reconstructed and classified according to various physics categories.

The guideline of the triggering strategy is as follows:

1. First, muon and electron/positron candidates are identified by pretrigger systems:
   - The muon pretrigger identifies muon candidates via coincidence in the last two superlayers of the muon detector.
   - The electron pretrigger selects electrons, with transverse energy above 1 GeV, using the cluster energy deposited in ECAL.
2. The pretriggers define the search window for the FLT.
3. If an event is accepted by FLT, the complete event is copied into the Second Level Buffer (SLB), the data storage for the SLT processing.
4. SLT accepted events are sent to the 4LT for full reconstruction.

For the majority of the triggered data taken during 2002-2003 period the FLT required at least one FLT track found and at least two SLT pretrigger candidates originating from the same pretrigger source which was used as a seed to the FLT tracks. The FLT output recorded both the FLT tracks and the pretrigger seeds. The SLT was seeded directly from the pretrigger information.

The main advantage of this scheme compared to the designed requirement of two FLT tracks is the increase in the efficiency [69]. However, the requirement of only one track in the FLT gives much less rejection and, thus, high input rate to SLT. Therefore, the trigger could not run at high interaction rates as the design trigger.

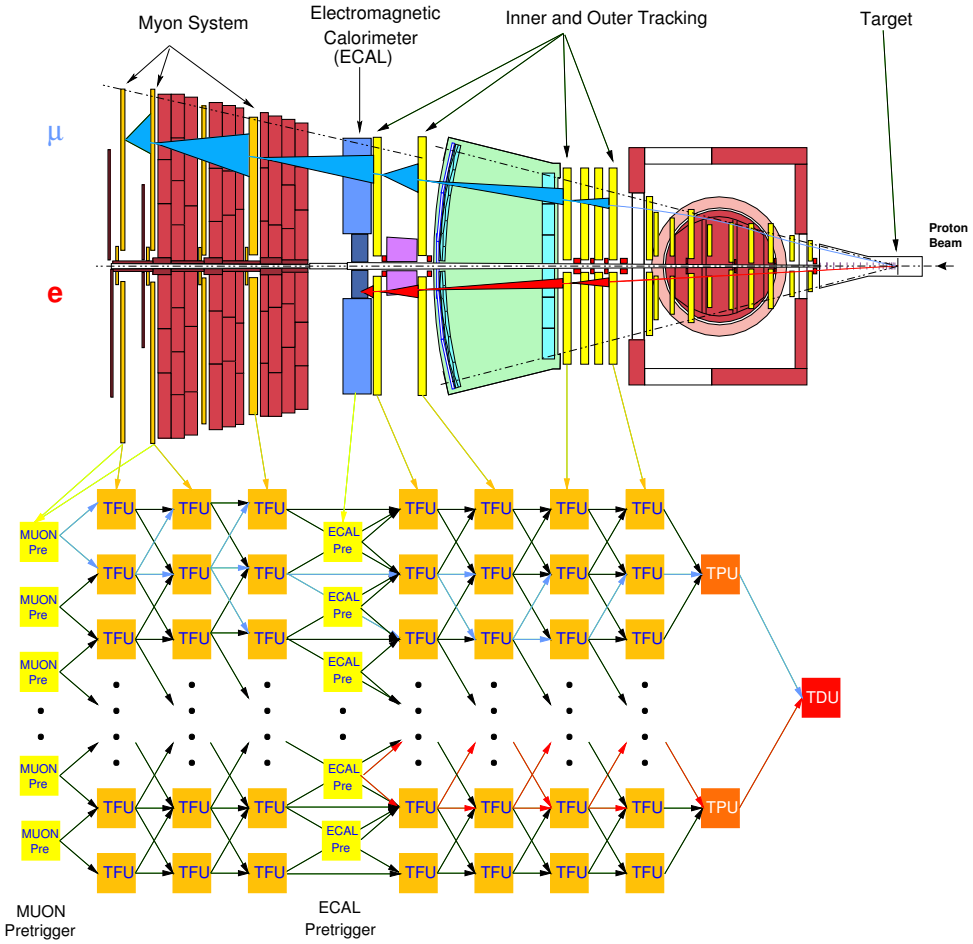

Figure 3.13: *Schematic view of the First Level Trigger (FLT).*

3.7.1 The First Level Trigger

The First Level Trigger (FLT) is designed to trace particles trough the tracking chambers behind the magnet. After track seeding by the pretriggers, the FLT traces the track opposite to its flight direction. The tracking procedure is region of interest (RoI) based, i.e. only a small part of a detector layer is probed by each search iteration (Fig 3.13). The location and size of the RoI are determined by the previous tracking steps. So called Track Finding Units (TFUs) are the central part of the FLT. They decode messages, check for detector hits, extrapolate tracks and send the updated messages off to the following TFUs. With this method a very high data volume is processed at very high rates. It needs to be pointed out that the FLT tracking requires a hit in every trigger tracking layer; an electron, for example, has to be detected by 12 layers of four OTR superlayers.

Once tracks are reconstructed, their kinematical parameters, i.e. momentum, charge and invariant mass of track pairs are determined by the Track Parameter Unit (TPU) and the Trigger Decision Unit (TDU) respectively. In such a way, FLT can apply p_T cut on individual tracks and mass cuts on pairs of tracks. The trigger decision is derived and is

distributed by the Fast Control System (FCS), which initiates the transfer of the buffered data from the detector front-end electronics to the second level buffers (SLB).

The FLT was designed under the assumption of very efficient trigger hardware operation, e.g. pretrigger sources and tracking detectors, whose positions are known precisely. However, the design requirement were not completely fulfilled. This lead to lowering of the efficiency. During the running in 2002-2003 the trigger efficiently to find a track from J/Ψ decay was of order 55 % and 80 % for di-muon and di-electron decays, respectively [70].

3.7.2 The Second Level Trigger

The Second Level Trigger (SLT) is a software trigger running on a farm of 240 PCs. The SLT algorithm is structured in different steps, see Table 3.4. Only the data needed at a given step and limited to a given RoI are requested from SLB. After each step tracks are rejected if certain condition is not satisfied. If, after track rejection, the trigger requirements cannot be fulfilled, the full event is rejected.

The RoIs in the SLT are defined by the input seeds from the previous trigger levels. Using the concept of RoIs, tracks are refined by following them backward through the tracking chambers behind the magnet. The drift time in the OTR chambers provides the input from a refined track fit based on Kalman filter techniques for track propagation trough the magnetic field. After propagating them, new RoIs, used for searching the tracks in the VDS, are defined. The following step applies a Kalman filter algorithm using the information form VDS. In such a way, ghosts [1] and tracks not coming from the interaction region are highly suppressed. In general, the SLT improves the track resolution in comparison to the FLT by an order of magnitude.

In addition, SLT requires a pair of tracks to come from the common vertex in order to reject combinations of leptons from different interactions as well as to enhance the J/Ψ candidates from secondary vertices downstream the interaction region. At the same time the invariant mass of the lepton candidates is calculated. This gives the possibility to cut on the invariant mass around J/Ψ mass in order to enhance heavy quark physics. However in the trigger scheme of 2002-2003 run this cut was not applied [71].

During the 2002-2003 running period the trigger efficiency to find a track from $J/\Psi \rightarrow \mu^+\mu^-$ decay was of order 43% [72].

3.8 Data Acquisition System (DAQ) and Offline Processing

The DAQ [73] integrates the higher level trigger systems (SLT and 4LT), the logging and archiving steps and the interconnections between all of them.

[1] A ghost track is a random combination of reconstructed hits.

Table 3.4: *The individual steps in the SLT algorithm.*

Step	Filtering task
1. Slicer	Removal of so called ghosts by requiring a certain number of hits on an approximately straight line (inside a slice of a RoI). Hits from 0^o layers in the tracking chambers located downstream the magnet are used.
2. RefitX	Hits used in the first step are fitted in zx plane by applying Kalman filter technique and the correspondent track parameters are calculated. The candidates are rejected if the amount of hits is too low or the χ^2 of the fit is too poor.
3. RefitY	Using hits in stereo layers of the tracking chambers downstream the magnet, the track parameters in the zy plane are extracted with the help of a Kalman filter.
4. L2Sili	Track propagation to the VDS with a Kalman filter approach. The parameters in the bending and non-bending planes are calculated separately.
5. L2Vertex	Two tracks are required to stem from a common vertex within the errors.

Table 3.5: *Input rate, trigger latency and data volume for each level of triggering [73].*

Triggering level	Input Rate	Latency	Data Volume
FLT	10 MHz	$< 12\ \mu s$	5 TB/s
SLT	50 kHz	$4\ \mu s$	250 MB/s (25 GB/s for SLB)
4LT	50 Hz	$4s$	5 MB/s

The SLT steps are done in a 240-node PC farm. The nodes are equipped with an Intel Celeron 1.3 GHz processor, 256 MB RAM and a Fast Ethernet network interface card. No hard disk is present in the nodes. They load at booting time the Linux operating system through the network from a server. This feature extremely eases the maintenance and allows to power cycle the nodes without any previous proper shutdown of the operating system. The PCs are equipped with two custom-made cards: one CAN card for remote power control and hardware monitoring and a special PCI interface card for connecting the node to the data acquisition, a 40 MB/s bandwidth full-duplex link, to receive the accepted events by the first level trigger [74]. The maximum input rate into the trigger farm is 50 kHz. The typical output rate is 50 Hz (Table 3.5).

The full event reconstruction and fourth level trigger step are done in a 100-dual processor PC farm. Each node is equipped with two Intel Pentium III 500 MHz processors, 256 MB RAM and a Fast Ethernet network interface card. Like in the second level trigger

farm, the operating system is Linux and the nodes are equipped with a CAN card. The full event reconstruction is run online, thus providing a prompt input for physics analysis. The online reconstruction provides as well information for online calibration, alignment and high level data quality assessments. The 4LT classifies reconstructed events according to various physics categories and creates event directories for faster data access during offline analysis.

As the detector is better understood, the reconstruction packages further developed and improved calibration and alignment constants become available, the event data need to be reprocessed. In addition, large samples of simulated events are required for data analysis.

The event data reprocessing works similarly as the usual online processing scheme. Only the source of the data is different. Instead of getting into the reconstruction farm raw events from the DAQ system via the trigger farm, an additional process retrieves data files from tape and distributes the events into the trigger and reconstruction farm nodes. The trigger farm nodes are also used for running the online event reconstruction in this mode since no triggering is needed during the reprocessing. The system is able to provide events without introducing any overhead, saturating the farms processing power.

The same scheme is used to run Monte Carlo production in the online farms. No event distribution is needed in this case. The Monte Carlo events are generated in the farm nodes, the detector simulation, trigger simulation, digitization and event reconstruction are performed, and finally they are sent to the logger.

The common roof for high level triggering, online and offline reconstruction, Monte Carlo simulations and physical analysis is provided by ARTE (Analysis and Reconstruction Tool) [75]. It provides a general program steering tool and facilities for input/output, memory management as well as iterative program control. ARTE is developed under UNIX system. Originally developed in Fortran 77, the software was later rewritten in C/C++.

3.9 Monte Carlo Simulation

The standard Monte Carlo simulation (MC) is based on the combination of PYTHIA generator [76] and FRITIOF [77, 78]. The inclusion of the FRITIOF package is demanded by the need to describe nuclear effects[2]. The default scheme of event simulation is done in several steps:

- First, a J/Ψ or $\chi_c \to \gamma J/\Psi$ is generated using PYTHIA through the hard scattering processes:

$$\begin{array}{rcl} g+g & \to & J/\Psi + g, \\ g+g & \to & \chi_{ci} + g, \quad i = 0, 1, 2. \end{array} \tag{3.3}$$

  Only interactions of gluons are considered. The differential cross-section is calculated according to the CSM production mechanism, using CTEQ2L [76] parton

[2]PYTHIA is restricted to the collision of nucleons.

momentum distributions. The low-p_T production process are not included in the scheme. Therefore, the sum of the transverse momenta of the reaction products must exceed 1 GeV/c. Any polarization is neglected.

- In a second step, the energy excess, left after charmonium has been generated, is used to generate the rest of the pA interaction ("soft" interactions generation) using FRITIOF.

- In a third step, a J/ψ event is combined with n other inelastic interactions to simulate several interactions per event (pile-up), as observed in the data. The number n is distributed according to Poisson statistics with a mean value of 0.5 determined from the mean experimental interaction rate.

- The detector response is then simulated using GEANT 3.21 [79] and includes measured hit resolutions, mapping of inefficient channels and electronic noise.

- Finally, the simulated events are processed by the same trigger and reconstruction codes as the data. In order to achieve better description of the trigger as well as particle multiplicities for each simulated event, trigger and multiplicity weights are introduced.

The physics processes leading to charmonium production is only partially taken into account during simulation of hard scattering processes. This is not enough to achieve a realistic estimate of efficiencies. Therefore, it is necessary to introduce for the simulated events kinematical weights such that all inclusive spectra are forced to agree with experimental data. The benchmark for the J/Ψ distributions is the measured J/Ψ cross-section from the fixed-target experiment E789 [80], which was running 800 GeV $p-Au$ collisions. The cross-section is factorized into a transverse part (a function of p_T) and a longitudinal part (a function of x_F), see relation (2.13). The shapes of inclusive distributions in p_T and x_F are assumed to be identical for E789 and HERA-B beam energies. Weight factors are attributed to all (p_T, x_F) bins, defining an overall weighting function $W(p_T, x_F)$. The procedure is simplified by the fact that the p_T and x_F spectra are uncorrelated [78], and therefore:

$$W(p_T, x_F) \simeq W_{p_T}(p_T) W_{x_F}(x_F)$$

The weighing functions $W_{p_T}(p_T)$ and $W_{x_F}(x_F)$ are determined by fitting the ratio of E789 spectra and simulated distributions, first for the inclusive p_T^2 distribution, then for the inclusive x_F distribution, once weighting according to W_{p_T} has already been applied.

The following χ_c branching ratios are used in the simulations:

$$\begin{aligned} Br(\chi_{c0} \to \gamma J/\Psi) &= 0.66\% \\ Br(\chi_{c1} \to \gamma J/\Psi) &= 27.3\% \\ Br(\chi_{c2} \to \gamma J/\Psi) &= 13.5\% \end{aligned} \tag{3.4}$$

The feed-down from χ_c states amounts to about 37% of all simulated J/Ψ's. The ratio of χ_{c1} to χ_{c2} states in the simulation is taken to be 0.6. The details concerning simulated

signals and their parameters are further discussed in later chapters, when measurements will be described.

Chapter 4

J/Ψ data

Starting from this chapter, we will present a study of the relative production of charmonium states (J/Ψ and χ_c) in proton-nucleus collisions:

$$\begin{array}{rcl} pA & \rightarrow & J/\Psi + X \\ pA & \rightarrow & \chi_c + X. \end{array} \tag{4.1}$$

We consider leptonic decays of J/Ψ and radiative decays of χ_c:

$$\begin{array}{rcll} J/\Psi & \rightarrow & l^+l^- & ; \quad l = e, \mu \\ \chi_c & \rightarrow & \gamma J/\Psi. & \end{array} \tag{4.2}$$

The study is based on data produced in the interactions of protons with carbon (C), tungsten (W) and titanium (Ti) targets[1]. Data were collected by the HERA-B detector, between October 2002 and March 2003, using a set of triggers tuned to enhance and log di-lepton J/Ψ events: $J/\Psi \rightarrow e^+e^-$ and $J/\Psi \rightarrow \mu^+\mu^-$, after an on-line lepton reconstruction, followed by a selection. The resulting number of recorded J/Ψ events is about 300,000. The analysis proceeds through the following steps:

- Reconstruction of $J/\Psi \rightarrow l^+l^-$ decays.
- Search for photon candidates in the calorimeter.
- Reconstruction of χ_c particles by pairing the photon candidates and the reconstructed J/ψ.
- Estimation of background with the help of the so-called event mixing technique.
- Determination of the photon efficiencies with Monte Carlo simulated events.
- Evaluation of the fraction of J/Ψ produced via χ_c decays, R_{χ_c}, and comparison of several nuclear target materials.

[1] In the di-muon data we have also a small number of J/Ψ events (about 300) produced on palladium (Pd) wire $a2$.

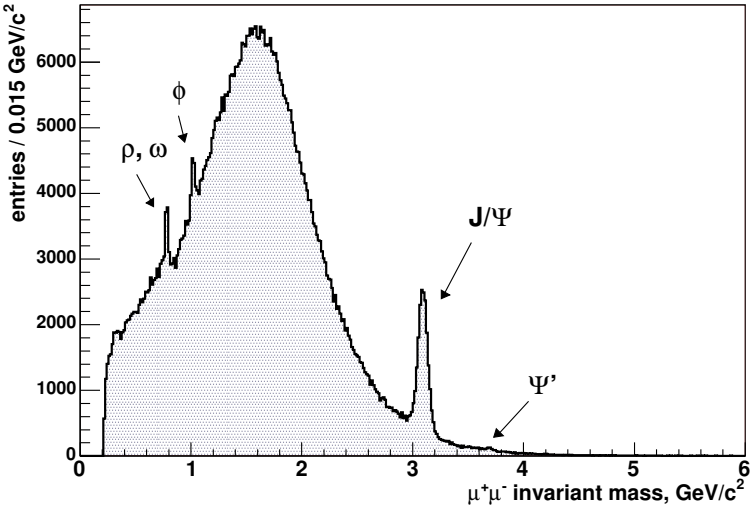

Figure 4.1: *The invariant mass of the opposite charged muon candidates. The peaks on the top of the background correspond to ρ, ω, ϕ, J/Ψ and $\Psi^{'}$ mesons.*

- Extraction of the ratio of production cross-sections of the χ_{c1} and χ_{c2} states by using converted photons.

In this chapter, we will discuss the reconstruction of the J/Ψ leptonic decays, determined by examining the invariant mass of two leptons of opposite charges. We will describe the analysis chain leading to a clean sample of events containing a J/Ψ. It will be followed by the description of the search for the χ_c radiative decays, presented in chapter 5. Chapter 6, then, will provide the details related to the measurement of the fraction of J/Ψ particles produced via χ_c decays in pA collisions, summarizing the results given in chapters 4 and 5. The final chapter, chapter 7, will be dedicated to illuminate the study of the relative production of χ_{c1} and χ_{c2} states.

4.1 Data Samples

Data, used in the analysis, were taken in so-called runs with assigned numbers from 19890 to 21304. The runs were combined in groups according to the type of trigger and wire material used. We consider only events from runs with a di-lepton trigger, which was working in two channels[2] simultaneously. Figure 4.1 shows the di-muon spectrum corresponding to all triggered events accumulated in this channel, which exposes clean signals of ρ, ω, ϕ, J/Ψ and $\Psi^{'}$ mesons. Several target wires were used in two different configurations: single-wire or double-wire. These are summarized in Table 4.1, together with the corresponding accumulated event statistics. The data for a particular wire are separated by comparing the z-position of the reconstructed di-lepton vertex, z_{ll}. Only events, in which di-lepton vertex is within a window of three standard deviations compared

[2]i.e di-muon and di-electron channels; by electron we mean e^+ or e^-.

Table 4.1: *Event data statistics sorted out according to target configuration and wire materials.*

Target Configuration	Wire Material(s)	Collected events
below 1 (b1)	(C)	19181628
inner 1 (i1)	$(W), (W + Re)$	1751558
bellow 2 (b2)	$(Ti), (W + Re)$	6889432
outer 2 (o2)	$(C), (W)$	6847006
inner 2 (i2)	(C)	22268640
inner1 + inner2	$(W) + (C)$	17127057
inner1+below2	$(W) + (Ti), (W + Re)$	22983333
below1+outer2	$(W) + (C), (W)$	42432108
below1+inner2	$(W) + (C)$	12987401
below1+below2	$(W) + (C)$	2856471

to the position of the wire, z_{wire},

$$|z_{ll} - z_{wire}| < 0.19\ cm, \tag{4.3}$$

are analyzed. z_{wire} (Table 4.2) and corresponding resolution are estimated from a fit to the di-muon vertex z-coordinate distributions (Fig. 4.2) with a Gaussian. The distributions are obtained using single wire runs and double-wire runs with two wires distributed over two stations.

In di-muon channel we analyze all available data, while in the di-electron channel only data collected in year 2002 with single carbon wire $i2$ are considered.

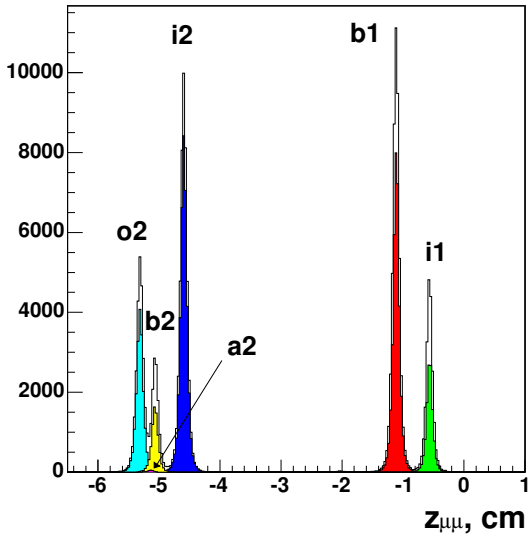

Figure 4.2: *z coordinate of di-muon vertices. The peaks correspond to $o2$, $a2$, $b2$, $b1$ and $i1$ target wires as indicated in plot. Shaded and empty histograms correspond to different selection levels.*

Table 4.2: *z coordinate of wires used in data-taking. The values are estimated using reconstructed di-muon vertices.*

Wire	$i1$	$b1$	$i2$	$b2$	$a2$	$o2$
z, cm	-0.56 *	-1.10	-4.59	-5.07	-5.14	-5.31

* In runs 20509, 20512 the position of $i1$ wire is -2.04 cm, as it was broken during the operation.

4.2 Data Quality

In order to get an accurate measurement, it is important that the data are of high reliability. The quality of the data depends on the performance of the detector. Unstable operation of subdetectors may have a negative influence on data quality. Therefore, it is crucial to check the goodness of the information coming from subtdetectors and exclude from consideration all troublesome points (e.g. presence of dead/hot channels), which spoil the data.

The quality of data is checked by studying hit multiplicities in the tracking devices. The mean number of reconstructed hits, N_{hit}, as well as the number of hits associated with a track, N_{hit}^{track}. N_{hit} is proportional to the mean number of working channels, while the difference between N_{hit} and N_{hit}^{track} provides information about hot channels. A given run is considered as low quality run if N_{hit} or N_{hit}^{track}/N_{hit} falls out of a $\pm 5\sigma$ window around the overall mean value, averaged over the whole data taking period (Fig. 4.3). A random trigger, which operated in parallel with the J/Ψ trigger and data quality histograms [81], allowed an efficient control data quality.

The stability of the operation of tracking programs was checked by studying the ratio of the tracks which have OTR and/or ITR hits to the number of tracks which have VDS hits (Fig. 4.4). The mean value of this ratio is independent on the interaction rate, but is sensitive to the operation conditions of the reconstruction packages as well as the working conditions of the corresponding subdetectors. Therefore, the constant ratio corresponds to a stable operation conditions and reliable data quality.

The alignment quality was investigated using residuals between matched VDS and OTR/ITR segments. For each pair, track segments were extrapolated inside the magnet to the point $z = 415$ cm and the difference in position and slopes in zx and zy planes were compared (see Fig. 4.5). The residual distributions are expected to exhibit a clear symmetric peak with mean value around zero. This, together with the stability in time, indicates a good alignment, upon which the momentum reconstruction is dependent.

The stability of ECAL operation was investigated by examining the behavior of the following quantities:

- The total energy deposited in the calorimeter for each bunch crossing (Fig. 4.6). Uniformity of this distribution indicated a stable distribution of interactions with respect to the bunch structure.

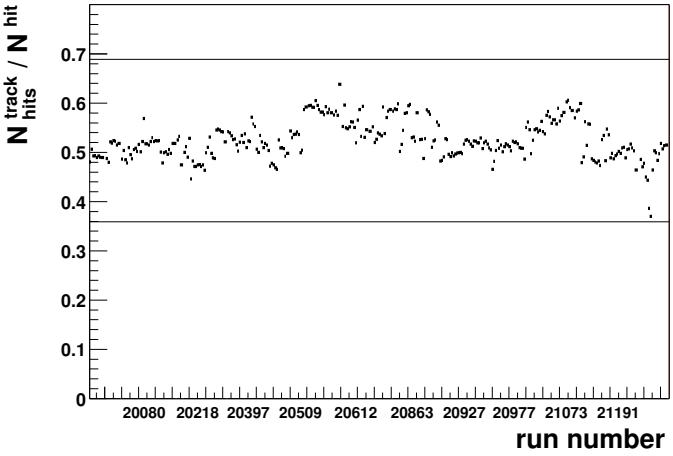

Figure 4.3: *The ratio N_{hit}^{track}/N_{hit} per run. Here N_{hit}^{track} is the number of hits attributed to the reconstructed tracks and N^{hit} is the reconstructed hits in all subdetectors. The horizontal lines show $\pm 5\sigma$ boundaries.*

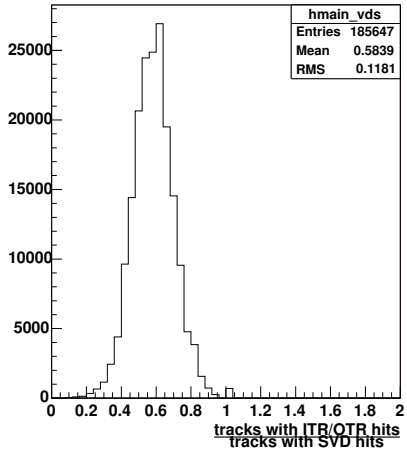

Figure 4.4: *Ratio of the number of tracks with hits in OTR/ITR to the number of tracks with hits in VDS, presented for one run.*

- The event rate for each readout board (Fig. 4.7). It helped to identify bad working boards. In the ideal case of ECAL operation the boards behave identically for each event and the distribution of number of events per readout board should be flat. Eventual problems are identified with the drops in the distribution, which correspond to bad working readout boards. Although the fraction of such bad boards is usually small, it is important to monitor them for acceptance determination.

- The ECAL cluster occupancy. It is important for the localization of "hot" channels. This will be further discussed in subsection 5.2.2).

The stability of the calorimeter calibration was inspected using the π^0 signal. The parameters of the π^0 peak (i.e. width and position) obtained after the offline reconstruction[3] were compared to similar quantities obtained on-line. Stable parameters and stable variation between offline and on-line values lead to stable calibration constants.

Occupancy plots allow to monitor the MUON system. The number of hits accumulated in each readout channel is considered as a function of the geometrical position of the channel (see Fig. 4.8). The normal behavior of the occupancy distribution is proportional to $1/r^2$, where r is the radial distance from the proton beam pipe. The deviation from this behavior may indicate the presence of failures in the detector performance. A much smaller (higher) occupancy compared to the expectation shows the presence of dead (hot) channels. Such channels are systematically detected and masked. The study of the occupancy distribution helps to recover cable swapping and mark the presence of not working readout boards.

[3]We use 3^d reprocessing of data.

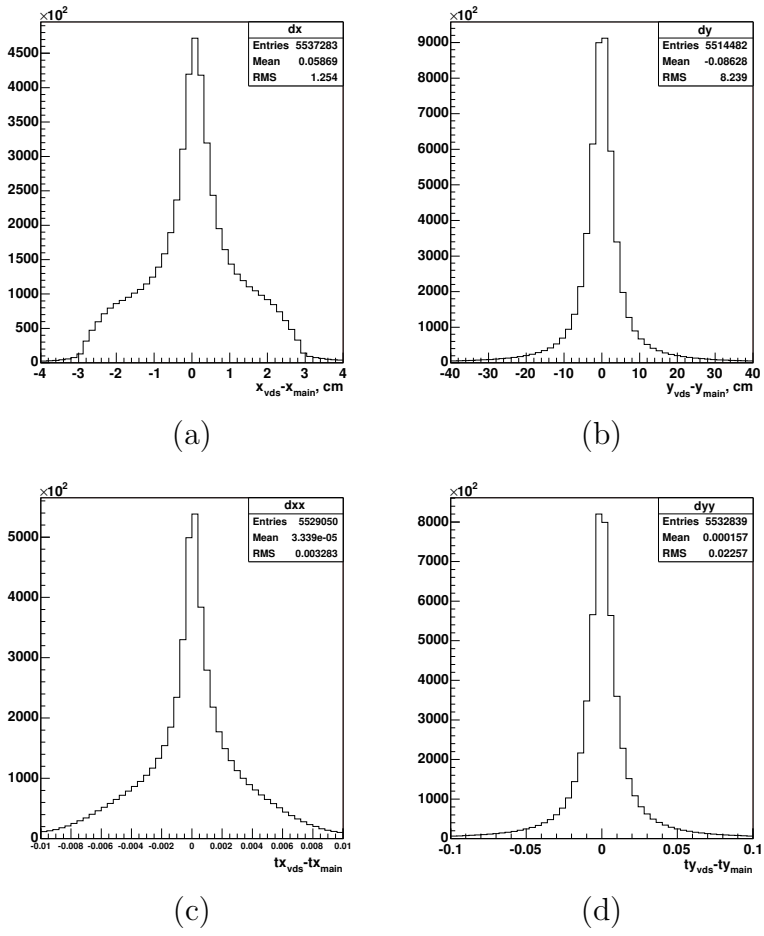

Figure 4.5: *The difference in track parameters x (a), y (b), slope in zx plane, tx, (c) and slope in zy plane, ty, (c), for OTR/ITR and VDS segments extrapolated to $z = 415$ cm. The plots correspond to one run.*

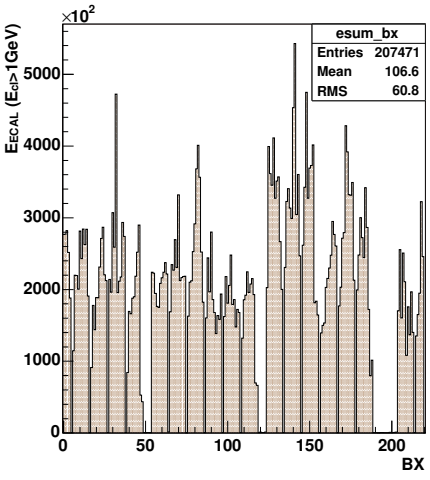

Figure 4.6: *A distribution of the released energy in ECAL for each bunch crossing, which corresponds to one run.*

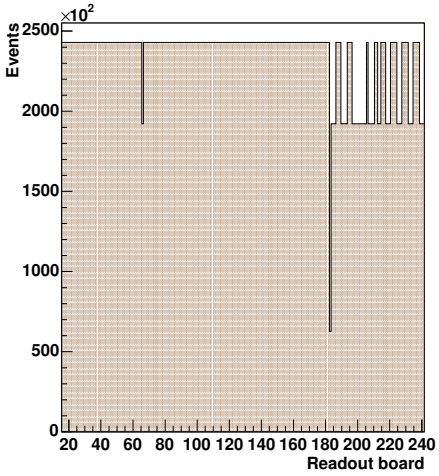

Figure 4.7: *A distribution of number of events per readout board, which correspond to one run.*

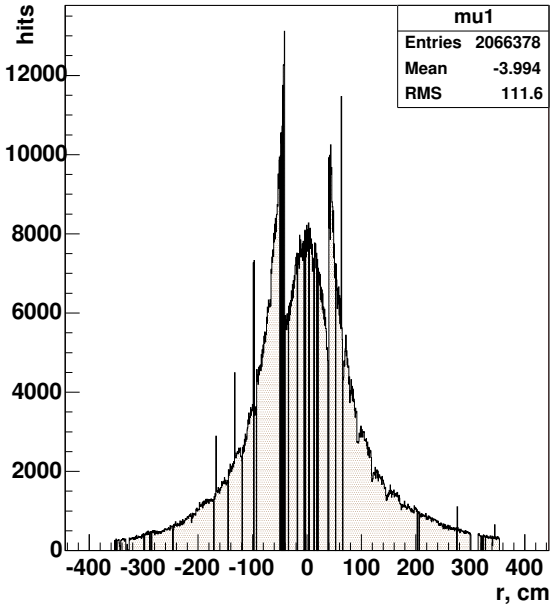

Figure 4.8: *A occupancy distribution of the tube chambers of the first superlayer of MUON system for one run. The number of hits accumulated in each readout channel is plotted as a function of the radial distance to the proton beam pipe, r.*

In addition, data can be impaired by several effects present when the beam protons hit the target. These are:

- The coasting beam effect, leading to the interactions within a time interval different from the one expected from the bunch structure of the proton beam [82], when wires are inserted into the halo of the beam. This is due to protons which scattered in the accelerator medium and thus lost their time correlation with the beam. Such interactions should either be kept at low rate or simply rejected.

- The non-homogeneous distribution of protons within a bunch, leading to possible multiple interactions in a given event. This is not a real problem for the present analysis because the probability for a J/Ψ event is independent on the number of interactions per event (only one J/Ψ is accepted per event). There is thus no influence on R_{χ_c}.

- Events occurring outside the target. In this case the J/Ψ vertex is located significantly far from the wire position, such that it is easy to identify these off-target events and, subsequently, remove them. The amount is found to be small and has a minor impact on the measured quantities.

4.3 Selection of leptons

The reconstruction of the J/Ψ begins from the search for leptons in offline reconstructed di-lepton triggered events. The events were reconstructed using ARTE-04-01-r3. The

alignment and calibration constants were based on the KEYBOOK 27 [75]. Common requirements are set for both electron and muon candidates:

- Triggered tracks with signature in the VDS, such that vertexing can be performed.
- A track is required not to be marked as a clone [4].

4.3.1 Trigger requirements

The J/Ψ trigger has several important requirements [71]:

- At least one FLT-track must be found by the first level trigger and at least two pretrigger candidates must originate from the same pretrigger source (electron or muon). The pretrigger information serves as a seed for SLT.
- The geometrical acceptance for the trigger tracks (muons and electrons) is limited to $25 - 150$ $mrad$ (which correspond to the OTR tracker acceptance). The outer limits of the muon and electron detection were restricted by the MUON and ECAL boundaries.
- A track is accepted by the trigger as
  − a muon candidate, if it is identified by the MUON system and has a momentum larger than 5 GeV/c;
  − an electron candidate, if it has an associated cluster reconstructed in ECAL and the transverse energy, E_T^{cl}, of the cluster is larger than $1GeV$ (Fig. 4.9).
- Each pair of accepted tracks is required to come from a common vertex.

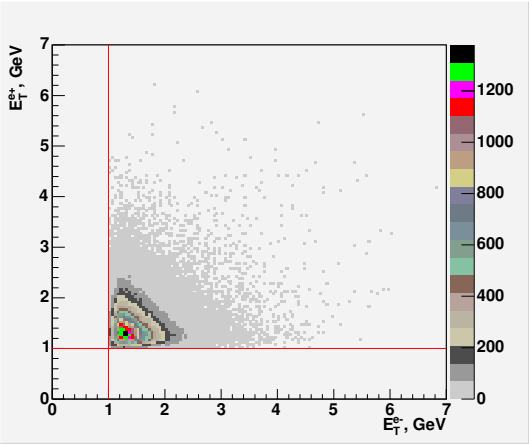

Figure 4.9: *Transverse cluster energy E_T^{cl} measured in the ECAL for e^+ and e^- candidates for $J/\Psi \rightarrow e^+e^-$ signal. The value of E_T^{cl} is obtained using the cluster energy measured in ECAL, with the assumption that the particles that caused the shower come from the interaction point, following a linear trajectory. The coordinates of the reconstructed e^+e^- vertex are taken as the coordinates of the interaction point. The lines on the plot indicate applied cut, $E_T^{cl} > 1GeV$.*

[4] A track is usually obtained by matching the segments reconstructed in different subdetectors. This matching between the subdetectors may generate a situation when a segment is used several times to form a track. Such tracks are referred to as clones. In case of multiple usage of segments only one reconstructed tracks is accepted among the tracks with similar characteristics. The choice is based on the hit information from subdetectors and the quality of the track fit.

The trigger requirements are optimized with respect to the amount of transferred information and decision speed [55, 71]. The kinematical parameters of the leptons are determined by the kinematics of the J/Ψ. Therefore, the spectra of J/Ψ transverse momentum, $p_T^{J/\Psi}$, and Feynman x, $x_F^{J/\Psi}$ [5], are usually used for the trigger efficiency studies. In general, the efficiency of the trigger to detect J/Ψ is about $\varepsilon_{trig} \sim 10\%$. The value is independent of the wire position and material.

4.3.2 Muon selection

We identify a reconstructed charged track triggered by SLT as a muon candidate if

- the number of hits in the VDS (N_{vds}), in the main tracker (N_{main}), which is the sum of OTR and ITR hits, and in the MUON system (N_{muon}) satisfy the relations: $N_{vds} > 5$, $N_{main} > 8$ and $N_{muon} > 4$;
- the track is not attributed to as a clone track;
- the MUON likelihood (ratio of the measured hits in the MUON system to the expected ones) is $L_\mu > 0.05$;
- its measured momentum (p_μ) is in the range: $6 < p_\mu < 200\ GeV/c$.

We require at least two oppositely charged muon candidates per event, which come from a common vertex and have invariant mass is in the range: $0 < M_{\mu\mu} < 20\ GeV/c^2$. A common vertex is attributed to a muon pair if the χ^2 probability of the vertex fit [83] satisfies the condition: $\mathcal{P}_{vert}(\chi^2) > 10^{-5}$.

4.3.3 Electron selection

In order to select electron candidates we use the following requirements for tracks that passed di-electron trigger requirements and that went through offline reconstruction:

- Tracks must have reconstructed segments in the vertex detector system (VDS) as well as in the pattern chambers (PC).
- They are not marked as clones.
- Their momenta have to be in the range: $4 < p_e < 400\ GeV/c$.
- Each track must have an assigned reconstructed cluster in ECAL.
- In order to suppress random track-cluster combinations, the ratio between the cluster energy and track momentum, E/p, is required to satisfy the condition (Fig 4.10): $E/p > 0.75$, for each track.

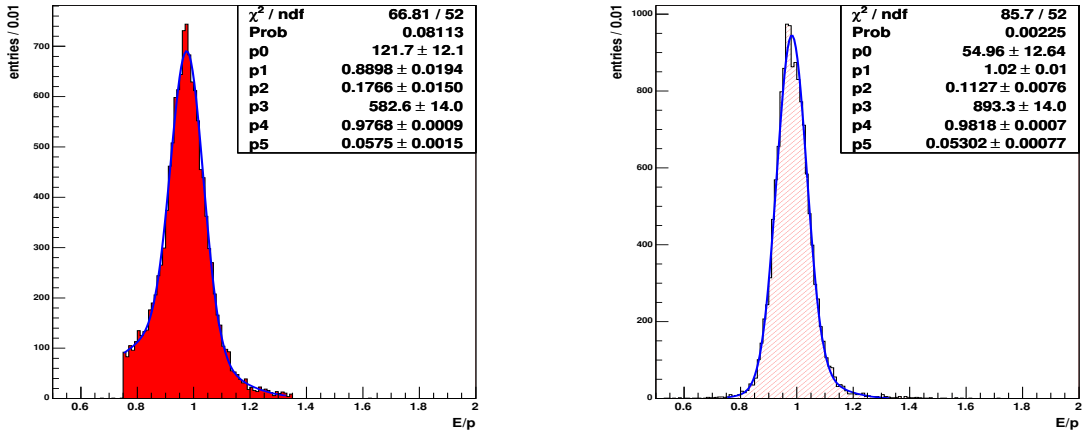

(a) (b)

Figure 4.10: *The ratio of the energy of ECAL cluster to the $e^{\pm}$ track momentum, E/p: (a) Carbon di-electron data ($i2$ wire); (b) Monte Carlo simulation for $i2$. The fit is performed using two-Gaussian parametrization. The width and position of the narrower Gaussian ($\sigma_{E/p}$ and $\langle E/p \rangle$ denoted as $p5$ and $p4$ in plots) are used to define additional selection limits.*

A pair of electron candidates is required to come from a common vertex with the the χ^2 probability of the vertex fit [83] $\mathcal{P}_{vert}(\chi^2) > 5 \times 10^{-3}$.

Due to its low mass, the electron has a high probability to radiate bremsstrahlung photons when passing through the detector. Such energy losses make the reconstruction of particle momenta more subtle. However, this can be used to further reduce background from hadrons. In order to achieve that, a search for associated bremsstrahlung photons is performed for each electron candidate. If any bremsstrahlung cluster is found, its energy is added to the energy of the electron candidate and, consequently, the momentum is recalculated.

The search for bremsstrahlung photons is restricted to emissions inside the VDS. The bremsstrahlung radiation after magnet has a minor impact on the momentum measurement. The energy losses inside the magnet are considered to be completely lost.

Bremsstrahlung recovery is based on the search of an isolated electromagnetic cluster in the area where the photon candidate is expected to hit the ECAL. When bremsstrahlung radiation occurs upstream the magnet, the photon follows the initial electron direction. A linear extrapolation to the ECAL plane (Fig 4.11) gives the following photon's impact position, (x_0,y_0),

$$\begin{aligned} x_0 &= x_{vert} + \frac{p_x}{p_z}(z_{ECAL} - z_{vert}) \\ y_0 &= y_{vert} + \frac{p_y}{p_z}(z_{ECAL} - z_{vert}) \quad . \end{aligned} \tag{4.4}$$

[5] As a benchmark the spectra measured by the E789 experiment [80] were used.

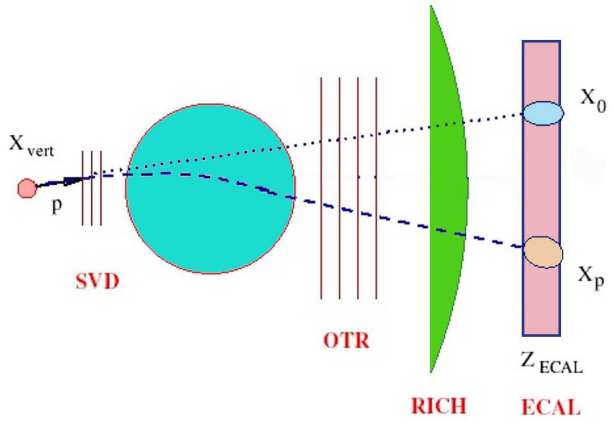

Figure 4.11: *Schematic view of an electron track passing the detector and radiating a bremsstrahlung photon in front of the magnet.*

The cluster caused by bremsstrahlung radiation is the one closest to the extrapolated point. We required that the difference between the cluster position and the impact position does not exceed 8.4 *cm* for the outer part of ECAL, 4.2 *cm* for the middle part and 1.7 *cm* for the inner part. The values listed above correspond to 75% of a typical cell width (Table 3.2).

4.4 J/Ψ reconstruction

4.4.1 Signal in di-muon channel

The invariant mass distribution of $\mu^+\mu^-$ pairs is shown in Fig. 4.12 for real data corresponding to all available statistics. In the fit, shown on the plot, we describe the J/Ψ signal by a Gaussian, while the background is parametrized by an exponential:

$$\frac{dN}{dM} = \frac{N_0}{\sigma_M\sqrt{2\pi}} \exp\left[-\frac{(M-M_0)^2}{2\sigma_M^2}\right] + P_4 \exp\left[-P_5 M\right] \tag{4.5}$$

As can be seen from the data and Monte Carlo (Fig. 4.13) plots the parametrization of the J/Ψ signal with a single Gaussian fails to describe the tails of the signal. This leads to an underestimation of the signal of about of 3%. A similar value was reported in the study [84]. The presence of such tails is due to the energy losses of muons while they traverse the detector. This, in turn, reflects in non-Gaussian tails in the momemtum resolution. Radiative J/Ψ decays, $J/\Psi \to \mu^+\mu^-\gamma$, are the source for the lower part of the tail. However, the effect is less pronounced when data are plotted for a specific wire material and/or target configuration (Fig. 4.14). In the present analysis, we assume that the systematic effects coming from the Gaussian parametrization of $J/\Psi \to \mu^+\mu^-$ signal are of the same level in data and simulations and, therefore, will cancel in the ratio R_{χ_c}.

A comparison between data (Fig. 4.12) and simulation (Fig. 4.13) shows a clear shift of the signal position by 6 MeV/c^2 . The signal width is wider for data than for MC by 12 MeV/c^2. This is more than the mass uncertainty, which is less than 1 MeV/c^2. These discrepancies are due to a misalignment of the detector components, which is not

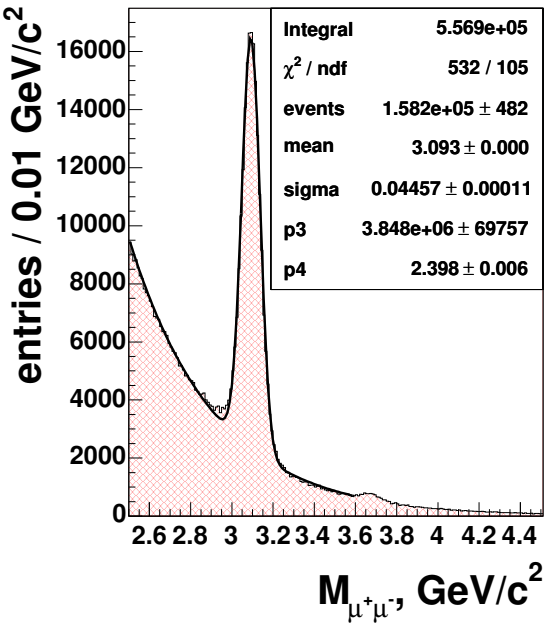

Figure 4.12: *$\mu^+\mu^-$ invariant mass spectrum obtained with all available di-muon triggered data. The J/Ψ signal is parametrized by a Gaussian, whereas the background is described by an exponential (parameters $p3$ and $p4$ on the plot). The fit parameters describing the J/Ψ signal are:*

$N_{J/\Psi}$ *(events)*	158421 ± 482
$M_{J/\Psi}$, MeV/c^2 *(mean)*	3093.0 ± 0.1
$\sigma_{M_{J/\Psi}}$, MeV/c^2 *(sigma)*	44.6 ± 0.1

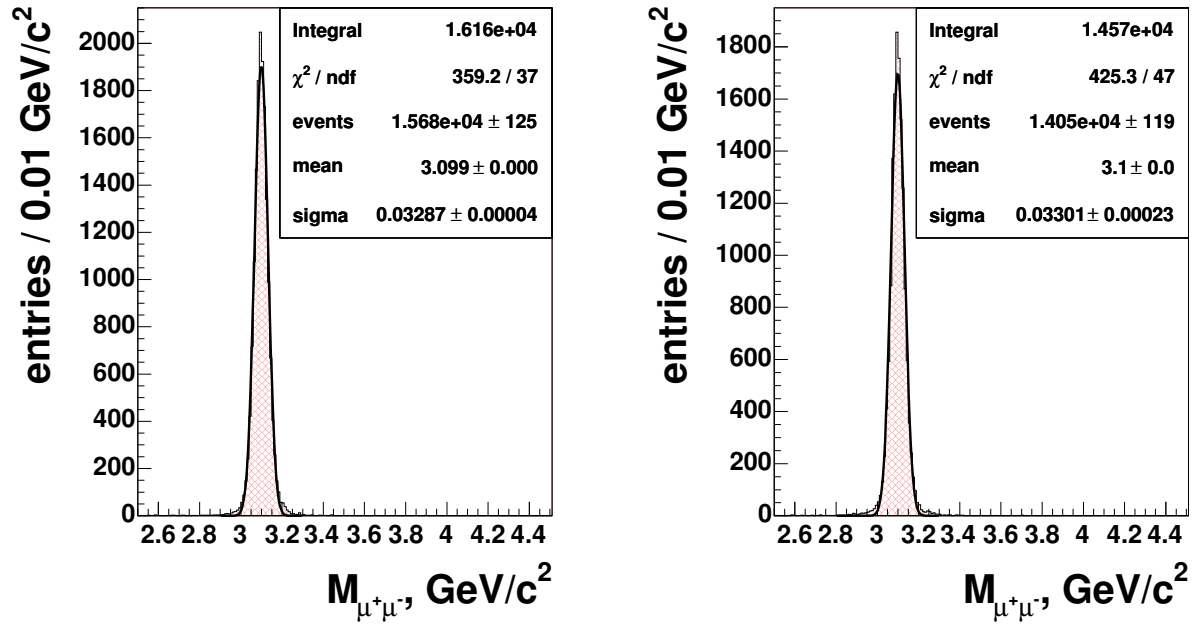

(a) (b)

Figure 4.13: *Simulated $J/\Psi \to \mu^+\mu^-$ signal for carbon wire $i2$: $N_{J/\Psi}$ (events) $= 15683 \pm 125$, $M_{J/\Psi}$, MeV/c^2 (mean) $= 3099.3 \pm 0.3$ MeV/c^2, $\sigma_{M_{J/\Psi}}$, MeV/c^2 (sigma) $= 32.9 \pm 0.1$ MeV/c^2 (a), and tungsten wire $i1$: $N_{J/\Psi}$ (events) $= 14050 \pm 119$, $M_{J/\Psi}$, MeV/c^2 (mean) $= 3099.6 \pm 0.2$ MeV/c^2, $\sigma_{M_{J/\Psi}}$, MeV/c^2 (sigma) $= 33.0 \pm 0.3$ MeV/c^2 (b). In both cases the fit is done using Gaussian parametrization of the signal.*

properly described in the simulation. For instance, a shift of 3 mm in the position of the layers in the VDS could partly reproduce the above effects for data taken in year 2000 [85]. Furthermore, other effects, like a rotation of one of the subdetectors with respect to others, can contribute to the observed shifts. The relative shifts of the subdetectors have a minor influence on the χ_c parameters.

Table 4.3: *Analyzed J/Ψ statistics from 2002-2003 running period.*

Wire Material(s)	$N_{J/\Psi}$	$M_{J/\Psi}$ $[MeV/c^2]$	$\sigma_{M_{J/\Psi}}$ $[MeV/c^2]$
Carbon	100008 ± 391	3092.9 ± 0.1	44.4 ± 0.1
Tungsten	49812 ± 281	3093.0 ± 0.3	45.2 ± 0.2
Titanium	8049 ± 107	3094.4 ± 0.7	43.0 ± 0.2
Combined	158241 ± 482	3093.0 ± 0.1	44.6 ± 0.1

Table 4.4: *J/Ψ Monte Carlo statistics*

Wire Material(s)	$N_{J/\Psi}$	$M_{J/\Psi}$ $[MeV/c^2]$	$\sigma_{M_{J/\Psi}}$ $[MeV/c^2]$
Carbon ($i2$)	15683 ± 125	3099.3 ± 0.3	32.9 ± 0.1
Tungsten ($i1$)	14050 ± 119	3099.6 ± 0.3	33.0 ± 0.2

Following Monte Carlo simulations, the combined trigger and selection efficiency for $J/\Psi \to \mu^+\mu^-$ is about $\varepsilon^{sel}_{trig} \approx 8\%$. The statistics of the J/Ψ selection used in the analysis for each target material and the parameters of the signal are summarized in Tables 4.3 and 4.4 for data and Monte Carlo, respectively. The J/Ψ mass distributions, corresponding to different wires are shown in Fig. 4.14.

4.4.2 Background to muons from J/Ψ decays.

There is definitely more background under the J/Ψ peak in data (Fig. 4.12) than in MC (Fig 4.13). This is due to the fact that, in general, Monte Carlo simulation is based only on the $gg \to \chi_c X$ and $gg \to J/\Psi X$ processes, and does not include other hard processes which may occur when a proton hits the target.

The main components of the background to the muons from $J/\Psi \to \mu^+\mu^-$ decay are:

- Charged hadrons and ghost tracks, appearing due to random combination of hits that passed the trigger and the selection criteria. A fraction of 23% of the tracks passing VDS and OTR per inelastic event satisfy the trigger and muon candidate selection criteria (see subsection 4.3.2): $\varepsilon^{cand}_{tr} \approx 23\%$. The mean number of such tracks is about $N_{tr} \approx 8$.

- Pion or kaon decay in flight, $h \to \mu\nu$, where $h = \pi^{\pm}, K^{\pm}$ lead to background muons in about: $\varepsilon^{\mu}_{h} = 0.27\ (GeV/c)/p$ [86].

- Open charm semi-leptonic decays ($c \to s\mu\nu_\mu$), Drell-Yan muon pairs ($q\overline{q} \to \mu^+\mu^-$), as well as leptonic and semi-leptonic decays of bottom hadrons are also sources of background to J/Ψ muons.

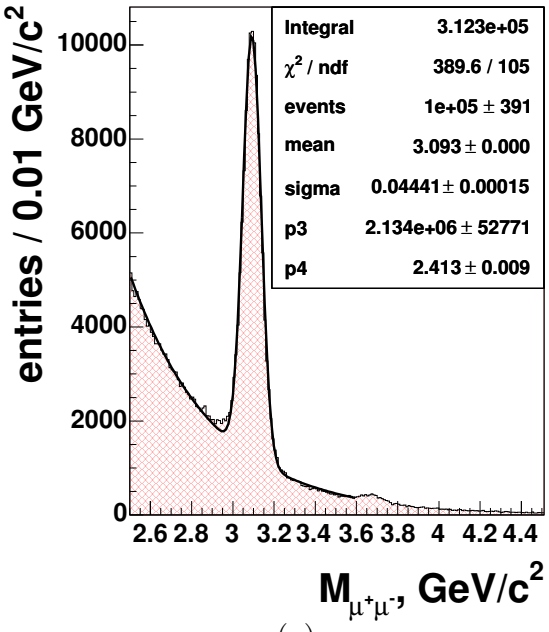

(a)

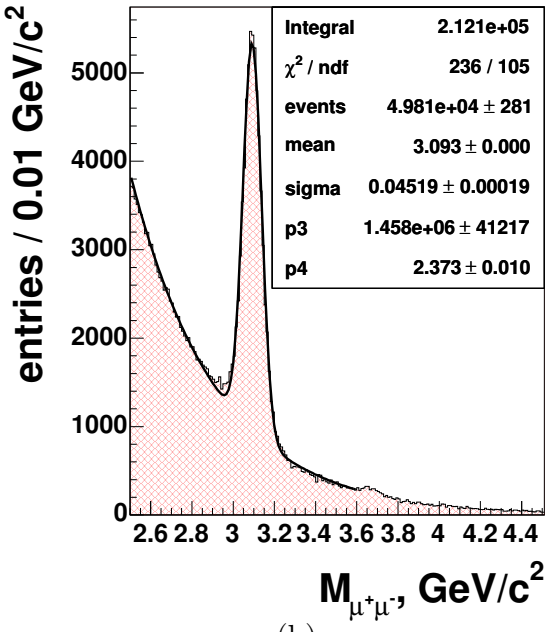

(b)

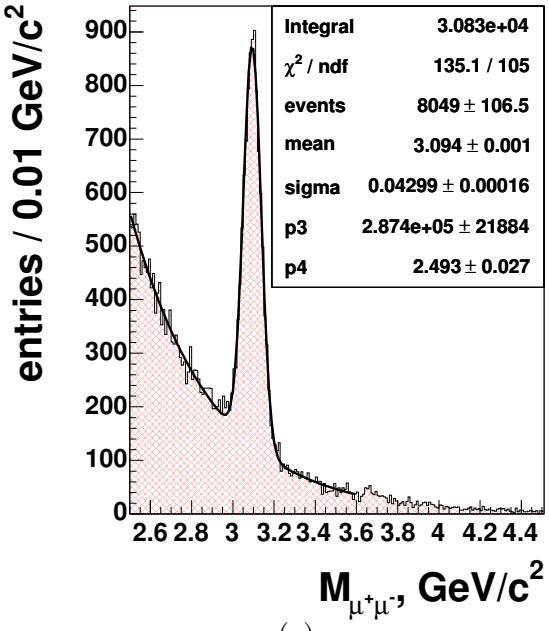

(c)

Figure 4.14: *J/Ψ mass distribution obtained for different target materials: (a) data collected with carbon (C) target ($b1$ and $i2$ wires); (b) data collected with tungsten (W) target ($i1$, $o2$ and $b2$ in 2003 wires); (c) data collected titanium (Ti) target with ($b2$ wire in 2002). The wire separation in case of double-wire operation was done using the coordinates of reconstructed dimuon vertex (equation 4.3). The fit shown on the plots is identical to the one presented in Fig. 4.12. The fit results are summarized in Table 4.3.*

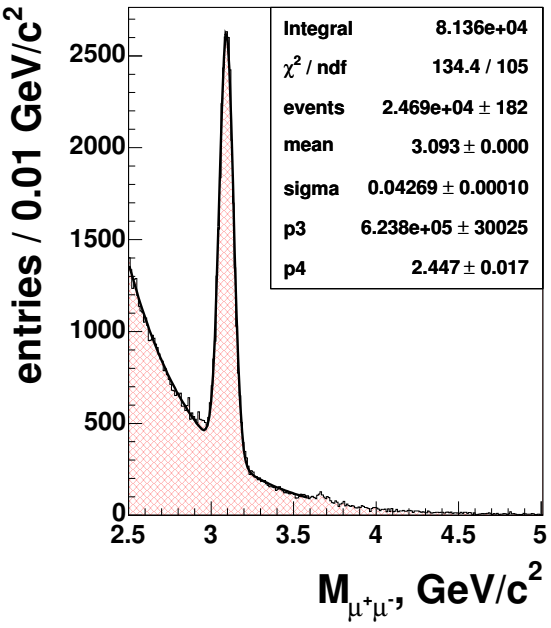

Figure 4.15: *J/Ψ mass distribution obtained with i2 (C) wire running in single wire target mode in 2002. The fit, shown on the plot, is similar to that one in Fig. 4.12. The parameters describing the J/Ψsignal are:*

$N_{J/\Psi}$ *(events)*	24688 ± 191
$M_{J/\Psi}$, MeV/c^2 *(mean)*	3093.0 ± 0.4
$\sigma_{M_{J/\Psi}}$, MeV/c^2 *(sigma)*	42.7 ± 0.3

The fraction of ghost tracks before particle identification could be quite high. A study, performed on the data from 2000 commissioning run, showed that the level of ghost tracks before particle identification is applied could be as high as 6 % [87]. It was shown, however, that the probability to pass the identification criteria (MUON likelihood) is significantly smaller compared to that of real tracks. Therefore, we do not expect a significant fraction of ghosts in the data. Moreover, as far as ghost tracks are created on a random basis, they do not cluster systematically and, thus, their influence on the present analysis is minor. To make an exact estimate of the ratio of ghost tracks, a detailed Monte Carlo study must be performed with the aim to reproduce accurately all the effects observed in the real data.

The background under the J/Ψ peak is predominantly due to random combinations of reconstructed tracks. The only correlation between such tracks is the presence of a common vertex. Using the distributions obtained with ^{12}C wire (see Fig. 4.15), let us go through the main components of the background. The trigger and selection efficiency for two reconstructed tracks is $\varepsilon_{trig} \approx 10\%$. It is independent on the nature of the track, whether it is a charged hadron or a muon. The probability to select a pair of oppositely charged tracks identified as muons with an invariant mass lying within $M \in [2.5, 5]\ GeV/c^2$ is

$$P^{\mu}_{rand} = N_{tr} \left(\varepsilon^{cand}_{tr} \varepsilon^{\mu}_{h}\right)^2 \varepsilon^{rand}_{M} \varepsilon_{trig} \approx 1.7 \times 10^{-7}. \tag{4.6}$$

Here, we use the value $\varepsilon^{\mu}_{h} \approx 2\%$ integrated over the total momentum range. ε^{rand}_{M} is the fraction of pairs in the mass window $M \in [2.5, 5]$. To evaluate it we examine the invariant mass distribution for pairs of oppositely charged tracks, weighted using the factor $(\varepsilon^{\mu}_{h})^2 = \frac{(0.27)^2}{p1 \cdot p2}$. The tracks are required to meet the trigger and muon selection

criteria. For $M > 1.5\ GeV/c^2$, the mass distribution can be described by the exponential

$$\frac{dN}{dM} = N_{tr}^{pair} \exp\left[-3.3\ M\right], \tag{4.7}$$

which, through integration within the window $[2.5, 5]\ GeV/c^2$ and normalization to the total integral, leads to an estimated value of $\varepsilon_M^{rand} \approx 1\%$.

The fraction of real muons coming from the primary vertex, hence not from D or B meson decays, is small compared to hadrons misidentified as muons. The contribution of such "muons" can be neglected. Thus, the number of random combinations in the final sample is given by

$$N_{rand} = \frac{N_{J/\Psi}}{Br(J/\Psi \to \mu^+\mu^-)\varepsilon_{trig}} \frac{\sigma_{inel}}{\sigma_{J/\Psi}} P_{rand}^{\mu} \approx 68,000 \tag{4.8}$$

where σ_{inel} is taken to be equal to $34\ mb/nucleon$ [88] and $\sigma_{J/\Psi} = 357\ nb/nucleon$ [89]. The estimated value (4.8) is compatible with the number of background combinations obtained from the di-muon invariant mass spectra for carbon wire, $N_{back}^{data} = N^{pair} - N_{J/\Psi} = 81,360 - 24,688 \approx 57,000$ (see Fig. 4.15).

The contribution from the combinations of muons from semi-leptonic decays of charmed mesons, e.g. $D \to K\mu\nu_\mu$, with respect to random combinations is

$$\frac{N_{c\bar{c}}}{N_{rand}} = \frac{\sigma_{c\bar{c}}}{\sigma_{inel}} \frac{Br(c\bar{c} \to \mu^+\mu^- X)(\varepsilon_{\mu-c}^{cand})^2 \varepsilon_M^{c\bar{c}} \varepsilon_{trig}}{P_{rand}^{\mu}} \approx 4 \times 10^{-2}. \tag{4.9}$$

The semi-leptonic charm branching ratio is taken to be the average over different charmed particles: $Br(c \to \mu X) = 0.085$ [20] ($Br(c\bar{c} \to \mu^+\mu^- X) = Br^2(c \to \mu X)$) and $\sigma_{c\bar{c}} = 39\ \mu b/nucleon$ [90]. The efficiency to detect muons from charmed particle decays and the probability that the pair invariant mass are within the mass window $M \in [2.5, 5]\ GeV/c^2$ are obtained from Monte Carlo simulations: $\varepsilon_{\mu-c}^{cand} \approx 19\%$ and $\varepsilon_M^{c\bar{c}} \approx 22\%$.

The contribution from leptonic and semi-leptonic decays of b-mesons an baryons is negligible. It is estimated in a similar way as for open charm above

$$\frac{N_{b\bar{b}}}{N_{rand}} = \frac{\sigma_{b\bar{b}}}{\sigma_{inel}} \frac{Br(b\bar{b} \to \mu^+\mu^- X)(\varepsilon_{\mu-b}^{cand})^2 \varepsilon_M^{b\bar{b}} \varepsilon_{trig}}{P_{rand}^{\mu}} \approx 4 \times 10^{-4}. \tag{4.10}$$

The probability for a muon to be in the HERA-B acceptance and satisfy the selection criteria is found to be $\varepsilon_{\mu-b}^{cand} \approx 54\ \%$. The probability that the reconstructed muon pair has an invariant mass within $M \in [2.5, 5]\ GeV/c^2$, including $B \to J/\Psi X$ decays, is $\varepsilon_M^{b\bar{b}} \approx 20\%$. The $b\bar{b}$ production cross-section has been measured by HERA-B: $\sigma_{b\bar{b}} = 32\ nb/nucleon$ [91]. The probability for the process $b\bar{b} \to \mu^+\mu^- X$ is evaluated according to

$$\begin{aligned} Br(b\bar{b} \to \mu^+\mu^- X) = \ & Br^2(b \to \mu X) + \\ & Br(b \to J/\Psi X) \cdot Br(J/\Psi \to \mu^+\mu^-) \approx 0.013, \end{aligned} \tag{4.11}$$

where $Br(b \to \mu X) = 10.95\%$, $Br(b \to J/\Psi X) = 1.16\%$ and $Br(J/\Psi \to \mu^+\mu^-) \approx 5.88\%$ [20].

The fraction of Drell-Yan pairs with respect to the $\mu^+\mu^-$ pairs from J/Ψ decay is estimated to be about 4%. Using the E722 measurement of the cross-section of Drell-Yan process [92], one can estimate the probability for a pair of muons to be produced in the invariant mass range [2.5,5] GeV/c^2 following the formula [93]:

$$\frac{d\sigma}{dM_{\mu^+\mu^-}} = 7.1 \exp\left[-0.917 M_{\mu^+\mu^-}\sqrt{s_1/s_2}\right], \tag{4.12}$$

where $\sqrt{s_1} = 38.9GeV$ and $\sqrt{s_2} = 41.6GeV$ are the pN c.m.s. energies in E772 and HERA-B, respectively. The value of the cross-section obtained by integration of equation (4.12) in the range [2.5,5] GeV/c^2 is 0.8 nb. We assume that the efficiency to detect Drell-Yan pairs is of the same order as the J/Ψ detection efficiency: $R_\varepsilon = \frac{\varepsilon_{DY}}{\varepsilon_{J/\Psi}} \approx 1$. Thus, for the $25,000$ reconstructed $J/\Psi \to \mu^+\mu^-$ decays the amount of Drell-Yan $\mu^+\mu^-$ pairs is expected to be ~ 930, which is rather small compared to the combinatorial background.

To summarize, the main contribution to the background under $J/\Psi \to \mu^+\mu^-$ is due to random combinations. With respect to that, muons from semi-leptonic decays of open charm contribute in a proportion of $1:25$, approximately. The contribution from decays of mesons containing bottom quark is negligible being of order 10^{-4} %. The fraction of Drell-Yan pairs in the background is estimated to be at the level of 1.6%.

4.4.3 Nuclear effects

Having at our disposal a considerable amount of J/Ψ produced in pA collisions, it is tempting to take a look at nuclear effects. The dependence of J/Ψ production on the target material can be studied by investigating the ratios of the $p_T^{J/\Psi}$ and $x_F^{J/\Psi}$ spectra obtained with tungsten ($i1$) and carbon ($i2$) during their simultaneous operation in 2002. This is very convenient, because it allows to omit many complications related to reconstruction and triggering, as they cancel in the ratio.

The production cross section can be factorized according to equation (2.31):

$$\sigma_{pA} = \sigma_{pN} A^\alpha. \tag{4.13}$$

The difference in geometrical acceptances due to different wire positions is small and can be ignored. The same is true for the the difference in trigger and selection efficiencies for J/Ψ stemming from different wires. Thus, if the factorization (4.13) holds, the resulting distribution obtained in the ratio depend only on the nuclear effects and overall normalization factor.

We compare our results to the measurement done by the E866 collaboration [94]. They reported the dependency on the atomic mass, which is parametrized as:

$$\begin{aligned} \alpha(x_F^{J/\Psi}) &= 0.9600(1 - 0.0519 \cdot x_F - 0.3380 \cdot x_F^2) \\ \alpha(p_T^{J/\Psi}) &= 0.8700(1 + 0.0604 \cdot p_T + 0.0107 \cdot p_T^2) \end{aligned} \tag{4.14}$$

The data analyzed by E866 collaboration were taken in the collision of 800 GeV protons with a nuclear target in a kinematical range corresponding to $x_F^{J/\Psi}$ interval $(-0.1, 0.93)$

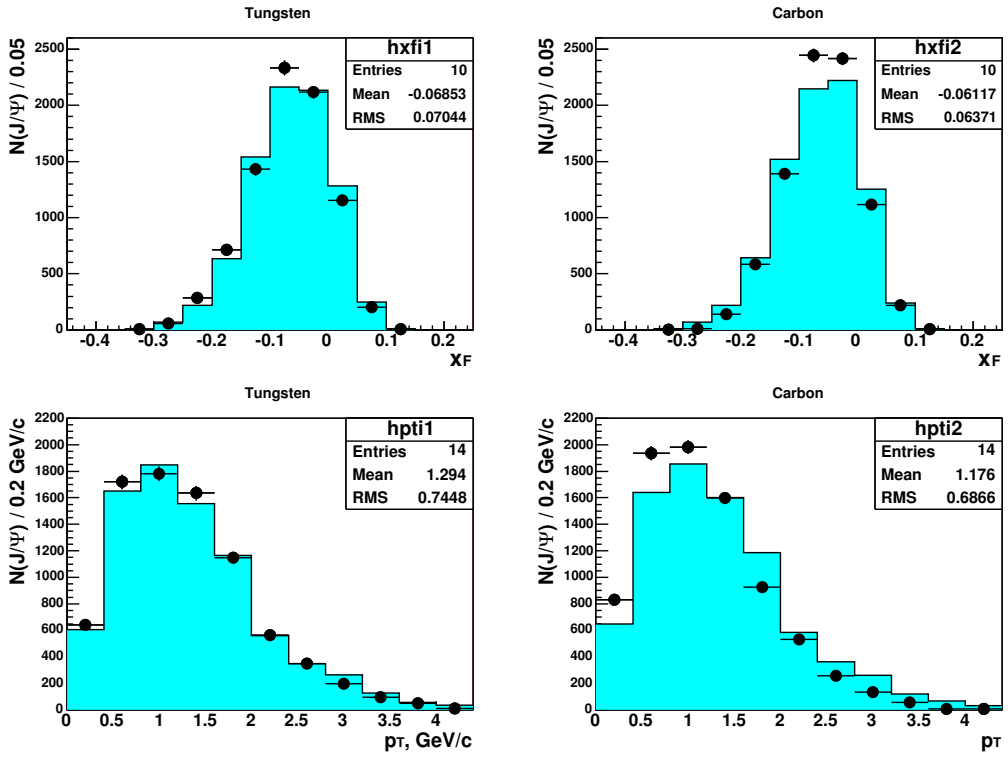

Figure 4.16: $x_F^{J/\Psi}$ *(upper plots) and* $p_T^{J/\Psi}$ *(lower plots)* J/Ψ *spectra obtained with tungsten (left plots) and carbon (right plots) wires. The number of* J/Ψ *in each bin is estimated by fitting the corresponding di-*μ *invariant mass spectrum obtained for the given bin. The measured spectra are shown by markers, while filled histograms correspond to Monte Carlo simulations. The kinematical distributions are not corrected for acceptance.*

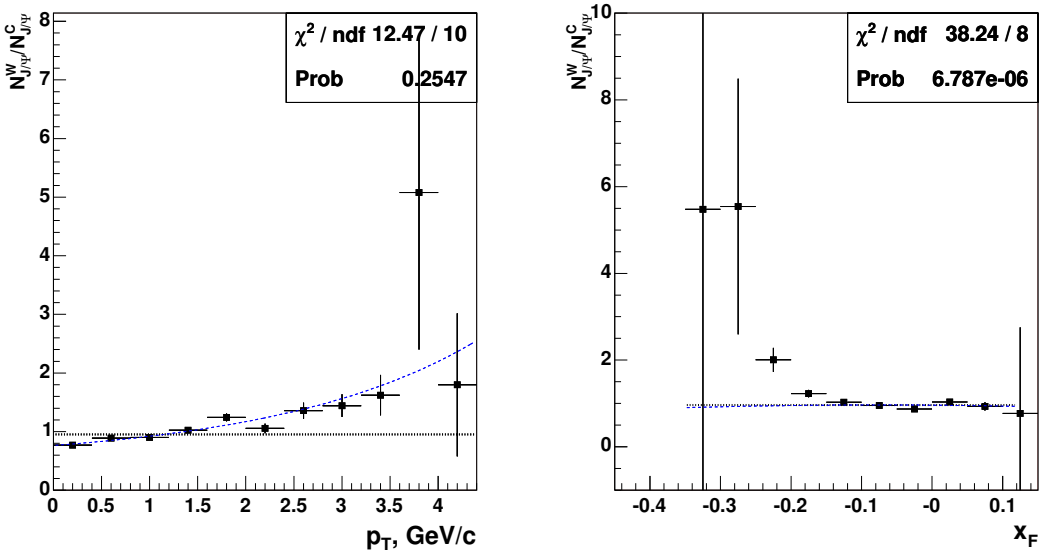

Figure 4.17: *The ratio of* $p_T^{J/\Psi}$ *(a) and* $x_F^{J/\Psi}$ *(b) spectra of* J/Ψ *obtained with tungsten and carbon wires. The dotted lines correspond to a horizontal line parametrization, while dashed lines correspond to the parametrization (4.14) measured by E866.* J/Ψ *is detected via its di-muon decay channel.*

and $p_T^{J/\Psi}$ interval $(0, 4)$ (GeV/c). This is complementary to the experimental conditions of HERA-B, where the $x_F^{J/\Psi}$ acceptance is limited by the interval $(-0.35, 0.15)$. The HERA-B x_F and p_T spectra of J/Ψ obtained from tungsten and carbon data (about 8,000 reconstructed J/Ψ for each target material) are shown in Fig. 4.16. The corresponding ratios $N_W^{J/\Psi}(x_F)/N_C^{J/\Psi}(x_F)$ and $N_W^{J/\Psi}(p_T)/N_C^{J/\Psi}(p_T)$ in therms of $x_F^{J/\Psi}$ and $p_T^{J/\Psi}$ are shown in Fig. 4.17.

If the production of the J/Ψ meson is independent of the target material the ratio of the J/Ψ rate on tungsten wire to the J/Ψ rate on the carbon wire must be described by a flat line. As can be seen in Fig. 4.17(a) this is not the case. The horizontal line does not describe the $p_T^{J/\Psi}$ distribution. On the other hand, the E866 parametrization (4.14) (dashed line in Fig. 4.17) fits rather well to the observed $p_T^{J/\Psi}$ spectrum. This indicates that nuclear effects play some role in the production of J/Ψ.

The $N_W(J/\Psi)/N_C(J/\Psi)$ distribution for the $x_F^{J/\Psi}$ interval $(-0.35, 0.15)$ (Fig. 4.17(b)) can be described neither by a horizontal line nor using the results from the E866 experiment. One should notice, however, that the kinematical x_F acceptances in E866 and HERA-B are different, while the dependency on the target material is expected to vary with x_F. Thus, if one considers only the region with $x_F^{J/\Psi}$ values larger than -0.1 (i.e. overlap with the E866 experiment), both assumptions are rather adequate. This indicates stronger dependence of the $x_F^{J/\Psi}$ spectrum on the target material for slow J/Ψ ($x_F^{J/\Psi} < -0.2$). This is the case, when the $c\bar{c}$ pair can turn into the physical state being still inside the nucleus.

The results obtained agree rather well with the E866 measurement, showing the presence of a dependency of the J/Ψ production on target material as well as its non trivial behavior with respect to J/Ψ kinematics.

4.4.4 Signal in di-electron channel

The $J/\Psi \to e^+e^-$ signal is reconstructed using the invariant mass of the pair of oppositely charged electron candidates. In addition, one of the track in the selected pair is required to have a reconstructed bremsstrahlung cluster. The invariant mass distribution is shown in Fig. 4.21(a) for data and in Fig. 4.20(a) for Monte Carlo. A clear J/Ψ signal is visible (on top a large background in the case of data). The shape of the signal region is parameterized according to

$$\frac{dN_{J/\Psi}}{dM} = N_{J/\Psi}\frac{2}{\sigma_M(\sqrt{2\pi}+\pi\sigma_{tail})}\cdot\begin{cases}\exp\left[-\frac{(M-\langle M\rangle)^2}{2\sigma_M^2}\right] & , \quad M > \langle M\rangle \\ \frac{1}{1+\left(\frac{M-\langle M\rangle}{\sigma_M\sigma_{tail}}\right)^2} & , \quad M < \langle M\rangle\end{cases} \tag{4.15}$$

$N_{J/\Psi}$ is the number of reconstructed J/Ψ particles, $\langle M\rangle$ is the position of the peak maximum and equivalent to the mean value of the Gaussian. σ_M is the width of the Gaussian [6] and σ_{tail} is a parameter which takes into account the radiative losses due to the emission of bremsstrahlung photons. The values of both σ_M and σ_{tail} reflect the

[6] In some plots σ_M is denoted simply as σ.

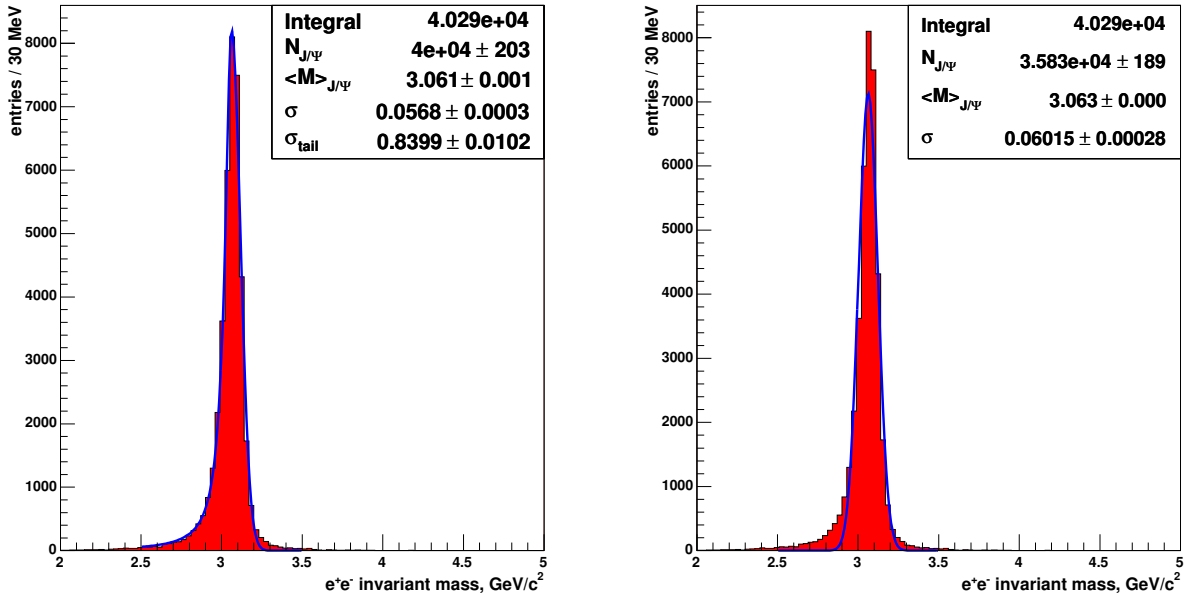

(a) (b)

Figure 4.18: *Monte Carlo simulation of* $J/\Psi \rightarrow e^+e^-$. *The fit of the signal using the parametrization form Eq. 4.15 (a) gives rather good description of the signal, while the fit with a single Gaussian (b) results in an underestimation of the signal by about* 11%.

detector resolution. The shape of the signal is tested on Monte Carlo simulated events (Fig. 4.18). The background under the signal is parametrized with the following function:

$$N_{back} = P_4(M - P_5)^2 \exp\left[-P_6 M\right]. \tag{4.16}$$

The sources of background are mainly:

- Track-cluster random matches.
- Wrong combinations of the reconstructed electromagnetic cluster with ghost or hadron tracks.
- Hadrons that are identified as electrons, losing all their energy in the ECAL. However, the probability for high energetic hadrons to be stopped in the ECAL is rather low, being less than 1 %. A requirement of transverse energy larger than 1 *GeV* (Fig. 4.9) allows such a reduction.
- Wrong bremsstrahlung assignment. Studying the $K_s^0 \rightarrow \pi^+\pi^-$ decay[7], using the data collected in 2000 it was shown that the probability to assign a random bremsstrahlung candidate to a background track was $\varepsilon_{brems}^{fake} = 5\%$ [95].

[7]See Appendix A for more details about $K_s^0 \rightarrow \pi^+\pi^-$.

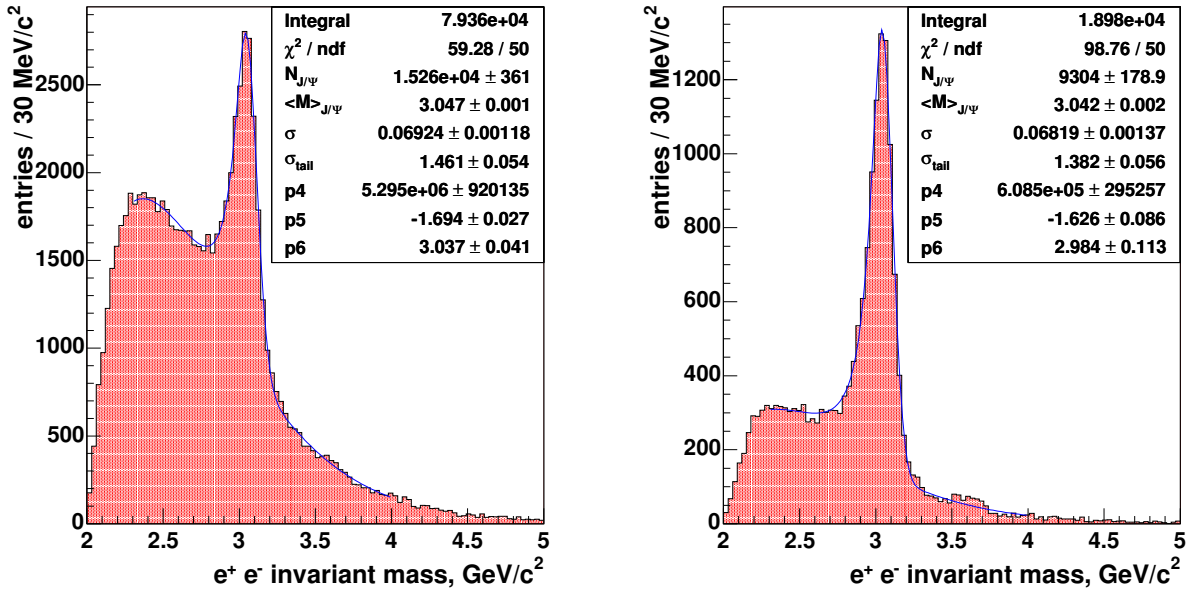

(a) (b)

Figure 4.19: *e^+e^- invariant mass for carbon data (wire i2): (a) loose selection described in the text (subsection 4.3.3); (b) with additional requirements (1)-(3) in Table 4.5.*

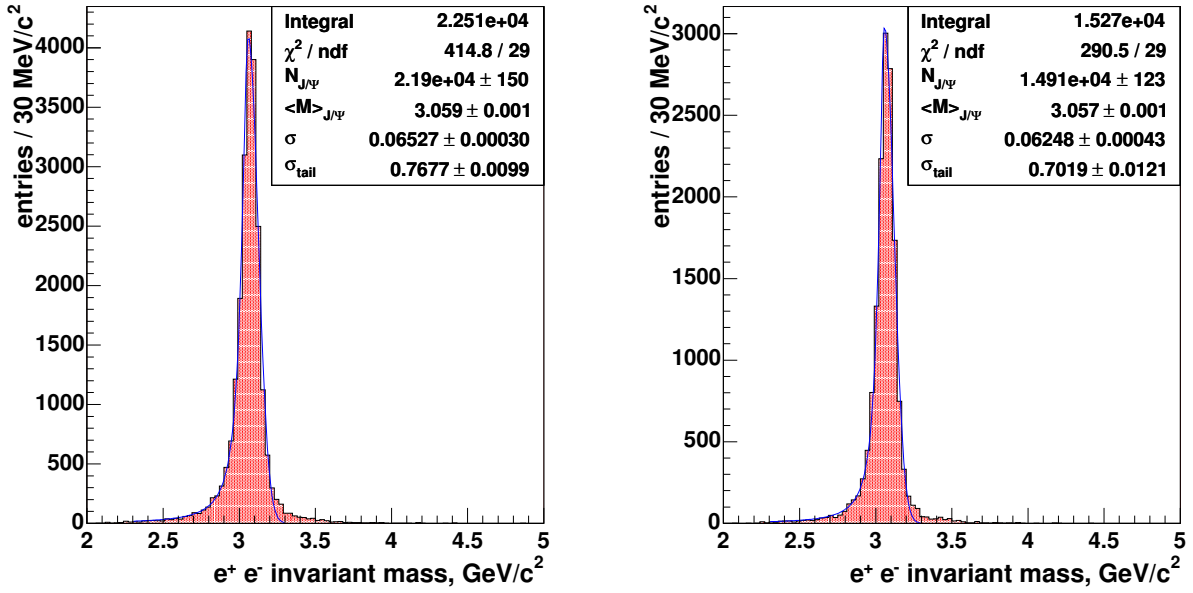

(a) (b)

Figure 4.20: *The same as in Fig. 4.21 but for Monte Carlo simulations.*

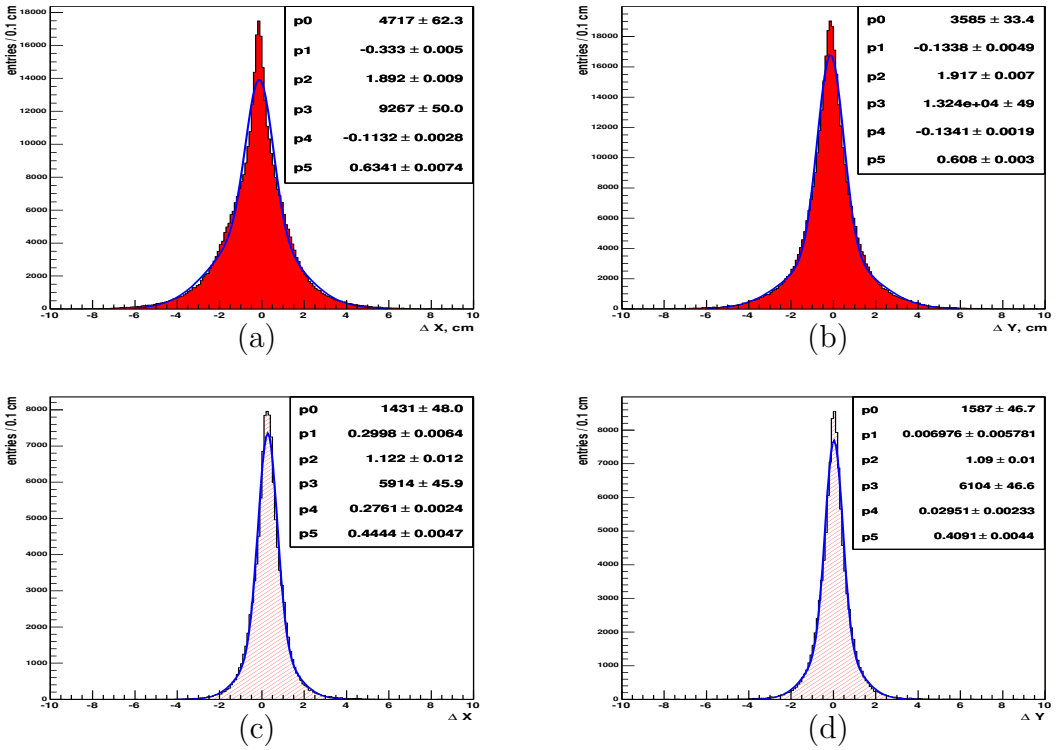

Figure 4.21: *Residuals between the reconstructed position of the ECAL cluster and extrapolated track impact point to ECAL, i.e.* $\Delta X = |x_{cl} - x_{tr}|$ *(a) and* $\Delta Y = |y_{cl} - y_{tr}|$ *(b), respectively. The fit is performed using two-Gaussian parametrization. (c) and (d) represent correspondent distributions for Monte Carlo simulations.*

Table 4.5: $J/\Psi \to e^+e^-$ *selection criteria. The values of* σ *and* $\langle E/p \rangle$ *are obtained from a fit to the corresponding distribution from data and Monte Carlo (Fig. 4.10).* ε_{data} *and* ε_{MC} *show the fraction of the* J/Ψ *signal left when a cut is applied, for data and Monte Carlo, respectively.*

Cut	Value	ε_{data}, %	ε_{MC}, %
Loose selection (after trigger and reconstruction):			
Bremsstrahlung tag	1 brems. photon	100 %	100 %
Vertex fit probability	$P_{vert}(\chi^2) > 0.005$	93.9 ± 3.3	96.9 ± 0.9
Additional requirements:			
1. E/p ratio	$\frac{E}{p} > \langle E/p \rangle - 1.5\sigma_{E/p}$ $\frac{E}{p} < \langle E/p \rangle + 2.5\sigma_{E/p}$	76.2 ± 2.7	78.0 ± 0.8
2. ΔX and ΔY (cm)	$\lvert\Delta x + 0.113\rvert < 1.902$, $\lvert\Delta y + 0.134\rvert < 1.824$	83.0 ± 2.7	85.4 ± 0.9
3. Cluster shape	$asym > 0.8$	96.4 ± 3.2	98.3 ± 0.9
Total		61.0 ± 1.8	65.0 ± 1.1
Hard bremsstrahlung tag :	2 brems. photon	21.2 ± 0.8	20.5 ± 0.3

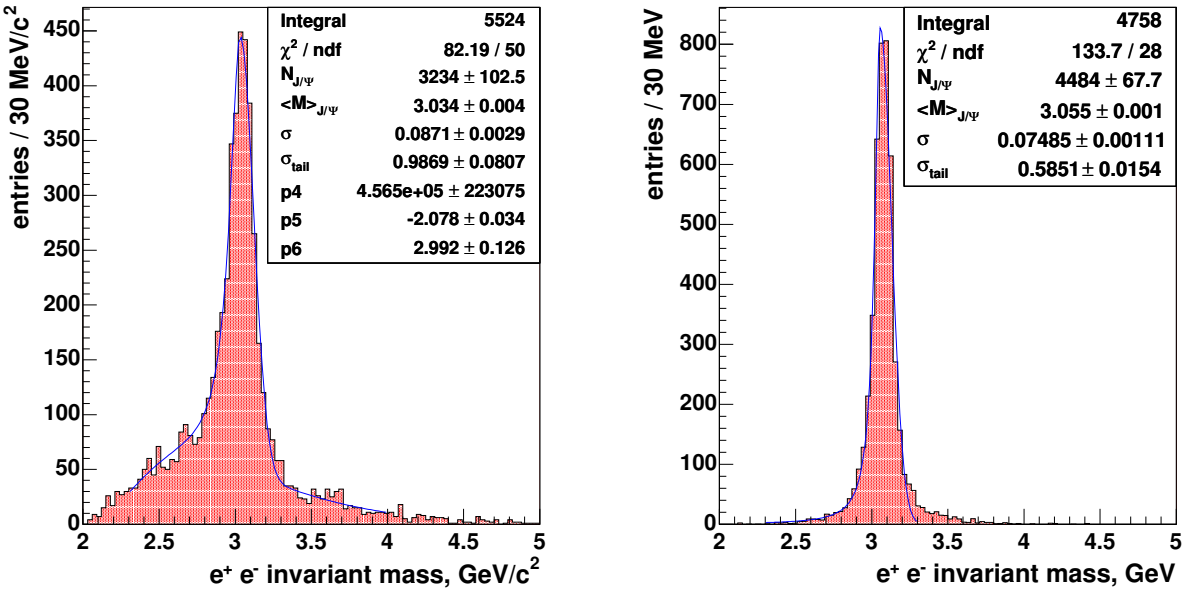

(a) (b)

Figure 4.22: *e^+e^- invariant mass distribution after requirement that each of the tracks has an associated bremsstrahlung cluster reconstructed in the calorimeter. (a) and (b) show the mass spectra for data and Monte Carlo, respectively.*

To reduce the level of background and, thus, improve the signal to background ratio, more cuts are applied. A cut on the residuals $|\Delta x| = |x_{cl} - x_{tr}|$ and $|\Delta y| = |y_{cl} - y_{tr}|$, between the reconstructed cluster position and the coordinates of tracks entry point into ECAL (Fig. 4.21), suppresses track-cluster random matches. The track entry point into ECAL is obtained by extrapolating the track parameters to the ECAL plane, e.g, $z = z_{ECAL}$ (Fig 4.11). Wrong combinations, as well as misidentified hadrons are further reduced by a stronger requirement on E/p ratio ($\langle E/p\rangle - 1.5\sigma_{E/p} < E/p < \langle E/p\rangle + 2.5\sigma_{E/p}$, see Fig. 4.10) and by a cluster shape cut ($asym > 0.8$). The latter is defined as the energy of the three most energetic cells of the cluster to the total cluster energy.

The values corresponding to the above cuts are summarized in Table 4.5. Their effect on the signal and background are shown in Fig. 4.21(b) and Fig. 4.20(b) for data and MC, respectively. The requirement of an associated bremsstrahlung photon candidate for each of the two electron candidates has an "efficiency" $\varepsilon_{2\,brems}$ of about 21%, relative to the requirement of one bremsstrahlung photon per J/ψ candidate, and suppresses the background by a factor of 28. The values are also confirmed by Monte Carlo studies ($\varepsilon^{MC}_{2\,brems} \sim 20.5\%$), which indicates that the present Monte Carlo simulation provides a good description of the detector component material. The J/Ψ mass distribution after requirement of two bremsstrahlung photons is sown in Fig. 4.22. In the Mote Carlo distribution (Fig. 4.22(b)), it is possible to observe clearly a high-mass tail. It is due

to events where photons produced in association with J/Ψ are mistakenly included as a bremsstrahlung. In data the same effect is hidden within the background under J/Ψ (Fig. 4.22(b)), which suggests that the rate of such events is low.

The next step consists of finding a photon candidate, such that χ_c radiative decays could be reconstructed. To search for χ_c decays, the events lying in an appropriate mass window are further analyzed. Only one J/Ψ candidate is accepted per bunch crossing. If two or more candidates satisfy the selection criteria, the candidate with the best di-electron vertex fit is chosen.

Chapter 5

$\chi_c \to J/\Psi$ radiative decays

5.1 Introduction

In this chapter, we will present the χ_c signal obtained in proton-Carbon (pC), proton-Tungsten (pW) and proton-Titanium (pTi) collisions. The signal corresponding to the combined data set is also shown. The radiative $\chi_c \to \gamma J/\Psi$ decays are reconstructed by pairing isolated photon candidates with $\mu^+\mu^-$ and e^+e^- pairs falling in the J/ψ mass window:

$$\begin{array}{rcccl} 2.99 & < & M_{\mu^+\mu^-} & < & 3.19 \quad (GeV/c^2) \\ 2.90 & < & M_{e^+e^-} & < & 3.25 \quad (GeV/c^2) \end{array} \tag{5.1}$$

The analysis proceeds through the following steps:

- Reconstruction of $J/\Psi \to l^+l^-$ decays.
- Search for photon candidates.
- Reconstruction of χ_c particles by pairing the photon candidates and the reconstructed J/ψ.
- Estimation of background with the help of so-called event mixing technique.
- Determination of the photon efficiencies with Monte Carlo simulated events.
- Extraction of R_{χ_c} and comparison of several nuclear target materials.

The selection of a sample of events containing a J/ψ particle is described in the previous chapter. Two decay channels were used: $J/\psi \to \mu^+\mu^-$ and $J/\psi \to e^+e^-$. Only one J/Ψ candidate per event (i.e. per bunch crossing) is used for the χ_c search. If several candidates passed the selection criteria, then the candidate with the best di-lepton vertex fit is considered further. A χ_c is then examined through the mass difference distribution

$$\Delta M = M_{\gamma J/\Psi} - M_{J/\Psi}, \tag{5.2}$$

shown in Fig. 5.1(upper left plot). In the formula (5.2), $M_{\gamma J/\Psi}$ is the invariant mass of the J/Ψ and γ system (Fig. 5.1(upper right plot)), while $M_{J/\Psi}$ is the mass of the J/Ψ candidate (Fig. 5.1(lower plot)). The invariant mass of the J/Ψ and the photon is determined according to the following formula

$$M_{\gamma J/\Psi} = \sqrt{M^2_{J/\Psi} + 2E_\gamma E_{J/\Psi} - 2\vec{p}_\gamma \vec{p}_{J/\Psi}}, \tag{5.3}$$

where $(E_{J/\Psi}, \vec{p}_{J/\Psi})$ and $(E_\gamma, \vec{p}_\gamma)$ are the four-momenta of J/Ψ and γ candidates, respectively. The energy is related to the mass through

$$E_{J/\Psi} = \sqrt{\vec{p}^2_{J/\Psi} + M^2_{J/\Psi}}. \tag{5.4}$$

The masses of χ_{ci}, $(i = 0, 1, 2)$ and the corresponding ΔM values are summarized in Table 5.1. It is advantageous to use ΔM instead of $M(\gamma J/\Psi)$ because the impact of the

Table 5.1: *Mass of the χ_c states [20].*

State	M, GeV/c^2	$M - M_{J/\Psi}$, GeV/c^2
χ_{c0}	3.417	0.320
χ_{c1}	3.511	0.414
χ_{c2}	3.556	0.459

uncertainty related to the J/Ψ mass resolution, $\delta M_{J/\Psi}$, is minimized. The contribution to the χ_c invariant mass resolution [1] can be simplified to

$$\delta M_{\chi_c} = \frac{M_{J/\Psi}}{M_{\chi_c}} \cdot \delta M_{J/\Psi} \simeq 0.877 \cdot \delta M_{J/\Psi} \tag{5.5}$$

On the other hand, the contribution to the resolution of the mass difference, ΔM, is significantly smaller

$$\delta(\Delta M) = \left| \frac{M_{J/\Psi}}{M_{\chi_c}} - 1 \right| \delta M_{J/\Psi} = 0.123 \cdot \delta M_{J/\Psi} \tag{5.6}$$

This leads to the resolution ratio:

$$\left| \frac{\delta M_{\chi_c}}{\delta(\Delta M)} \right| = \left| \frac{M_{J/\Psi}}{\Delta M} \right| \approx 7. \tag{5.7}$$

[1] We neglected the correlation between $M_{J/\Psi}$ and direction of the $\vec{p}_{J/\Psi}$, as well as the uncertainty related to the determination of the photon momentum.

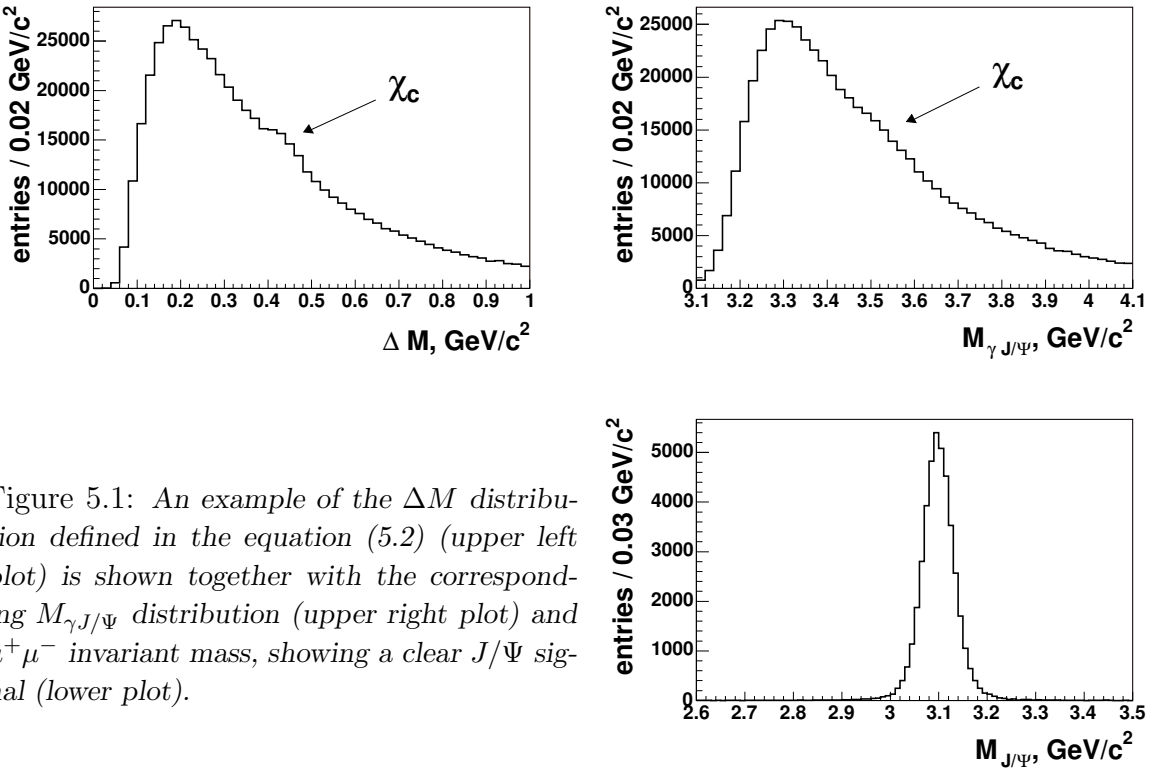

Figure 5.1: *An example of the ΔM distribution defined in the equation (5.2) (upper left plot) is shown together with the corresponding $M_{\gamma J/\Psi}$ distribution (upper right plot) and $\mu^+\mu^-$ invariant mass, showing a clear J/Ψ signal (lower plot).*

5.2 Search for isolated photons

The reconstruction of the photon is done

1. either by measuring the energy released in ECAL,
2. or by reconstructing e^+e^- pairs from photon conversions:

$$\gamma + (Z, A) \rightarrow (Z, A) + e^+e^-. \tag{5.8}$$

The first case, described in this chapter, results in a higher efficiency. The calorimeter energy resolution - resulting in the ΔM_{χ_c} resolution of order 40 MeV - does not allow a separation of the χ_{c1} and χ_{c2} states, which have a mass difference of about 46 MeV. On the other hand, the second case (above), to reconstruct γ pair conversions implies to take advantage of the reconstruction of charged tracks. The momentum resolution of the tracking system is, in principle, sufficient to separate the two states. However, the efficiency of the method is rather low, as we will see in chapter 7.

5.2.1 Cluster reconstruction in ECAL

Cluster reconstruction in ECAL is performed by the standard program CARE [96]. A cluster is defined as 3×3 calorimeter cells, with a local maximum deposited energy in the

central cell. The energy of the cluster, E^{cl}, is determined by the energy sum of all 9 cells (or less if dead channels were present):

$$E^{cl} = \sum_{k=1}^{N_{cells}} E_k \tag{5.9}$$

where E_k is the energy of one cell and N_{cells} is the number of cells building the cluster. The electronic noise is rejected by requiring a minimum deposited energy in any cell of 0.15, 0.10, 0.05 (GeV) for the inner, middle, outer part of ECAL, respectively. The momentum direction of the reconstructed photon is estimated by connecting the reconstructed dilepton vertex and the cluster coordinates measured in the calorimeter. The determination of the cluster coordinates, x and y, proceeds according to the formula:

$$\begin{array}{rclcrcl} x_{cl} & = & x_{cent} & + & A \cdot Arsh\left[B \cdot (x_{cog} & - & x_{cent})\right] \quad , \\ y_{cl} & = & y_{cent} & + & A \cdot Arsh\left[B \cdot (y_{cog} & - & y_{cent})\right] \quad , \end{array} \tag{5.10}$$

where x_{cent} and y_{cent} are the coordinates of the central cell. A and B are ECAL internal parameters. x_{cog} and y_{cog} are defined as

$$\begin{array}{rcl} x_{cog} & = & \sum_{k=1}^{N_{cell}} \cdot \frac{x_k E_k}{E^{cl}} \\ y_{cog} & = & \sum_{k=1}^{N_{cell}} \cdot \frac{y_k E_k}{E^{cl}} \quad . \end{array} \tag{5.11}$$

Knowing x and y coordinates of the cluster, its z coordinate is defined as the position of the maximum of the shower, which corresponds to about 7.5 radiation lengths from the calorimeter entry plane. Thereby, it is assumed that the photon originates from the interaction point while determining the value of the z coordinate

$$z_{cl} = A' + B' ln(E), \tag{5.12}$$

where A' and B' are constants determined for each part of calorimeter through simulation of its response [97].

The reconstruction of the ECAL cluster depends on the position of dead channels, energy resolution and noise level, upon which the stability of the pedestals is dependent.

5.2.2 Dead and Hot channels

Inaccuracies in the calorimeter performance, such as hot and dead channels, are studied using cluster occupancy distributions.

Not working channels can be divided into the following groups

- those with unstable or defect readout boards,
- and those with dead channels randomly distributed.

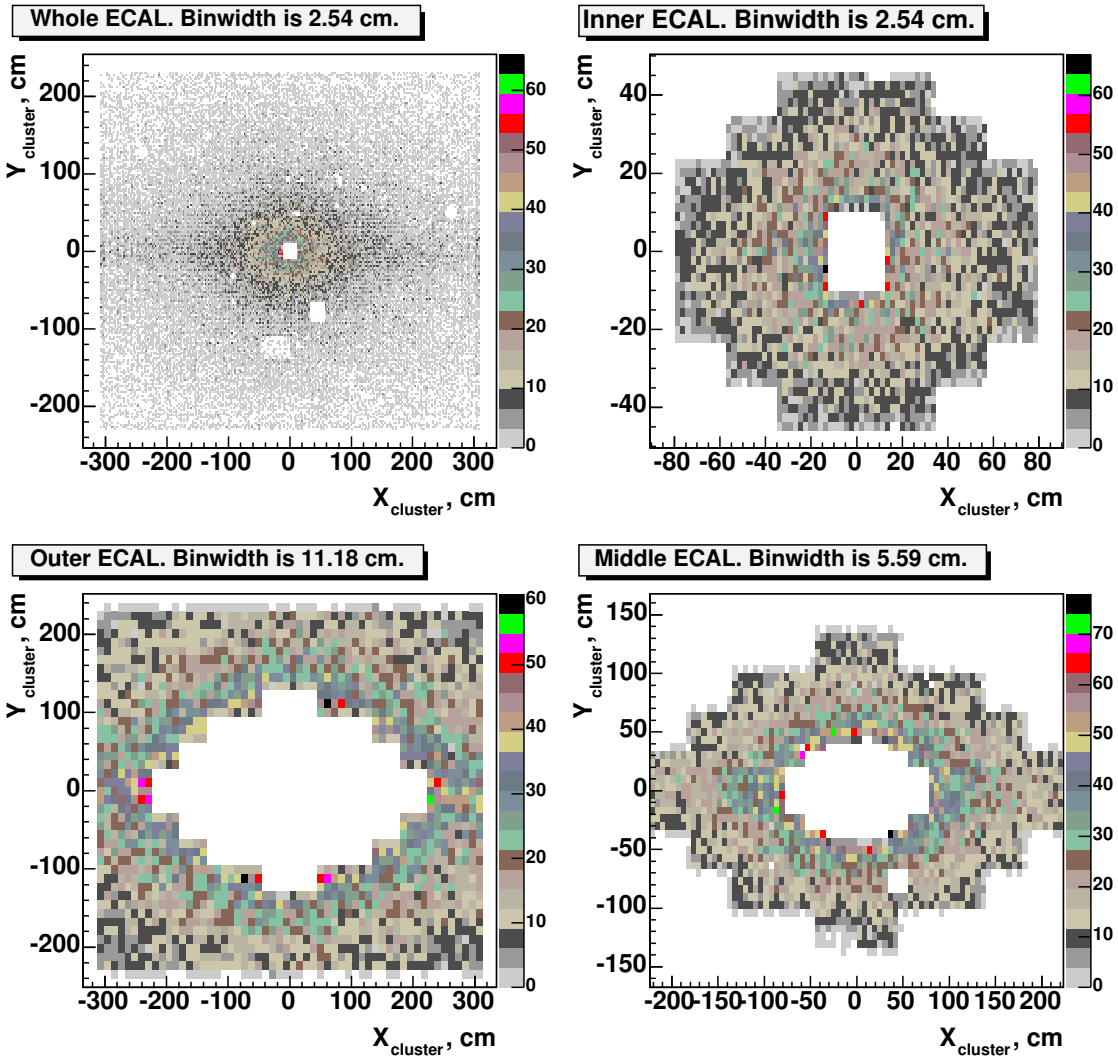

Figure 5.2: *Calorimeter occupancy within a run (20881) projected on the xy coordinate plane. The upper left plot depicts the whole calorimeter. The upper right, lower right and lower left plots show the distributions for the inner, middle and outer part of the calorimeter, respectively.*

Data related to the first group are excluded from the analysis. The effect on the final ΔM distribution of clusters with dead central and/or peripheral cells is not investigated. However, from the studies based on data 2000 [99] it follows that the presence of randomly distributed dead channels should not affect the reconstruction of the χ_c signal and, therefore, should not contain any systematic influence on our results.

Hot channels are defined as channels with a large number of reconstructed clusters relative to any neighboring cells. Such channels have to be masked during the reconstruction by application of masking tables with already known dead and hot channels [2]. In addition, in order to avoid any systematic effects on the ΔM distribution due to artificial clusters, we examine triggered events selected for the χ_c search. To localize hot channels we examine cluster occupancy distributions for all events within a run (Fig. 5.2). The search is conducted in each part of the calorimeter separately. Investigating projections of the occupancy distributions for the inner, middle and outer parts of ECAL we do not find any systematic peaks.

5.2.3 Calorimeter energy resolution

The cluster energy and spatial resolutions are defined as

$$\begin{array}{rcl} \frac{\sigma E^{cl}}{E^{cl}} & = & \frac{C_1}{\sqrt{E^{cl}(GeV)}} \oplus C_2 \\ \sigma_{x,y}(cm) & = & \frac{D_1}{\sqrt{E^{cl}(GeV)}} \oplus D_2 \end{array} \tag{5.13}$$

where C_1, D_1 and C_2, D_2 are so-called stochastic and constant terms. The constant terms are related to the intrinsic resolution of the calorimeter and uncertainties in the calibration. In principle, there should be third term for noise in electronics. However, it has a negligible contribution to the resolution and, therefore, is usually neglected.

The detailed study of the performance of the inner part of the calorimeter was carried using data from the 2000 commissioning run [63]. The energy resolution achieved was

$$\frac{0.225(GeV)^{1/2}}{\sqrt{E}} \oplus 0.017. \tag{5.14}$$

It was also shown, that for clusters with energy less than 5 GeV the uncertainty on the energy estimation was more than 10%, while for more energetic clusters the uncertainty approched the design value of 2% [10, 55].

The performance of ECAL in the 2002-2003 run was improved relative to year 2000 (see Table 5.2). Monte Carlo simulations, based on a realistic description of the detector in 2002, predict a χ_c ΔM resolution of $\sim 37 MeV/c^2$, to be compared to $\sim 45 MeV/c^2$ in the previous running period. The expected resolution of each single state (χ_{c1} or χ_{c2}) is about $27 - 30$ MeV. Taking into account the mass difference between the two states (46 MeV/c^2 [20]), it becomes clear that the present energy resolution does not allow a separate study of χ_{c1} and χ_{c2}.

[2] The reconstruction correspond to the 3^d reprocessing of data.

Table 5.2: *Energy and spatial resolution of the calorimeter. The values measured in 2002-2003 [98] are compared to the design ones.*

	inner	middle	outer
Design values			
C1 ($GeV^{1/2}$)	0.170	0.095	0.095
C2	0.016	0.010	0.010
D1 ($cmGeV^{1/2}$)	1.1	1.9	2.2
D2	0.16	0.20	0.66
Performance in 2002-2003			
C1 ($GeV^{1/2}$)	0.205	0.118	0.108
C2	0.012	0.014	< 0.02
D1 ($cmGeV^{1/2}$)	1.25	1.37	2.17
D2	0.02	0.28	0.28

5.2.4 Selection of radiative χ_c photons

The search for photons form $\chi_c \to \gamma J/\Psi$ decays is done by studying the information from the whole ECAL except the region near the beam pipe where the occupancy is too high (up to 30%). The exclusion of this area of the calorimeter is achieved by imposing the following requirement on the reconstructed cluster coordinates:

$$\frac{x_{cl}^2}{4} + y_{cl}^2 > 484\ cm^2. \tag{5.15}$$

The effect of this cut is summarized in Fig. 5.3. Besides photons and electrons, other particles, such as muons and charged pions, entering the active volume of the calorimeter, can deposit energy. To avoid such clusters due to soft secondary particles as well as noise clusters the requirement on cluster energy, $E_{cl} > 3.0\ GeV$ (Fig. 5.4(a)), and cluster transverse energy , $E_T^{cl} > 0.1\ GeV$ (Fig. 5.5(a)), are imposed. The cuts on cluster energy and cluster transverse energy reshape the ΔM distribution (Fig. 5.4(b) and Fig. 5.5(b)). Hadronic background is further reduced by requiring that the ratio of the energy of three most energetic cells of the cluster to the total cluster energy, $asym$, satisfies the following relation:

$$asym = \frac{\sum_{i=1}^{3} E_i^{max}}{E_{clus}} \quad > \quad 0.8. \tag{5.16}$$

The $asym$ distribution before and after the cut is shown in Fig. 5.6(a). The corresponding ΔM distributions are presented in Fig. 5.6(b).

The rejection of the cluster caused by electrons or positrons is done using ECAL cluster reconstructed track assignment [96]. A cluster is not considered any further if it has an associated reconstructed track starting upstream or inside the magnet (i.e. $z < 600cm$).

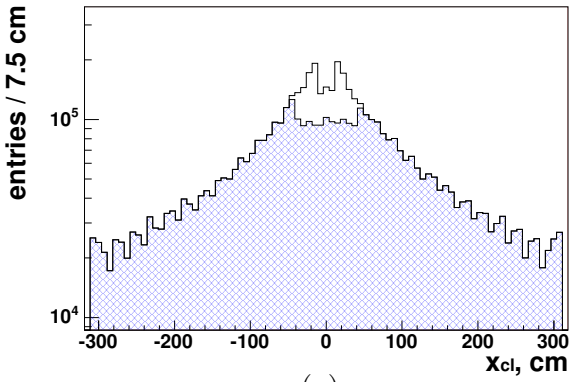

(a)

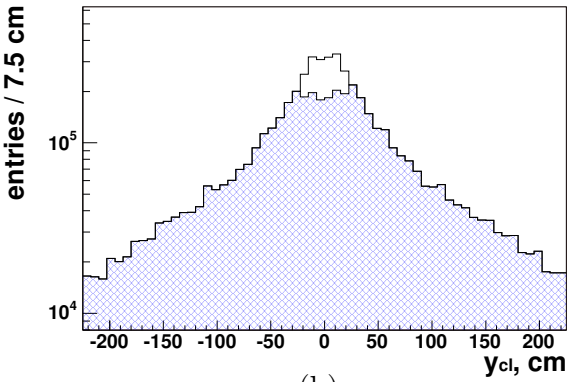

(b)

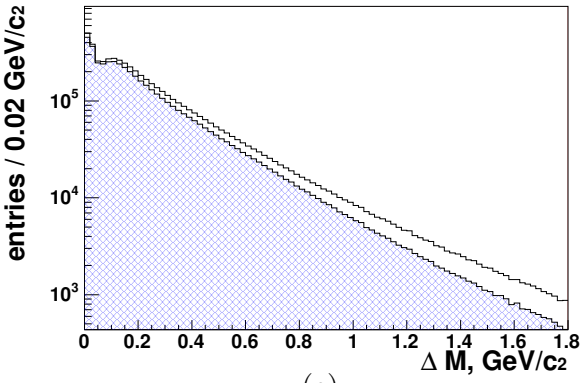

(c)

Figure 5.3: *Exclusion of the innermost part of ECAL according to relation (5.15): (a) x coordinate of the reconstructed cluster position; (b) y coordinate of the reconstructed cluster position. (c) ΔM distribution. The plots show the distributions before (unfilled histogram) and after (filled histogram) the cut.*

In contrast, clusters with associated short tracks (i.e. starting downstream the magnet) are accepted for analysis. This allows to partly recover the χ_c signal due to photon conversions. In addition, to make sure that the track pointing to the clusters is not just a coincidence, the momentum directions of the photon and track are required to be collinear (see Fig. 5.7(a,b))

$$\begin{array}{rcl} \mid (p_x/p_z)_{track} - (p_x/p_z)_{cl} \mid & < & 0.1 \\ \mid (p_y/p_z)_{track} - (p_y/p_z)_{cl} \mid & < & 0.1 \end{array} \tag{5.17}$$

The probability of the photon to convert in the detector material downstream of the magnet is about 42%, and is determined from Monte Carlo simulations. The effect of the rejection of the clusters due to long charged tracks is shown in Fig. 5.7(c).

An additional requirement on the photon candidate is done in order to suppress background photons coming from $\pi^0 \to \gamma\gamma$ decays. Namely, any pairs of clusters with invariant mass in the vicinity of the π^0 mass

$$95 \;<\; M_{\gamma\gamma} \;<\; 175 \quad MeV/c^2. \tag{5.18}$$

are removed from consideration (see Fig. 5.8)

Following the energy conservation and taking into account the known mass difference between χ_c and J/Ψ (Table 5.1) the momenta of photon and J/Ψ from $\chi_c \to \gamma J/\Psi$ decay

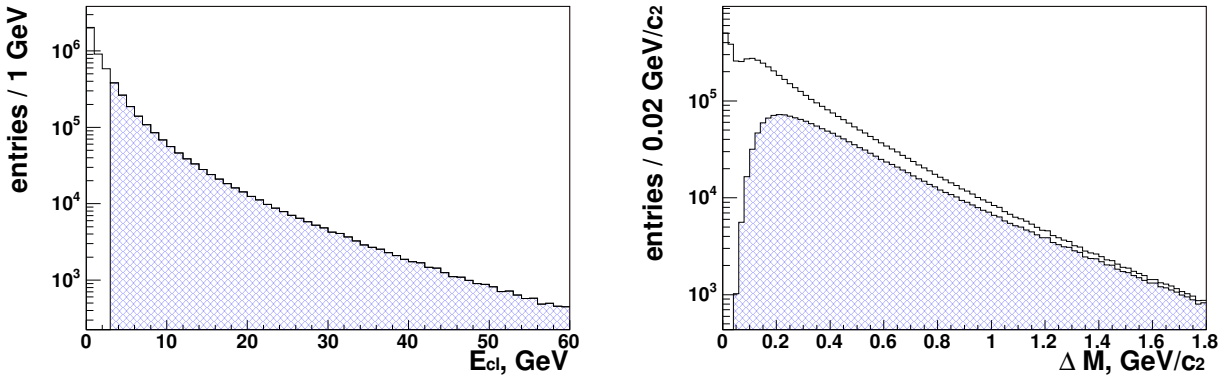

(a) (b)

Figure 5.4: *Cut on ECAL cluster energy: (a) ECAL cluster energy. The filled histogram shows the distribution after a cut ($E > 3\ GeV$) has been applied. (b) ΔM distribution before (unfilled histogram) and after (filled histogram) the energy cut.*

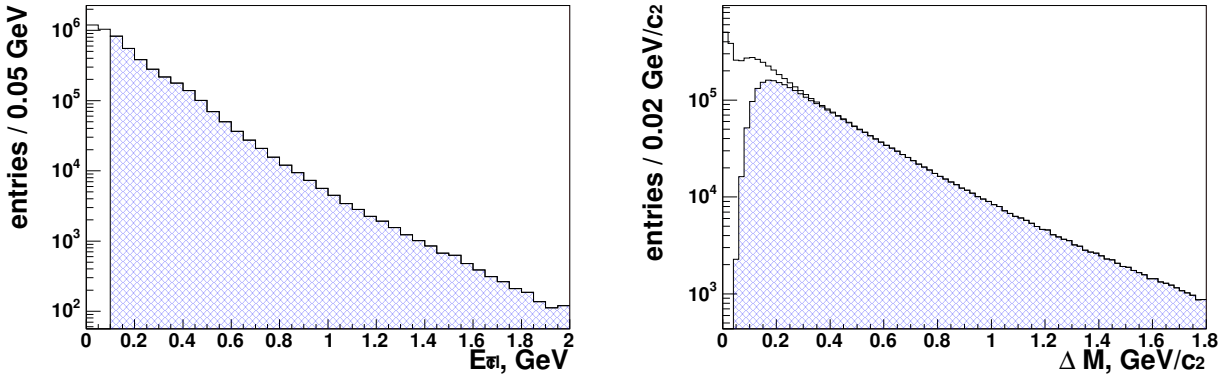

(a) (b)

Figure 5.5: *Cut on ECAL cluster transverse energy: (a) ECAL cluster transverse energy of the cluster. The filled histogram shows the distribution after a cut ($E_T^{cl} > 0.1\ GeV$) has been applied. (b) ΔM distribution before (unfilled histogram) and after (filled histogram) the cut.*

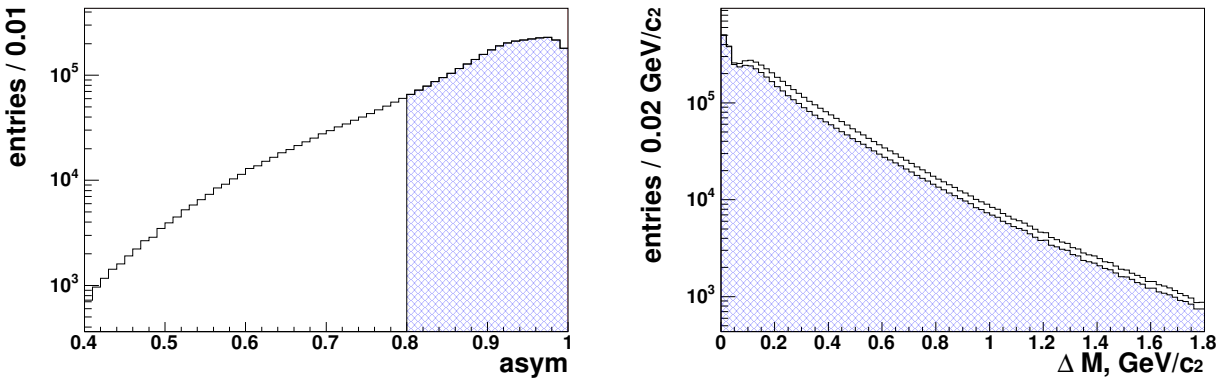

(a) (b)

Figure 5.6: *Cut on the cluster shape: (a) Ratio of energy from three most energetic cells to the total cluster energy (asym); the filled histogram indicates the cut asym* > 0.8. *(b)* ΔM *distribution before (unfilled histogram) and after (filled histogram) the cluster shape cut.*

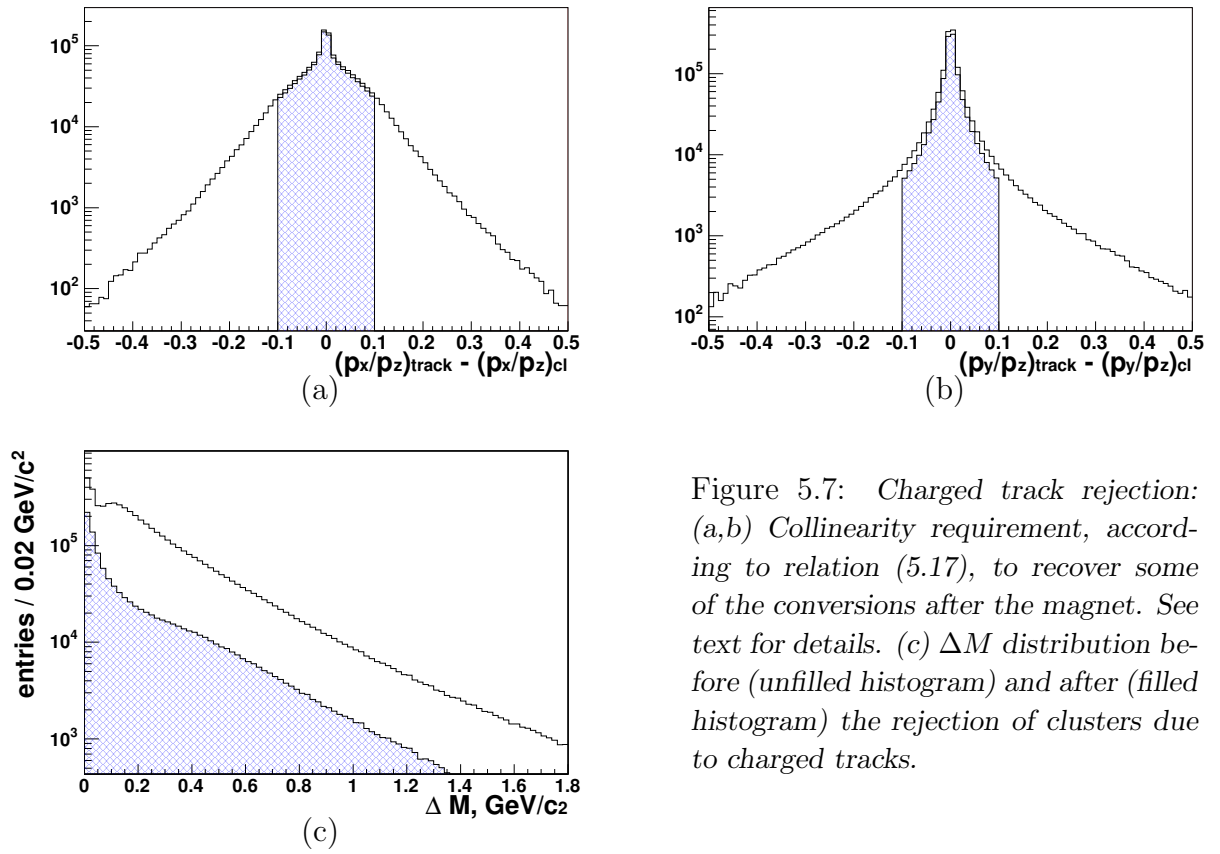

(a) (b)

(c)

Figure 5.7: *Charged track rejection: (a,b) Collinearity requirement, according to relation (5.17), to recover some of the conversions after the magnet. See text for details. (c)* ΔM *distribution before (unfilled histogram) and after (filled histogram) the rejection of clusters due to charged tracks.*

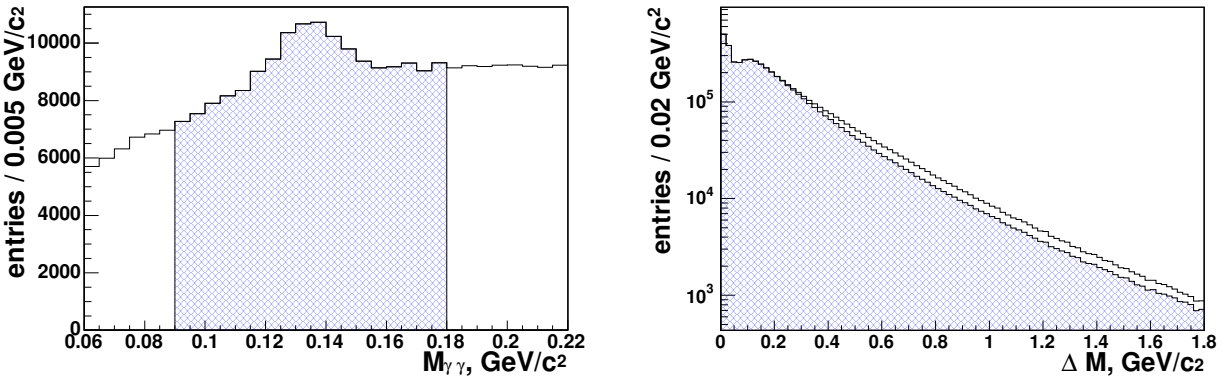

(a) (b)

Figure 5.8: π^0 *rejection: (a)* $\gamma\gamma$ *invariant mass. Photons contributing to the* π^0 *region (filled area) are not considered in the isolated photon search. (b)* ΔM *distribution before (unfilled histogram) and after (filled histogram) the* π^0 *cut.*

in the χ_c rest frame are expected to be $\sim 0.2\ GeV/c$. As a result J/Ψ and γ move almost parallel in the lab frame (see Fig. 5.9). It implies that kinematical limitations of J/Ψ imposed by trigger will also have an influence on the photon kinematics. Subsequently, the effect of the cuts may depend on the type of trigger used. To a first approximation, however, these dependencies are neglected and the photon selection in di-μ and di-e data is similar. The only difference is that in di-e case the clusters assigned to the triggered tracks as well as clusters reconstructed as bremsstrahlung radiation are removed from the isolated photon search.

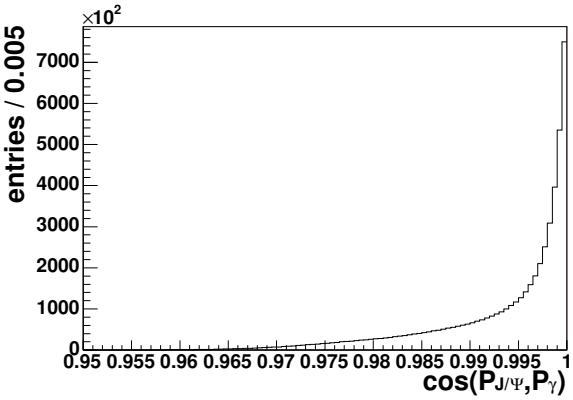

Figure 5.9: *Opening angle between* J/Ψ *and* γ*, calculated in the lab frame.*

5.2.5 Efficiencies

The influence of the photon selection criteria on the signal is studied with the help of Monte Carlo simulation. The signal distributions are obtained by matching the reconstructed cluster to the Monte Carlo particle it stems from. For this purpose, we compared the cluster position (x_{cl}, y_{cl}) to the coordinates of the simulated particle entry point into the calorimeter (x_{MC}, y_{MC}). A cluster is assigned to a given Monte Carlo simulated photon if the radial distance, r, satisfies the following relation:

$$r = \sqrt{(x_{cl} - x_{MC})^2 + (y_{cl} - y_{MC})^2} < 0.75\ d, \tag{5.19}$$

where d is the size of an ECAL cell (see Table 3.2). In case of multiple choices, the match with the smallest r is chosen. The result of the matching procedure is depicted in Fig. 5.10. The left plot of the figure shows the simulated mass difference ΔM for all $\gamma J/\psi$ combinations (points with error bars), together with the case where clusters are matched to χ_c photons (filled histogram). In the matching we also consider e^+e^- pairs, originating from photon conversions downstream of the magnet. The probability for such processes is about 42%. In cases, when both e^+ and e^- contribute to the same cluster the assignment was done in the same way as described above. However, some conversion pairs can produce two clusters in the calorimeter. According to simulations, this happens in 22% of all conversions occuring downstream the magmet. Fortunately, such events are distributed rather smoothly over the considered ΔM range and their contribution to the signal is negligible (Fig. 5.10). They can be safely regarded as background. Fig. 5.11 shows matched χ_c signal for simulation for $i2$ carbon wire (a), for $i1$ tungsten wire (b) and for merged $i1i2$ sample (c).

While the effect due to a particular cut was studied using the signal obtained from the matching, their cumulative efficiency, i.e. photon detection efficiency, was estimated using the signal extracted from a fit [3] to the simulated ΔM distribution. The efficiency to detect photons coming from χ_c decays is defined as follows:

$$\varepsilon_\gamma = \frac{N^{MC}_{reco}(\chi_c)}{N^{MC}_{J/\Psi}}. \tag{5.20}$$

$N^{MC}_{reco}(\chi_c)$ is the number of the χ_c events obtained from a fit to ΔM distributions. $N^{MC}_{J/\Psi}$ is the number of reconstructed J/Ψ particles stemming from χ_c decays, which passed the J/Ψ selection. $N^{MC}_{J/\Psi}$ is obtained from a fit to the simulated $\mu^+\mu^-$ invariant mass distribution. As far as the uncertainties related to the fitting procedure are the same for data and simulations, the estimation of photon efficiency by fitting the Monte Carlo ΔM (Fig. 5.10, point with error bars) is preferable. Whereas the use of the "matched" distribution (Fig. 5.10, filled histogram) may impose some systematic error in the γ efficiency determination related to the uncertainties in the matching.

[3] We will describe it in the next section

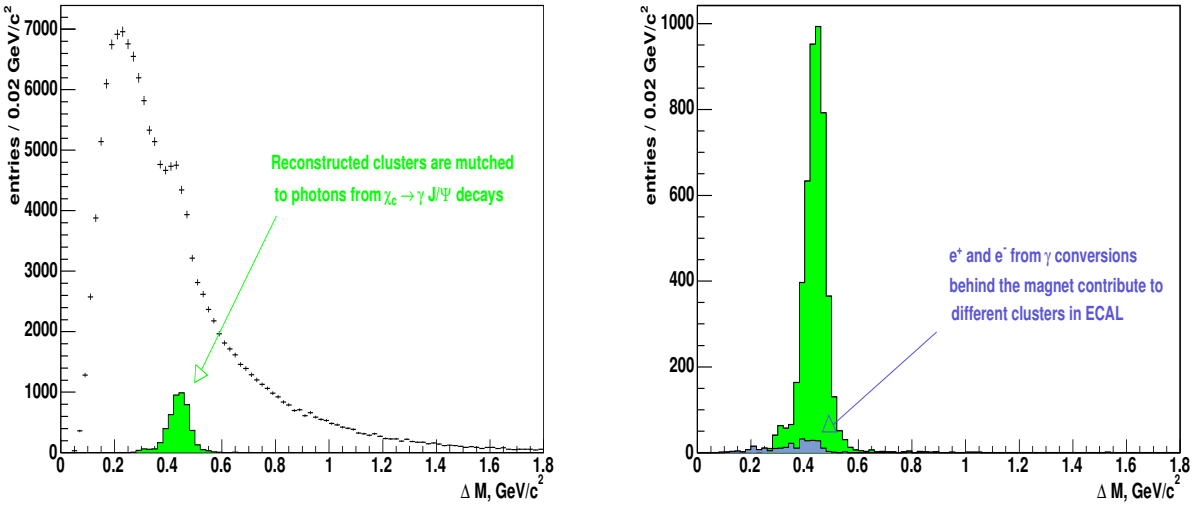

Figure 5.10: ΔM *distribution obtained form Monte Carlo simulations. Left plot: distribution of all* $\gamma J/\Psi$ *combinations. The filled histogram is for the clusters matched to* χ_c *photons. The same histogram is shown again on the right plot (filled hologram), together with a small contribution from clusters due to conversions downstream of the magnet, producing two separate* e^+ *and* e^- *clusters (histogram on the bottom).*

5.3 χ_c reconstruction.

Having reconstructed both J/ψ and photon candidates, we may start the process of the χ_c signal extraction. The specificity of the analysis is that the estimation of the χ_c yield strongly depends on the background description. As already introduced in section 5.1, the search for χ_c is done by investigating the ΔM distribution (Fig. 5.1(upper left plot)), which is the difference between the invariant mass of the J/Ψ and γ system, $M(J/\Psi\gamma)$ (Fig. 5.1(upper right plot)), and the mass of the J/Ψ, $M(J/\Psi)$ (Fig. 5.1(lower plot)).

ΔM is determined for each combination of J/Ψ and γ candidates within an event. Normally, the analyzed J/Ψ events contain many γ candidates measured by ECAL in a wide energy range. This results in a large combinatorial background, where both particles either come from two different sources or are wrongly interpreted as the J/Ψ and/or γ. Only one $\gamma J/\Psi$ pair may come from the same source, i.e. from either $\chi_c \to \gamma J/\Psi$ signal or background due to decays of heavy mesons to $J/\Psi X$. As a consequence the signal is partly washed out appearing as a bump on the top of a predominantly combinatorial background. Hence, a reliable parametrization and control of the background is essential in extracting the signal, otherwise large systematic errors can be induced. The necessity of a faithful background description, as we will see in the following, reflects on the way we optimize the selection criteria used in the isolated photon search.

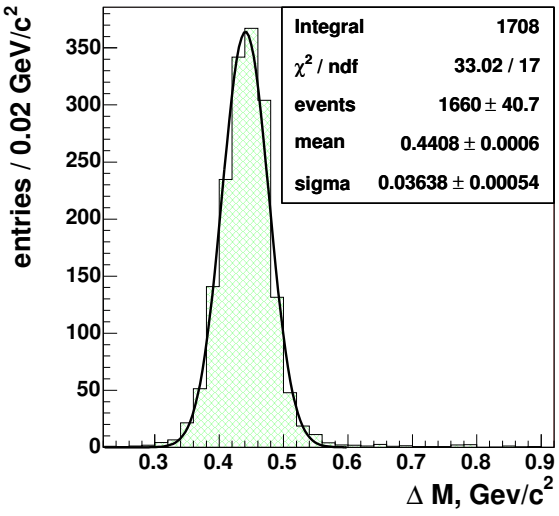

(a)

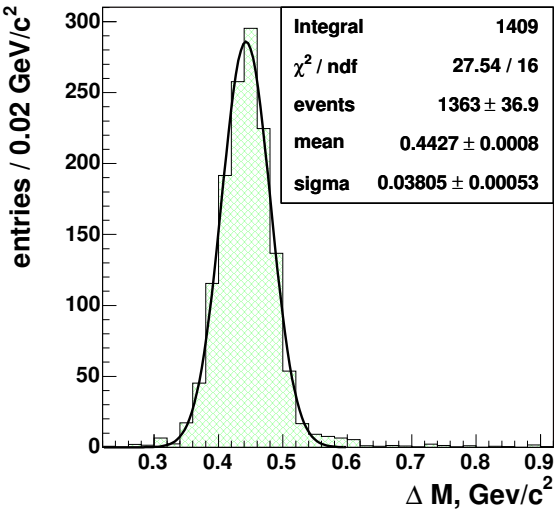

(b)

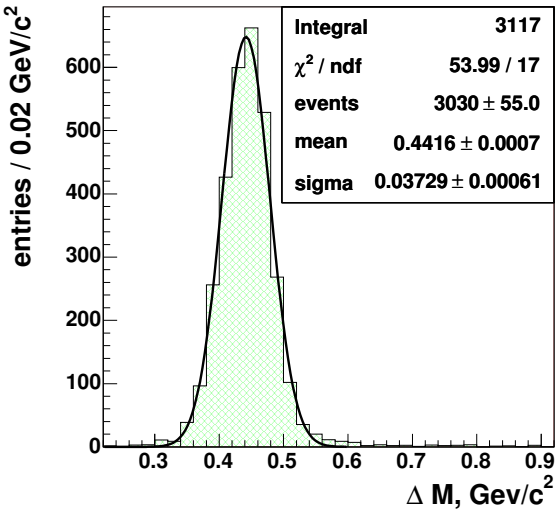

(c)

Figure 5.11: *Monte Carlo simulations. Matched χ_c signal. (a) simulation for $i2$ carbon wire. (b) simulation for $i1$ tungsten wire. (c) Collective distribution for the summed sample, corresponding to the simulations for $i2$ and $i1$ wires. The fit shown on the plots is performed using a Gaussian parametrization. The parameters, also presented on the plots, correspond to number of χ_c events (events), signal position (mean) and width (sigma).*

5.3.1 Background to $\chi_c \rightarrow \gamma J/\Psi$

As mentioned in the introduction to this section, the background to $\chi_c \rightarrow \gamma J/\Psi$ consists mainly of random combinations of J/Ψ and photon candidates. Possible correlated contributions to that may come from decays of heavier mesons into $J/\Psi X$. The fraction of J/Ψ originating from $\psi^{'}$ decays is about 8% [20]. The fraction of photons arising from $\psi' \rightarrow J/\Psi\pi^0\pi^0$ decays which pass the energy cut $E > 3.0\ GeV$ is negligible, as is the fraction of pions misidentified as photons from $\Psi^{'} \rightarrow J/\Psi\pi^+\pi^-$ decays. The production of $b\bar{b}$ pairs in HERA-B is suppressed by a factor of 10^{-3} relative to $c\bar{c}$ production. Due to this fact, the number of J/Ψ and γ combinations originated in decays of mesons containing b-quark (Υ, χ_b) and satisfying the selection criteria is neglegible.

According to Monte Carlo simulations, the fraction of reconstructed $\chi_{c0} \rightarrow \gamma J/\Psi$ decays is expected to be of the order of 4% of the observed χ_c signal, which is of the same order as the present statistical uncertainties. Therefore, the contribution to the ΔM distribution coming from χ_{c0} radiative decays can safely be neglected.

In di-electron data additional sources of background to the $\chi_c \rightarrow \gamma J/\Psi$ signal have to be taken into account. One of them is the radiative decay $J/\Psi \rightarrow \gamma e^+e^-$, which has a branching ratio of about 0.88×10^{-3} [20]. Beside that, clusters created by J/Ψ decay electrons and clusters due to bremsstrahlung photons emitted by such electrons bring additional correlations to ΔM spectrum. In order to avoid such unwanted correlations, clusters attributed to e^+ or e^- from J/Ψ decays are removed from the χ_c search. Reconstructed bremsstrahlung photons are also rejected on the same purpose. On the contrary, bremsstrahlung clusters are not expected in the di-muon data, and the fraction of J/Ψ radiative decays is negligible.

We conclude that, to a large extent, the ΔM distribution can be considered to consist mainly of random $\gamma J/\Psi$ combinations and real χ_c events. The challenge is, thus, to describe the background as accurately as possible.

5.3.2 Event mixing

To get an accurate estimate of the background, the event mixing technique [100] has been applied. The general idea is to exhibit correlations between two particles, e.g. J/Ψ and γ, coming from the decay $\chi_c \rightarrow \gamma J/\Psi$. It consists in using the mass difference distribution obtained using J/Ψ and isolated photons taken from two different events. The intuitive idea supporting this method is that the "mixed" distribution displays all features of the reaction, including the systematics related to experimental device or event reconstruction, except the correlation of interest. At the same time, calculated background distributions resulting from fits, interpolation, phase space, or Monte Carlo prescriptions may miss some aspects of underlying information. In what follows, a mass difference spectrum will be referred to as *same event* distribution (ΔM) when the contributing particles are from the same event, and *mixed event* distribution (ΔM_{mix}) when the particles are taken from different events.

The event mixing is performed by coupling the events we selected for the $\chi_c \rightarrow \gamma J/\Psi$

search. Precisely, the event mixing is achieved by pairing isolated photons[4] from a given event with J/Ψ candidates from a certain number, N_{rm}, of previous and successive events. Being exact, we use $N_{rm}/2$ previous and $N_{rm}/2$ successive events. In case when the number of previous or successive events is less than $N_{rm}/2$, we use all of them. We refer to N_{rm} as mixing range.

Several factors have an influence on the choice of the mixing range number. First of all, it is the necessity of a statistically significant background estimate. In order to minimize the statistical uncertainty, we require that the background estimated by event mixing should be, say, an order of magnitude larger than the corresponding same event distribution. On the other hand, the data taken during different period of time might correspond to different detector and trigger conditions. Therefore, it is important that the events, which we use in the mixing, are from the nearest runs. This puts an upper boundary for mixing range number. Another point, which restricts us from using large values for N_{rm}, is the demand for minimum computing time, while performing the event mixing. Based on the above considerations, our choice of N_{rm} is ranged between 100 and 400, depending on the size of the data set.

5.3.3 Corrections to the mixed background estimate

Caution should be observed when the analysis of large statistics data samples is performed, as discrepancies between same and mixed event distributions, due to effects which can otherwise be neglected, might become significant. These could lead to wrong estimation of the signal and, thus, introduce systematic errors. Let us mention two of these effects, which are relevant in our analysis.

The first is the fact, that the particles within a given event are kinematically constrained by the transverse momentum conservation:

$$\vec{p}_T = \sum_i \vec{p}_T^{\,i} = 0, \tag{5.21}$$

where $\vec{p}_T^{\,i}$ in the transverse momentum of i-th particle produced in the event. J/Ψ, having non-zero transverse momentum, forces the total momentum of the remaining particles in the event to be directed in the opposite side: $\vec{p}_T^{\,J/\Psi} = -\vec{p}_T^{\,rest}$. This brings a non-vanishing anti-correlation of momenta $\langle \vec{p}_T^{\,J/\Psi} \cdot \vec{p}_T^{\,i} \rangle < 0$, which, in turn, makes the mean angle between the J/Ψ and other particles larger for real events[5] than for mixed ones. Accordingly, same event ΔM distribution appears to be wider than ΔM_{mix}. In order to minimize the effect of the kinematical constraint in real events one has to introduce a similar constraint in the mixing, thus requiring similar $\vec{p}_T$ direction for J/Ψ in both events used for mixing.

[4]The isolated photons used in the mixing were selected by applying the criteria identical to the photon selection used in the χ_c search (see Table 5.3).

[5]Here and farther on in the discussion on the background evaluation *real event* stands to emphasize the difference of the measured and simulated events which result in the same event distributions from the events modelled by the event mixing which result in mixed event distributions.

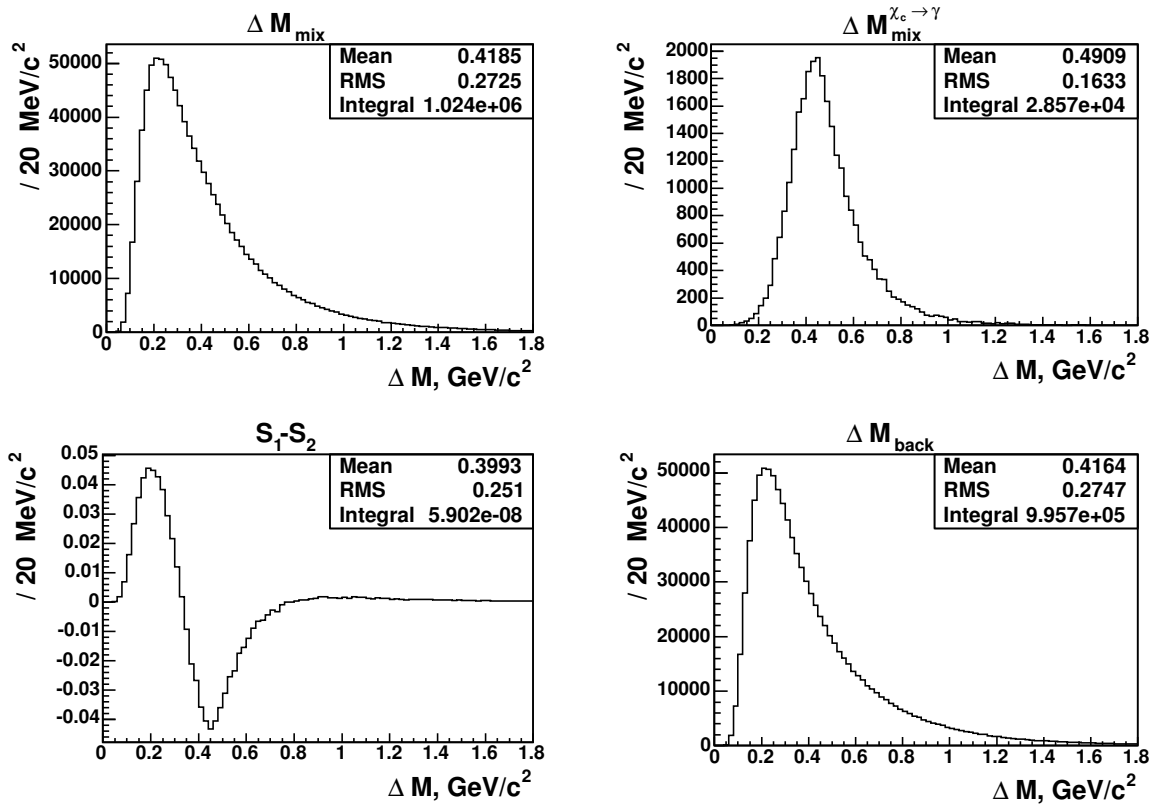

Figure 5.12: *Monte Carlo correction to the mixed background distribution due to χ_c photons: (Top left) ΔM_{mix} distribution with both background photons and photons hailing from χ_c decays. (Top right) $\Delta M_{mix}^{\chi_c \to \gamma}$ distribution which includes only $\gamma J/\Psi$ combinations in which photons come from χ_c decays. (Bottom left) $S_1 - S_2$ distribution (see definition in equation (5.28). It gives the correction term f_c (5.35), which is added to the F_{fit}, once normalized to the number of signal events (5.34). (Bottom right) Corrected background distribution ΔM_{back}.*

To achieve that a cut on the azimuthal angle of J/Ψ is imposed [101]:

$$\begin{aligned} |\Delta\phi| = |\phi_i^{J/\Psi} - \phi_j^{J/\Psi} + 2\pi k| < 0.3\ rad, \\ \phi^{J/\Psi} = arctg\left(\frac{p_y^{J/\Psi}}{p_x^{J/\Psi}}\right) + \pi n, \end{aligned} \tag{5.22}$$

where i and j denote that particles are from different events, $p_x^{J/\Psi}$ and $p_y^{J/\Psi}$ are measured components of J/Ψ momentum; $n = 0$ for $p_x^{J/\Psi} > 0$ and $n = 1$ for $p_x^{J/\Psi} < 0$. The choice of k is based on the requirement that $|\Delta\phi|$ is minimal, i.e. $k = 0, \pm 1$.

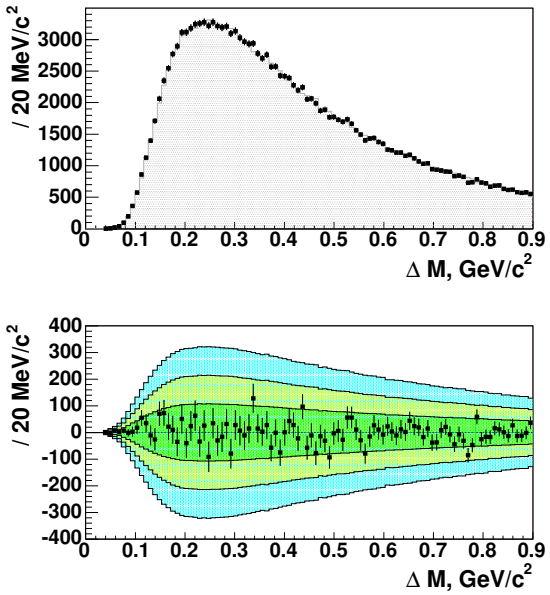

Figure 5.13: *Event mixing test: (Top) The $\Delta M = M(\gamma\mu^+\mu^-) - M(\mu^+\mu^-)$ is plotted for cases when $M(\mu^+\mu^-)$ is taken from the J/Ψ side-bands and γ from the same event (points with error bars). The filled histogram shows the ΔM_{mix} when $\mu^+\mu^-$ and γ are taken from different events. (Bottom) Difference between the ΔM and ΔM_{mix} (points with error bars) is plotted. The filled stripes correspond to 1, 2 and 3 standard deviations of the background estimate.*

Another source of discrepancy is due to combinations of γ coming from χ_c decays with J/Ψ candidates in the mixed ΔM_{mix} distribution (Fig. 5.12(top left)). Such $\gamma J/\Psi$ pairs represent unwanted correlations in the background estimated by simple pairing γ and J/Ψ from different events. The combinations of γ, which do not come from χ_c decays, and J/Ψ have the same mass difference distribution no matter whether they belong to the same event or not. This distribution, in fact, is the background distribution we are seeking for[6] and in the following it is referred to as ΔM_{back} (Fig. 5.12(bottom right)). On the contrary, the mass difference distribution for J/Ψ and γ coming from two different χ_c mesons (i.e. mixed events) varies from the distribution obtained with the two particles produced in the same χ_c decay [7]. This is because in mixed events, the two different χ_c, which emit J/Ψ and γ, may have a finite relative velocity, and the sum of the two particles momenta in the reference frame of those sources is not zero in general. As a consequence,

[6] We assume the purely combinatorial background.

[7] Because the kinematics of J/Ψ stemming from χ_c radiative decays is very similar to the kinematics of the direct J/Ψ the combinations of the χ_c photons and direct J/Ψ mesons will contribute to $\Delta M_{mix}^{\chi_c \rightarrow \gamma}$ in the mixing as well.

the relative momentum and, hence, mass difference distribution is wider for mixed events, which nevertheless peaks at the position where the signal is expected. In order to avoid such complications we correct the shape of the mixed ΔM_{mix} by removing the $\Delta M_{mix}^{\chi_c\to\gamma}$ part.

Let us consider the ΔM_{mix} distribution obtained by pairing the photon from a given event k containing $\chi_c \to \gamma J/\Psi$ decay with the reconstructed J/Ψ from a number N_{mr} other events

$$\Delta M_{mix,\,k} = \Delta M^k_{back} + \Delta M^{\chi_c\to\gamma}_{mix,\,k}\ . \tag{5.23}$$

We can define the background distribution ΔM^k_{back}, normalized to the same event ΔM_k as

$$\begin{aligned}(1/N_{mr})\Delta M^k_{back} &= (1/N_{mr})\left(\Delta M_{mix,\,k} - \Delta M^{\chi_c\to\gamma}_{mix,\,k}\right)\\ &= (1/N_{mr})\left(N_{mr}(N^k_\gamma+1)\cdot S^k_1 - N_{mr}\cdot S^k_2\right)\\ &= N^k_\gamma\cdot S^k_1 + (S^k_1 - S^k_2).\end{aligned} \tag{5.24}$$

Here the N^k_γ is the number of background photons in the event and S_1 and S_2 are the shapes of $\Delta M_{mix,\,k}$ and $\Delta M^{\chi_c\to\gamma}_{mix,\,k}$ distributions, respectively. The S_1 and S_2 are defined as

$$S^k_1 = \frac{1}{I^k_1}\Delta M_{mix,\,k} \tag{5.25}$$

$$S^k_2 = \frac{1}{I^k_2}\Delta M^{\chi_c\to\gamma}_{mix,\,k}\ , \tag{5.26}$$

with I^k_1 and I^k_2 being the integrals of the $\Delta M_{mix,\,k}$ and $\Delta M^{\chi_c\to\gamma}_{mix,\,k}$ distributions, respectively. Integrating over all events, we obtain the background estimate for the whole data sample:

$$\frac{N_{J/\Psi}}{N_{mr}}\Delta M_{back} = N_\gamma\cdot S_1 + N_{\chi_c}\cdot(S_1 - S_2), \tag{5.27}$$

Where $N_{J/\Psi}$, N_γ and N_{χ_c} are present in the sample numbers of J/Ψ candidates, isolated photons and $\chi_c \to \gamma J/\Psi$ decays, respectively. The shapes S_1 and S_2 are defined as

$$S_1 = \Delta M_{mix}/I_1 = \sum_{k=1}^{N_{J/\Psi}} \frac{1}{I^k_1}\Delta M_{mix,\,k} \tag{5.28}$$

$$S_2 = \Delta M^{\chi_c\to\gamma}_{mix}/I_2 = \sum_{k=1}^{N_{J/\Psi}} \frac{1}{I^k_2}\Delta M^{\chi_c\to\gamma}_{mix,\,k}\ , \tag{5.29}$$

with I_1 and I_2 being the integrals of the ΔM_{mix} and $\Delta M^{\chi_c\to\gamma}_{mix}$ distributions, respectively. The difference between the shapes S_1 and S_2 is depicted in Fig. 5.12(bottom left).

Following the formula (5.27), the estimation of the background evolves into evaluating the mixed ΔM_{mix} distribution and dislodging the $\Delta M^{\chi_c\to\gamma}_{mix}$ component from it. The latter is evaluated by using Monte Carlo simulations, where we can easily disentangle the contribution of $\gamma J/\Psi$ pairs, with J/Ψ mesons and photons born in χ_c decays picked up from different events (see Fig. 5.12 (upper left plot)).

The conformity of the background estimate is checked by combining $\mu^+\mu^-$ pairs from J/Ψ side bands (i.e. 5σ away from $M_{J/\Psi}$) with all photon candidates from the same event (Fig. 5.13(top, points with error bars)). The ΔM_{mix} distribution obtained trough mixing (Fig. 5.13(top, filled histogram)) should be identical to the "side band" distribution. The difference between the two, indeed, is compatible with zero as demonstrated by Fig. 5.13(bottom).

In summary, the shape of the predominantly combinatorial background in the ΔM distribution is obtained by combining J/Ψ candidates with photon candidates from different events in the way described above. The same standard selection cuts are applied to both real and mixed events. The mixed distribution, ΔM_{mix}, in combination with the corrections described above reproduce the shape of the ΔM distribution everywhere except the χ_c signal.

5.3.4 Photon selection optimization

Most widely, the selection criteria is refined by maximization of the signal significance, i.e optimizing the signal to background ratio, defined as

$$\frac{S}{\sqrt{B+S}} \simeq \frac{S}{\sqrt{B}} \tag{5.30}$$

so that

$$\frac{S}{\sqrt{B}} \to \frac{N_{\chi_c}}{\Delta N_{\chi_c}}, \tag{5.31}$$

where the ΔN_{χ_c} is the uncertainty in the N_{χ_c} determination. The value $S = N_{\chi_c}$ is assumed to be proportional to $N_{J/\Psi} \cdot \varepsilon_\gamma$, with $N_{J/\Psi}$ being measured and ε_γ being determined from Monte Carlo simulation. The quantity B, which is the number of background entries under the signal, contributes significantly to the uncertainty ΔN_{χ_c}.

However, parameter values optimized according to (5.30, 5.31) are quite often inappropriate. One reason, is that the direct use may result in significant decrease in signal abundance. Moreover, it could make the background parametrized by the event mixing to peak under the signal. This is rather problematic for the extraction of the N_{χ_c}, because the background distribution fluctuates a lot around its peak. As an example, we consider the cut on the cluster transverse energy, E_T^{cl}. The optimized cut value, for which the significance (5.30) is maximal, is associated with more than 60 % drop in the number of signal events (see Fig 5.14). Furthermore, a hard E_T^{cl} cut leads to the background peaked close to the signal position, bringing additional uncertainties in the estimation of the number of reconstructed χ_c particles (see Fig. 5.15). Under such circumstances our choice of the selection criteria presented in previous sections was based on the following principles:

- Keep the shape of the background under the χ_c signal as simple and stable as possible.

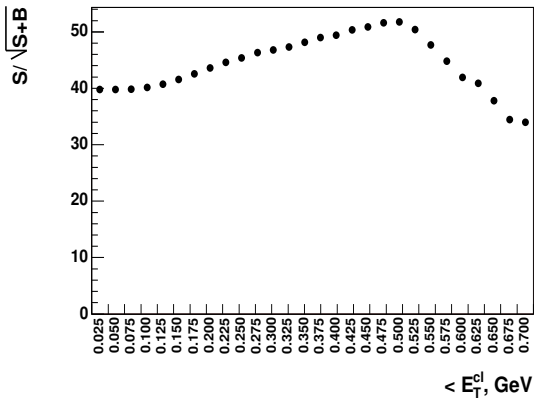

Figure 5.14: (To the right) *Cut on cluster transverse energy E_T^{cl}. Top: Significance versus the cut value. Bottom: Efficiency of the cut with respect to the simulated signal (dots) and measured background (solid line) for different values of the E_T^{cl} cut.*

Figure 5.15: *An example of ΔM distribution obtained in di-muon triggered data, when $E_T^{cl} > 250\ (MeV)$ cut is applied.*

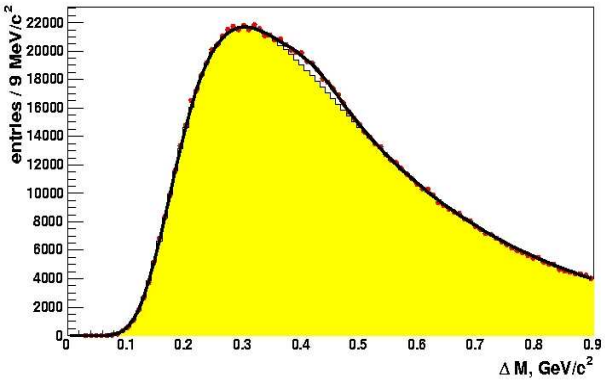

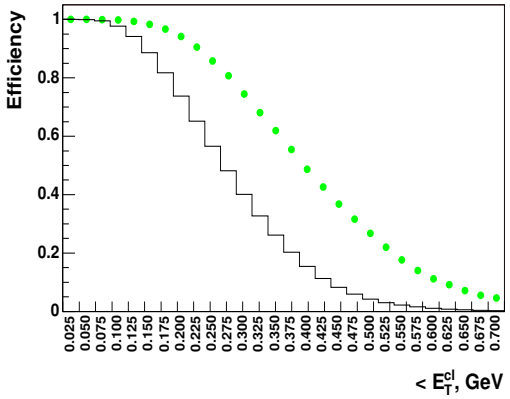

- The losses in the signal should not exceed the level of, say, 20 %, as estimated using Monte Carlo simulations.

Following such consideration, we tried to find a combination of the selection criteria which would keep the background peak far from the signal position and, at the same time, not cause big signal losses. The stability of the background estimate with respect to the cuts was checked by comparing ΔM distribution with no χ_c inside[8] with the mixed ΔM obtained for the given data set.

5.3.5 Fit to mass difference distribution

To extract the signal we perform a fit to the same event ΔM distribution with a non-analytical background description. In the fit, we used a function $\mathcal{F}_s$ for the parametrization of the signal and the ΔM_{back} distribution for the background description:

$$F_{fit} = \mathcal{F}_s + C_s \cdot \Delta M_{back}\ . \tag{5.32}$$

[8]In the simulation the distribution was obtained by using the events with no $\chi_c \to \gamma J/\Psi$ inside, while in the data we operated with the events corresponding to side-bands of the J/Ψ mass distribution.

Here C_s is the normalization factor of the background distribution. The precise description of the estimation of ΔM_{back} is given in the subsection 5.3.3 (see equation (5.27), Fig. 5.12(bottom right)). $\mathcal{F}_s$ can be represented either by a single Gaussian or by combination of two Gaussians. From the Monte Carlo we expect a mass resolution for the χ_c signal of about $37 - 39\ MeV/c^2$, which is comparable to the mass difference between χ_{c1} and χ_{c2} states (Table 5.1). With the present statistics, it is insufficient to separate the χ_{c1} and χ_{c2} states. Therefore, a single Gaussian is used to describe the signal:

$$\mathcal{F}_s = N_{\chi_c} \cdot \frac{dx}{\sqrt{2\pi}\sigma_{\Delta M_{\chi c}}} \exp\left[-\frac{(\Delta M - \langle \Delta M \rangle_{\chi_c})^2}{2\sigma^2_{\Delta M_{\chi c}}}\right], \tag{5.33}$$

where N_{χ_c} is the integral of the Gaussian, which corresponds to the number of signal events; $\langle \Delta M \rangle_{\chi_c}$ and $\sigma_{\Delta M_{\chi c}}$ are the mean value and width of the Gaussian, respectively; dx is the bin width of the histograms representing the distributions. Replacing the ΔM_{back} with the value defined in the formula (5.27) the fit function (5.32) becomes [9]

$$F_{fit}(x) = N_{\chi_c} \cdot \left(\frac{dx}{\sqrt{2\pi}\sigma_{\Delta M_{\chi c}}} \exp\left[-\frac{(\Delta M - \langle \Delta M \rangle_{\chi_c})^2}{2\sigma^2_{\Delta M_{\chi c}}}\right] + f_c\right) + C_s \cdot \Delta M_{mix}\ , \tag{5.34}$$

$$f_c = (S_1 - S_2) = \frac{\Delta M_{mix}}{I_1} - \frac{\Delta M^{\chi_c \rightarrow \gamma}_{mix}}{I_2}\ . \tag{5.35}$$

Here ΔM_{mix} represents the mixed event distribution which contains all $\gamma J/\Psi$ combinations (Fig. 5.12(top left)). It is obtained in the event mixing by taking into account the requirement (5.22). $\Delta M^{\chi_c \rightarrow \gamma}_{mix}$ represents the distributions with combinations of J/Ψ and χ_c photons belonging to different events (Fig. 5.12(top right)). I_1 and I_2 are the integrals of the ΔM_{mix} and $\Delta M^{\chi_c \rightarrow \gamma}_{mix}$ distributions, respectively. The parameters N_{χ_c}, $\langle \Delta M \rangle_{\chi_c}$, $\sigma_{\Delta M_{\chi c}}$ and dx are the same as in the (5.33), while the shapes S_1 and S_2 are given by equations (5.28-5.29) (see also Fig. 5.12(bottom left)). The parametrization (5.34-5.35) accommodates, thus, two corrections to the mixed mass difference distribution (see equations (5.22) and (5.27)).

We use the Monte Carlo simulation to test the parametrization. For that, we compare the output from the fit to ΔM distributions to the signal obtained through the matching (see subsection 5.2.5). From the results of the comparison (see Fig. 5.16) we conclude that the parametrization given by (5.34) provides a reliable description of the signal and background.

The importance of the corrections to the mass difference distribution obtained in the mixing is evaluated by performing the fit with exclusion of one of the corrections or both of them. This corresponds to three situations:

- We do not use the corrections due to the kinematical constraint in the same event distribution (see equation (5.22)), but we take into account the correlations in the

[9] In some plots, N_{χ_c}, $\langle \Delta M \rangle_{\chi_c}$, $\sigma_{\Delta M_{\chi c}}$ and C_s are denoted as *events*, *mean*, *sigma* and *b.scale* respectively.

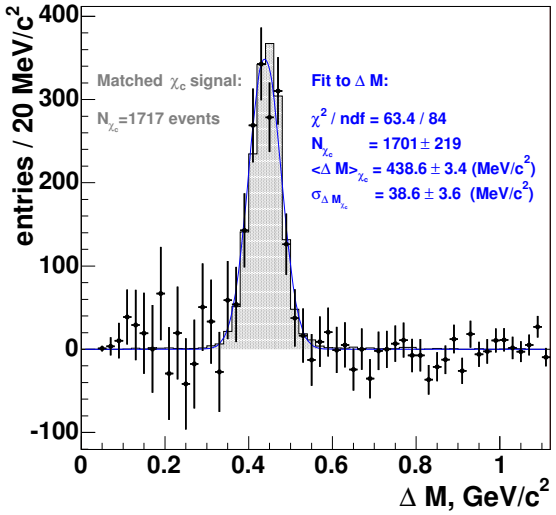

Figure 5.16: *Comparison of the results from fit to ΔM and matching. The dots with error bars show the signal (after background subtraction) resulting from the fit according to parametrization (5.34), whereas the filled histogram shows the signal obtained through the matching procedure. The distributions correspond to the simulation for $i2$ carbon wire.*

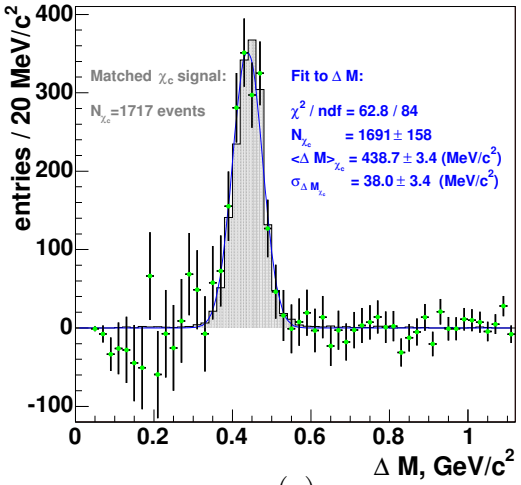

(a)

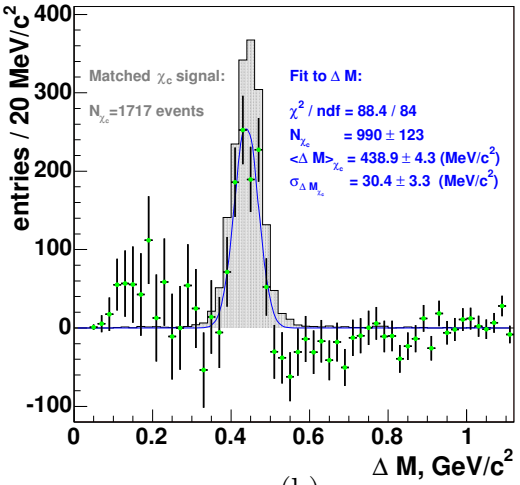

(b)

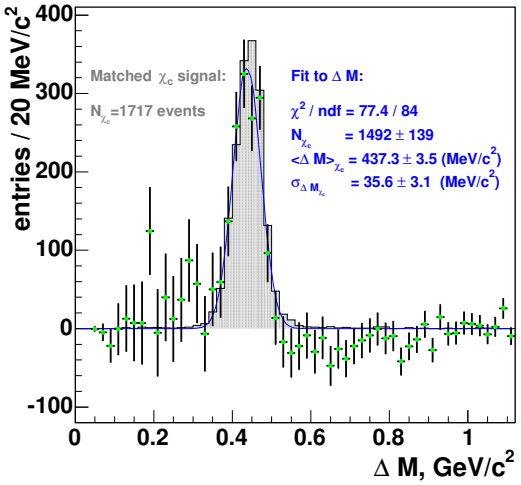

(c)

Figure 5.17: *Effect of the corrections to the mixed background on the fit results. In the fit to ΔM: (a) The effect of correlations due to the kinematical constraint in the same event distribution is not taken into account (case I). (b) The effect of correlations due to the $\gamma J/\Psi$ combinations with photons hailing from $\chi_c \to \gamma J/\Psi$ decays is not taken into account (case II). (c) Both effects are not taken into account (case III). As in Fig. 5.16, the distributions correspond to the simulation for $i2$ carbon wire.*

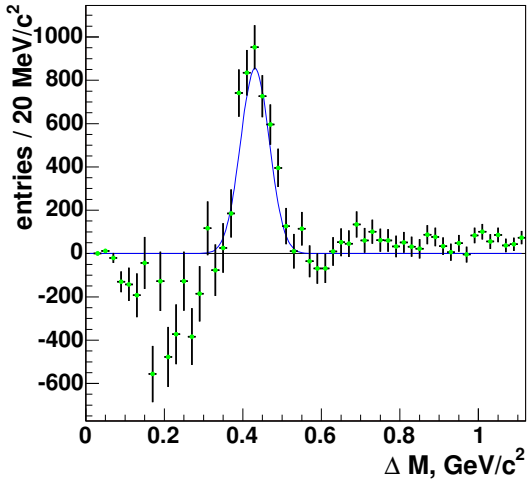

Figure 5.18: *The same as in Fig. 5.17(a) but distribution correspond to carbon data.*

mixed ΔM_{mix} distribution due to the $\gamma J/\Psi$ combinations in which photons originate in $\chi_c \rightarrow \gamma J/\Psi$ decays (see equation 5.27). We will refer to the fit performed under such conditions as *case I*.

- In the *case II* we do not balance the correlations due to the $\gamma J/\Psi$ combinations with photons hailing from $\chi_c \rightarrow \gamma J/\Psi$ decays (5.27). We consider, however, the effect of the kinematical constraint in the same event distribution (5.22).
- At last, we neglect both of the modifications to the mixed ΔM_{mix} (*case III*).

We inspect the three cases above by performing the fit to the simulated mass difference distribution and compare the fit output with the matched χ_c signal. The results corresponding to *case II* and *case III* end in the wrong description of the signal and background as it can be seen in Fig 5.17(b,c). Surprisingly, when we use the parametrization corresponding to *case I*, the signal estimated in the fit is close to the matched one. However, the description of the lower part of the ΔM distribution is rather deficient as it is shown in Fig. 5.17(a). This is even more pronounced in data (see Fig. 5.18). Therefore, the parametrization (5.34), which includes both corrections to the mixed mass difference distribution, is used to extract the signal. It is important to notice one substantial specificity of parametrization (5.34), related to the uncertainty in the signal determination resulting from the fit:

- the signal uncertainty, which results from the fit to ΔM, includes the ambiguity due to adjustment to the shape of the background estimated in the mixing (term f_c in equation 5.34).

Issues related to the signal error, resulting from to the fit to ΔM, will be discussed further in section 6.4, where we will present a study of systematic uncertainties.

The two following sections summarize the results of the reconstruction of the $\chi_c \rightarrow \gamma J/\Psi$ decays, with J/Ψ detected via its leptonic decays.

5.4 χ_c results: $\mu^+\mu^-$ triggered data

In this section, the results obtained using di-muon data will be presented. First, we will introduce the χ_c signal produced in proton-Carbon (^{12}C) interactions in year 2002 with the single $i2$ wire. Then we will extend to all carbon data ($i2$ and $b2$ wires) collected with di-muon trigger. In a next attempt the signals, corresponding to collisions of protons with Tungsten (^{184}W, $i1$ and $o2$ wires) and Titanium (^{48}Ti, $b2$ wire) targets, will be discussed. At the end, we will present a combined χ_c signal, obtained on a full di-muon data set, which corresponds to about 129,000 reconstructed $J/\Psi \to \mu^+\mu^-$ at the present selection level. The results related to di-electron triggered data will be considered in section 5.5.

Table 5.3: *Summary of the cuts used to reconstruct $\chi_c \to \gamma J/\Psi$, with $J/\Psi \to \mu^+\mu^-$ and γ reconstructed in the ECAL.*

Cut	Value	Efficiency
Additional J/Ψ cut:		
MUON likelihood for J/Ψ tracks	$L_\mu > 0.7$	80.3 %
χ_c's photons selection:		
Inner most part of ECAL is excluded	$x_{cl}^2/4 + y_{cl}^2 > 484cm$	86.9 %
Energy of the cluster	$E > 3\ GeV$	84.0 %
Transverse energy of the cluster	$E_T > 0.1\ GeV$	99.5 %
Cluster shape	$asym > 0.8$	95.8 %
Long charged track Short charged tracks	*suppressed* $\lvert(px/pz)_{track} - (px/pz)_{cluster}\rvert < 0.1$ $\lvert(py/pz)_{track} - (py/pz)_{cluster}\rvert < 0.1$	82.5 %
Rejection of photons from $\pi^0 \to \gamma\gamma$	$0.095 < M_{\gamma\gamma} < 0.175\ GeV/c^2$	90.3 %
Total		51.8 %

Table 5.3 summarizes the requirements used for $J/\Psi \to \mu^+\mu^-$ and isolated photon searches, together with the selection cut efficiencies obtained with Monte Carlo simulations. Although studied extensively with the $i2$ Carbon wire, these selection criteria were then extended to the other data sets, such that the photon selection used in the analysis was identical for different target materials.

5.4.1 Proton-Carbon collisions

We start our discussion with the signal corresponding to the data set obtained with single $i2$ (C) wire in 2002. The reason for doing that is that we have used these data extensively for the selection optimization. The ΔM spectra for data and for Monte Carlo simulations for $i2$ wire are presented in Fig. 5.19 and Fig. 5.20, respectively. They are shown along with the fit, performed according to parametrization (5.34). The distributions exhibit an enhancement around $420 - 440\ MeV/c^2$, which we associate with the χ_c signal corre-

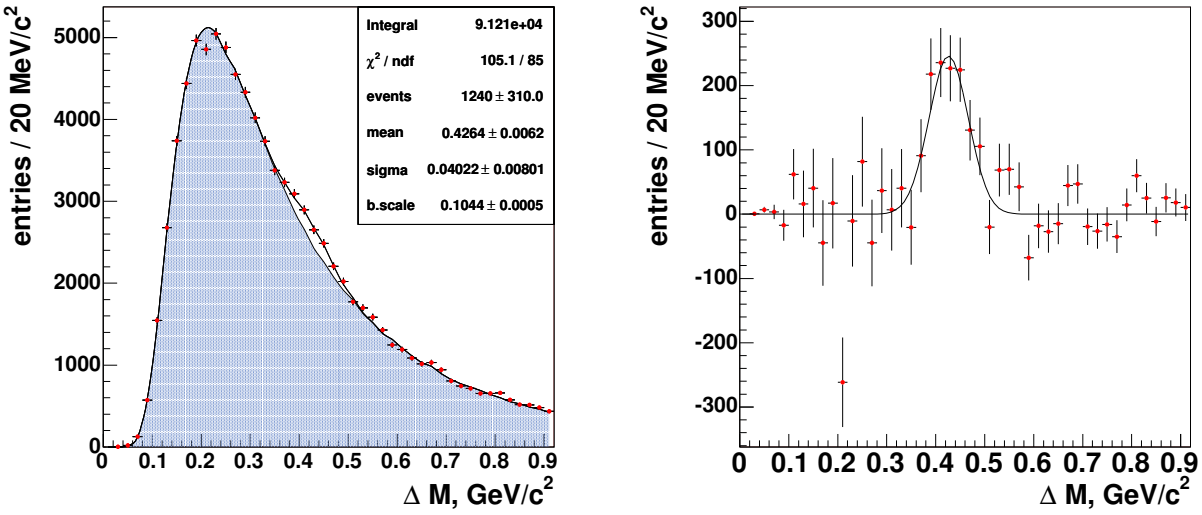

Figure 5.19: *On the left: The ΔM distribution for carbon data ($i2$ wire) from 2002. The presented fit is performed by using the parametrization (5.34). The fit parameters, events, mean, sigma and b.scale, shown in the plot, correspond to the number of χ_c events, $N^{i2}_{\chi_c}$, position of the signal, $\langle \Delta M \rangle^{i2}_{\chi_c}$, its width, $\sigma^{i2}_{\Delta M_{\chi_c}}$, and the normalization of the background, respectively. The filled histogram represents the combinatorial background estimated by event mixing. On the right: The background subtracted signal is shown. Solid line correspond to a Gaussian from the fit to the ΔM.*

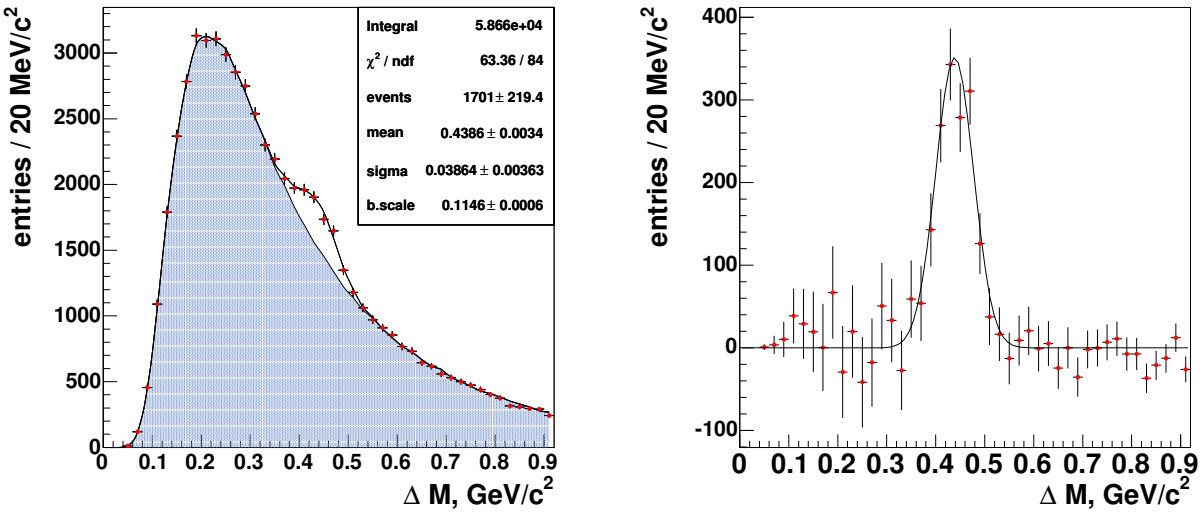

Figure 5.20: *The same as in Fig. 5.19 except the ΔM distributions correspond to the simulation for carbon wire $i2$.*

Table 5.4: *χ_c in i2(C) data from 2002. The number of selected J/Ψ events ($N^{i2}_{J/\Psi}$), the number of J/Ψ's passing the $|M_{J/\Psi} - 3.093| < 0.1 GeV/c^2$ mass window ($N^{i2\ m.w.}_{J/\Psi}$), the number of observed χ_c ($N^{i2}_{\chi_c}$) as well as signal position ($\langle\Delta M\rangle^{i2}_{\chi_c}$), width ($\sigma^{i2}_{\Delta M_{\chi_c}}$) and χ^2 per degree of freedom for the ΔM fit. The quoted errors are statistical.*

$i2$ data (carbon) from 2002	
$N_{J/\Psi}$	20242 ± 161
$N^{m.w.}_{J/\Psi}$	19865 ± 158
$N^{i2}_{\chi_c}$	1240 ± 310
$\langle\Delta M\rangle^{i2}_{\chi_c}$, GeV/c^2	0.426 ± 0.006
$\sigma^{i2}_{\Delta M_{\chi_c}}$, GeV/c^2	0.040 ± 0.008
$(\chi^2/n.d.f.)_{\chi_c\ fit}$	105.1/85

Table 5.5: *The same as Table 5.4 but for entire carbon data sample.*

All carbon data ($i2$ and $b1$)	
$N_{J/\Psi}$	81607 ± 322
$N^{m.w.}_{J/\Psi}$	79722 ± 315
$N^{C}_{\chi_c}$	4807 ± 576
$\langle\Delta M\rangle^{C}_{\chi_c}$, GeV/c^2	0.431 ± 0.003
$\sigma^{C}_{\Delta M_{\chi_c}}$, GeV/c^2	0.041 ± 0.004
$(\chi^2/n.d.f.)_{\chi_c\ fit}$	105.2/85

sponding to the sum of the two charmonium states χ_{c1} and χ_{c2}. In the fit, the position, width and normalization of the Gaussian, as well as the normalization of the background, are left free. We observe

$$N^{i2}_{\chi_c} = 1240 \pm 310$$

$\chi_c \to \gamma J/\Psi$ decays in the $i2$ sample from 2002. The width of the Gaussian obtained from the fit to the data,

$$\sigma^{i2}_{\Delta M_{\chi_c}} = 40 \pm 8\ MeV/c^2,$$

is compatible with the Monte Carlo prediction ($36 - 39\ MeV/c^2$; see Fig. 5.11,5.20). The position of the Gaussian in data,

$$\langle\Delta M\rangle^{i2}_{\chi_c} = 426 \pm 6\ MeV/c^2,$$

is slightly smaller than the Monte Carlo estimate ($439 - 441\ MeV/c^2$; see Fig. 5.20,5.11). This can be related to the χ_{c1} to χ_{c2} ratio used to generate Monte Carlo events. This ratio may be smaller than the actual one leading to a larger fraction of χ_{c2} events in the χ_c signal compared to the data. As a result, the position of the χ_c signal is shifted towards χ_{c2} mass is the simulations. It can also be an effect of misalignment and miscalibration. Nevertheless, such effects should be of small order, as far as both values (i.e. position of the Gaussian in the data and the simulation) are approaching each other within the given uncertainties. The background subtracted distributions are shown on the left plots of Fig.5.19-5.20. Outside the χ_c signal, both Monte Carlo and data distributions show similar behavior: flat with larger fluctuations around the peak of the background distributions. Although, the absolute values of the deviations are large they are distributed essentially

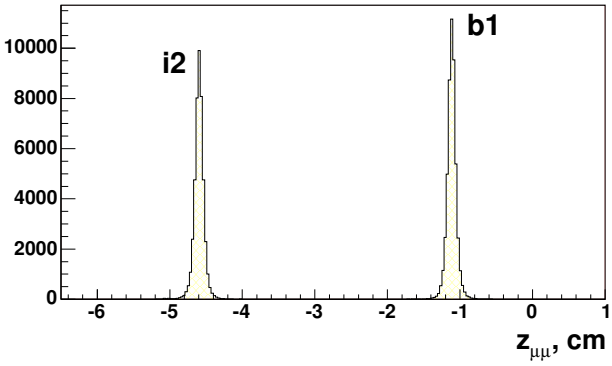

Figure 5.21: *Carbon data. z coordinate of reconstructed di-muon vertex. Two peaks correspond to $b1$ and $i2$ carbon wires as denoted on the picture. The wire separation in case of double-wire operation is done by comparing the coordinates of reconstructed di-muon vertex and target (4.3).*

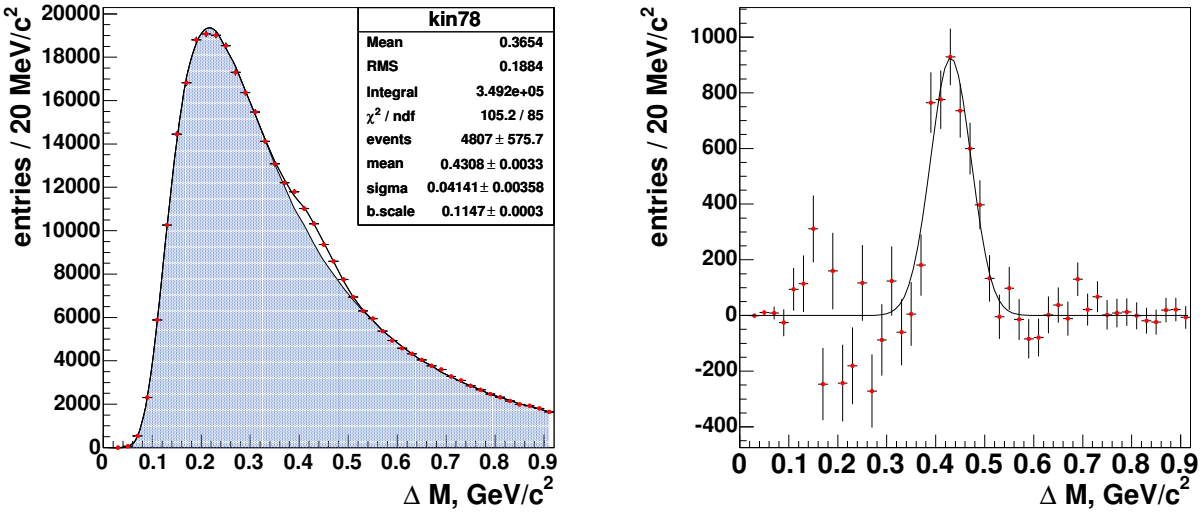

Figure 5.22: *The same as in Fig. 5.19 except the ΔM distributions correspond to all di-μ triggered data obtained with carbon wires $i2$ and $b1$.*

within one standard deviation (see Fig. 5.13), peaking around zero. The significance of the signal, defined as $N_{\chi_c}/\Delta N_{\chi_c}$ the signal to the square root of the background (see equation 5.31), is about 4 standard deviations. The number of χ_c events as well as the number of J/Ψ events are summarized in Table 5.4.

Extending our analysis to all carbon data ($i2$ and $b1$ wires (Fig. 5.21) in several configurations, see Table 4.1) collected in di-muon channel during HERA-B operation in 2002-2003, which accommodate about 81,600 J/Ψ particles, we reconstruct

$$N^C_{\chi_c} = 4807 \pm 576 \tag{5.36}$$

χ_c events. The corresponding ΔM distribution is presented in Fig. 5.22(left) and in Fig. 5.22(right) after background subtraction. The features it exhibits are similar to that observed in $i2$ sample from 2002. The fit of the distribution is identical to the fit described above. The resulting parameters are shown in summary form in Table 5.5. They comply

with the values obtained using smaller data sample corresponding to $i2$ data recorded in 2002.

5.4.2 Proton-Tungsten collisions

The di-muon data set obtained in the interaction of protons with nuclei of tungsten wires $i1$, $o2$ as well as $b2$ in 2003 (see Fig. 5.23), correspond to about 40,300 reconstructed $J/\Psi \rightarrow \mu^+\mu^-$ decays. The resulting ΔM distribution is shown in Fig. 5.24(left). As in the case of carbon data, the fit, shown in the plots, is performed according to the parametrization given by equation (5.34). The position, normalization of the Gaussian and the normalization of the background are left free in the fit. However, due to a large particle multiplicity produced in pW interaction the width of the Gaussian is fixed. The large multiplicity results in a higher level of background under J/Ψ signal compared to carbon data. This, in turn, increase combinatorics in the ΔM spectrum in case of tungsten data, and, thus, dilutes the χ_c signal. As a consequence, the fit with the width being a free parameter may result in a significant deviation in the number of signal events. In this light, we fix the width of the Gaussian in the fit to ΔM to 38 MeV/c^2, relying on the Monte Carlo results for the width of the χ_c signal (Fig. 5.11(b)). The uncertainty related to it is taken into account in the estimation of systematic error, as will be described in section 6.4.

Table 5.6: *χ_c in proton-Tungsten collisions. The number of selected J/Ψ events ($N^W_{J/\Psi}$), the number of J/Ψ's passing the $|M_{J/\Psi} - 3.093| < 0.1 GeV/c^2$ mass window ($N^{W\ m.w.}_{J/\Psi}$), the number of observed χ_c ($N^W_{\chi_c}$) as well as signal position ($\langle\Delta M\rangle^W_{\chi_c}$), width ($\sigma^W_{\Delta M_{\chi_c}}$) and χ^2 per degree of freedom for the ΔM fit. The quoted errors are statistical.*

All tungsten(W) data ($i1$, $o2$ and $b2$ from 2003)	
$N_{J/\Psi}$	40301 ± 241
$N^{m.w.}_{J/\Psi}$	39253 ± 235
$N^W_{\chi_c}$	1907 ± 283
$\langle\Delta M\rangle^W_{\chi_c}$, GeV/c^2	0.425 ± 0.006
$\sigma^W_{\Delta M_{\chi_c}}$, GeV/c^2	0.038 ($fixed$)
$(\chi^2/n.d.f.)_{\chi_c\ fit}$	90.1/86

The number of χ_c radiative decays reconstructed for tungsten data is

$$N^W_{\chi_c} = 1907 \pm 283.$$

The position of the reconstructed χ_c peak, resulting from the fit,

$$\langle\Delta M\rangle^W_{\chi_c} = 425 \pm 6\ MeV/c^2$$

agrees well with the corresponding quantity of the χ_c signal obtained with carbon wire (see Table 5.5). It is also shifted towards lower values in ΔM distribution compared to the Monte Carlo expectation. The distribution with the subtracted background is shown in Fig. 5.24(right). As in carbon case, it is flat outside the signal region with larger uncertainties in the lower part. The numbers related to the χ_c signal for tungsten data are given in Table 5.6.

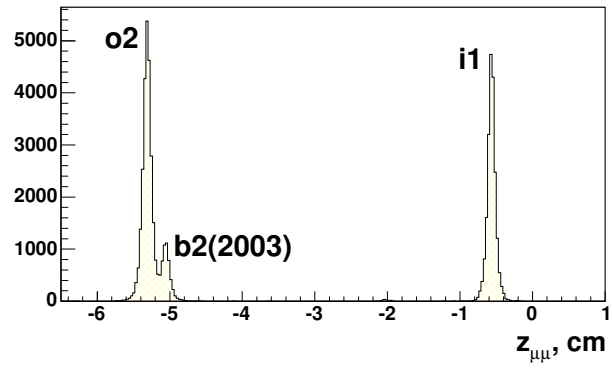

Figure 5.23: *Tungsten data. z coordinate of reconstructed di-muon vertex. The three peaks correspond to o2, b2 and i1 tungsten wires as denoted on the picture. The wire b2 originally was made of carbon and was charged to tungsten later (see Table 3.1). The wire separation in case of double-wire operation is done by comparing the coordinates of reconstructed di-muon vertex and target (4.3).*

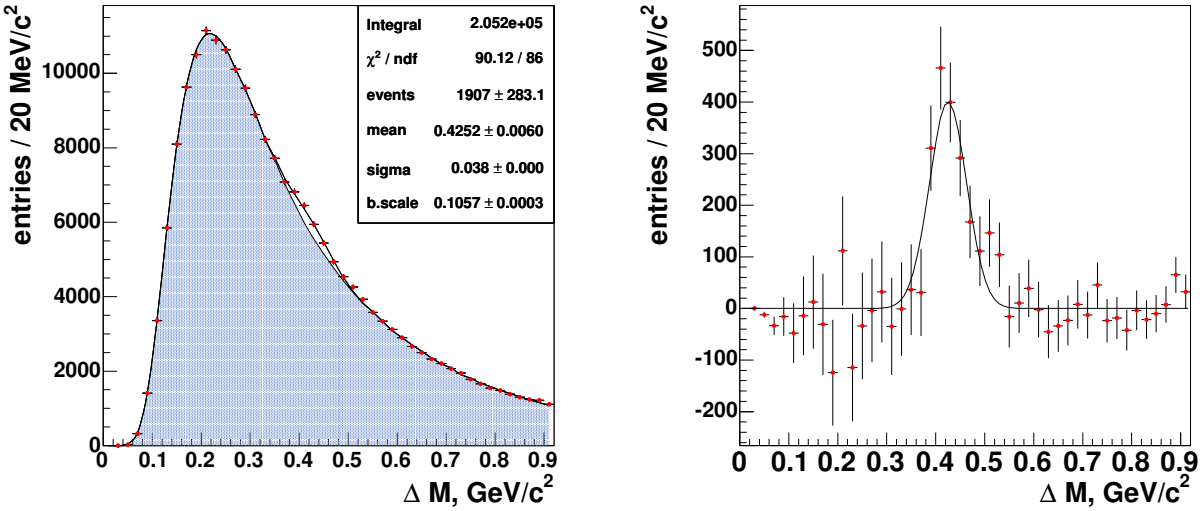

Figure 5.24: *On the left: The ΔM distribution for tungsten data (i1,o2 and b2 in 2002 wires). The presented fit is performed by using the parametrization (5.34). The fit parameters, events, mean, sigma and b.scale, shown in the plot, correspond to the number of χ_c events, $N^W_{\chi_c}$, position of the signal, $\langle \Delta M \rangle^W_{\chi_c}$, its width, $\sigma^W_{\Delta M_{\chi_c}}$, and the normalization of the background, respectively. In the fit, the width of the Gaussian is fixed to the values of 38 MeV/c^2. The filled histogram represent the combinatorial background estimated by event mixing. On the right: The background subtracted signal is shown. Solid line correspond to a Gaussian from the fit to the ΔM.*

5.4.3 Proton-Titanium collisions

The data set corresponding to proton-titanium interactions were obtained with b2 wire in 2002. The data set correspond to about 6,800 reconstructed $J/\Psi \to \mu^+\mu^-$ decays. The resulting ΔM distribution is shown in Fig. 5.25(left), along with the fit (5.34) (solid line) and the combinatorial background estimated by event mixing (filled histogram). In the fit to ΔM, the width of the signal is fixed to $\sigma^{Ti}_{\Delta M_{\chi_c}} = 38\ MeV/c^2$. Other parameters

Table 5.7: *χ_c in proton-Titanium collisions. The number of selected J/Ψ events ($N^{Ti}_{J/\Psi}$), the number of J/Ψ's passing the $|M_{J/\Psi} - 3.093| < 0.1 GeV/c^2$ mass window ($N^{Ti\ m.w.}_{J/\Psi}$), the number of observed χ_c ($N^{Ti}_{\chi_c}$) as well as signal position ($\langle\Delta M\rangle^{Ti}_{\chi_c}$), width ($\sigma^{Ti}_{\Delta M_{\chi_c}}$) and χ^2 per degree of freedom for the ΔM fit. The quoted errors are statistical.*

All titanium ($b2$ in 2002) data	
$N_{J/\Psi}$	6806 ± 97
$N^{m.w.}_{J/\Psi}$	6669 ± 95
$N^{Ti}_{\chi_c}$	339 ± 113
$\langle\Delta M\rangle^{Ti}_{\chi_c}$, GeV/c^2	0.431 ± 0.012
$\sigma^{Ti}_{\Delta M_{\chi_c}}$, GeV/c^2	$0.038\ (fixed)$
$(\chi^2/n.d.f.)_{\chi_c\ fit}$	111.9/85

describing the signal as well as background normalization are left free. We reconstruct

$$N^{Ti}_{\chi_c} = 339 \pm 113$$

χ_c events for titanium data. The signal significance (5.31) is about three standard deviations. The position of the signal,

$$\langle\Delta M\rangle^{Ti}_{\chi_c} = 431 \pm 12\ MeV/c^2,$$

resulting from the fit, is in agreement with the results obtained with other target materials as well as with Monte Carlo expectation, although being associated with large uncertainties. The bulky errors reflect limited statistics and ambiguities in the background estimate. This is clearly evident in the background subtracted distribution (Fig. 5.25(right)), which exhibits large fluctuations in the lower part of the spectrum. Table 5.7 summarizes the numbers related to the χ_c signal obtained in collisions of protons with titanium wire.

5.4.4 Combined signal

Combining all events, recorded with di-muon trigger and passed the selection described above, we obtain a set of data corresponding to about 129,000 reconstructed J/Ψ. The resulting ΔM distribution, demonstrating a clear χ_c signal, is shown in Fig. 5.26(left). The fit to the ΔM distribution is also presented in the plot. All parameters are left free in the fit. In total, we detect

$$N^{\mu\mu}_{\chi_c} = 6729 \pm 729$$

Table 5.8: *χ_c in combined di-muon data set. The number of selected J/Ψ events ($N_{J/\Psi}$), the number of J/Ψ's passing the $|M_{J/\Psi} - 3.093| < 0.1 GeV/c^2$ mass window ($N^{m.w.}_{J/\Psi}$), the number of observed χ_c ($N^{\mu\mu}_{\chi_c}$) as well as signal position ($\langle\Delta M\rangle^{\mu\mu}_{\chi_c}$), width ($\sigma^{\mu\mu}_{\Delta M_{\chi_c}}$) and χ^2 per degree of freedom for the ΔM fit. The quoted errors are statistical.*

All di-μ data	
$N_{J/\Psi}$	129016 ± 421
$N^{m.w.}_{J/\Psi}$	126049 ± 411
$N^{\mu\mu}_{\chi_c}$	6729 ± 729
$\langle\Delta M\rangle^{\mu\mu}_{\chi_c}$, GeV/c^2	0.429 ± 0.003
$\sigma^{\mu\mu}_{\chi_c}$, GeV/c^2	0.040 ± 0.003
$(\chi^2/n.d.f.)_{\chi_c\ fit}$	115.9/85

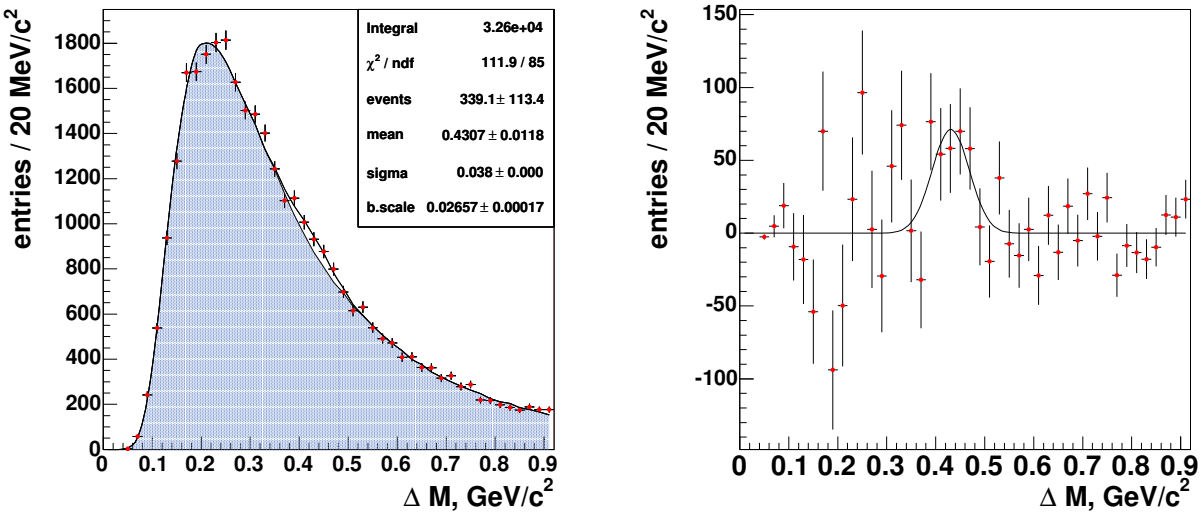

Figure 5.25: *On the left: The ΔM distribution for titanium data (b2 wire in 2002). The presented fit is performed by using the parametrization (5.34). The fit parameters, events, mean, sigma and b.scale, shown in the plot, correspond to the number of χ_c events, $N^{Ti}_{\chi_c}$, position of the signal, $\langle \Delta M \rangle^{Ti}_{\chi_c}$, its width, $\sigma^{Ti}_{\Delta M_{\chi_c}}$, and the normalization of the background, respectively. The filled histogram represents the combinatorial background estimated by event mixing. On the right: The background subtracted signal is shown. Solid line correspond to a Gaussian from the fit to the ΔM.*

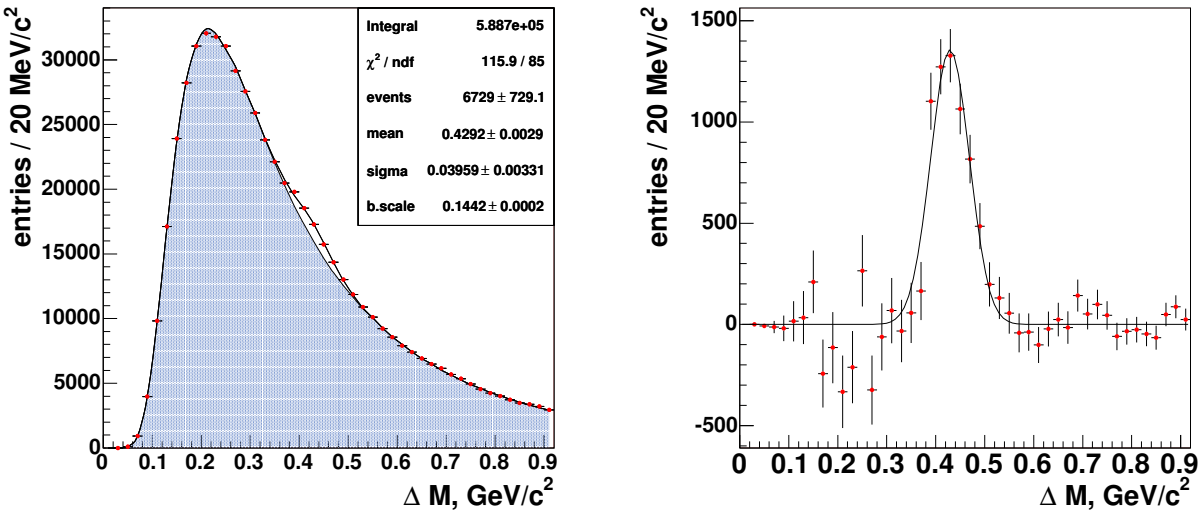

Figure 5.26: *On the left: The ΔM distribution for combined data set. The presented fit is performed by using the parametrization (5.34). The fit parameters, events, mean, sigma and b.scale, shown in the plot, correspond to the number of χ_c events, N_{χ_c}, position of the signal, $\langle \Delta M \rangle_{\chi_c}$, its width, $\sigma_{\Delta M_{\chi_c}}$, and the normalization of the background, respectively. The filled histogram represents the combinatorial background estimated by event mixing. On the right: The background subtracted signal is shown. Solid line correspond to a Gaussian from the fit to the ΔM.*

Table 5.9: *χ_c signal for di-muon data sets. Presented are the numbers of χ_c decays reconstructed for carbon, $N^C_{\chi_c}$, tungsten, $N^W_{\chi_c}$, titanium, $N^{Ti}_{\chi_c}$, and combined, N_{χ_c}, data sets.*

$N^C_{\chi_c}$	$N^W_{\chi_c}$	$N^{Ti}_{\chi_c}$	N_{χ_c}
4807 ± 576	1907 ± 283	339 ± 113	6729 ± 729

$\chi_c \to \gamma J/\Psi$ radiative decays. The width of the Gaussian resulting from the fit,

$$\sigma^{\mu\mu}_{\Delta M_{\chi c}} = 40 \pm 3\ MeV/c^2,$$

is in an excellent agreement with the value obtained from the carbon data analysis. It also agrees with the Monte Carlo expectation ($\sim 38 MeV/c^2$). The position of the signal, obtained from the fit to data,

$$\langle \Delta M \rangle^{\mu\mu}_{\chi_c} = 429 \pm 3\ MeV/c^2,$$

is similar to the carbon and tungsten results, and is shifted with respect to the Monte Carlo expectations. The background subtracted distribution is shown on the 5.26(right). The numbers related to the signal are displayed in Table 5.8. In short, the combined χ_c signal and related ΔM distribution exhibit all aspects apparent in the results corresponding to data sets attributed to a particular target material.

Table 5.9 presents a summary of the results of the χ_c search for di-muon triggered data.

5.5 χ_c results: e^+e^- triggered data

The di-electron events used in this analysis were obtained with the single $i2$ carbon wire in operation. The data set corresponds to about 16,000 reconstructed $J/\Psi \to e^+e^-$ decays, which comprises about 12 % of the available statistics in this channel. As in the di-muon case we split the study in two phases. As the first step, we tried to test our analysis on a part of data, aiming to clarify and solve possible problems. At the second step, we considered to extend further to the whole statistics. However, the analysis of di-electron data represents a higher complexity compared to the di-muon channel. In this respect, we have encountered some difficulties, namely in modeling the background under χ_c, which obstructed us in advancing beyond the first step. Therefore, we present only the information that we have learned using a small part of di-electron data.

As far as we operate with rather limited statistics in this case, a loose selection of $J/\Psi \to e^+e^-$ decays is chosen (see subsection 4.3.3 and Fig. 4.21(a)). In principle, it is possible to improve the signal to background ratio by applying additional requirements such as cut in harder E/p distribution and study of the track-ECAL match (see subsection 4.4.4). We notice, however, that the cumulative effect of such cuts is different for data and Monte Carlo. Additional cuts for data reduce the signal by 7% more compared

Table 5.10: *Summary of photon selection criteria in di-electron channel.*

Cut	Value	Efficiency
Inner most part of ECAL is excluded	$x^2/4 + y^2 > 484cm$	86.7 %
Energy of the cluster	$E > 3\,GeV$	85.1
Transverse energy of the cluster	$E_T > 0.1\,GeV$	99.4 %
Cluster shape	$asym > 0.8$	96.3 %
Long charged track Short charged tracks	*suppressed* $\lvert(px/pz)_{track} - (px/pz)_{cluster}\rvert < 0.1$ $\lvert(py/pz)_{track} - (py/pz)_{cluster}\rvert < 0.1$	81.7 %
Rejection of photons from $\pi^0 \to \gamma\gamma$	$0.095 < M_{\gamma\gamma} < 0.175\ GeV/c^2$	89.3 %
e bremsstrahlung clusters	rejected	100 %
e ECAL clusters	rejected	100 %
Total		51.5 %

Table 5.11: *χ_c in di-electron data. The number of selected J/Ψ events ($N^{ee}_{J/\Psi}$), the number of J/Ψ's passing the $|M_{J/\Psi} - 3.093| < 0.1 GeV/c^2$ mass window ($N^{ee\ m.w.}_{J/\Psi}$), the number of observed χ_c ($N^{ee}_{\chi_c}$) as well as signal position ($\langle\Delta M\rangle^{ee}_{\chi_c}$), width ($\sigma^{ee}_{\Delta M_{\chi_c}}$) and χ^2 per degree of freedom for the ΔM fit. The quoted errors are statistical.*

Di-electron data from 2002, $i2$(C) wire	
$N^{ee}_{J/\Psi}$	15260 ± 361
$N^{ee\ m.w.}_{J/\Psi}$	15260 ± 361
$N^{ee}_{\chi_c}$	627 ± 176
$\langle\Delta M\rangle^{ee}_{\chi_c}$, GeV/c^2	0.429 ± 0.009
$\sigma^{ee}_{\Delta M_{\chi_c}}$, GeV/c^2	0.038 fixed
$(\chi^2/n.d.f.)_{\chi_c\ fit}$	97.3/86

to Monte Carlo (see Fig. 4.21-4.20 and Table 4.5). The usage of such requirements may cause trouble, as we use Monte Carlo simulation for efficiency studies. Hence, we do not apply such cuts, trying to avoid possible complications.

The photon selection is similar to that used in di-muon data analysis. The only difference is that the clusters assigned to e^+ or e^- tracks or reconstructed as a bremsstrahlung photon are removed from the search for isolated photon. Table 5.10 summarizes the requirements used to select γ candidate in search for $\chi_c \to \gamma J/\Psi$, where $J/\Psi \to e^+e^-$. The corresponding ΔM distribution is shown in Fig. 5.27(left). The fit (5.34) to the ΔM distribution are also presented in the plot. The background subtracted distribution is shown in Fig. 5.27(right). In the mass difference spectrum, at the place where signal is expected, we observe an enhancement of events corresponding to about 3 standard deviations above the background [10]. It is attributed to the χ_c signal, which comprises two, χ_{c1} and χ_{c2}, charmonium states. In the present situation, however, the background estimated by event mixing (filled histogram in Fig. 5.27(left)) is rather poor and fails to describe the part corresponding to the lower values of ΔM. As it can be seen from the subtracted distribution (Fig. 5.27(b)) the deviations around the background peak are

[10]The significance is defined as $N_{\chi_c}/\Delta N_{\chi_c}$, see equation (5.31).

quite significant. The Monte Carlo distributions exhibit similar feature (Fig. 5.28). In order to minimize negative effects due to discrepancies in background description, we fix, in the fit, the width of the Gaussian to 38 MeV/c^2, the value predicted by Monte Carlo simulation (Fig. 5.29). The origin of the discrepancies present in the background estimate is not really understood. Most reasonable explanation, which we have found, is that the discrepancies are due to lost photons, which electrons radiate while passing the detector. However, to draw more precise conclusion an additional investigation must be implemented. Anyhow, the disagreement in the background estimate is located outside the signal region. This, and the fact that the background for higher ΔM values is reproduced rather well, allow to assume that the observed discrepancy is not apparent in the signal region and the estimate of the χ_c rate is fruitful. The correspondence between the result from the fit to the simulated ΔM (Fig. 5.28) and the matched signal (Fig. 5.29) is another justification for measured χ_c.

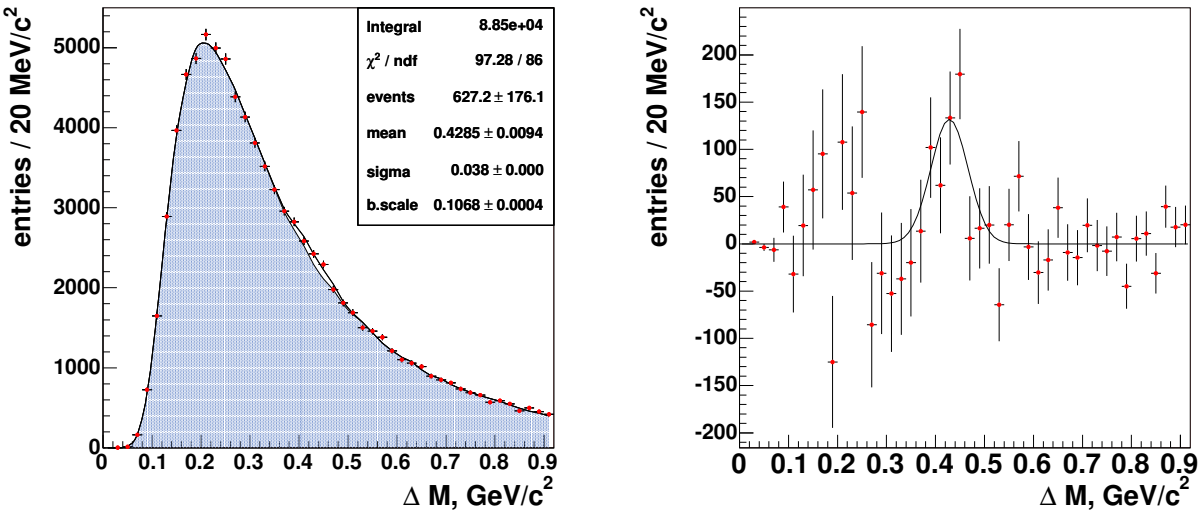

(a) (b)

Figure 5.27: *On the left: The ΔM distribution for carbon data collected with di-electron trigger. The presented fit is performed by using the parametrization (5.34). The fit parameters, events, mean, sigma and b.scale, shown in the plot, correspond to the number of χ_c events, $N^{ee}_{\chi_c}$, position of the signal, $\langle\Delta M\rangle^{ee}_{\chi_c}$, its width, $\sigma^{ee}_{\Delta M_{\chi_c}}$, and the normalization of the background, respectively. The filled histogram represents the combinatorial background estimated by event mixing. On the right: The background subtracted signal is shown. Solid line correspond to a Gaussian from the fit to the ΔM.*

The parameters of the signal obtained from the fit are summarized in Table 5.11. The observed number of χ_c events correspond to

$$N^{ee}_{\chi_c} = 627 \pm 176.$$

The position of the χ_c peak,

$$\langle \Delta M \rangle^{ee}_{J/\Psi} = 429 \pm 9 \; MeV/c^2,$$

is compatible with the results obtained for di-muon data. As in the di-muon case, it is slightly shifted towards smaller values compared to the Monte Carlo estimate ($\sim$ 439 MeV/c^2).

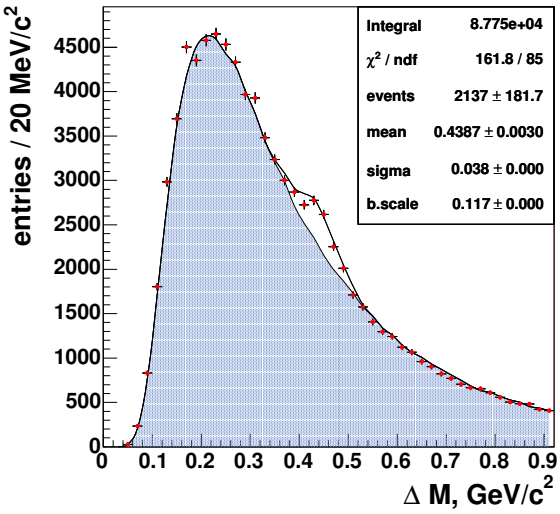

(a)

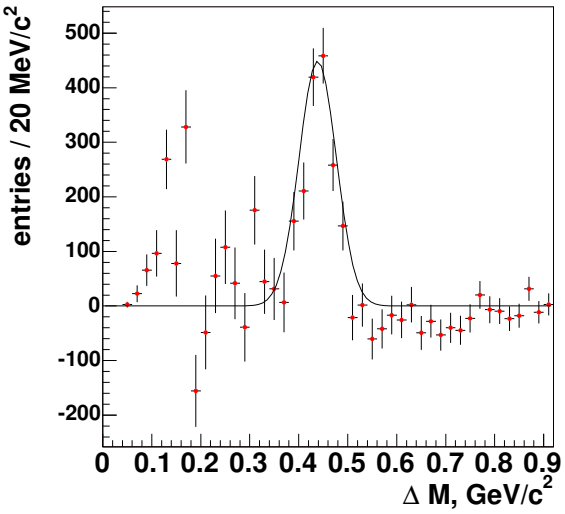

(b)

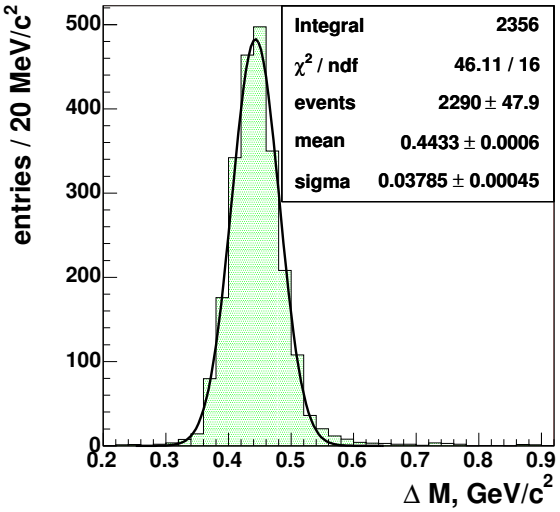

Figure 5.28: *(Top) The same as in Figure 5.27 but for Monte Carlo simulations for i2 wire.*

Figure 5.29: *(Left) Monte Carlo simulations for i2 carbon wire: Matched χ_c signal. The fit shown on the plot is performed using a Gaussian parametrization. The parameters, also presented on the plot, correspond to the number of χ_c events (events), signal position (mean) and width (sigma).*

Chapter 6

Fraction of J/Ψ produced via χ_C decays

In this chapter we will present a measurement of the fraction of J/Ψ particles produced via χ_c radiative decays in pA collisions:

$$R_{\chi_c} = \frac{\sigma_{\chi_{c1}} Br(\chi_{c1} \to \gamma J/\Psi) + \sigma_{\chi_{c2}} Br(\chi_{c2} \to \gamma J/\Psi)}{\sigma_{J/\Psi\ all}} \tag{6.1}$$

where $\sigma_{\chi_{c1,2}}$ and $\sigma_{J/\Psi}$ are the $\chi_{c1,2}$ and J/Ψ production cross-sections, respectively; $Br(\chi_{c1,2} \to \gamma J/\Psi)$ is the quantum probability (branching ratio) for the states $\chi_{c1,2}$ to decay into a photon and J/Ψ particle. The production cross-sections can be parametrized as follows

$$\sigma_{\chi_{ci}} = \frac{N_{\chi_{ci}}}{\mathcal{L}\varepsilon_{\chi_{ci}} Br(\chi_{ci} \to \gamma J/\Psi) Br(J/\Psi \to l^+l^-)}. \tag{6.2}$$

$$\sigma_{J/\Psi} = \frac{N_{J/\Psi}}{\mathcal{L}\varepsilon_{J/\Psi} Br(J/\Psi \to l^+l^-)}. \tag{6.3}$$

$N_{\chi_{ci}}$ and $N_{J/\Psi}$ are the observed numbers of χ_{ci} and J/Ψ events, respectively, $\mathcal{L}$ is the luminosity and $Br(J/\Psi \to l^+l^-)$ and $Br(\chi_{ci} \to \gamma J/\Psi)$ are the branching ratios for the J/Ψ leptonic and χ_c radiative decays, respectively. The efficiency to detect χ_c particle, $\varepsilon_{\chi_{ci}}$, is the product of the J/Ψ detection efficiency and γ detection efficiency: $\varepsilon_{\chi_{ci}} = \varepsilon_{J/\Psi} \cdot \varepsilon_\gamma$. Most of the quantities entering the cross-section formulae (6.1-6.3) are similar for J/Ψ and χ_c, and thus cancel in the ratio R_{χ_c}. The cancellation reduces the systematical error considerably. The latter simply depends on the number of particles observed and on the efficiency to detect photons taking origin from χ_c decays. The difference between the efficiencies for direct J/Ψ and those from χ_c radiative decays is expected to be less than a few percent. The following expression is thus used for the ratio R_{χ_c}

$$R_{\chi_c} = \frac{\sum_{i=1,2} N_{\chi_{ci}}}{N_{J/\Psi}\varepsilon_\gamma} \cdot \rho_\varepsilon, \quad \rho_\varepsilon = \frac{\varepsilon_{J/\Psi\ all}}{\varepsilon_{J/\Psi\ from\ \chi_c}}, \tag{6.4}$$

where ρ_ε represents the ratio of detection efficiency for all J/Ψ to the efficiency for J/Ψ stemming from χ_c decays.

Section 6.1 reminds details about the photon efficiency determination. In section 6.2 the results on the fraction of the J/Ψ produced though the χ_c radiative decays are presented. First we will describe the extraction of the R_{χ_c} value, using $i2$ data sample, on which we trained our analysis. Then we will present the R_{χ_c} ratio for data acquired in interaction of protons with nuclei of carbon, tungsten and titanium in the kinematical range $-0.35 \leq x_F^{J/\Psi} \leq 0.15$. The A-dependence of R_{χ_c} will be further studied in section 6.3, where the R_{χ_c} x_F distributions will be presented for carbon and tungsten data, in the range between $-0.18 \leq x_F^{J/\Psi} \leq 0.06$. Section 6.4 will be devoted to the study of systematical uncertainties attributed to the measured values. In the last section (i.e. section 6.5) the result corresponding to combined di-muon data set will be presented, along with a comparison to the experimental values obtained in previous fixed target experiments.

6.1 Photon efficiency

As mentioned in subsection 5.2.5 of the previous chapter (see Eq.(5.20)), the photon detection efficiency, ε_γ, was defined as

$$\varepsilon_\gamma = \frac{N_{reco}^{MC}(\chi_c)}{N_{J/\Psi}^{MC}}, \tag{6.5}$$

where $N_{reco}^{MC}(\chi_c)$ is the χ_c signal extracted from a fit to the ΔM distribution, when both the J/Ψ and the photon selections are applied, while $N_{J/\Psi}^{MC}$ is the number of J/Ψ from χ_c decays surviving the J/Ψ selection, prior to the search for isolated photon. The evaluation of the photon efficiency was based on Monte Carlo simulations, where we can easily uncouple the χ_c decays. Three cases were considered (see Fig. 5.11):

1. First, the photon detection efficiency was studied using the simulation done for the $i2$ wire. In the simulation the generated events corresponded to the pC collisions (see chapter 3, section 3.9 for details concerning Monte Carlo simulations).

2. We also evaluated the efficiency using the simulation in which the generated events corresponded to the pW interactions and reconstruction was tuned to reproduce the collisions with $i1$ wire.

3. At last, the value of ε_γ was studied using both simulated samples together. In this way we try to reproduce a situation when the data were taken with different wire positions and materials.

The efficiency estimated in the first case is used in analysis of carbon data, while for tungsten data we use the value estimated in case 2. The combined data set is analyzed

using the efficiency estimate from the collective study of the simulation for carbon and tungsten wires (case 3). It is also used in the evaluation of the R_{χ_c} for titanium data. The estimated values of the photon detection efficiency lie in the range between 28 % (for tungsten wire) and 36 % (for carbon wire). The photon efficiency corresponding to the combined data is evaluated to be about 31 %.

From the simulations we also determine the quantity of ρ_ε, which enters equation (6.4). According to Monte Carlo, the value of ρ_ε is independent of the target material and position. It is estimated to be $\rho_\varepsilon = 1.03 \pm 0.01$. The proximity of the ρ_ε value to unity reflects the fact that the kinematics, triggering and reconstruction of the direct J/Ψ and J/Ψ due to χ_c decays are very similar.

Table 6.1 provides a summary of the efficiency studies. The last column represents the photon efficiency for di-electron triggered data, estimated using a specific Monte Carlo simulation (see Fig. 5.28 and 5.29).

Table 6.1: *Photon efficiency evaluated for the pC and pW collisions at $i1$ and $i2$ wires.*

	di-muon			di-electron
Wire	$i2$	$i1$	$i1, i2$	$i2$
Material	C	W	W, C	C
ε_γ, %	35.8 ± 4.6	27.8 ± 4.8	31.1 ± 3.3	26.1 ± 2.2
ρ_ε, %	1.03 ± 0.01			–

When data obtained with carbon (tungsten) wires are analyzed, it is assumed that the efficiencies for $i2$ and $b1$ ($o2$, $b2$ and $i1$) wires are the same, neglecting possible dependencies on wire positions. Therefore, in both cases the photon efficiencies are determined using specific simulations for $i2$ and $i1$, respectively.

6.2 R_{χ_c} results

The J/Ψ and χ_c statistics corresponding to $i2$ carbon data from 2002 are given in Table 5.4. The table also presents the number of J/Ψ mesons, falling into the mass window given by equation (5.1). Substituting these numbers and the values of the efficiencies presented in Table 6.1 into equation 6.4, we obtain the experimental values for R_{χ_c}, which is

$$R_{\chi_c} = 0.180 \pm 0.050_{stat} \pm 0.032_{syst}, \tag{6.6}$$

where the first uncertainty is statistical and the second is systematical. The treatment of systematical uncertainties will be discussed in section 6.4.

Since a significant fraction of the observed J/Ψ mesons come from χ_c radiative decays, a study of the A-dependence of χ_c production in proton-nucleus collisions is necessary for the understanding of the J/Ψ A-dependence. No measurement of χ_c A-dependence has

been made so far. Therefore, the study of R_{χ_c} with respect to the target material may bring some additional information.

If the A-dependence of χ_c is the same as that of the J/Ψ, than the R_{χ_c} ratio should be independent of the type of material used as a target. This would validate the picture of a formation of all charmonium states through the color-octet states, as suggested by the color evaporation model (CEM) [8]. On the other hand, if the nuclear dependences of χ_c and J/Ψ are quantitatively different, then R_{χ_c} should vary with A, as described within the non-relativistic QCD (NRQCD) [5, 6]. The NRQCD predictions assume χ_c production through predominantly color-singlet states, while direct J/Ψ via color-octet states, and different pre-resonant states interact differently with the nuclear medium [1].

For that reason we determine the R_{χ_c} ratio separately for three data sets used in the analysis, which correspond to pC, pW and pTi collisions. Tables 5.5, 5.6 and 5.7 outline the numbers of J/Ψ and χ_c mesons reconstructed for each data sample. For data obtained in pC collisions we also estimate the value of R_{χ_c} using a set of data recorded with di-electron trigger. The J/Ψ and χ_c statistics for this case can be found in Table 5.11. Because we analyze only limited amount of data in di-electron channel, the precision of the measured value of R_{χ_c} is rather low. Certainly, the precision of the result in this channel would improve if the analysis were extended to all available data. However, due to much higher complexity of the analysis of di-electron data we limited ourselves to one data set.

To obtain the experimental values for R_{χ_c} corresponding to different A, we substitute the numbers of reconstructed J/Ψ and χ_c, estimated for each of analyzed data sets, as well as related values for the photon efficiencies (see Table 6.1) into equation 6.4. Comparing the result obtained using all di-muon data collected with carbon wires with the result corresponding to the $i2$ data from 2002 (6.6), we notice a rather good correspondence. The results obtained on the fraction of J/Ψ coming from the χ_c radiative decays, R_{χ_c},

Table 6.2: *Summary of R_{χ_c} results. The errors listed for R_{χ_c} (last column) are statistical and systematical, respectively (see section 6.4).*

Trigger	Data	$N_{\chi_c}/N_{J/\Psi}$, %	ε_γ, %	R_{χ_c}
di-μ	pC (A=12)	5.89 ± 0.71	35.8 ± 4.6	$0.173 \pm 0.030_{stat} \pm 0.031_{syst}$
	pW (A=184)	4.73 ± 0.70	27.8 ± 4.8	$0.180 \pm 0.041_{stat} \pm 0.032_{syst}$
	pTi(A=48)	3.92 ± 2.17	31.1 ± 3.3	$0.163 \pm 0.057_{stat} \pm 0.029_{syst}$
di-e	pC ($i2$)	4.11 ± 1.16	26.1 ± 2.2	$0.157 \pm 0.044_{stat} \pm 0.030_{syst}$*

* In the evaluation of R_{χ_c} in di-electron channel it is assumed that the relative efficiency for J/Ψ is equal to unity, $\rho_\varepsilon = 1$.

are summarized in Table 6.2.

[1] A brief introduction to CEM and NRQCD approaches have been presented in chapter 2, section 2.4, during the discussion of the charmonium production.

The values of R_{χ_c} obtained for different wires and with different trigger modes agree well between each other. Only the value obtained with titanium seems lower. However, the signal statistics is quite low in this case, and, consequently the errors are large. Therefore, the small drop in the R_{χ_c} value for titanium is likely to be just a statistical fluctuation, rather than atomic number dependence. The resemblance between the values of R_{χ_c} obtained on carbon (A=12) and tungsten (A=184) appear to indicate that there is no nuclear dependence of the ratio. Consequently, the nuclear dependences of J/Ψ and χ_c production is rather similar. Fig. 6.1 shows R_{χ_c} for three different wire materials, i.e. carbon, titanium (A=48) and tungsten.

The similarity of the χ_c and J/Ψ A-dependences strengthen the plausibility of color-octet production of all states favoring CEM prediction for fixed-target energies. However, the predictions based on NRQCD approach cannot be fully ruled out at the present level of experimental uncertainties.

The nuclear dependence will be further quantified in the following section.

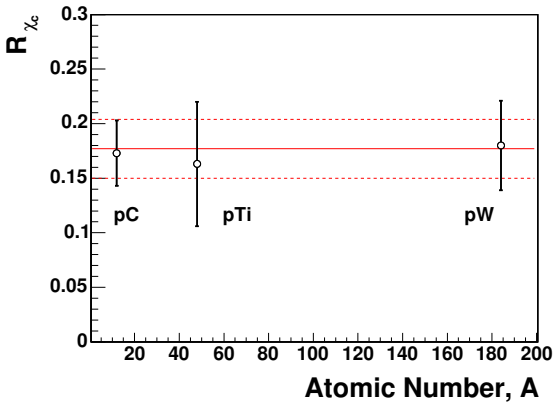

Figure 6.1: *R_{χ_c} measured for different wire material (di-muon data). Solid line represents the combined value of R_{χ_c}, while the dashed lines indicate the corresponding uncertainty (see section 6.5). The errors are statistical.*

6.3 R_{χ_c} differential distribution

The signals acquired in pC and pW collisions using the di-muon trigger are large enough to be divided into ranges of longitudinal momentum fraction x_F (see equation 2.6) and, consequently, investigate the R_{χ_c} dependence on Feynman x.

To obtain the R_{χ_c} x_F spectra we divide the $\mu^+\mu^-$ invariant mass distribution, after the standard J/Ψ selection (chapter 4, subsection 4.3.2), into x_F bins of size 0.06. Each bin then undergoes the fit for the J/Ψ signal. In the fit we use a Gaussian to describe the signal and an exponential or a polynomial for background parametrization. The shape of the background under the J/Ψ peak strongly depends on the kinematical range. In the marginal cases the fit with an exponential parametrization of the background is less appropriate and a second order polynomial gives a better χ^2 probability. A comparison between the exponential and polynomial parameterizations, studied on the di-muon distribution over the whole x_F range, shows no difference in signal multiplicity. The numbers, corresponding to the J/Ψ signal per x_F bin are summarized in Appendix B (see

Tables B.2-B.7). The raw x_F spectra of the J/Ψ meson obtained for carbon and tungsten data are presented in Fig. 6.2.

In the next step, the search for an isolated photon is performed for each bin of x_F. This is followed by the determination of the ΔM distributions in ranges of x_F. The reconstruction of the photon is identical to that used for the integrated signals (see Table 5.3). The χ_c signals are then extracted from a fit to ΔM (similarly to the entire signals, see subsection 5.3.5 and Appendix B). In order to compensate for limited statistics and inaccuracies in the background description, we fix the width of the χ_c peak to 38 MeV/c^2 in the fit. The resulting χ_c x_F spectra are shown in Fig. 6.3 (a) and (b) for carbon and tungsten data, respectively. The corresponding efficiencies to find a χ_c photon are estimated from the Monte Carlo simulation following the prescription given in section 6.1. Fig. 6.4 displays the x_F distribution of the photon detection efficiency for carbon (Fig. 6.4(a)) and tungsten (Fig. 6.4(b)) wires.

Having determined the x_F spectra of J/Ψ and χ_c, as well as the differential x_F distribution of the photon efficiency, we are able to evaluate the dependences of the R_{χ_c} ratio on x_F, using equation (6.4). The resulting R_{χ_c} x_F distributions are shown in Fig. 6.5, where the distribution obtained for combined data set are also indicated. For each target material we managed to reconstruct a χ_c signal and, thus, evaluate R_{χ_c} in five x_F bins in the ranges $-0.18 \leq x_F \leq 0.12$ (C) and $-0.24 \leq x_F \leq 0.06$ (W), respectively. This gives a possibility to compare the R_{χ_c} x_F spectra extending from $x_F = -0.18$ to $x_F = 0.06$. Up to the present moment, only one experiment [12] has presented differential distributions of χ_c production, although with a small sample that leaves rather big ambiguities in the comparison of χ_c and J/Ψ x_F distributions. Therefore, the study of the dependence of the R_{χ_c} ratio on the Feynman variable, x_F, may put some light on the problem. A similar behavior of the x_F spectra of R_{χ_c} for different target material may indicate that χ_c and J/Ψ have a similar nuclear dependence. Any difference between carbon and titanium x_F spectra of R_{χ_c} would signify that the nuclear medium affects the production of J/Ψ and χ_c mesons in a different manner.

As it can be seen in Fig. 6.5 and Fig. 6.6, in the given kinematical range both distributions look similar. This implies similar A-dependences for J/Ψ and χ_c production, which agrees with the CEM calculations [32], based on the assumption of the universality of charmonium hadronization trough soft gluon emission. On the other hand, this seems to disfavor the NRQCD prediction, suggesting different A-dependences for χ_c and J/Ψ [32]. However, the experimental uncertainties are still quite large for an ultimate conclusion. Moreover, the NRQCD calculations [32] include nuclear absorption only. At the same time other effects, such as co-moving absorption and final state energy loss, may play an important role in the process of charmonium hadronization.

The presence of the χ_c signal in tungsten data in bin $-0.24 \leq x_F \leq -0.18$ and absence of it in carbon data and vice versa for bin $0.06 \leq x_F \leq 0.12$ is in accord with the observed ratio of J/Ψ spectra obtained with tungsten and carbon targets (Fig. 4.17). It may be attributed to weaker J/Ψ and χ_c A-dependences in the range of larger negative x_F. Most likely, however, it is an effect of target wire spatial layout. Carbon data were acquired with $i2$ and $b1$ wires, whereas tungsten data correspond to $b2$, $o2$ and $i1$ target wires. A more

conclusive statement would require an extension of the R_{χ_c} measurement into the range of intermediate and large negative x_F ($x_F < -0.3$). This would be also a more conclusive test of CEM, which predicts a difference in the A-dependencies of the charmonium states at $x_F \leq -0.3$. Unfortunately, this region is not accessible in the present data.

Any further conclusion would require a larger set of more precise data.

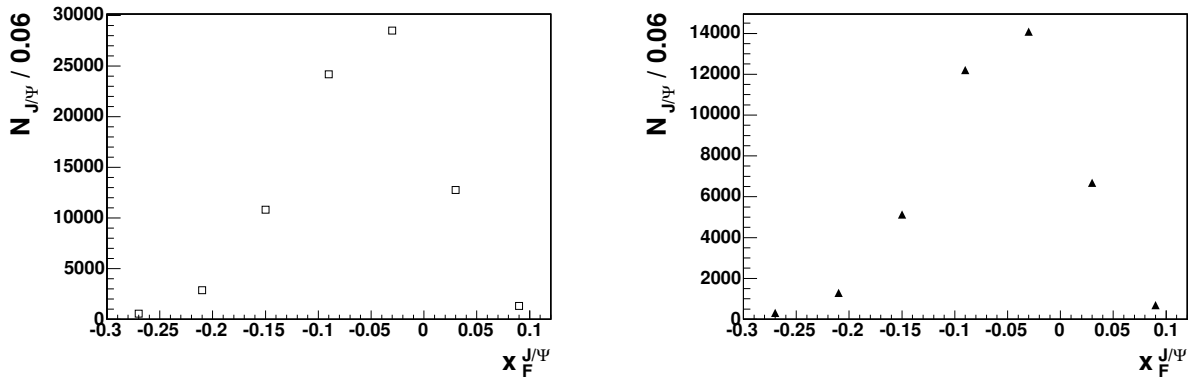

Figure 6.2: *x_F spectra of J/Ψ for carbon (a) and tungsten (b) data.*

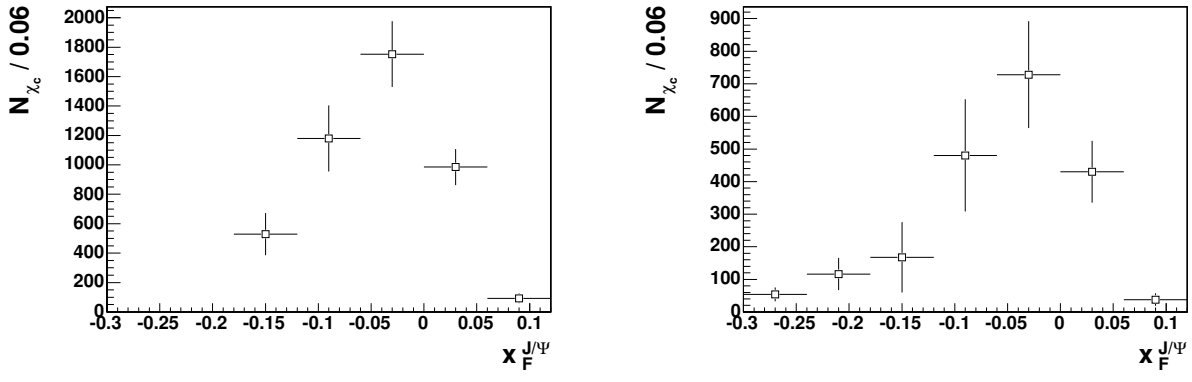

Figure 6.3: *x_F spectra of χ_c for carbon (a) and tungsten (b) data.*

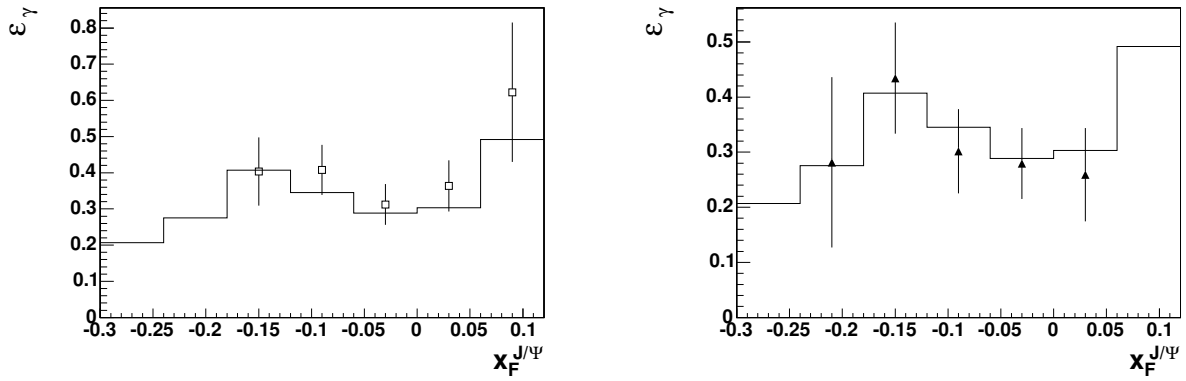

(a) (b)

Figure 6.4: *x_F spectra of χ_c photon detection efficiency for carbon (a) and tungsten (b) data. Solid line on both plots show the efficiency determined for the combined Monte Carlo data set (i.e. $i1{+}i2$).*

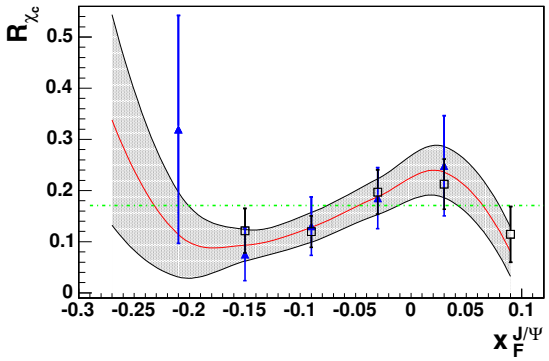

Figure 6.5: *x_F spectra of R_{χ_c} for carbon (open boxes) and tungsten (filled triangles) data. The x_F spectra of R_{χ_c} for combined data sample is shown by the solid line with the shadowed area corresponding to one standard deviation (statistical only). The dot-dashed line shows the value of R_{χ_c} measured for the combined data set in whole x_F range of J/Ψ.*

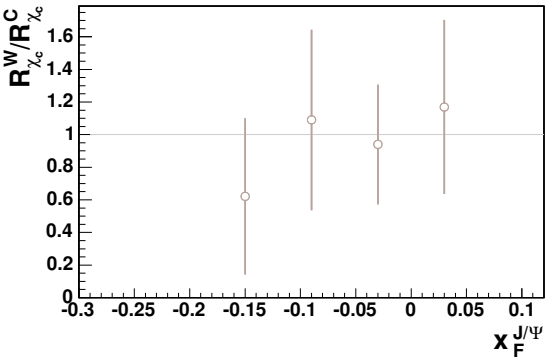

Figure 6.6: *Ratio of x_F spectra of R_{χ_c} obtained for tungsten (W) and carbon (C) data.*

6.4 Study of systematical uncertainties

In the following sections we will describe the contributions to the total systematical uncertainty. We study systematical uncertainties of different nature.

- The first group concerns the systematical effects introduced by the selection cuts. In these checks the analysis is repeated by varying the selection cuts one by one both for data and Monte Carlo samples. The ratio R_{χ_c} is measured as a function of the cuts on J/Ψ mass window, energy and transverse energy of the ECAL cluster, π^0 mass window, exclusion of the innermost part of the ECAL, and the number of cells building a cluster. The corresponding plots are presented in Appendix C (Fig. C.1-C.6). The relative difference between the ratio R_{χ_c} resulting from the systematic check and the average is considered as the systematical uncertainty. The variation of the cut on the photon energy E results in a variation of R_{χ_c} by 9%. The dependence on other cuts is less important (see Table 6.3, item 1). Adding in quadrature the contribution from all cuts we obtain the 10 % error introduced by photon selection.

- The second group includes the systematical uncertainties related to the signal extraction methods. This involves partition of the histogram into bins, estimation of the background and fitting procedure.

  The fit of the the ΔM divided in bins of width 10, 15, 25 and 30 MeV/c^2 results in a deviation in the yield of the χ_c events of about 6 % compared to the division in 20 MeV/c^2 bins. This gives rise to a 6 % uncertainty in the value of R_{χ_c}, which is taken as the systematical uncertainty due to the choice of the bin size.

  Using Monte Carlo simulation (see section 3.9 and 6.1), the systematical uncertainty attributed to the fit used to extract the χ_c signal can be evaluated. To estimate such inaccuracy, the signal obtained from a fit to ΔM is compared to the matched signal fitted with a Gaussian (see subsection 5.2.5). This results in an 3 % uncertainty in the signal and, consequantly, in $N_{\chi_c}/N_{J/\Psi}$ ratio. However, similar errors also affect the photon efficiency ε_γ defined in equation (6.5). As far as both quantities, $N_{\chi_c}/N_{J/\Psi}$ and ε_γ, enter the R_{χ_c} evaluation (6.4), they cancel in the ratio. Therefore, no systematical error is assigned to that.

  To examine the background description, we investigate the fit to the simulated ΔM distribution, using different background estimates. We compare the mixed background to the background obtained using a subset of events without χ_c's. The signal extracted from the fit with the mixed background estimate (see equation (5.34)) is associated with an error, which we refer to as statistical, of about 11 %. If we use the ΔM distribution with no χ_c, instead, the error comes down to about 4 %. This implies a 10 % uncertainty associated with the event mixing (see subsections 5.3.2, 5.3.3, as well as equations (5.22, 5.27)). Because this error is the part of the statistical error attributed to χ_c signal, its value is not included in the evaluation of total systematical error.

On the contrary, the influence of the choice of mixing range in the background estimation (see subsection 5.3.2) on R_{χ_c} was taken into account in the evaluation of the systematical error. Varying the mixing range between 50 and 200, we estimate an error of 1 % defined as the maximal ralative deviation of R_{χ_c}.

In summary, the total systematical uncertainty related to the signal extraction is about 8% (Table 6.3, item 2).

- The third group is related to the Monte Carlo simulation. To confirm the Monte Carlo description of the detector material composition and acceptance which affects the photon detection efficiency, we compare the bremsstrahlung tag probability determined from data and Monte Carlo. The bremsstrahlung efficiency $\varepsilon_{brems.}$ was evaluated using the method described in [89]. It consist of a comparison of the $J/\Psi \to e^+e^-$ signals obtained with requirement of one ($N_{12}^{J/\Psi}$) and two ($N_2^{J/\Psi}$) reconstructed bremsstrahlung photons (see Fig. 4.21(a) and 4.22(a), respectively). Under the assumption of no correlation between the emission of two electrons $\varepsilon_{brems.}$ can be calculated as
$$\varepsilon_{brems.} = \frac{2}{1 + N_{12}^{J/\Psi}/N_2^{J/\Psi}}.$$
The values obtained for data ($\varepsilon_{brems.} \sim 35\%$) and Monte Carlo ($\varepsilon_{brems.} \sim 34\%$, see Fig. 4.20(a) and 4.22(b)) are in a good agreement. Therefore, no systmatical uncertainty is attribute to the Monte Carlo description of the detecor material and acceptance. However, we attribute a 12.5 % systmatical uncertainty related to the accuracy of the Monte Carlo estimate for photon efficiency ε_γ (item 3 in Table 6.3). It is evaluated by comparing the efficiencies for different materials (Table 6.1, item 3).

- The fourth group extends the study of systematical uncertainties to data detected studied using the $J/\Psi \to e^+e^-$ decays. For this channel the systematical effects due to selection criteria, signal extraction, Monte Caro simulation are expected to be the same as in case of di-muon data. An additional uncertainty in the analysis of the data collected in the di-electron channel is related to the parametrization of the bremsstrahlung tail and background under the $J/\Psi \to e^+e^-$ signal. It has been studied by comparing the results from the fit to different ranges of the e^+e^- invariant mass distribution, as well as to distributions with different histogram binnings. This results in a deviation in the yield of $J/\Psi \to e^+e^-$ decays of about 5%, which is taken as the systmatical error due to the parametrization (4.15) (Table 6.3, item 4).

The parameters estimated from Monte Carlo simulations can be different for different models used in the simulation. A comparison of x_F distributions of J/Ψ simulated with color-singlet and color-octet production mechanisms shows a difference in the number of simulated J/Ψ within the acceptance of HERA-B of about 13 %. Unfortunately, this is not enough to make an estimate of the uncertainty related to the production mechanism. For this purpose a full simulation based on different production mechanisms is necessary.

Such simulation was not availale at the time. Threrefore we do not study the contribution to the systematical uncertainty due to the model dependence of the simulations.

The polarization of the χ_c affects the reconstruction efficiency of χ_c, however, like the previous experiments, we have assumed no polarization and have neglected the uncertainty related to it. We also expect a negligible contribution to the systematical error due to calibration scales and constants.

Table 6.3: *Contributions to the relative systematical uncertainty. For the calculation of the total uncertainty the correlation in the systematical errors of the different samples is taken into account.*

	Source	di-muon data	di-electron data
1.	Selection criteria		
	J/Ψ mass window	3 %	
	Energy	9 %	
	Transverse energy	3 %	
	π^0 mass window	2 %	
	Exclusion of the innermost part of ECAL	3 %	
	Number of cells	1 %	
	Aggregate	11 %	
2.	Signal extraction		
	Histogram binning	6 %	
	Fit to ΔM	3 %	
	Background under χ_c	10 % *	
	Mixing range	1 %	
	Fixing the width of the χ_c signal	5 %	
	Aggregate	8 %	
3.	Monte Carlo	12.5 %	
4.	Fit to di-electron invariant mass distribution		5 %
	Total	18 %	19 %

* Being a part of the statistical uncertainty, it is not included in the estimation of the total systematical error.

Assuming that all individual systematical errors are uncorrelated, the total systematical error is obtained by summing in quadrature the single contributions. The resulting value of the total systematical uncertainty on R_{χ_c} is 18 % for di-muon data and 19 % for di-electron data (see Table 6.3).

6.5 Combined result and interpretation

The experimental value R_{χ_c} obtained for the combined data set in the di-muon channel is

$$R_{\chi_c} = 0.177 \pm 0.026_{stat} \pm 0.032_{syst}, \tag{6.7}$$

where the first uncertainty is statistical and the second is systematical. The J/Ψ and χ_c statistics corresponding to the combined value of R_{χ_c} is given in Table 5.8. In the evaluation of R_{χ_c} we use the photon efficiency, estimated with the help of cumulative sample of simulated data (case 3, see 6.1 and Table 6.1). Combined ratio (6.7) admits the results obtained for smaller di-muon data sets. It is also in rather good agreement with the corresponding value obtained for di-electron data (see Table 6.2).

Table 6.4: *Experimental results on R_{χ_c} obtained in pA, pp, $p\bar{p}$, πp and πA experiments referred in [49, 50] and [51]*

.

Experiment	Interaction	$\sqrt{s}$, GeV	R_{χ_c}
proton-nucleus collisions			
E610	pBe	19.4, 21.7	0.47 ± 0.23
E705	pLi	23.8	0.30 ± 0.04
E771	pSi	38.8	0.74 ± 0.17
HERA-B	pC, Ti	41.6	0.32 ± 0.10
pp and $p\bar{p}$ collisions			
R702	pp	52, 63	$0.15^{+0.10}_{-0.15}$
ISR	pp	62	0.47 ± 0.08
CDF	$p\bar{p}$	1800	0.297 ± 0.059
πp and πA collisions			
IHEP140	$\pi^- p$	8.5	0.44 ± 0.16
WA11	$\pi^- Be$	16.8, 18.7	0.30 ± 0.05
E610	$\pi^- Be$	18.9	0.31 ± 0.10
E673	$\pi^- H_2, Be$	20.2	0.70 ± 0.28
E369	$\pi^- Be$	20.6	0.37 ± 0.09
E705	$\pi^- Li$	23.8	0.37 ± 0.03
E705	$\pi^+ Li$	23.8	0.40 ± 0.04
E672/706	$\pi^- Be$	31.1	0.443 ± 0.054

Figure 6.7 shows a comparison of the experimental value 6.7 obtained in the present work (filled box) with the results from previous experiments [49, 50] (see Table 6.4). As it can be seen, our measurement is compatible with most of previous measurements performed with incident protons [49, 51] and pions [50]. It lies within one and half standard deviations with respect to the value measured by HERA-B using a limited set of data from run in 2000 [51] (filled thriangle). The CDF result 0.297 ± 0.059 [34] is not shown

in Fig. 6.7, since its kinematic acceptance differs strongly from the other experiments. The value quoted for E771 has been calculated from the published cross sections [49] and branching ratios [102]. The error bars, shown in the plot, include both the statistical and the systematical uncertainties.

Theoretical predictions based on color-singlet model (CSM) [4] and non-relativistic QCD (NRQCD) [6, 5], assumptions about the production mechanism are also shown in Fig. 6.7 (dashed and solid lines, respectively) [103]. The color evaporation model (CEM) [8] assumes a constant ratio, independent of the energy or type of projectile, as well as type of the target. However, it leaves the ratio as the parameter which has to be estimated experimentally.

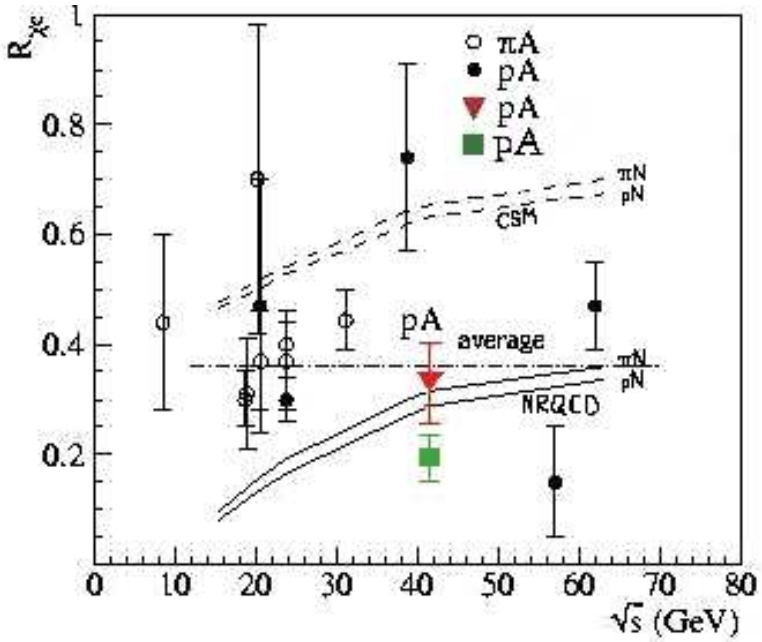

Figure 6.7: *Comparison of our measurement of R_{χ_c} (filled box) with those of other pp, pA [49] (filled circles, filled triangle) and πA [50] (open circles) experiments. Also shown are predictions for pN and πN interactions obtained from Monte Carlo [63] based on the NRQCD (solid), CSM (dashed) . The CEM predicts a constant ratio, but does not specify its value. The dot-dashed line is the average of pp, $p\bar{p}$ and pA measurements (excluding the result presented in this work).*

In the CSM, hadronization of pre-resonant $c\bar{c}$ pair to J/Ψ requires the emission of a hard gluon, lowering thus the probability of the production via color-singlet states. On the other side, χ_c could be produced directly via color-singlets and, thus, the J/Ψ production should be dominated by χ_c decays. This is in contradiction with the measured ratio (6.7), which shows incompleteness of CSM. The predictions based on the Non-Relativistic QCD (NRQCD) factorization approach, which includes the production via color-octet mechanism as well, seem to be close to the experimental result obtained in the present analysis. However, a flat energy dependence predicted by the Color Evaporation

Model (CEM), which states the universality of charmonium hadronization, fits rather well to the available data points within the experimental uncertainties. Moreover, the measurement of the R_{χ_c} x_F distributions, presented in the section 6.3 seem to reinforce the assumption that charmonium production in proton-nucleus collision can be essentially described within CEM. However, the present theoretical and experimental uncertainties are still quite large to qualify or disqualify any of models.

Chapter 7

Study of relative production of χ_{c1} and χ_{c2} states

In this chapter we present the study of the reconstruction of $\chi_{c1} \to \gamma J/\Psi$ and $\chi_{c2} \to \gamma J/\Psi$ decays exploiting the pair production mechanism. The main goal of the analysis is to measure the relative cross sections of the χ_{c1} and χ_{c2} produced in pA (A=C,W,Re,Ti; see Table 3.1) collisions at $\sqrt{s} = 41.6\ GeV$. Knowledge of this ratio is necessary for any model that calculates J/Ψ production through radiative χ_c decay, and can be an important standard for comparing production models. We study the process $pA \to \chi_{c1,2}X$, $\chi_{c1,2} \to \gamma J/\Psi$, $J/\Psi \to l^+l^-$ $(l = e, \mu)$ and $\gamma + (Z, A) \to e^+e^- + (Z, A)$. The analysis chain passes through

- reconstruction of $J/\Psi \to l^+l^-$ decays,
- search for the photon candidates using pair production (photon pair conversion) processes,
- search for the χ_c particles by reconstructing the invariant mass of the photon-J/Ψ pairs for each combination within a given event,
- estimation of the background using the event mixing technique,
- determination of the efficiencies using Monte Carlo simulations (see chapter 3, section 3.9),
- extraction of the relative production cross section, $\sigma_{\chi_{c1}}/\sigma_{\chi_{c2}}$, of χ_{c1} and χ_{c2} states of charmonium:

$$\frac{\sigma_{\chi_{c1}}}{\sigma_{\chi_{c2}}} = \frac{N_{\chi_{c1}}}{N_{\chi_{c2}}} \cdot \frac{\varepsilon_{\chi_{c2}}}{\varepsilon_{\chi_{c1}}} \cdot \frac{Br(\chi_{c2} \to \gamma J/\Psi)}{Br(\chi_{c1} \to \gamma J/\Psi)}, \tag{7.1}$$

  where $N_{\chi_{ci}}$ is the number of observed χ_{ci} particles; $\varepsilon_{\chi_{ci}}$ and $Br(\chi_{ci} \to \gamma J/\Psi)$ are the detection efficiency and branching ratio, respectively; $i = 1, 2$.

The reconstruction of the $J/\Psi \to l^+l^-$ decay proceeds as described in chapter 4 (section 4.2). The final state photons are reconstructed through photon conversions to e^+e^- pairs.

The χ_{c1} and χ_{c2} signals are then investigated through the mass difference distribution ΔM_{conv}, defined as

$$\Delta M_{conv} = M((e^+e^-)J/\Psi) - M(J/\Psi), \tag{7.2}$$

where $M((e^+e^-)J/\Psi)$ is the invariant mass of an electron-positron pair and a J/Ψ, whereas $M(J/\Psi)$ is the reconstructed mass of the J/Ψ meson. The main idea is to employ tracking devices for the photon detection in order to measure the momentum of the photon, which results in a better ΔM_{conv} resolution compared to the one obtained using ECAL data. Mass difference resolution is determined by the uncertainties in the momentum determination of tracks, which varies from 1 % at 1.5 GeV/c up to 1.8 % at 100 GeV/c [1] [104]. The contribution to the deviation of ΔM_{conv} due to the uncertainties in the momentum measurement of $e^{\pm}$ candidates is about 5 time smaller than the deviation due to the uncertainties related to the cluster energy (taking the energy resolution of the ECAL averaged over the cluster energy spectrum as 10 %)[2]. Adding the contribution from the J/Ψ's muons, the overall gaining factor in the resolution becomes 3.5, which leads to the resulting ΔM_{conv} resolution of about $10-12$ MeV/c^2. Taking account of the mass difference between χ_{c1} and χ_{c2} states (46 MeV/c^2 [20], see also Table 5.1), the precision of the ΔM_{conv} determination should be enough to distinguish the two states and, thereby, to perform the measurement using data taken during the 2002-2003 HERA-B operation.

Due to limited statistics and the small probability to detect converting photons from χ_c decays the combined data sample, obtained with the different target materials, is used in the analysis.

The relative acceptance for χ_{c1} and χ_{c2} states is studied with Monte Carlo $\chi_c \to \gamma J/\Psi$ events generated for $i2$ (C) and $i1$ (W) wires (see chapter 3, section 3.9, as well as chapter 6, section 6.1), which are used as input to the detector and trigger simulations.

7.1 γ reconstruction through conversion into e^+e^- pair

7.1.1 Reconstruction of the photon pair conversions

The photon is reconstructed using the pair production process. In order to achieve high enough ΔM_{conv} resolution for χ_{c1} and χ_{c2} separation (which implies a precise estimation of the photon momentum), we restrict ourself to the conversions in the first part of the VDS, such that the produced electron and positron can create their signatures in the vertex detector. The probability for such processes is about 10 %.

The basic element of the reconstruction of the photon pair conversion is to look for one segment in front of the magnet and two segments behind the magnet.

[1] The momentum resolution avereged over momentum spectrum of the charged particles is about 1.25 %

[2] The ΔM resolution in this case is about 38 MeV/c^2 (see chapter 5, subsection 5.2.5).

Both the electron and the positron, created in the conversion of a photon in the VDS, abide the initial direction of the photon, i.e. their trajectories in the VDS are collinear. This results in that the e^+e^- conversion pair is reconstructed in the VDS, the area free of magnetic field, as one track. Downstream of the VDS, however, the electron and the positron drift apart under the action of the magnetic field. Since the main bending component of the magnetic field is headed along the y axis, the trajectories split in zx plane, while in the zy plane the e^+ and e^- trajectories stay nearly collinear. This greatly facilitates the selection of photon conversions. Thus, in order to select the e^+e^- pair conversion candidates we inspect tracks which have alike segments in the VDS and distinct segments downstream of the magnet. To control that the VDS segments of the tracks are indeed similar, we compare the e^+ and e^- slopes in the zx and zy planes, reconstructed at the first measured point. The slopes, $\tan\theta_{zk}$ $(k = x, y)$, are defined as

$$\tan\theta_{zk} = \frac{p_k}{p_z}, \tag{7.3}$$

with p_k and p_z being the components of the reconstructed momentum, $k = x, y$. We require the difference between e^+ and e^- slopes to be less than 2.5×10^{-3}. To make sure that the tracks are separated by the magnetic field, we require a separation between two tracks projected onto the zx plane at the point $z = 700\ cm$ (the entry point to the pattern tracker) of order of $10\ cm$.

The applicability of the above idea is checked using the $\pi^0 \to \gamma\gamma$ decay (see the following subsection).

7.1.2 Conversions and π^0 signal

We study two gamma decays of π^0 mesons, $\pi^0 \to \gamma\gamma$, to confirm the usage of the pair production mechanism for the study of the χ_c particles produced in HERA-B. We reconstruct one of the photons as an ECAL cluster and the other as an e^+e^- pair, created in the interaction of γ with the VDS medium. Then we pair two gamma candidates to calculate the invariant mass. To suppress the background due to soft secondary particles, noise clusters and hadronic showers we use the following requirements for the ECAL clusters:

- energy deposited should exceed the limit of $3\ GeV$,
- the transverse energy of the cluster should be bigger than $0.3\ GeV$,
- the ratio of energy from three most energetic cells to the total energy of the cluster, $asym$, should be bigger that 0.8 (see Fig. 5.6).

The $e^\pm$ candidates are selected using the following considerations:

- we require two oppositely charged tracks with the reconstructed segments in the VDS and OTR/ITR;

- as mentioned in the previous section, the difference between e^+ and e^- slopes (7.3) is required to be less than 2.5×10^{-3}, whereas the segments in the main tracker are demanded to be separated in the zx coordinate plane (see later Fig. 7.10(a)). This assures that we deal with photon pair conversions. Moreover, it minimizes the possibility to reconstruct Dalitz decays $\pi^0 \to \gamma e^+ e^-$;

- in order to eliminate ghost tracks[3], it is required for each $e^\pm$ candidate to have an associated ECAL cluster such that the energy to momentum ratio, E/p, satisfies the condition $0.7 < E/p < 1.1$;

- the total transverse momentum of the e^+e^- pair should exceed the limit of 0.3 GeV/c.

For each e^+e pair, that satisfies the criteria above, a vertex fit[4] is performed. The mass of the pair is not constrained. The e^+e^- vertex is required to be located downstream of the interaction point. The momentum of the pair, obtained from the e^+e^- vertex fit, should exceed the limit of 3 GeV/c, while the e^+e^- invariant mass satisfies the condition: $M_{e^+e^-} < 0.002\ GeV/c^2$.

The search for the $\pi^0 \to \gamma[\gamma \to e^+e^-]$, with one of the photons reconstructed through pair production mechanism, is done using sets of data obtained with different trigger conditions, i.e. random trigger and di-muon trigger. It is also checked using Monte Carlo simulations. The corresponding distributions of the invariant mass of the $\gamma(e^+e^-)$ system are presented in Fig. 7.1. The signal is observed in all distributions, validating our assumptions about the reconstruction of converted photons. The position of the peak is at about $125.0 \pm 1.0\ MeV/c^2$ for random trigger data (Fig. 7.1(a)) and $130.7 \pm 0.4\ MeV/c^2$ for the corresponding simulations (Fig. 7.1(b)). In the case of di-muon trigger data this parameter is $127.4 \pm 1.0\ MeV/c^2$ (Fig. 7.1(c)). All these numbers are below the nominal value of $135 MeV/c^2$ [20]. This can be explained by the radiation losses of the electron and/or positron and misalignment. The width of the π^0 peak is $14.2 \pm 1.1\ MeV/c^2$ and $13.7 \pm 1.1\ MeV/c^2$ for di-muon triggered and random triggered data, respectively. The Monte Carlo value is $10.6 \pm 1.0\ MeV/c^2$. The parameters of the π^0 signal are summarized in Table 7.1. Apparent discrepancies between the values corresponding to different data sets and simulation may be related to the uncertainties in alignment and calibration.

In addition we investigate the effect of radiation losses of electron-positron pairs. The search for a bremsstrahlung photon emitted by the electron or positron in front of the magnet is carried out for each selected e^+e^- pair[5]. If such a photon is found, the corresponding kinematical parameters of the pair are corrected. This slightly recovers the position of the π^0 peak (see Fig. 7.2, Table 7.2). However, the correction of the e^+e^- momentum, without bremsstrahlung requirement, results in the reduction of the signal by 15-17 % (Fig. 7.2, Table 7.2). Moreover, the requirement of the presence of the identified bremsstrahlung photon reduces the signal multiplicity by more than 80%, while

[3] A random combination of reconstructed hits.

[4] With the help of GROVER package [83]

[5] The search for bremsstrahlung losses was similar to the one used to reconstruct $J/\Psi \to e^+e^-$ decays (see Fig. 4.11).

Table 7.1: *The numbers related to the $\pi^0 \to \gamma\gamma$ signal (Fig. 7.1).*

Trigger	Di-muon trigger	Random Trigger	
Data Set	2002-2003 Data	2002 Data	Monte Carlo
$N(\pi^0)$	665 ± 61	300 ± 31	240 ± 26
M_{π^0}, MeV/c^2	127.4 ± 1.0	125.0 ± 1.0	130.7 ± 0.4
σ_{π^0}, MeV/c^2	14.2 ± 1.1	13.7 ± 1.1	10.6 ± 1.0

Table 7.2: *The numbers related to the $\pi^0 \to \gamma\gamma$ signal. Bremsstrahlung reconstruction is applied but not required (Fig. 7.2).*

Trigger	Di-muon trigger	Random Trigger	
Data Set	2002-2003 Data	2002 Data	Monte Carlo
$N(\pi^0)$	553 ± 56	255 ± 31	194 ± 23
M_{π^0}, MeV/c^2	129.9 ± 1.1	126.2 ± 1.2	133.1 ± 1.0
σ_{π^0}, MeV/c^2	14.9 ± 1.1	13.2 ± 1.5	9.0 ± 1.0

the background rate decreases only by 70 %. Under such circumstances the usage of the bremmstrahlung identification becomes inappropriate.

One should also notice, that it is not straightforward to make an analogy between $\pi^0 \to \gamma\gamma$ and $\chi_c \to \gamma J/\Psi$ signals since the photons from π^0 meson are in a different kinematical range than those stemming from χ_c particles. In addition, the reconstructed two photon invariant mass, where one of the photons is detected via γ-conversion, still has an uncertainty related to the ECAL cluster measurements. On the other hand, the resolution of ΔM_{conv} is determined essentially by the uncertainties in the momentum of e^+e^- pair.

As a conclusion, we would like to stress two points from this section:

- the exercise with the π^0 signal shows that the reconstruction of the photon using the pair production in the VDS is possible and gives a good resolution;
- however, such reconstruction is associated with very low efficiencies. π^0 with one converted photon constitute a tiny fraction of the π^0 signal, where both photons are detected in ECAL
$$\frac{N(\pi^0 \to \gamma[\gamma \to e^+e^-])}{N(\pi^0 \to \gamma\gamma)} \sim 10^{-4}.$$

7.1.3 Selection of e^+e^- conversions of χ_c photons.

The next step is the reconstruction of the photons originating in the decays of χ_c mesons. The search for photon conversion candidates starts with an examination of all additional

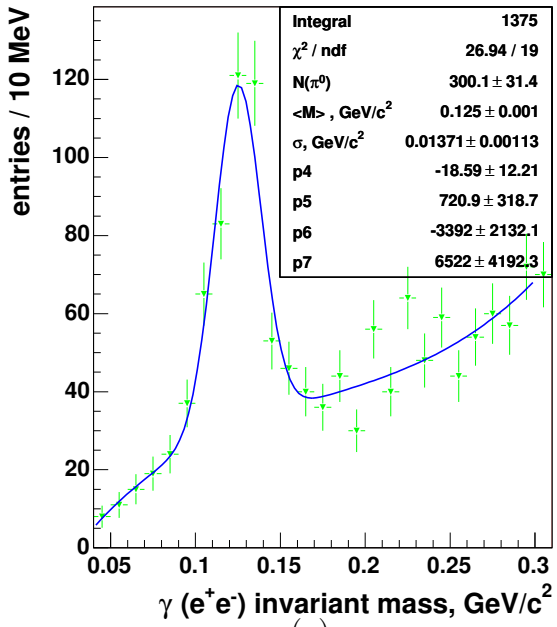

(a)

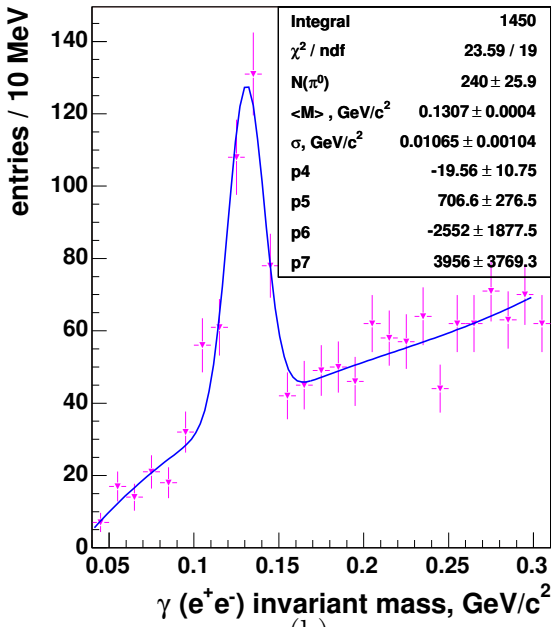

(b)

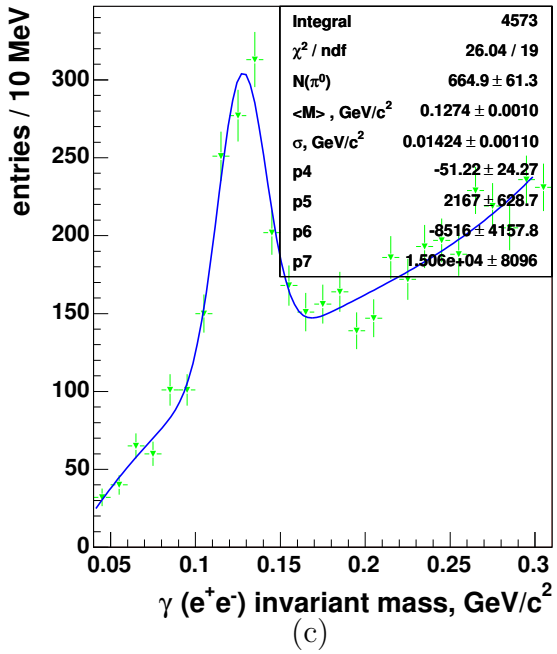

(c)

Figure 7.1: *The invariant mass of the γ and e^+e^- pair is presented. The distributions represent random trigger data (a) and corresponding Monte Carlo simulations (b) as well as di-muon trigger data from 2002-2003. The observed signal correspond to the reconstructed $\pi^0 \to \gamma\gamma$ decays using the photon pair conversions in the vertex detector to detect one of the photons. The fit is done using a Gaussian for the signal parametrization and a 3^d order polynomial to describe the background (see Table 7.1 for details).*

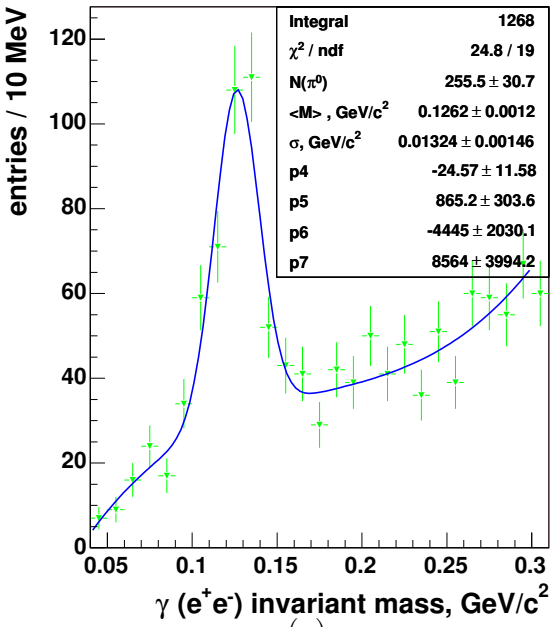

(a)

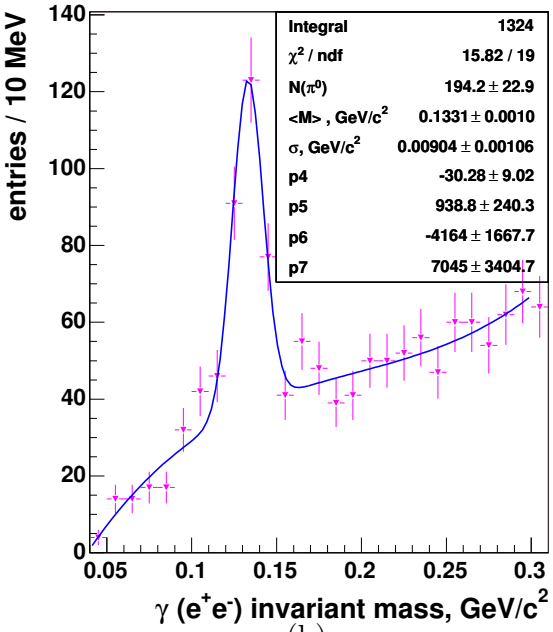

(b)

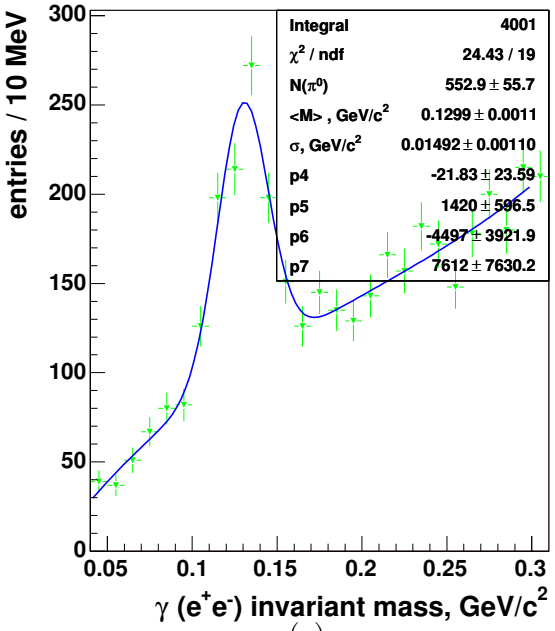

(c)

Figure 7.2: *The same as Fig. 7.1 except that the momentum of e^+e^- pair used to calculate the $\gamma(e^+e^-)$ invariant mass is corrected for bremsstrahlung hypothesis when found (see text and Table 7.2 for details).*

tracks found in each J/Ψ event. The J/Ψ event is defined as a di-muon event[6] in which the J/Ψ vertex fit probability satisfied the relation:

$$\mathcal{P}_{vert}(\chi^2) > 0.005,$$

and the invariant mass of the muons lied within J/Ψ mass window within three standard deviations (Fig. 7.3). Each considered track is required to have a signature in the VDS (at least five reconstructed hits) and in the superlayers of the OTR and/or the ITR (at least ten reconstructed hits). The slopes of the segments in the vertex detector were required to satisfy the conditions:

$$\left|\tan(\theta^+_{zx}) - \tan(\theta^-_{zx})\right| < 2.5 \times 10^{-3} \tag{7.4}$$

and

$$\left|\tan(\theta^+_{zy}) - \tan(\theta^-_{zy})\right| < 2.5 \times 10^{-3}, \tag{7.5}$$

where $\tan(\theta_{zx})$ is the track slope in the zx plane and $\tan(\theta_{zy})$ represents a similar quantity in the zy plane (see Fig. 7.4); "$-$" and "$+$" denote electron or positron. The requirements (7.4, 7.5) are made to ensure that the pair has a common segment in the VDS. It also constrains the e^+e^- invariant mass to peak around zero value (Fig. 7.5). Besides, the e^+e^- invariant mass squared, $M^2_{e^+e^-}$, is required to satisfy the condition

$$\left|M^2_{e^+e^-}\right| \leq (4\ MeV/c^2)^2. \tag{7.6}$$

We impose the supplementary limitation on the mass of the electron-positron system to further reduce the background and, thus, to improve the signal to background ratio. The cut value is optimized by using the signal from Monte Carlo simulations and the background from the side bands of the measured ΔM_{conv} distribution, where no signal is expected (Fig. 7.6).

In addition, the transverse momentum of the pair, $p_T^{e^+e^-}$, is required to be bigger than $0.12\ GeV/c$ (Fig. 7.7). According to simulations, χ_c's photons usually have p_T^γ values larger than the value of the applied cut. Therefore, such requirement causes no losses in signal multiplicity, while it results in a reduction of the background rate (see Fig. 5.14(bottom)). We do not use the optimal value, which is about $0.18\ GeV/c$ (Fig. 7.8), in order to avoid that the background in ΔM_{conv} distribution peaks where the signal is expected.

To reduce the background due to hadron and ghost tracks we necessitate that the ratio of the energy sum of the e^+ and e^- clusters to the total momentum of the e^+e^- pair conforms to the requirement (Fig. 7.9):

$$0.7 \ < \ \frac{E^{cl}_{e^+} + E^{cl}_{e^-}}{p^{e^+e^-}} \ < \ 1.3, \tag{7.7}$$

where $E^{cl}_{e^\pm}$ is the energy of the cluster associated with the e^+ or e^- track, and $p^{e^+e^-}$ is the e^+e^- momentum. This cut allows to remove nearly 90 % of the background.

[6]See chapter 4, subsection 4.3.2 for muon selection.

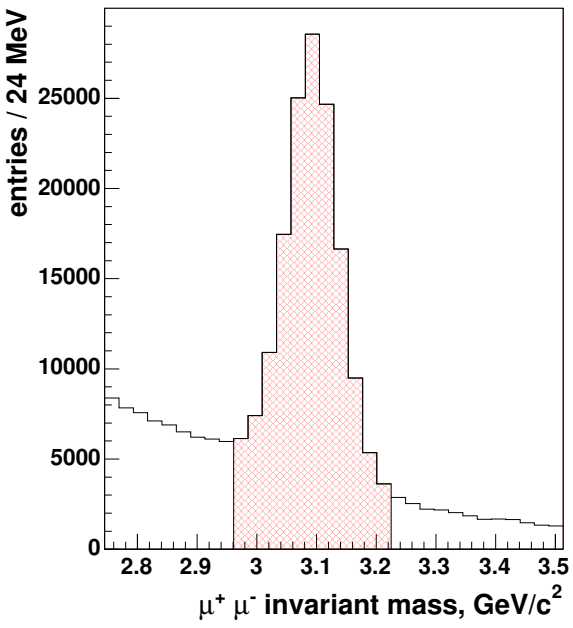

Figure 7.3: *$\mu^+\mu^-$ invariant mass. The shaded area represents the J/Ψ events used for χ_c search. It corresponds to a mass window of three standard deviations, i.e. $|M_{J/\Psi} - 3.093| < 3\sigma_{M_{J/\Psi}}$, with $\sigma_{M_{J/\Psi}} = 0.044 GeV/c^2$. The fit with the Gaussian for the signal parametrization and an exponential for the background description results in the number of the reconstructed $J/\Psi \to \mu^+\mu^-$ decays $N(J/\Psi) = 149934 \pm 474$, with the mean value and width of the Gaussian being equal to $\langle M(J/\Psi)\rangle = 3.0932 \pm 0.0001\ GeV/c^2$ and $\sigma(J/\Psi) = 0.0444 \pm 0.0001\ GeV/c^2$, respectively.*

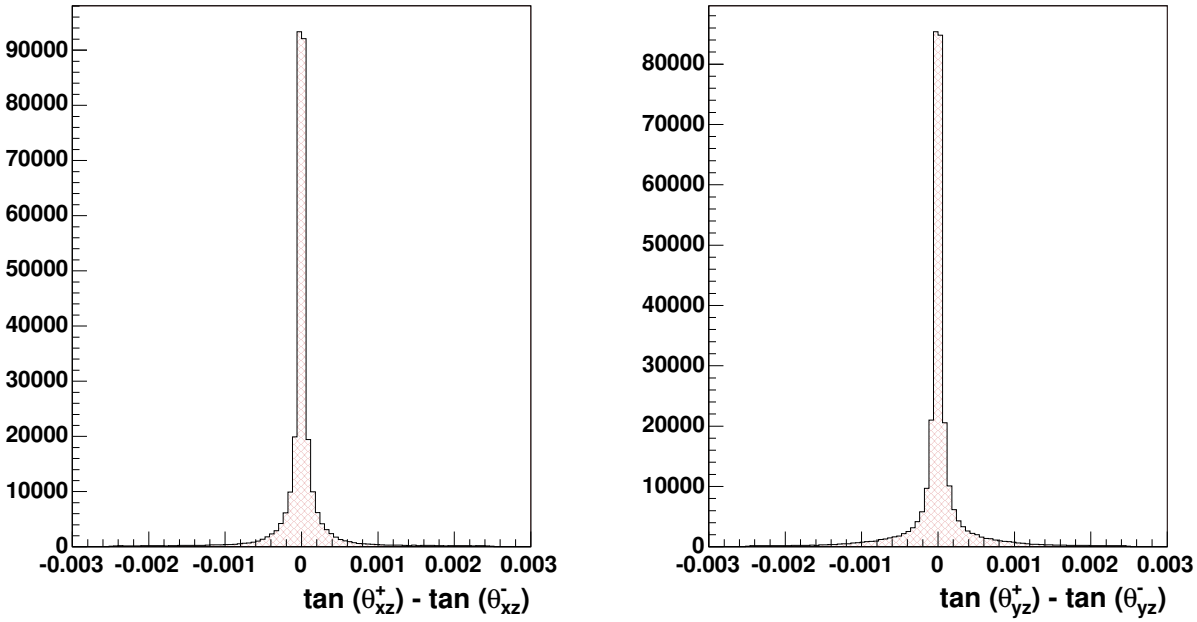

(a) (b)

Figure 7.4: *Difference between e^+ and e^- track slopes in zx coordinate plane (a) and zy coordinate plane (b).*

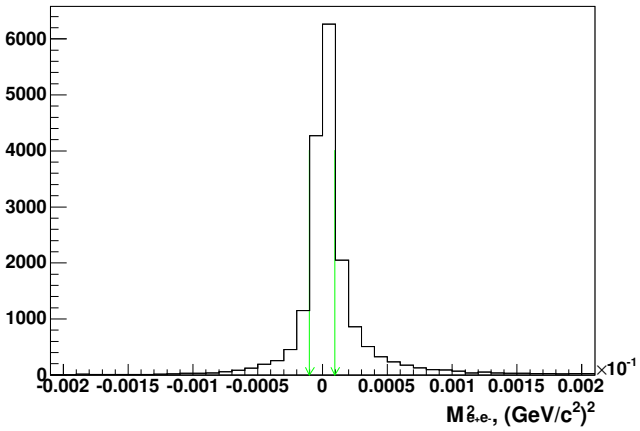

Figure 7.5: *Squared invariant mass of e^+e^- pair. The arrows show the upper and lower limits corresponding to the cut given by equation 7.6. Events between the limits are accepted in the analysis. The distribution is obtained after other selection criteria have been applied.*

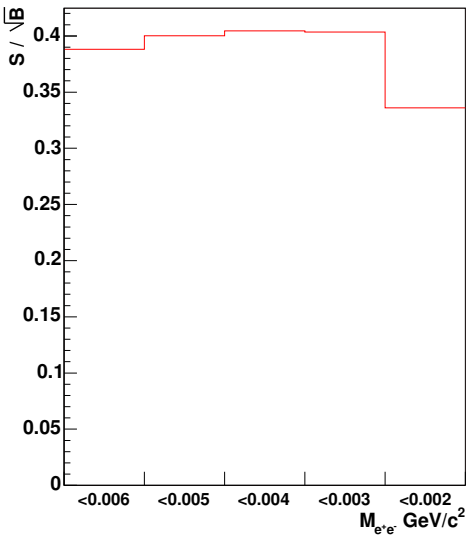

Figure 7.6: *$S/\sqrt{B}$ ratio as a function of $M^2_{e^+e^-}$ cut. The values for signal, S, are obtained from Monte Carlo simulations, while the values for background, B, are taken from side-bands of the ΔM_{conv} distribution ($0.3\ GeV/c^2 > \Delta M_{conv}$ and $\Delta M_{conv} > 0.5\ GeV/c^2$).*

In order to control that we operate with two distinct tracks in the main tracker (i.e. area behind the magnet), we study the Δx_{ot} distribution (see Fig. 7.10(a)), defined as

$$\Delta x_{ot} = x^+_{ot} - x^-_{ot}. \tag{7.8}$$

Here $x^\pm_{ot}$ is the x coordinate of the track at $z = 700\ cm$ and "$-$"/"$+$" denotes electron or positron. From Fig. 7.10(a) it is clearly seen that at the present selection level the two tracks are indeed separated. Therefore we do not apply any further requirement for the track separation behind the magnet. Along with that, we require that $e^\pm$ tracks stay nearly collinear in the zy plane. For that, we necessitate that the absolute values of Δy_{ot} do not exceed the limit of 1 cm (Fig. 7.10(b)). The quantity Δy_{ot}, similarly to Δx_{ot}, is defined as

$$\Delta y_{ot} = y^+_{ot} - y^-_{ot}, \tag{7.9}$$

where $y^\pm_{ot}$ is the y coordinate of the track at $z = 700\ cm$, and "$+$" and "$-$" stand for e^+ and e^-, respectively.

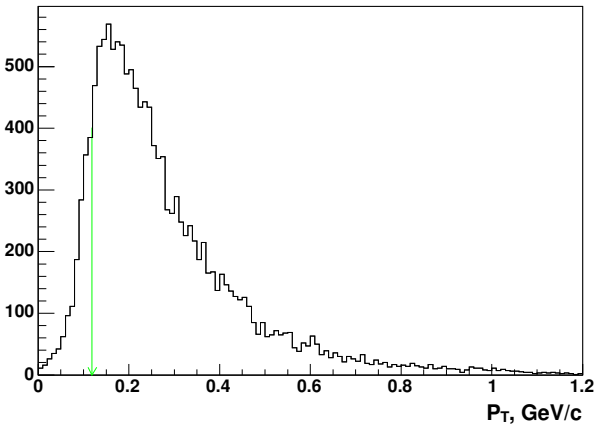

Figure 7.7: *Transverse momentum of e^+e^- pair. The arrow shows the cut corresponding to $p_T^{e^+e^-} = 0.12$ (GeV/c). Events above the limit are accepted in the analysis. The distribution is obtained after other selection criteria have been applied.*

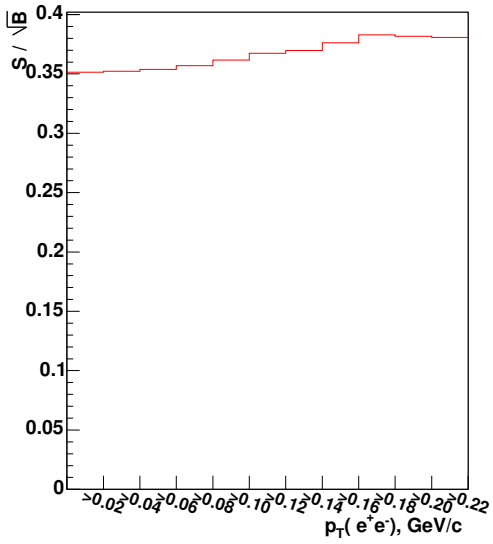

Figure 7.8: *$S/\sqrt{B}$ ratio as a function of $p_T^{e^+e^-}$ cut. The values for signal, S, are obtained from Monte Carlo simulations, while the values for background, B, are taken from side-bands of the ΔM_{conv} distribution ($0.3\ GeV/c^2 > \Delta M_{conv}$ and $\Delta M_{conv} > 0.5\ GeV/c^2$).*

The summary of the selection criteria is presented in Table 7.3.

The resulting ΔM_{conv} distribution, obtained using the criteria described above, is depicted in Fig. 7.11. Superimposed, the combinatorial background is shown. The background is mainly due to the photons resulting from the decay of light mesons (e.g. π^0, η, $K_s^0 \to \pi^0\pi^0$ etc), which are produced in association with the J/Ψ. The contribution from decays of heavier mesons is negligible. We model the background by pairing the J/Ψ and e^+e^- picked up from different events (i.e. by means of event mixing technique). Such mixed combinations undergo the selection identical to the cuts applied for the analysis of $J/\Psi(e^+e^-)$ pairs within the same event. The resulting "mixed" distribution reproduces the combinatorial background quite well, as can be seen in Fig. 7.11.

Figure 7.9: *The ratio of the energy sum of the e^+ and e^- clusters to the e^+e^- momentum. The arrows show the cut corresponding to* 0.7 *(lower limit) and* 1.3 *(upper limit) (see equation 7.7). Events between the limits are accepted in the analysis. The distribution is obtained after other selection criteria have been applied*

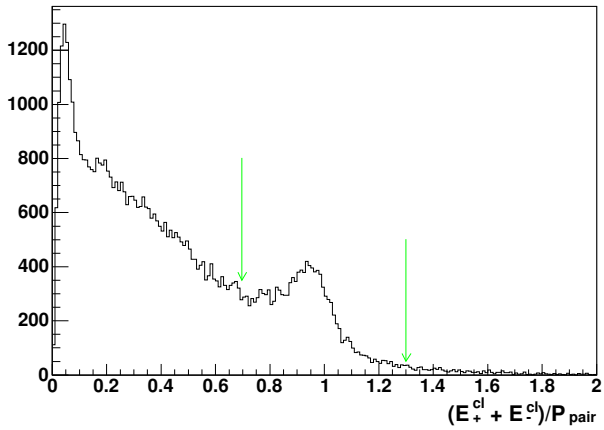

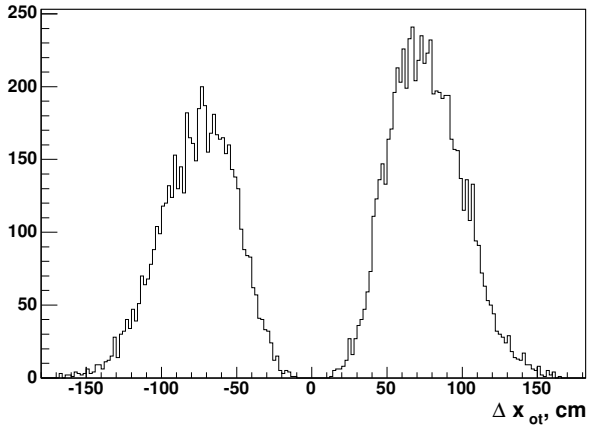

(a)

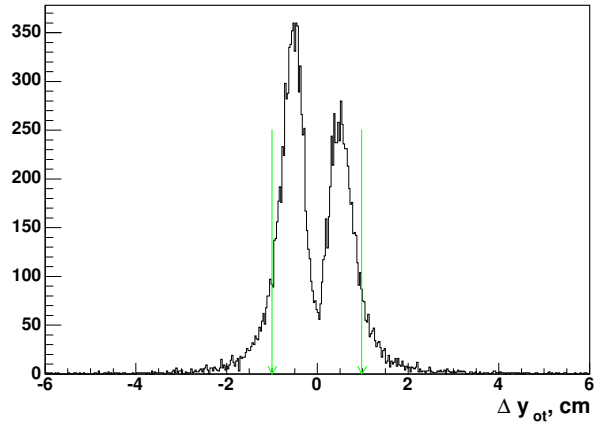

(b)

Figure 7.10: *Track separation behind the magnet: (a) Δx_{ot}, distance between tracks in zx coordinate plane behind the magnet ($z = 700$ cm). (b) Δy_{ot}, distance between tracks in zy coordinate plane behind the magnet ($z = 700$ cm). The observed two peaks are due to residual magnetic field along x axis, that slightly bends the trajectories of charged particles in zy direction.*

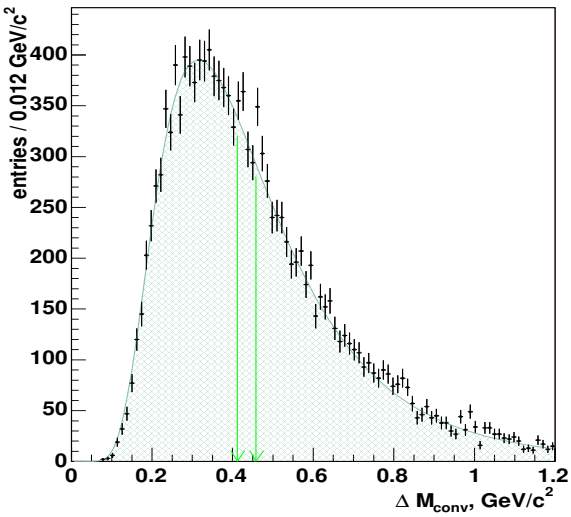

Figure 7.11: *ΔM_{conv} spectrum for di-muon trigger data (see equation (7.2) for the definition). The distribution is obtained using the selection listed in Table 7.3. The shaded background histogram is evaluated by using event mixing. The arrows indicate the positions of χ_{c1} (413.6 MeV/c^2) and χ_{c2} (459.3 MeV/c^2).*

Table 7.3: *Criteria for the selection of photon pair conversions.*

Cut	Value
$\lvert\tan(\theta^+_{zx}) - \tan(\theta^-_{zx})\rvert$	$< 2.5 \times 10^{-3}$
$\lvert\tan(\theta^+_{zy}) - \tan(\theta^-_{zy})\rvert$	$< 2.5 \times 10^{-3}$
$\lvert M^2_{e^+e^-}\rvert$	$\leq (4\ MeV/c^2)^2$
$p_T^{e^+e^-}$	$> 0.12\ GeV/c$
$(E^{cl}_+ + E^{cl}_-)/p^{e^+e^-}$	> 0.7 and < 1.3
$\lvert\Delta y_{ot}\rvert$	$< 1\ cm$

7.2 Efficiency determination

The evaluation of the relative production of χ_{c1} and χ_{c2} states requires the knowledge about the relative efficiency for these particles. We relay on the Monte Carlo simulation (for $i2$ (carbon) [7] and $i1 - b1$ (tungsten-carbon) [8] wire set-ups) in the determination of the detection efficiency ratio

$$\rho_{12} = \varepsilon_{\chi_{c2}}/\varepsilon_{\chi_{c1}},$$

where the overall efficiencies to detect χ_{c1} and χ_{c2} states can be written as

$$\varepsilon_{\chi_{ci}} = \varepsilon^{ee}_{\chi_{ci}} \cdot \varepsilon^{J/\Psi}_{\chi_{ci}}\ (i = 1, 2).$$

Here $\varepsilon^{J/\Psi}_{\chi_{ci}}$ and $\varepsilon^{ee}_{\chi_{ci}}$ are the efficiencies to detect the J/Ψ and converting photon stemming from χ_{ci} state, respectively. We use a set of simulated events, corresponding to about 125,000 reconstructed $J/\Psi \to \mu^+\mu^-$ decays (Fig. 7.12).

In the simulations, the initial ratio of χ_{c1} to χ_{c2} generated events is

$$\frac{N^{sim}_{\chi_{c1}} \cdot Br(\chi_{c1} \to J/\Psi)}{N^{sim}_{\chi_{c2}} \cdot Br(\chi_{c2} \to J/\Psi)} = 0.370 \pm 0.002 \tag{7.10}$$

The trigger, reconstruction and selection do not change the ratio of χ_{c1} to χ_{c2} appreciably (see Table 7.4), implying that the detection efficiencies for both states are essentially equal. The value of the efficiency ratio ρ_{12} is then extracted by counting the χ_{c1} and χ_{c2} matched signal events, i.e:

$$\rho_{12} = \frac{N^{r.m.}_{\chi_{c2}}}{N^{r.m.}_{\chi_{c1}}} \cdot \frac{N^{sim}_{\chi_{c1}} \cdot Br(\chi_{c1} \to J/\Psi)}{N^{sim}_{\chi_{c2}} \cdot Br(\chi_{c2} \to J/\Psi)}. \tag{7.11}$$

Here $N^{r.m.}_{\chi_{ci}}$ is the number of χ_{ci} matched signal events, $(i = 1, 2)$. The matched signal is defined as the reconstructed $\chi_{c1} \to \gamma J/\Psi$ or $\chi_{c2} \to \gamma J/\Psi$ events in which the e^+e^-

[7] */acs/mc4/p41000/d02.1205/w10001000/rec/run09_00025/*

[8] */acs/mc4/p41003/d02.1205/w10001000/rec/run09_00091/*, */acs/mc4/p41000/d02.1205/w10010000/rec/run09_00092/*

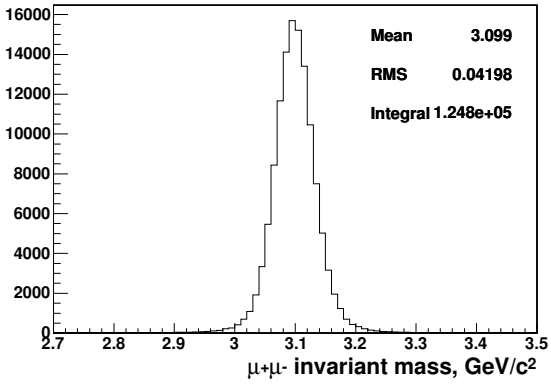

Figure 7.12: *Monte Carlo simulation: reconstructed* $J/\Psi \rightarrow \mu^+\mu^-$ *decays. The cut* $\mathcal{P}_{vert}(\chi^2) > 0.005$ *is applied.*

	All	$\lvert M_{J/\Psi} - 3.093\rvert < 0.132\ GeV/c^2$
$N^{all}_{J/\Psi}$	124,960	123,241
$N^{J/\Psi}_{\chi_{c1}}$	12,383	12,216
$N^{J/\Psi}_{\chi_{c2}}$	33,844	33,388
$\frac{N^{J/\Psi}_{\chi_{c1}}}{N^{J/\Psi}_{\chi_{c2}}}$	0.366 ± 0.004	0.366 ± 0.004
$N^{r.m.}_{\chi_{c1}}$	-	35
$N^{r.m.}_{\chi_{c1}}$	-	97
$\frac{N^{r.m.}_{\chi_{c1}}}{N^{r.m.}_{\chi_{c2}}}$	-	0.361 ± 0.071

Table 7.4: *Numbers related to the simulated* J/Ψ *and* $\chi_{c1,2}$ *signals: the total number of reconstructed* $J/\Psi \rightarrow \mu^+\mu^-$ *decays,* $N^{all}_{J/\Psi}$*; the number of* J/Ψ *coming from* χ_{c1} *decays,* $N^{\chi_{c1}}_{J/\Psi}$*, the number of* J/Ψ *from* χ_{c2} *decays,* $N^{\chi_{c2}}_{J/\Psi}$*, and their ratio; the matched* χ_{c1}*,* $N^{r.m.}_{\chi_{c1}}$*, and* χ_{c2}*,* $N^{r.m.}_{\chi_{c2}}$*, signals and the corresponding ratio.*

conversion pair candidates are matched to the simulated photons (Fig. 7.13). In the matching the track-particle assignment is performed by means of hit association [105]: the link of a reconstructed track to generated e^+ or e^- from a conversion of χ_c photon is established if a fraction of track hits has been caused by one of these particles. Substituting thus in equation 7.11 the numbers listed in Table 7.4 (see also Fig. 7.13) for matched signals and using the value (7.10), we obtain:

$$\rho_{12} = 1.03 \pm 0.21 \tag{7.12}$$

However, the usage of such counting procedure is accompanied with an uncertainty related to the matching performance. When we use matching, the detection efficiency for χ_{ci} $(i = 1, 2)$ state is represented by the efficiency product

$$\varepsilon_{\chi_{ci}} = \varepsilon_{i\ sel} \cdot \varepsilon_{i\ match},$$

where $\varepsilon_{i\ sel}$ is the contribution due to trigger and selection requirements, while $\varepsilon_{i\ match}$ is the matching efficiency, which is not really known and in the most general case its value might be different for different states. This can be a cause for a systematic deviation in the determination of ρ_{12}. In order to identify such uncertainties, we evaluated the value

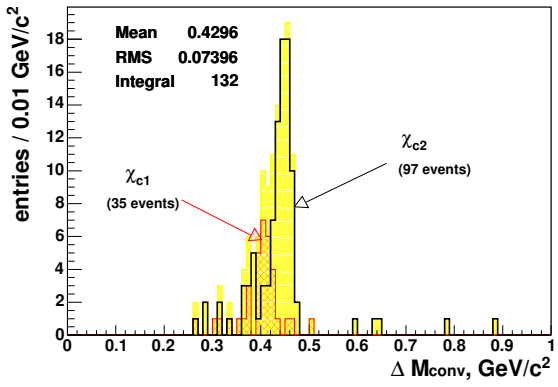

Figure 7.13: *Monte Carlo simulation: ΔM_{conv} distribution corresponding to the $\chi_{c1} \to \gamma J/\Psi$ and $\chi_{c2} \to \gamma J/\Psi$ events in which the e^+e^- conversion pair is matched to the simulated photon. The contributions from χ_{c1} is represented by shaded histogram, while the solid line shows the events corresponding to the χ_{c2} radiative decays. The corresponding multiplicities are also presented.*

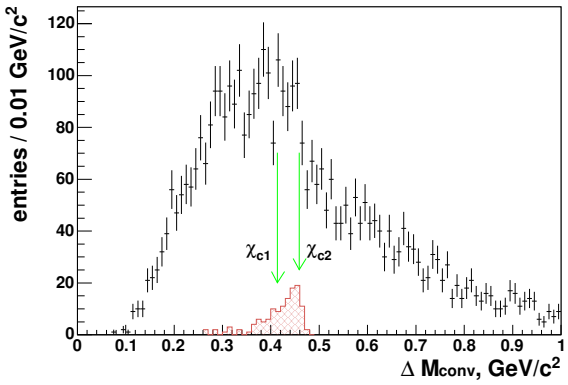

Figure 7.14: *Monte Carlo simulation: ΔM_{conv} distribution obtained from simulated $\chi_{c1} \to \gamma J/\Psi$ and $\chi_{c2} \to \gamma J/\Psi$ events after the application of the selection criteria summarized in subsection 7.1.3. The histogram on the bottom represents matched χ_{c1} and χ_{c2} signals.*

of ρ_{12} using the fit to the ΔM_{conv} distribution depicted in Fig. 7.14. To parametrize the χ_{c1} or χ_{c2} signal we use the function, $S^{fit}_{\chi_{ci}}$ $(i = 1, 2)$, which comprises a Gaussian and a term to describe the radiative tail:

$$S^{fit}_{\chi_{ci}} = N_{\chi_{ci}} \cdot \frac{2 \cdot dx}{\sigma_{\Delta M_{c.}} \left(\sqrt{2 \cdot \pi} + \pi \cdot \sigma^{tail}_{\Delta M_{c.}}\right)} \cdot \begin{cases} \exp\left(-\frac{(\Delta M_{conv} - \langle \Delta M_{c.} \rangle_{\chi_{ci}})^2}{2 \cdot \sigma^2_{\Delta M_{c.}}}\right), & M_{conv} > \langle \Delta M_{c.} \rangle_{\chi_{ci}} \\ \left(1 + \frac{(\Delta M_{conv} - \langle \Delta M_{c.} \rangle_{\chi_{ci}})^2}{(\sigma_{\Delta M_{c.}} \cdot \sigma^{tail}_{\Delta M_{c.}})^2}\right)^{-1}, & M_{conv} < \langle \Delta M_{c.} \rangle_{\chi_{ci}} \end{cases}, \tag{7.13}$$

where $N_{\chi_{ci}}$ is the number of χ_{ci} events $(i = 1, 2)$; dx is the width of the bin in the histogram; $\sigma_{\Delta M_{c.}}$ and $\langle \Delta M_{c.} \rangle_{\chi_{ci}}$ are the width and the position of the Gaussian, respectively; and $\sigma^{tail}_{\Delta M_{c.}}$ is the parameter related to the radiative tail [9]. The background is estimated with the help of the event mixing technique, omitting corrections (5.22) and (5.27)[10]. The final fit function is given by the following formula:

$$\mathcal{F} = S^{fit}_{\chi_{c1}} + S^{fit}_{\chi_{c2}} + C_s \cdot B, \tag{7.14}$$

where B is the mixed background normalized by the coefficient C_s. In the fit, $\sigma_{\Delta M_{c.}}$ and $\sigma^{tail}_{\Delta M_{c.}}$ are assumed to be similar for both states and the distance between two signals is

[9] In absence of the tail $\sigma^{tail}_{\Delta M_{c.}} = \sigma_{\Delta M_{c.}}$, which implies Gaussian parametrization for both parts of the distribution.

[10] See chapter 5, section 5.3 for more detail about the background evaluation.

fixed to the known value of the mass difference between χ_{c1} and χ_{c2} mesons, 45.7 MeV/c^2 [20]. Due to the limited Monte Carlo statistics and small rate of χ_{c1} events, we also fix $\sigma_{\Delta M_{c.}}$ to the value of 11 MeV/c^2. This value is extracted from a fit to the matched χ_{c2} distribution, performed according to parametrization (7.13). We examine the χ_{c2} signal, as it is larger compared to the χ_{c1} one. In order to compensate for low statistics of the matched events, we perform the fit to the χ_{c2} distribution for different bin sizes. The results of such procedure are presented in Fig. 7.15(a-e), and summarized in Table 7.5. In this way, we examine the dependence of $\sigma_{\Delta M_{c.}}$ on the bin size (Fig. 7.15(g)), which is essentially flat. The width

$$\sigma_{\Delta M_{c.}} = 11 \pm 1 \; MeV/c^2, \tag{7.15}$$

is then obtained as the average value for different binnings (horizontal line in Fig. 7.15(g)).

Table 7.5: *Results of the fit to matched χ_{c2} signal: Presented are the number of signal events, $N_{\chi_{c2}}$, the position, $\langle \Delta M_{c.} \rangle_{\chi_{c2}}$, and the width, $\sigma_{\Delta M_{c.}}$, of the signal, as well as the parameter for radiative tail, $\sigma^{tail}_{\Delta M_{c.}}$.*

Bin width	5 MeV/c^2	7.5 MeV/c^2	9 MeV/c^2	10 MeV/c^2	12 MeV/c^2
$N_{\chi_{c2}}$	88 ± 11	83 ± 10	88 ± 10	89 ± 10	89 ± 10
$\langle \Delta M_{.c} \rangle_{\chi_{c2}}$, MeV/c^2	456.0 ± 4.0	451.6 ± 2.9	451.2 ± 4.9	452.2 ± 0.7	449.2 ± 8.2
$\sigma_{\Delta M_{c.}}$, MeV/c^2	9.2 ± 3.2	11.6 ± 2.7	13.1 ± 4.6	10.8 ± 1.5	15.4 ± 5.6
$\sigma^{tail}_{\Delta M_{c.}}$, GeV/c^2	2.58 ± 1.17	1.69 ± 0.58	1.72 ± 0.91	1.88 ± 0.36	1.37 ± 0.91

Table 7.6: *Numbers related to the fit to simulated ΔM_{conv} presented in Fig. 7.16.*

Bin Width	5 MeV/c^2	7.5 MeV/c^2	9 MeV/c^2	10 MeV/c^2	12 MeV/c^2
$N_{\chi_{c1}}$	83 ± 48	81 ± 37	64 ± 37	59 ± 37	73 ± 37
$\langle \Delta M_{c.} \rangle_{\chi_{c1}}$, MeV/c^2	407.0 ± 5.0	402.3 ± 4.4	401.9 ± 4.3	403.0 ± 6.0	404.6 ± 4.5
$N_{\chi_{c2}}$	189 ± 66	162 ± 52	169 ± 58	165 ± 50	161 ± 50
$\langle \Delta M_{c.} \rangle_{\chi_{c2}}$, MeV/c^2	452.7 ± 5.4	448.3 ± 4.9	447.6 ± 4.8	448.7 ± 6.7	450.3 ± 4.9
$\sigma_{\Delta M_{c.}}$, MeV/c^2	11 $(fixed)$				
$\sigma^{tail}_{\Delta M_{c.}}$, GeV/c^2	3.49 ± 1.38	2.58 ± 1.00	2.59 ± 1.60	2.59 ± 1.05	2.67 ± 1.07
$N^{MC}_{\chi_{c1,2}}$	272 ± 82	243 ± 64	233 ± 69	224 ± 62	234 ± 62

The fit to the simulated ΔM_{conv} is shown in Fig. 7.16(a-e). As in the case of χ_{c2} matched signal it is performed using different histogram binnings. The variation of the relative efficiency (ρ_{12}) with the histogram bin sizes is shown in Fig. 7.16(g). The presented values of ρ_{12} are estimated using the numbers of χ_{c1} and χ_{c2} events from the given fit (Tabl. 7.6) and the value 0.370 ± 0.002 (7.10). As it can be seen, the relative efficiency

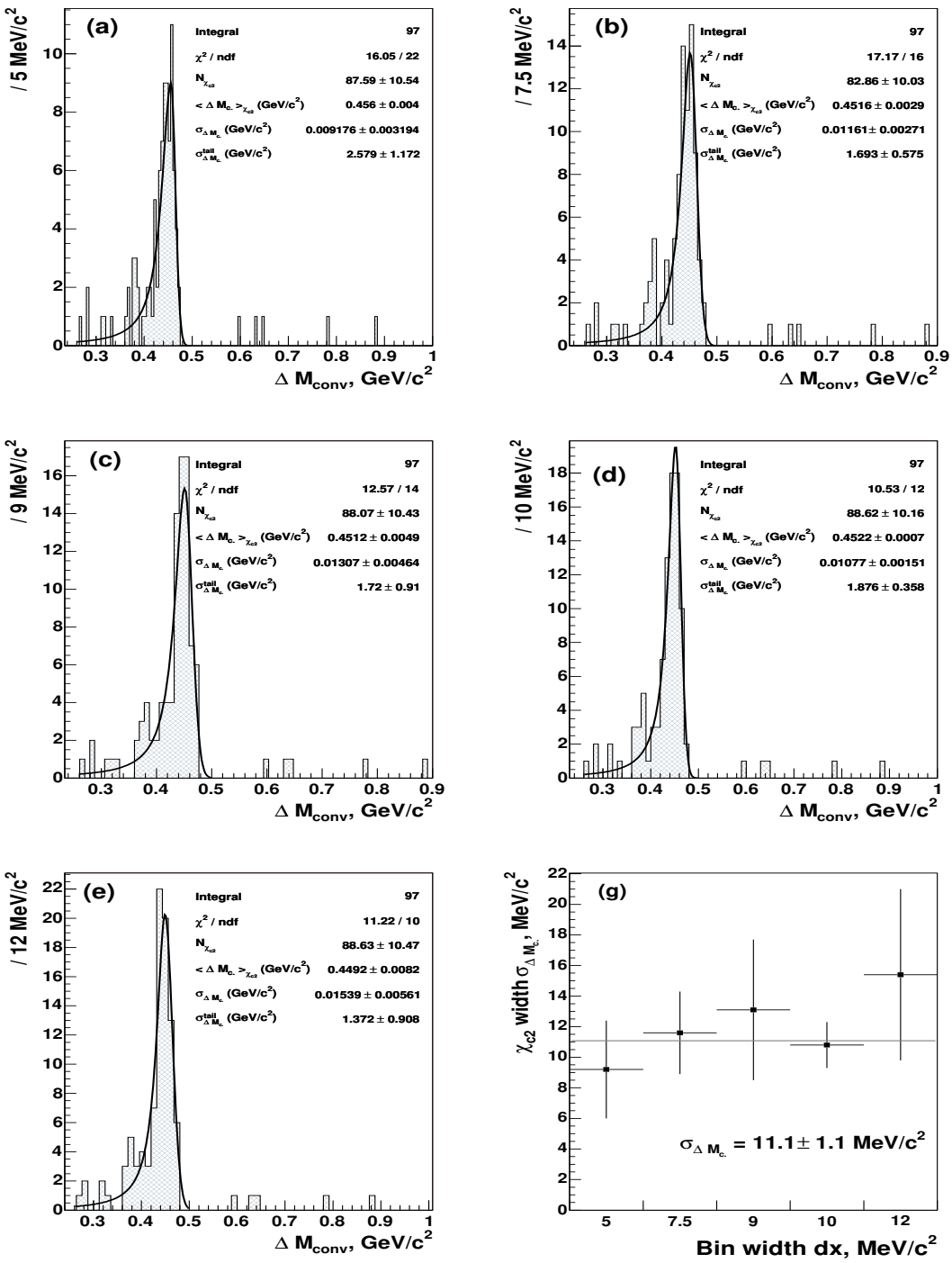

Figure 7.15: *The fit to the χ_{c2} matched signal according to parametrization (7.13). The fit is performed to distributions of different bin sizes (i.e. 5 MeV/c^2 (a), 7.5 MeV/c^2 (b), 9 MeV/c^2 (c), 10 MeV/c^2 (d) and 12 MeV/c^2(e)). In all cases, the number of particles obtained from the fit is compatible with the nominal number of χ_{c2} events (denoted as Integral on the plots). The values of the χ_{c2} width and position agree with each other within the errors. The same is true for radiative tail parameter (σ_{tail}). Plot (g) shows the width of the signal as a function of the bin size. Denoted value of $\sigma_{\Delta M_{c.}}$ is the mean value (horizontal line in plot (g)).*

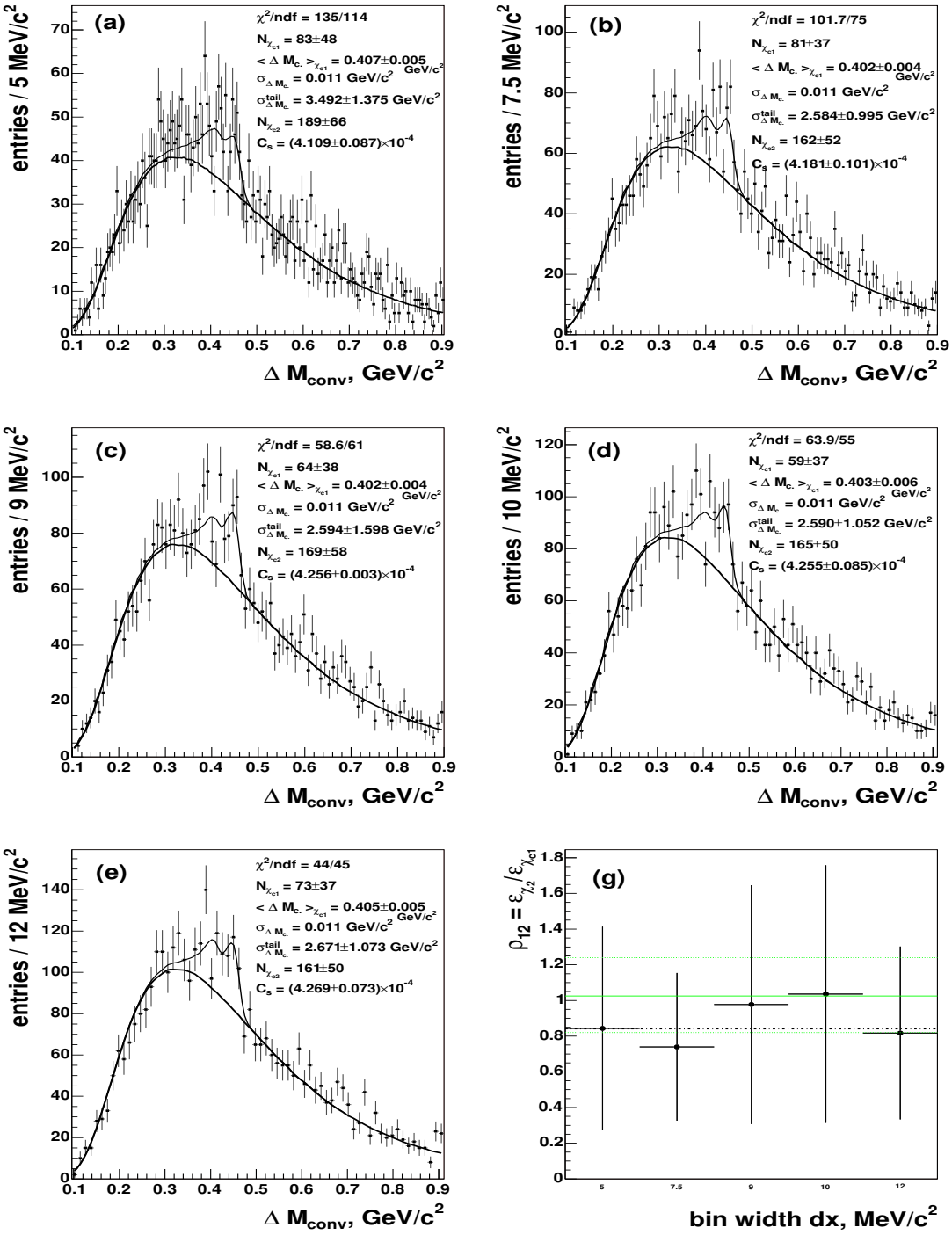

Figure 7.16: *Monte Carlo simulation: Fit to ΔM_{conv} for different bin sizes (i.e. 5 MeV/c^2 (a), 7.5 MeV/c^2 (b), 9 MeV/c^2 (c), 10 MeV/c^2 (d) and 12 MeV/c^2(e)) performed using parametrization (7.14). In the fit, the widths of the χ_{c1} and χ_{c2} peaks ($\sigma_{\Delta M_{c.}}$) are fixed to 11 MeV/c^2 (Fig. 7.15). Plot (g) shows the relative efficiency (ρ_{12}) as a function of the histogram bin sizes dx. In plot (g), the solid line represents the value $\rho_{12} = 1.03 \pm 0.21$ (7.12), while the doted lines show the associated statistical uncertainties. The dot-dashed line shows the average:* 0.84 ± 0.14.

exhibits a flat behavior with respect to bin size, being close to value 1.03 ± 0.21 (7.12) (solid line in Fig. 7.16(g)). The average (0.84 ± 0.14, dot-dashed line in the plot) deviates by about 18 % compared to value 1.03 ± 0.21 (7.12). This immutably translates to the uncertainty attributed to $\sigma_{\chi_{c1}}/\sigma_{\chi_{c2}}$, which will be taken into account when evaluating the systematic error.

7.3 The χ_{c1} and χ_{c2} signals

The fit to the ΔM_{conv} spectrum measured with di-muon data from run 2002-2003 is shown in Fig. 7.17. We do not observe any radiative tails associated with the signals in the measured ΔM_{conv} distribution, contrary to the Monte Carlo expectations. Therefore, the function representing the signal shape consists of two Gaussians only.

The absence of tails indicate apparent discrepancy between the simulated and measured signal distributions. However, this should not disturb our results, which are sensitive to the efficiency ratio ρ_{12}. The value of ρ_{12}, in turn, depends only on the Gaussian normalizations.

The background is evaluated using the event mixing. The characteristic width of the Gaussian is assumed to be the same for χ_{c1} and χ_{c2}. In the fit, it is fixed to the value of 11 (MeV/c^2), which we obtained from the simulations for χ_{c2} (Fig. 7.15(g)). The positions of the peaks are allowed to vary in the fit, but the difference between the two signals is constrained to the known $M_{\chi_{c2}} - M_{\chi_{c1}}$ mass difference of 45.7 (MeV/c^2) [20]. The background normalization is also allowed to vary.

Above the background we observe two bumps which we identify as χ_{c1} and χ_2 states of the charmonium system. The positions of χ_{c1} and χ_{c2}, obtained as a result of the fit, are

$$\begin{array}{l} \langle \Delta M_{c.} \rangle_{\chi_{c1}} = 422.7 \pm 3.1 \ MeV/c^2 \\ \langle \Delta M_{c.} \rangle_{\chi_{c2}} = 468.4 \pm 3.4 \ MeV/c^2 \end{array} \tag{7.16}$$

They are rather different from the world average values ($\Delta M^{pdg}_{\chi_{c1}} = 413.6 \ MeV/c^2$ and $\Delta M^{pdg}_{\chi_{c2}} = 459.3 \ MeV/c^2$). Both signals are equally shifted towards larger values of ΔM_{conv}. The reason for that can be a misalignment which is not properly taken into account during the reconstruction, and, thus, results in deviations in the $e^{\pm}$ momentum determination. In total, the fit gives

$$N_{\chi_{c1,2}} = 161 \pm 50 \tag{7.17}$$

$\chi_{c1,2}$ events, with the number of events obtained for χ_{c1} and χ_{c2} equal to

$$N_{\chi_{c1}} = 61 \pm 36 \ \text{ and } \ N_{\chi_{c2}} = 100 \pm 34,$$

respectively. The raw ratio of χ_{c1} and χ_{c2} is measured to be

$$\frac{N_{\chi_{c1}}}{N_{\chi_{c2}}} = 0.61 \pm 0.40 \tag{7.18}$$

for the full data sample.

7.4 Fraction of J/Ψ from χ_c decays

As a cross-check, we use the obtained result (7.17) to evaluate the fraction of J/Ψ produced through χ_c radiative decays, R_{χ_c}, defined by equation (6.4)

$$R_{\chi_c} = \frac{\sum_{i=1,2} N_{\chi_{ci}}}{N_{J/\Psi}\varepsilon_\gamma} \cdot \rho_\varepsilon, \quad \rho_\varepsilon = \frac{\varepsilon_{J/\Psi\ all}}{\varepsilon_{J/\Psi\ from\ \chi_c}}. \tag{7.19}$$

Here $\sum_{i=1,2} N_{\chi_{ci}}$ represents the χ_c signal, $N_{J/\Psi}$ is the number of reconstructed $J/\Psi \to \mu^+\mu^-$ decays, and ρ_ε is the efficiency ratio between all J/Ψ and J/Ψ from χ_c decays. Using the simulation results presented in Fig. 7.16, we can estimate the photon detection efficiency following the formula (6.5):

$$\varepsilon_\gamma = \frac{N^{MC}_{reco}(\chi_c)}{N^{MC}_{J/\Psi}}. \tag{7.20}$$

In this case, $N^{MC}_{reco} = N^{MC}_{\chi_{c1,2}}$ and is in the range (Table 7.6):

$$N^{MC}_{\chi_{c1,2}} \simeq 224 \div 272$$

The value of $N^{MC}_{J/\Psi}$ is equal

$$N^{MC}_{J/\Psi} = N^{\chi_{c1}}_{J/\Psi} + N^{\chi_{c2}}_{J/\Psi} = 45604 \pm 214$$

(see Table 7.4 for the values of $N^{\chi_{c1}}_{J/\Psi}$ and $N^{\chi_{c2}}_{J/\Psi}$). As a result we obtain a range for the photon detection efficiency $\varepsilon_\gamma \simeq (4.9 \div 5.9) \times 10^{-3}$. Substituting it in the equation (7.19) together with the numbers of observed χ_c, $N_{\chi_{c1,2}} = 161 \pm 50$ (7.17), and J/Ψ, $N_{J/\Psi} = 149,934$ (Fig. 7.3), events, we obtain the range for the R_{χ_c} ratio:

$$R_{\chi_c} \simeq 0.20 \div 0.23. \tag{7.21}$$

In the evaluation of R_{χ_c} we have used the following value for the efficiency ratio $\rho_\varepsilon = 1.03 \pm 0.01$ (Table 6.1). The obtained ratio (7.21) is in an excellent agreement with the measurement discussed in the previous chapter ($R_{\chi_c} = 0.177 \pm 0.048$ (6.7)), which justifies our considerations above.

7.5 Relative cross-section of χ_{c1} and χ_{c2}.

The main goal of the analysis presented in this chapter, is to measure the relative production cross-section of χ_{c1} and χ_{c2} states in pA collisions at $\sqrt{s} = 41.6\ GeV$. We define the ratio of prompt cross-sections for χ_{c1} and χ_{c2} as

$$\frac{\sigma_{\chi_{c1}}}{\sigma_{\chi_{c2}}} = \frac{N_{\chi_{c1}}\varepsilon_{\chi_{c2}} Br(\chi_{c2} \to \gamma J/\Psi)}{N_{\chi_{c2}}\varepsilon_{\chi_{c1}} Br(\chi_{c1} \to \gamma J/\Psi)} \tag{7.22}$$

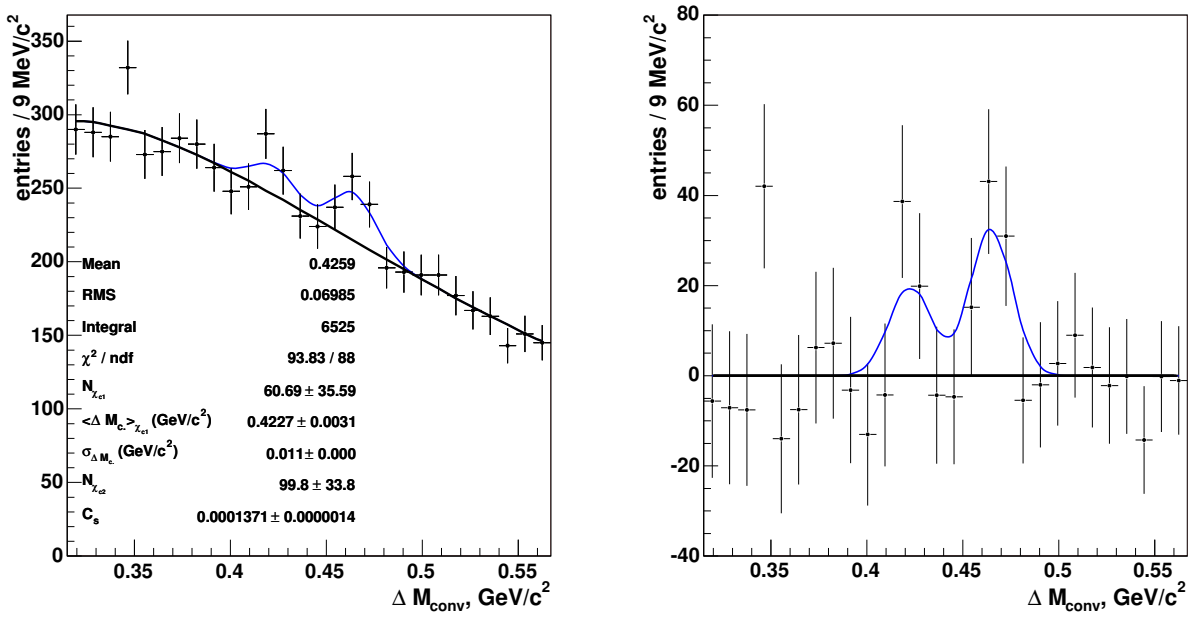

Figure 7.17: *(a) Mass difference distribution, $\Delta M_{conv} = M(J/\Psi(e^+e^-)) - M(e^+e^-)$, obtained using the entire di-muon trigger data sample from 2002-2003 run. The fit is done using Gaussian parametrization for χ_{c1} and χ_{c2} signals and the background estimate evaluated using the event mixing technique. In the fit: the widths of both states, $\sigma(\chi_{c1})$ and $\sigma(\chi_{c2})$, are assumed to be the same and are fixed to the value of 11 MeV; the distance between two peaks is fixed to the known value of the mass difference between two states, $M(\chi_{c1}) - M(\chi_{c2})$, which is about 45.7 (MeV/c^2) [20]; the normalization of the background (C_s) is left as free parameter. (b) The ΔM_{conv} distribution with subtracted background. The smooth line drawn through the data points correspond to the fit in (a) without the background term.*

where $\sigma(\chi_{ci})$ is the production cross-section, $N_{\chi_{ci}}$ is the number of observed events, $\varepsilon_{\chi_{ci}}$ is the overall efficiency, whereas $Br(\chi_{ci} \to \gamma J/\Psi)$ is the branching ratio into the $\gamma J/\Psi$ final state for each of the χ_{c1} and χ_{c2} states; $i = 1, 2$.

The observed ratio $N_{\chi_{c1}}/N_{\chi_{c2}}$ (7.18) is equal to

$$N_{\chi_{c1}}/N_{\chi_{c2}} = 0.61 \pm 0.40.$$

According to the Monte Carlo simulations, the overall efficiency ratio is (see equation 7.12):

$$\varepsilon_{\chi_{c2}}/\varepsilon_{\chi_{c1}} = 1.03 \pm 0.21.$$

The value of

$$\frac{Br(\chi_{c2} \to \gamma J/\Psi)}{Br(\chi_{c1} \to \gamma J/\Psi)} = 0.64 \pm 0.08$$

is taken from the the most recent review of particle physics [20].

Using these numbers, we estimate the ratio of χ_{c1} mesons to χ_{c2} mesons, produced in proton-nucleus interaction at HERA-B, to be

$$\frac{\sigma_{\chi_{c1}}}{\sigma_{\chi_{c2}}} = 0.40 \pm 0.27_{stat} \pm 0.14_{syst}, \tag{7.23}$$

where the first error is statistical, whereas the second is systematical. The systematical error is mainly due to the ambiguities in the efficiency determination (18 %), as mentioned previously, and the fit to the measured ΔM_{conv} distribution (27 %). The latter has been studied by changing the fit range as well as from the comparison to the output of the fit in which the width of the Gaussians has been considered as a free parameter. The contribution to the systematical error due to the uncertainty in the branching ratio is 12.5 %.

Table 7.7: *Experimental results on relative production cross-section for χ_{c1} and χ_{c2} states of charmonium. The listed results obtained in pA, pp, $p\bar{p}$, πp and πA experiments referred in [49, 50].*

.

Experiment	Interaction	$\sqrt{s}$, GeV	$\sigma(\chi_{c1})/\sigma(\chi_{c2})$
proton-nucleus collisions			
E610	pBe	19.4, 21.7	0.24 ± 0.28
E705	pLi	23.8	$0.08^{+0.25}_{-0.15}$
E771	pSi	38.8	0.53 ± 0.21
pp and $p\bar{p}$ collisions			
CDF	$p\bar{p}$	1800	1.04 ± 0.31*
πp and πA collisions			
WA11	$\pi^- Be$	16.8, 18.7	0.69 ± 0.24
E610	$\pi^- Be$	18.9	0.96 ± 0.64
E369	$\pi^- Be$	20.6	1.11 ± 0.49*
E705	$\pi^- Li$	23.8	$0.52^{+0.57}_{-0.27}$**
E672/706	$\pi^- Be$	31.1	0.57 ± 0.19

* Obtained using the $\sigma_{\chi_{c2}}/\sigma_{\chi_{c1}}$ measurement.
** Average for π^- and π^- data.

The presented result agrees well with the previous results (see Fig. 7.18) obtained in fixed target experiments [11], operating at lower energies. It appears to prefer the dominant χ_{c2} production compared to χ_{c1} in the proportion 5 : 2, which is consistent with the spin-symmetry expectation:

$$\frac{\sigma_{\chi_{c1}}}{\sigma_{\chi_{c2}}} \approx \frac{(2J+1)_{\chi_{c1}}}{(2J+1)_{\chi_{c2}}} = \frac{3}{5}$$

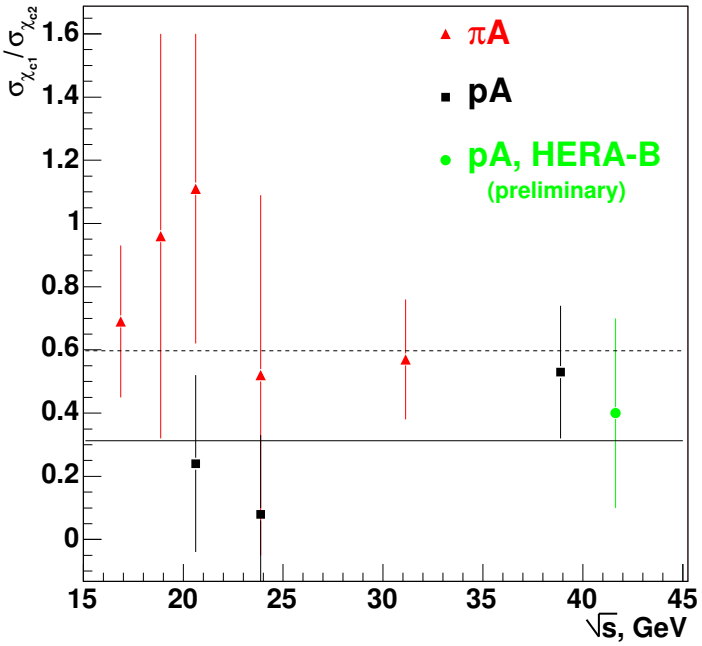

Figure 7.18: *Experimental results on $\sigma_{\chi_{c1}}/\sigma_{\chi_{c2}}$. Triangles depict the ratio measured in $\pi-$nucleus collisions, squares show the results from pA interactions and the circle represent our result (7.23), obtained in pA collisions at $\sqrt{s} = 41.6GeV$. The values obtained in the previous experiments are listed in Table 7.7. The lines represent the average for pA results (solid) and for all results (dashed), including CDF measurement [106].*

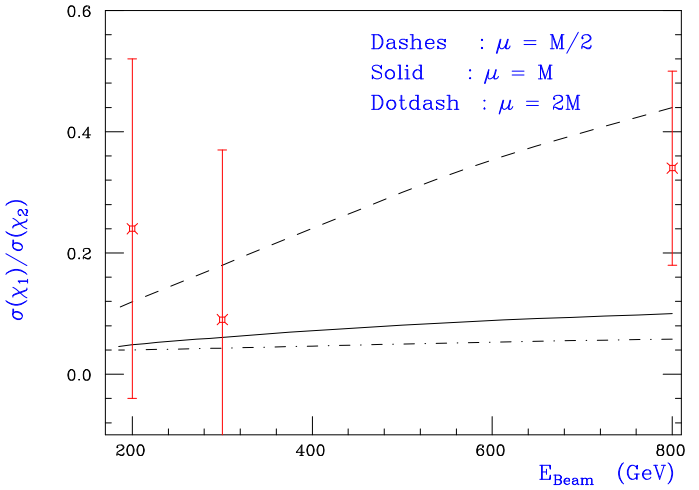

Figure 7.19: *Ratio of χ_{c1} to χ_{c2} production cross-sections in proton-nucleon collisions a a function of beam energy. The experimental values correspond to E610 measurement in pA collisions, E705 measurement in pA collisions and an average comprising E610 pA result and E705 pA, πA results and E771 pA result (see Tabl. 7.7). The plot is taken from reference [13].*

It also tolerates some theoretical predictions for fixed target energies based on NLO NRQCD[11] calculations [6, 13], if extrapolated to 920 GeV (see Fig. 7.19).

On the contrary, the values of $\sigma_{\chi_{c2}}/\sigma_{\chi_{c1}} = 0.96 \pm 0.29$ (not shown in Fig. 7.18) measured at $\sqrt{s} = 1.8\ TeV$ [106] prefer an approximately equal production of the two χ_{c1} and χ_{c2} states, which support some recent NRQCD calculations for the cross-section ratio in $p\bar{p}$ collisions, giving the value of 1.1 ± 0.2 [9, 13]. At first glance, this seems to differ with our measurement. However, the CDF result [106] was obtained in $p\bar{p}$ collisions at much higher energies, i.e $\sqrt{s} = 1.8\ TeV$. Moreover, the kinematical acceptances of two experiments (i.e. CDF and HERA-B) are in rather different ranges. Therefore, the comparison between results obtained at different center of mass energies is not straightforward, despite significant theoretical efforts to understand charmonium production in that environment [6, 28].

The measured $\sigma_{\chi_{c1}}/\sigma_{\chi_{c2}}$ ratio (7.23) is another experimental point obtained in pA interactions at $\sqrt{s} = 41.6\ GeV$. It can be considered as an additional input in constraining non-perturbative parameters present in the theoretical calculations [4, 5, 6, 8], although the error is large. Besides, our measurement may be helpful for better understanding of the polarization properties of χ_c and J/Ψ, since the calculations of the χ_{c1} to χ_{c2} production ratio are based on the same principles as those behind the polarization[12] predictions [13].

[11] See chapter 2, section 2.4 for details about charmonium production.

[12] See chapter 2, section 2.4 for definition.

Chapter 8

Conclusion

The work presented in this thesis has been done to study the phenomena of charmonium production in proton-nucleus collisions at HERA-B.

The importance of charmonium study is twofold. It is a nice look inside the QCD dynamics, which was used extensively to enhance our understanding of strong force, one of the four known fundamental interaction. On the other hand it has an engineering aspect. The J/Ψ meson, $^3S_1$ state of charmonium system, is often used as a tagging tool. Its rather high yield and relatively high branching ratio of the leptonic decays, $Br(J/\Psi \to l^+l^-) \sim 6\%$, $l = e, \mu$, are very suitable to be used as tag in studies of new phenomena in the less explored domains of Standard Model as well as in searches for new physics. However, the mechanism of charmonium production in hadron-hadron collisions is far from being understood in every detail, such that the uncertasinty related to J/Ψ production will make it difficult to make a solid statement about novel phenomena.

The pair of charm-anticharm quarks, which consequently develops into a charmonium state, can be produced either via color-singlet or color-octet mechanisms [9, 28]. The different theoretical models discuss the production of $c\bar{c}$ bound states treating differently the importance of the either of modes (i.e. color-octet and color-singlet). This often leads to contradictory predictions, which could be only resolved by reliable measurements. Therefore, it is very important to carry exhaustive tests of charmonium production, using various experimental facilities, colliding pions, protons, photons, electrons with each other as well as with nuclei) and studying rates, cross sections, polarizations, dependencies on the beam, target and collision energy, and so on.

In the present work we have reported on the study of the relative production of charmonium states produced in the collisions of 920 GeV protons with nuclear targets. The analyzed data set accumulated using different target materials correspond to about 300,000 J/Ψ, reconstructed in both di-muon and di-electron channels in the range between $x_F^{J/\Psi} \simeq -0.35$ and $x_F^{J/\Psi} \simeq 0.15$. We measured the fraction of J/Ψ produced via χ_c radiative decays in collisions of protons with carbon, titanium and tungsten targets using all di-muon data. For proton-carbon interaction we also estimated the R_{χ_c} ratio using a small set of di-electron data, which comprise about 12 % of all available statistics. The obtained results are summarized in Table 6.2. We have not observed any scaling of

R_{χ_c} ratio with the atomic number A (Fig. 6.1). This implies that the nuclear medium affect both χ_c and J/Ψ in a similar manner. We have also extended the study of R_{χ_c} A-dependence by measuring dependences of R_{χ_c} on $x_F^{J/\Psi}$ for carbon and tungsten di-muon data in the range $-0.18 \leq x_F^{J/\Psi} \leq 0.06$ (see Fig. 6.5 and 6.6). The similarity between the two differential spectra demonstrates alike nuclear dependence for J/Ψ and χ_c. This is in accord with the Color Evaporation Model (CEM) [8, 32] predictions. On the contrary, Non-Relativistic QCD (NRQCD) [6, 5, 32] predicts different A-dependences for J/Ψ and χ_c. However, a quantitative test of NRQCD predictions cannot be performed, as the predicted variations are of order of the experimental uncertainties in the given kinematical range. To arrive to such a goal would require a larger set of more precise data.

We have also presented the combined result for the entire di-muon data sample:

$$R_{\chi_c} = 0.177 \pm 0.026_{stat} \pm 0.032_{sys}, \tag{8.1}$$

where the first uncertainty is statistical only, whereas the second uncertainty is systematic. Our result for R_{χ_c} is compatible with the previous measurements [49, 50, 34] and the predictions based on the NRQCD factorization approach [5] are close to it (Fig. 6.7). This indicates that NRQCD may be the right concept for charmonium production description. However, with the present uncertainties CEM cannot be ruled out yet. On the other hand, Color-Singlet Model (CSM) [4] predicts values for R_{χ_c} which are significantly larger (Fig. 6.7).

In addition, the study of the relative production of χ_{c1} and χ_{c2} states has been performed. In this part of the analysis, we have used the photon pair conversion phenomenon to reconstruct photons. This has allowed to separate two χ_c states. Using all di-muon triggered data we reconstructed 61 ± 36 χ_{c1} and 100 ± 34 χ_{c2} mesons, although the errors are large. Using the efficiencies obtained from the simulations we have measured the ratio $\sigma_{\chi_{c1}}/\sigma_{\chi_{c2}}$:

$$\sigma_{\chi_{c1}}/\sigma_{\chi_{c2}} = 0.40 \pm 0.27_{stat} \pm 0.14_{syst}, \tag{8.2}$$

where the first error is statistical, whereas the second one is systematic. Our measurement (8.2) reveals the dominant χ_{c2} production compared to χ_{c1} in pA collisions at $\sqrt{s} = 41.6GeV$. Albeit large uncertainties, it may provide some information for further understanding of the production mechanisms. The experimental value (8.2) comply with the previous measurements obtained in fixed-target experiments [11] (see Fig. 7.18). It agrees also with the theoretical expectation for fixed-target energies based on NRQCD calculations [13, 6].

In summary, a measurement of the ratio of J/Ψ produced via radiative χ_c decays to all produced J/Ψ allows one to quantitatively test different models of quarkonium production. We present a new result based on data collected with the HERA-B spectrometer for the fraction of J/Ψ originating from radiative decays of χ_{c1} and χ_{c2} states produced in pA interactions. We have also measured relative production of χ_{c1} and χ_{c2} states of charmonium system. Our results reveal weak points in CSM, implying that the color-octet contribution is necessary for a consistent description of the charmonium production in pA interactions. The measured integrated ratios R_{χ_c} and $\sigma_{\chi_{c1}}/\sigma_{\chi_{c2}}$ are rather consistent

with the NRQCD predictions. On the other hand, the flat R_{χ_c} dependence on A and resemblance between the x_F differential spectra of R_{χ_c} obtained for different A shows a good agreement with the CEM assumption of a pre-resonant color-octet state passing through the target [8, 29]. To make a more conclusive statement on which mechanism governs the charmonium production would again require more data of better precision.

At the same time, the analysis has left some space to strengthen our measurements. First of all, a precise measurement of the integrated R_{χ_c} and $\sigma_{\chi_{c1}}/\sigma_{\chi_{c2}}$ ratios as well as R_{χ_c} differential distributions using the entire di-electron data set would be a demonstration of the reliability of the results.

Secondly, the precision of the $\sigma_{\chi_{c1}}/\sigma_{\chi_{c2}}$ measurement would be greatly improved if larger Monte Carlo statistics was used. In addition, an improvement might be achieved by recalculating track parameters of the selected e^+e^- pairs, using constraints consistent with the photon conversion hypothesis.

Finally, a study of the polarization of χ_c might provide a more exclusive test for the production mechanism of the charmonium production [9, 13, 107]. It could be performed by examining the angular distribution of the photon in the χ_c rest frame. However, the isolation of the χ_c photon from the combinatorial background associated to the χ_c signal would present a particular challenge in this case.

Perhaps in the nearest future HERA-B analyses will be able to provide such information. For any improvements beyond that, further studies based on larger, more precise data are necessary. This includes the extension of the existing kinematical limits of experimental results as well as other, more exclusive tests.

Appendix A

K_s^0 studies

A summary of the K_s^0 analysis[1] in the minimum bias data taken in April 2000 is presented. Using the $K_s^0 \to \pi^+\pi^-$ signal we estimate the ghost-rates as well as the efficiency. Finally we extract the $K^0/\bar{K}^0$ cross-section.

The data shown are mainly from run 14577 (carbon wire $i2$ and runs 14551-14554 (titanium wire $i1$). The runs were taken at a nominal interaction rate of 5 MHz. The data are compared to a simulation based on the event generator FRITIOF [78]. The number of simulated interactions per event follows a Poisson distribution with the mean value $\mu = 0.5$.

A.1 Introduction

The HERA-B detector is a fixed target spectrometer designed for research in the field of heavy quark physics: charm and, to a lesser extent, bottom. The spectrometer is divided into a vertex detector (VDS), employing silicon strip technology for precision measurement of vertices, and a main tracker, dedicated to tracking, momentum measurement and triggering. The pattern tracker, tracking devices placed between the magnet and the Ring Imaging Cherenkov Detector (RICH), is the most important component of the main tracker. It consists of four superlayers of outer (PC01-PC04) and inner (MS10-MS13) tracking devices (Fig.1), sufficient for standalone pattern recognition. The outer tracker (OTR) is built from honeycomb drift chambers with a tube diameter of 10 and 5 mm, for the outer and inner sectors, respectively. The inner tracker (ITR) uses Micro-Strip Gaseous Chambers with a Gas Electron Multiplier (MSGC-GEM). In a first step, tracks are reconstructed in the pattern tracker, according to the general concept of HERA-B. In the second step, the track segments found in the pattern tracker are propagated upstream trough the magnet. The resulting track is then matched to the segments reconstructed in the vertex detector. There exists a considerable amount of low-momentum tracks stemming from secondary interactions and in-flight decays. These tracks are strongly affected by multiple scattering. Together with a large track density this makes the probability

[1] prepared in March 2002.

of track-overlap relatively high. A reconstruction algorithm has to cope with clusters of hits from several nearby tracks. Consequently, the resolution of the left-right ambiguity becomes a difficult task. The goal of the present study is to answer two questions:

1. How large is the ghost-rate in the decay $K_s^0 \to \pi^+\pi^-$?

2. What is the corresponding track efficiency?

For this purpose a Monte Carlo sample[2] of minimum bias events with 0.5 interactions per event (Poisson distributed) has been used. The detector has been simulated using a scenario for the run 2000 detector geometry and performance. The following efficiencies and resolutions were used for the OTR and ITR:

$$\begin{array}{lll} \text{hit efficiency :} & \varepsilon_{OTR}^{hit} = 90\% & \varepsilon_{ITR}^{hit} = 86\% \\ \text{hit resolution :} & \sigma_{OTR}^{hit} = 500\mu m & \sigma_{ITR}^{hit} = 200\mu m \end{array} \tag{A.1}$$

The is referred to as "realistic" scenario.

The results are compared to a more "optimistic" scenario with

$$\begin{array}{lll} \text{hit efficiency :} & \varepsilon_{OTR}^{hit} = 95\% & \varepsilon_{ITR}^{hit} = 95\% \\ \text{hit resolution :} & \sigma_{OTR}^{hit} = 500\mu m & \sigma_{ITR}^{hit} = 200\mu m \end{array} \tag{A.2}$$

The evaluation of the ghost-rate level in K_s^0 was based on the correspondence: *reconstructed track* $\to$ *Monte Carlo particle*. The assignment was performed by means of hit matching [105]: a reconstructed track is assigned to a generated particle if the largest fraction - typically 70 % - of the reconstructed hits was caused by this particle. No boundary condition was requested during that procedure. The 70 % criterion was only used to sort out the selected events as described below.

The efficiency estimation was based on the correspondence *Monte Carlo particle* $\to$ *reconstructed track*. It is basically the same procedure as in the ghost level evaluation above. The assignment was done by using the hit matching technique. In this case, however, the momentum of a simulated particle is compared to the momenta of the corresponding reconstructed tracks. In order to avoid multiple assignment, only the best choice was considered.

A.2 K_s^0 signal

The two pion decay of the K_s^0 meson is reconstructed employing the VDS and the pattern tracker. The $\pi^+\pi^-$ invariant mass for four target materials is shown in Fig. A.2. Two oppositely charged tracks were required to come form a common vertex. The distance

[2]Monte Carlo samples (carbon: /acs/mc3/99.1013/10000/* and titanium: /acs/mc3/99.1014/inner1/*) were simulated with ARTE-03-08-r2, using geometry version 99.1013 (99.1014) for carbon (titanium) wire and were reconstructed with ARTE-03-09-r3 using the corresponding 99.1013 (99.1014) geometry versions. RANGER was used for pattern recognition. Magnet chambers were included in the reconstruction algorithm.

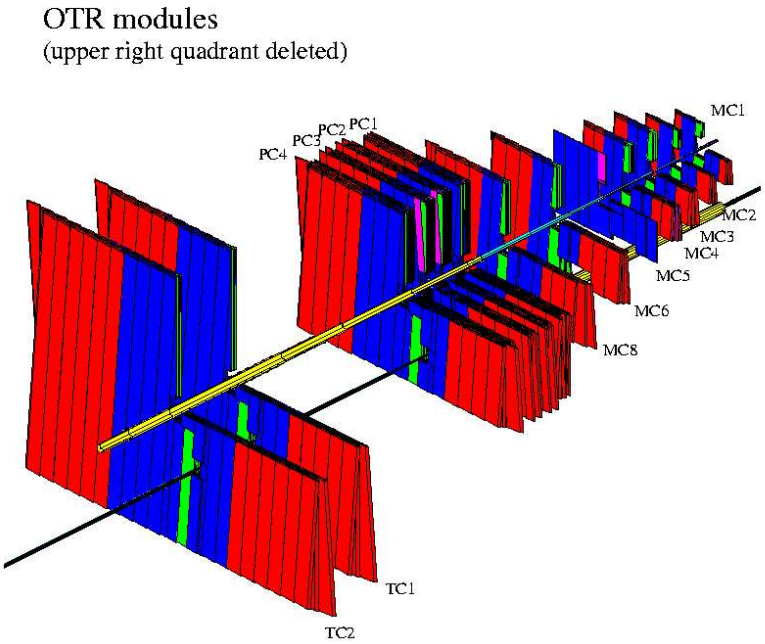

Figure A.1: *3D view of superlayers of the OTR [61].*

between two tracks (at the vertex position) must be less less than 0.4 mm (closest distance approach or CDA cut). The transverse distance to the primary vertex must be smaller than 0.6 mm (impact parameter cut). The reconstructed vertex must be located at least 1.3 mm (in the kaon CMS) downstream of the primary vertex (decay length cut). In addition the standard clone removal procedure, based on using clone flags for the VDS and the main tracker (inner + outer), was used. Both tracks were assigned the pion mass for the invariant mass calculation. The selection criteria are summarized in Table A.1. The parameters concerning reconstructed K_s^0 are collected in Tables A.2

Table A.1: *Standard selection cuts used for $K_s^0 \to \pi^+\pi^-$ reconstruction.*

cut	value
CDA	$< 0.4mm$
Impact Parameter	$< 0.6mm$
Decay Length	$> 1.3mm$
Minimum hits in VDS	≥ 5
Minimum hits in OTR	$(N_{ITR}^{hits} + N_{OTR}^{hits} \geq 10)$
	or $(N_{OTR}^{hits} \geq 10)$
	or $(N_{OTR}^{hits} \geq 7)$
Clone removal	

and A.3. The width of the measured mass peak is approximately 2 MeV higher than the Monte Carlo expectation (see Fig.A.3). The position of the mass peak is shifted by

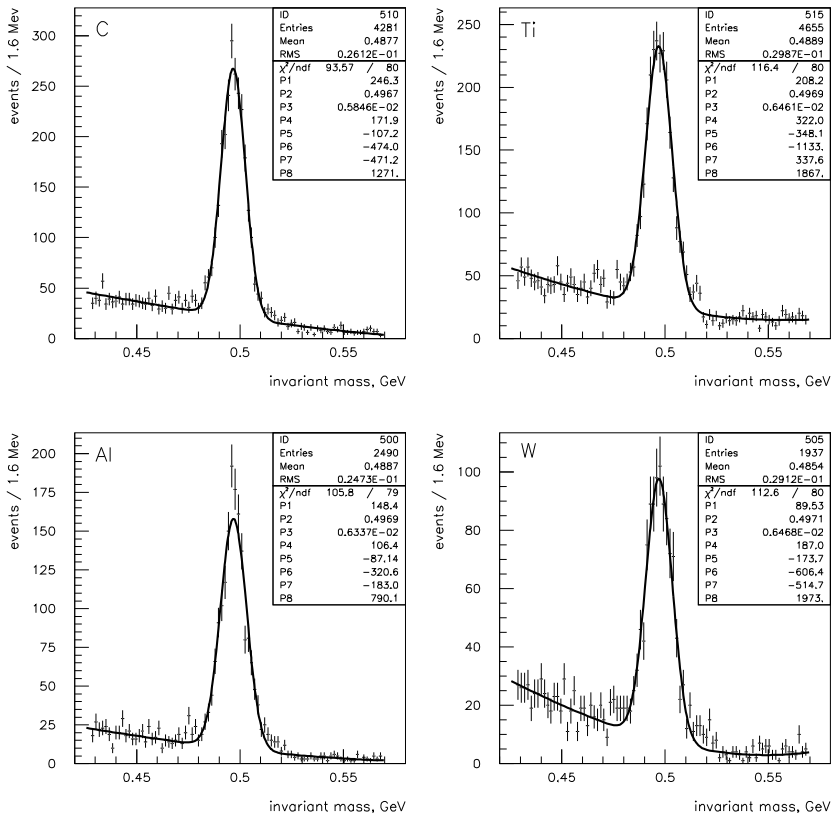

Figure A.2: *K^0_s reconstructed for four different materials: C - carbon (i2, run 14577); Ti - titanium (i1, runs 14551-14554); Al - aluminum (a2, runs 14605,14606) and W - tungsten (b2, runs 14639,14644) obtained from the minimum bias data taken in April 2000. The invariant mass distribution is fitted with a Gaussian (signal) and, a 5^{th} order polynomial (background).*

approximately 2 MeV to a lower mass region, relative to the simulated signal. The reason for these differences between data and Monte Carlo is not understood. In addition, there are discrepancies, in the signal/background ratio for some given cuts. The last indicate that the multiplicity is not properly reproduced in the simulation while there is a good agreement for the K^0_s inclusive distributions, as will be discussed in the next section.

A.3 Data - Monte Carlo comparison

Kinematical quantities (transverse momentum, p_T, momentum, p, Feynman variable, x_F, and pseudorapidity, η of the K^0_s, given by equation (A.3), as well as momentum and transverse momentum of the outgoing pions) were used in order to compare the Monte

Table A.2: *Measured K_s^0 signal and its parameters.*

target	# kaons	S/B (for 3σ)	mass, MeV	σ, MeV
C	2256 ± 67	4.63 ± 0.16	496.7 ± 0.1	5.8 ± 0.1
Ti	2108 ± 69	3.26 ± 0.13	497.0 ± 0.2	6.5 ± 0.2
Al	1473 ± 58	5.48 ± 0.35	496.9 ± 0.2	6.3 ± 0.2
W	907 ± 45	3.85 ± 0.49	497.1 ± 0.3	6.5 ± 0.3

Table A.3: *Simulated K_s^0 signal and its parameters.*

target	# kaons	S/B (for 3σ)	mass, MeV	σ, MeV
C	822 ± 41	8.0 ± 0.5	498.7 ± 0.2	3.9 ± 0.3
C	460 ± 29	6.1 ± 0.7	498.1 ± 0.2	3.8 ± 0.2

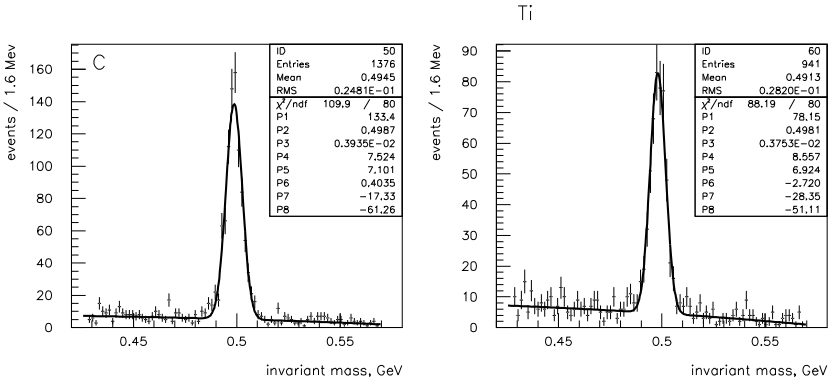

Figure A.3: *K_s^0 reconstructed Monte Carlo for two different materials: C - carbon (i2); Ti - titanium (i1). The invariant mass distribution is fitted with a Gaussian (signal) and a 5^{th} order polynomial (background). The plots were obtained with the "realistic" scenario (Eq.(A.1)).*

Carlo simulations to the measured data.

$$\begin{aligned} p_T &= \sqrt{(p_x^+ + p_x^-)^2 + (p_y^+ + p_y^-)^2} \\ p &= \sqrt{(p_x^+ + p_x^-)^2 + (p_y^+ + p_y^-)^2 + (p_z^+ + p_z^-)^2} \\ x_F &= \frac{2p_l^{cm}}{\sqrt{s}} = \frac{1}{m_p}\left[p_l - E\sqrt{\frac{E_{beam}-m_p}{E_{beam}+m_p}}\right] \\ \eta &= -log\left(tan\left(\frac{\theta}{2}\right)\right) \end{aligned} \tag{A.3}$$

where $p_i^{\pm}$, $(i = x, y, z)$ are components of the track momenta; p_l and E are the longitudinal momentum and energy of the kaon in the lab frame, respectively; p_l^{cm} is the longitudinal momentum of the kaon in the center of mass (CM) frame; $\sqrt{s}$ is the CM energy; θ is the angle between the beam direction and the direction of the particle; m_p is the proton mass; E_{beam} is the beam energy in the lab frame.

The comparison for two materials (carbon and titanium) shows quite good agreement for the distributions corresponding to K^0_s signal (Fig. A.5,A.7,A.8,A.10). The same analysis for the background distributions, obtained from the "K^0_s" side bands shows that the positively charged tracks behave in a different way from the tracks with negative charge (Fig. A.6,A.9).

The signal distributions (Fig. A.5,A.7,A.8,A.10) were obtained by applying the following cuts (in addition to those described in the Table A.1):

$$\begin{array}{c} decay\ length\ >\ 5\,mm \\ max(p^+/p^-, p^-/p^+) < 4. \end{array} \tag{A.4}$$

The resulting $\pi^+\pi^-$ invariant mass distribution obtained by applying the cuts above are shown in Fig. A.4. The background distributions, compared in Fig. A.6 and A.9, were

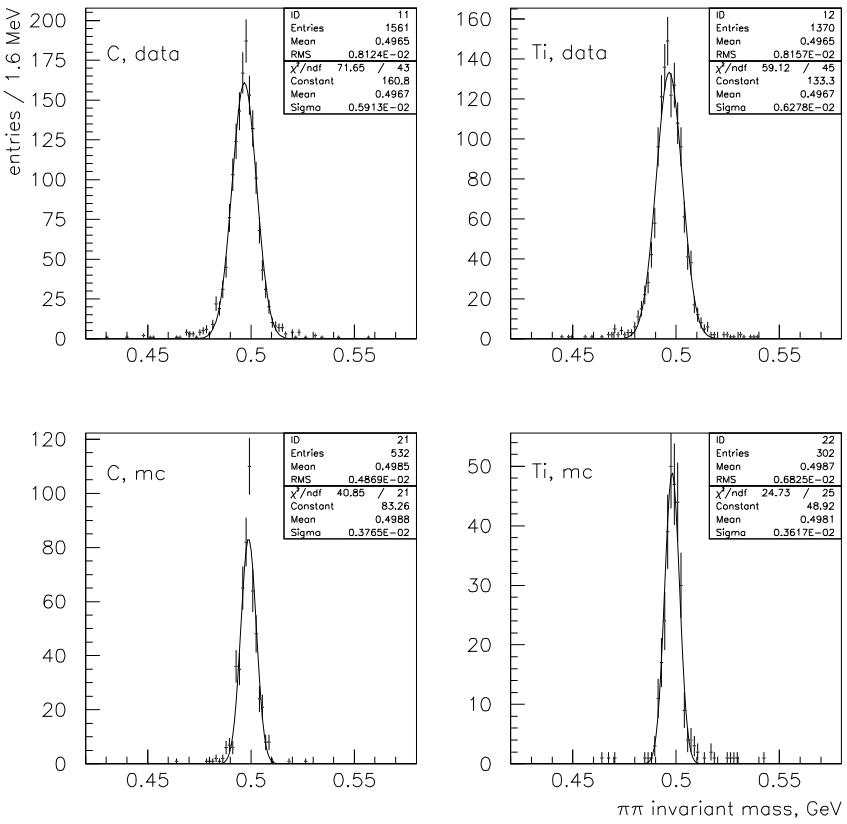

Figure A.4: *$\pi^+\pi^-$ invariant mass distribution obtained with the application of (A.4) in addition to the standard selection cuts, described in Table A.1 are presented for carbon (C) and titanium (Ti) targets in case of data (data) and Monte Carlo (MC). Monte Carlo distributions were obtained with the "realistic" scenario (Eq.(A.1)).*

obtained using the "K_s^0" side bands (outside 3σ) by employing only standard selection cuts, described in Table A.1.

The comparison *data - Monte Carlo*, shown in Fig. A.5-A.10, is done for the "realistic" detector simulation scenario (see Eq.(A.1)). The corresponding distributions for the "optimistic scenario (Eq.(A.2)) are not expected to be different.

A.4 Ghost Rates in $K_s^0 \to \pi^+\pi^-$ decay

The standard way to evaluate the ghost level is based on the hit matching technique, where a 70 % criterion is applied, as described in [105]. The ghost rate in $K_s^0 \to \pi^+\pi^-$ appears to be of order 18 (36) % in the pattern tracker for the carbon (titanium) target material. But looking at the invariant mass distribution of two tracks one of which does not satisfy the 70 % condition, it is found that they contribute to the signal (Fig. A.11, lower plot). That is a clear indication that the value obtained by the direct application of "70 % criterion" does not reflect the real number. Below that limit there subsists some mixture of physical tracks together with ghosts. It is possible to make an evaluation of real ghost rates by counting sorted tracks as a function to the 70 % limit. Table A.4 presents a summary.

Table A.4: *Different kinds of tracks in according to 70 % criterion.*

fraction of hits	kind of track	matched to
$> 70\%$ (physical tracks beyond any doubts)	good	$\pi^\pm$ from $K_s^0 \to \pi^+\pi^-$
		$\mu^\pm$ from $K_s^0 \to \pi^+\pi^-$, $\pi \to \mu\nu$
	other	a simulated track
$> 70\%$ (ghost candidates)	false ghost	$\pi^\pm$ from $K_s^0 \to \pi^+\pi^-$
		$\mu^\pm$ from $K_s^0 \to \pi^+\pi^-$, $\pi \to \mu\nu$
	other/ghost	a simulated track or ghost

The definition were as follows:

- "*good*": reconstructed track matched to K_s^0 track following the 70 % criterion (including the decay chain $\pi \to \mu\nu$).
- "*other*": reconstructed track matched to a simulated track (but not the pion or muon from the K_s^0 decay or subsequent pion decay) following 70 % criterion.
- "*false ghost*": reconstructed track matched to a simulated track with a fraction of common hits less then 70 % but contributes to the peak (e.g. it is supposed to be a physical one).
- "*other/ghost*": reconstructed track which does not satisfy the 70 % criterion and does not contribute to the signal.

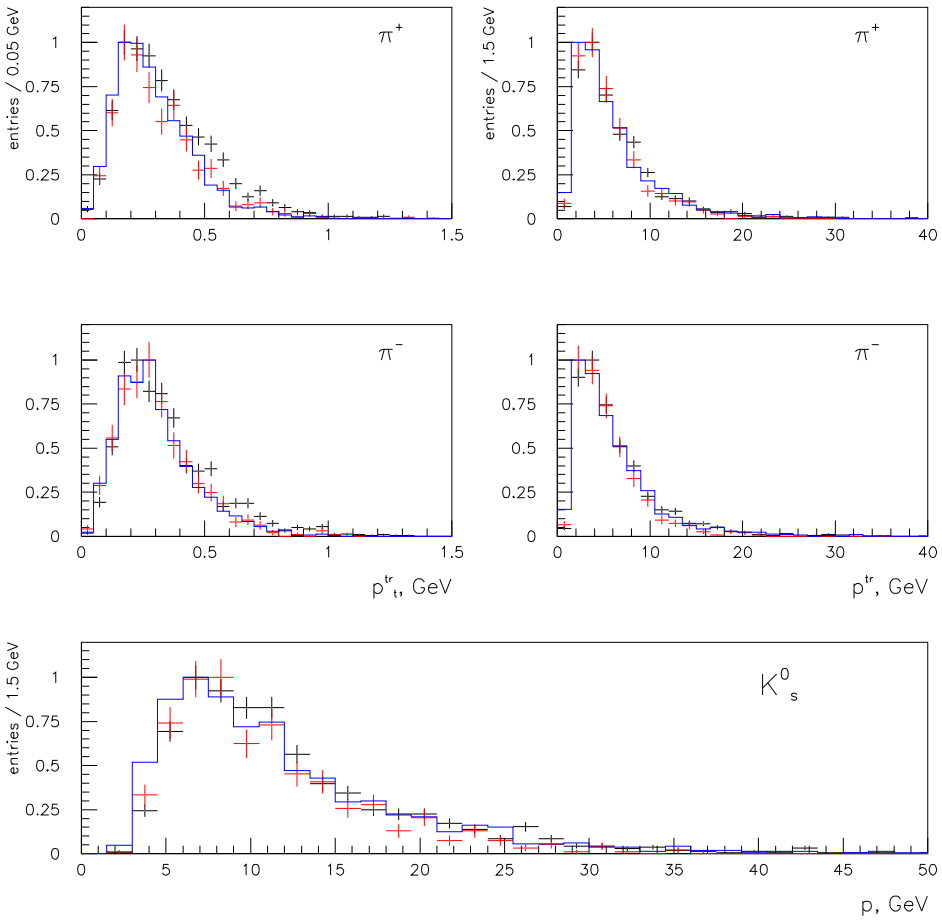

Figure A.5: *Transverse momentum of the tracks, p_t^{tr} , momentum of the tracks, p^{tr} , and reconstructed K_s^0 momentum, p, are presented for reconstructed data (black markers), Monte Carlo data simulated and reconstructed (light markers) and generator quantities (histogram) of carbon wire $i2$.*

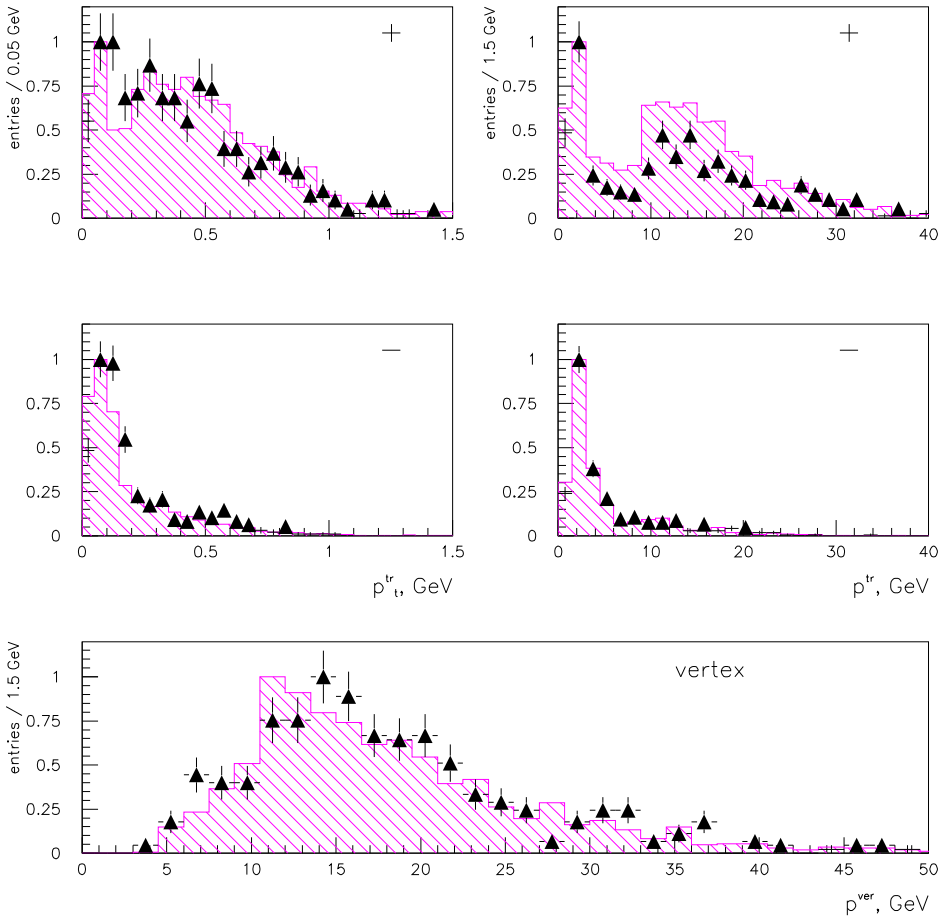

Figure A.6: *Transverse momentum of the tracks, p_t^{tr} , momentum of the tracks, p^{tr}, and reconstructed momentum, p, are presented for reconstructed data (markers), Monte Carlo data simulated and reconstructed (histogram) of carbon wire $i2$. Distributions correspond to the background events from "K_s^0" sidebands (outside 3σ region).*

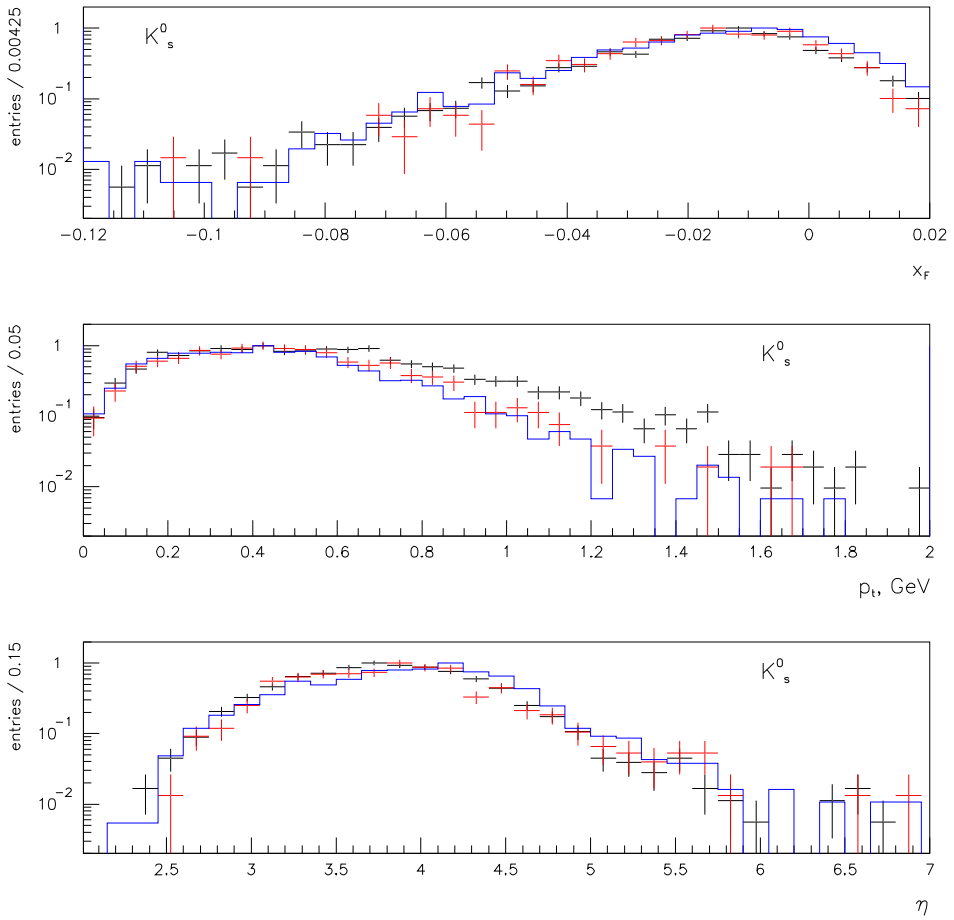

Figure A.7: *Feynman x, x_F, transverse momentum, p_t and pseudorapidity , η, of K^0_s are presented for reconstructed data (black markers), Monte Carlo data simulated and reconstructed(light markers) and generator quantities (blue histogram) of carbon wire $i2$.*

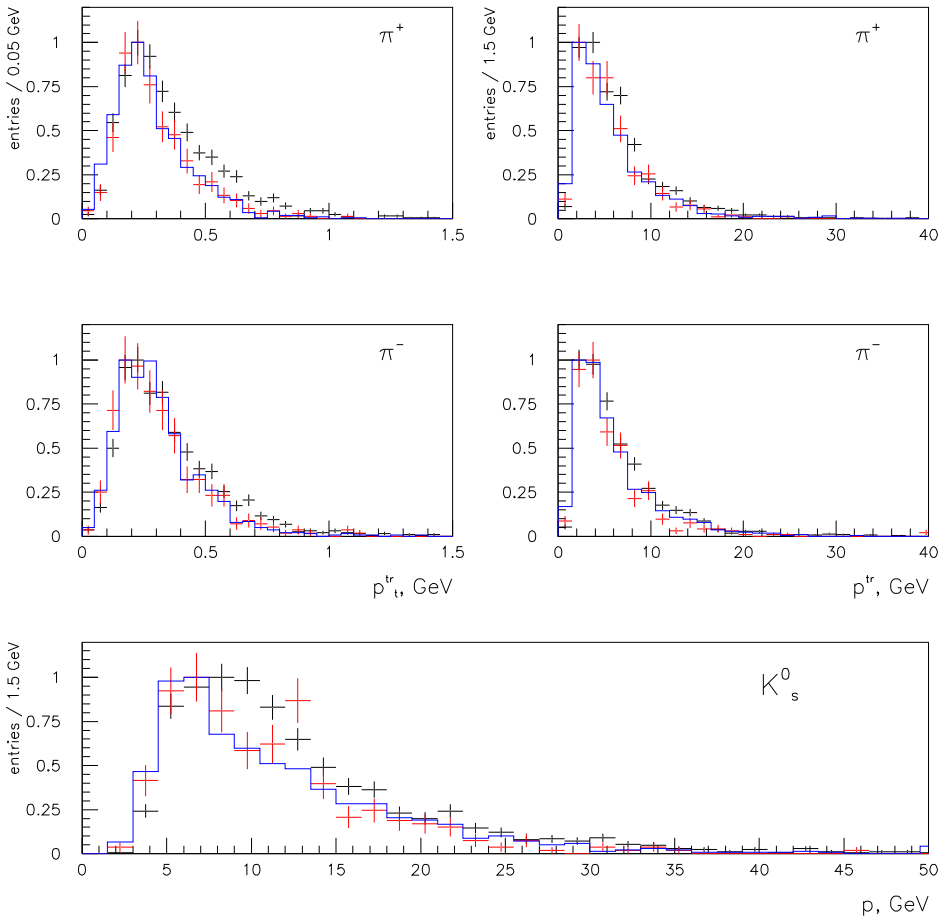

Figure A.8: *Transverse momentum of the tracks, p_t^{tr}, momentum of the tracks, p_t^{tr}, and reconstructed K_s^0 momentum, p, are presented for reconstructed data (black markers), Monte Carlo data simulated and reconstructed (red markers) and generator quantities (blue histogram) of titanium wire $i1$.*

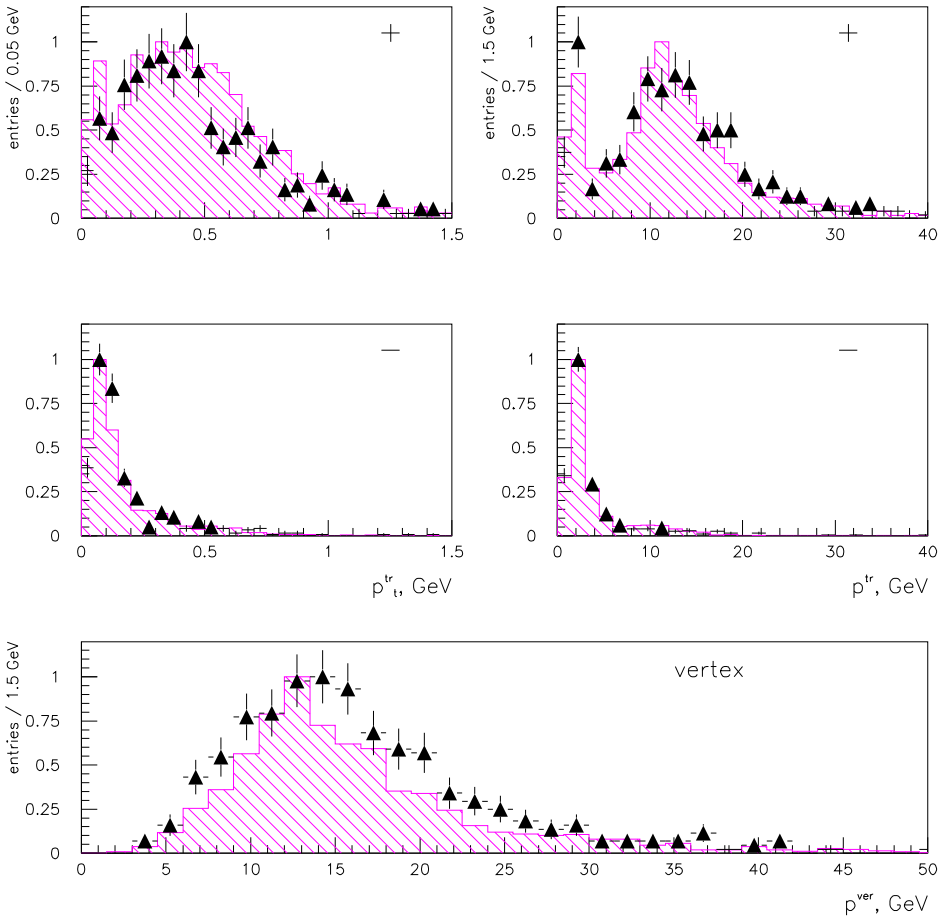

Figure A.9: *Transverse momentum of the tracks, p_t^{tr}, momentum of the tracks, p^{tr} , and reconstructed momentum, p, are presented for reconstructed data (markers), Monte Carlo data simulated and reconstructed (histogram) of titanium wire i*1*. Distributions correspond to the background events from "K^0_s" sidebands (outside 3σ region).*

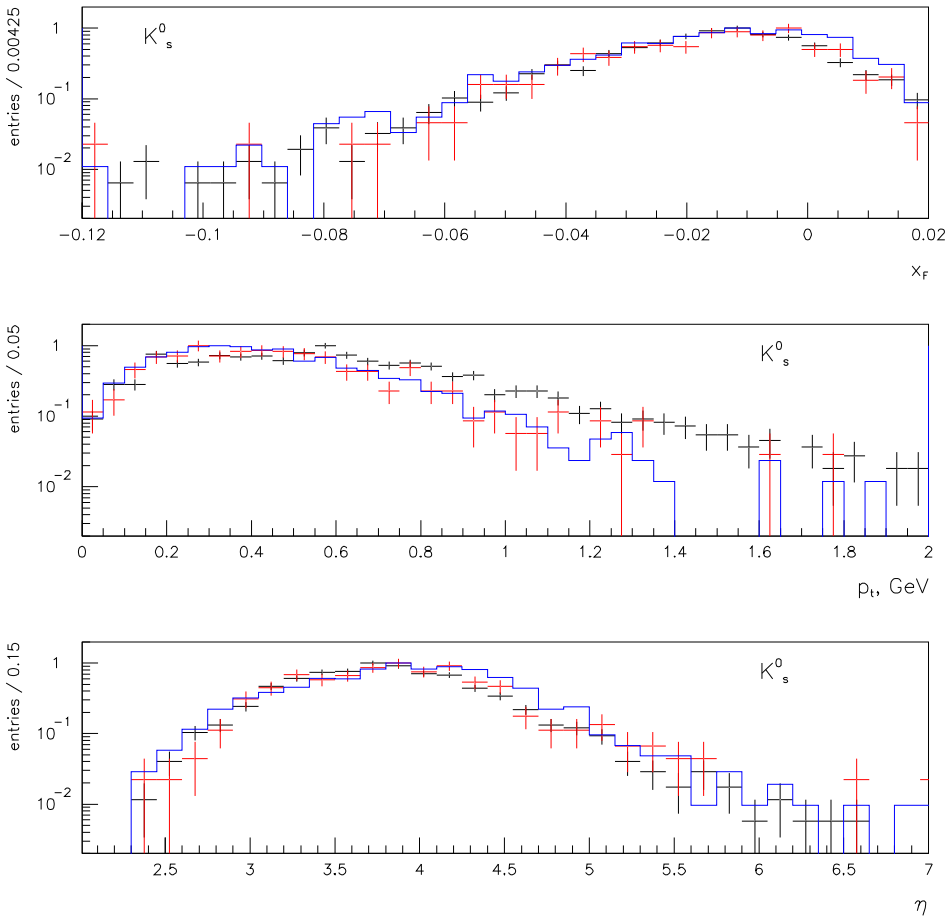

Figure A.10: *Feynman x, x_F, transverse momentum, p_t and pseudorapidity, η, of K_s^0 are presented for reconstructed data (black markers), Monte Carlo data simulated and reconstructed (light markers) and generator level (histogram) of titanium wire $i1$.*

Fig. A.11,A.12 show the corresponding invariant mass distributions for carbon. The number of tracks with a fraction of common hits less than 70 % that does not contribute to the signal but are physical can be determined in the following way:

$$N^{other}_{<70\%} = \frac{N^{false\ ghost}}{N^{good}} \cdot N^{other}.$$

The ghost rate in $K^0_s \to \pi^+\pi^-$ decay is:

$$R_{gh} = \frac{N^{other/ghost} - N^{other}_{<70\%}}{N^{false\ ghost} + N^{good}}.$$

One should notice that one of the tracks in the selected event is always matched to a Monte Carlo simulated pion coming from K^0_s with the fraction of common hits greater that 70 %.

The evaluated ghost rates for long tracks (VDS-OTR/ITR) in the pattern tracker using 50330 (21120) Monte Carlo simulated minimum bias events for carbon (titanium) target material are presented in Table A.5. The signal selection criteria, in this case, have been relaxed. We only require that two long charged VDS-OTR/ITR tracks form a vertex. The ghost rate, R_{gh}, evaluated for titanium target is twice higher than that for carbon. This might be connected to the fact that the track multiplicity in the case of titanium is much higher. The cuts usually exploited for the K^0_s selection (see Table A.1) have been applied in turn in order to investigate their influence on the ghost rate. It is clearly seen that the application of such cuts could reduce the problem significantly. The same analysis for the VDS gives a ghost rate less than 4 % for both target materials. The precision is in this case, however, much worse. Let us now go trough Table A.5. The

Table A.5: *Ghost rate in $K^0_s \to \pi^+\pi^-$ for titanium wire $i1$ and carbon wire $i2$.*

selection level	Ghost Rate, %		
	Carbon	Titanium	
	"realistic"	"realistic"	"optimistic"
0	9.8 ± 1.3 %	17.7 ± 3.5 %	18.2 ± 3.4 %
1	3.9 ± 1.0 %	2.1 ± 2.7 %	5.3 ± 2.2 %
2	1.5 ± 0.4 %	1.6 ± 0.6 %	1.0 ± 0.4 %
3	9.4 ± 1.4 %	17.1 ± 3.4 %	13.8 ± 3.5 %

meaning of the selection levels is as follows:

- *selection level 0*: all combinations of VDS-OTR/ITR tracks have been considered;
- *selection level 1*: those events have been used which have been left after standard application of clone removal (based on clone flags for VDS and main tracker);

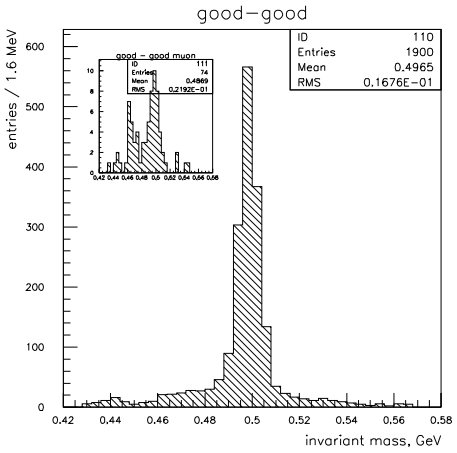

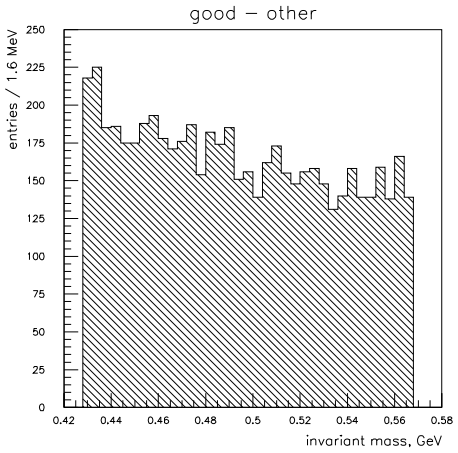

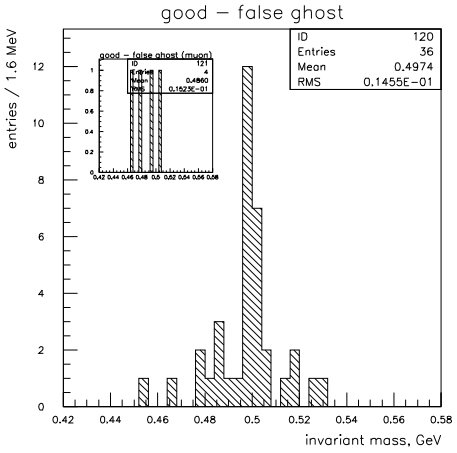

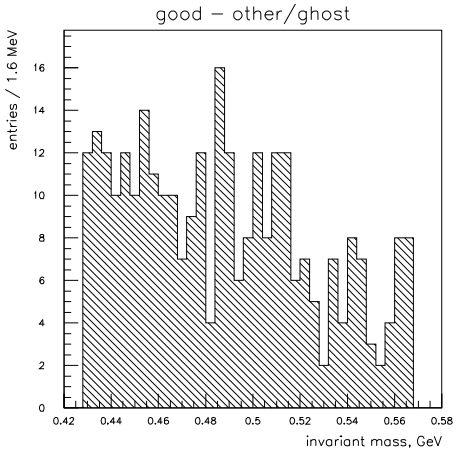

Figure A.11: *Monte Carlo selected events, sorted according to the 70 % limit, where both (upper plot) or one of the two tracks (lower plot) is always "good". The sample is for carbon wire $i2$ with only VDS-OTR/ITR charged track considered. The plots were obtained with the "realistic" scenario (Eq.(A.1)).*

Figure A.12: *Monte Carlo selected events, sorted according to the 70 % limit, where one of the two tracks is always "good". Upper plot shows the "good"- "other" combination, while lower plot shows "good"-"other/ghost". The sample is for carbon wire $i2$ with only VDS-OTR/ITR charged track considered. The plots were obtained with the "realistic" scenario (Eq.(A.1)).*

- *selection level 2*: only events which have been left after application of selection cuts such as CDA cut, impact parameter cut and decay length cut described in section 2 (Table A.1) have been used;

- *selection level 3*: only those events have been used, which have been left after track preselection based on requirement for tracks to have at least 5 reconstructed hits in VDS and 10 reconstructed hits in inner and outer tracker (or in outer tracker only or 7 reconstructed hits in inner tracker only, see Table A.1).

Comparing the numbers obtained by running a "realistic" simulation scenario (Eq.(A.1)) for titanium material with those obtained with an "optimistic" setting (Eq.(A.2)) shows no difference in ghost rate within the given errors. However, the track preselection is more efficient in removing ghosts in case of higher hit efficiencies.

A.5 Efficiency determination

Efficiencies related to the K_s^0 reconstruction are calculated for reference neutral kaons, selected to define the acceptance. *Reference kaons* are simulated $K_s^0 \to \pi^+\pi^-$ decays in normal inelastic proton nucleus interactions. The decay products must have a momentum $p > 1\ GeV$ and pass more than 3 VDS layers and 11 layers of the pattern tracker. As can be seen in Fig. A.13, most of the tracks originating from $K_s^0 \to \pi^+\pi^-$ cross more than 20 layers, in the pattern tracker. Nevertheless, in order not to loose tracks crossing less than 20 layers, the lowest limit was chosen to be 11 layers passed. Together with the above requirement, simulated charged pions were required to have a minimum number of associated hits in VDS and the pattern tracker (chosen to be 5 and 10, respectively). This allows to avoid non reconstructable tracks due to hit inefficiency and other complications (Fig. A.14). Thus the acceptance is defined as[3]

$$\varepsilon_{geo} = \frac{N^{ref}_{K_s^0 \to \pi^+\pi^-}}{N^{tot}_{K_s^0 \to \pi^+\pi^-}} \tag{A.5}$$

Reconstructed kaons are defined as $K_s^0 \to \pi^+\pi^-$ decays in which both of the pions have at least one assigned reconstructed track. The reconstruction efficiencies in VDS, ε^{VDS}_{reco}, in the pattern tracker, $\varepsilon^{Patt}_{reco}$, and in both of them together, ε_{reco}, are:

$$\varepsilon^{VDS}_{reco} = \frac{N^{VDS}_{K_s^0 \to \pi^+\pi^-}}{N^{ref}_{K_s^0 \to \pi^+\pi^-}} \tag{A.6}$$

$$\varepsilon^{Patt}_{reco} = \frac{N^{Patt}_{K_s^0 \to \pi^+\pi^-}}{N^{ref}_{K_s^0 \to \pi^+\pi^-}} \tag{A.7}$$

[3]The total number of $K_s^0 \to \pi^+\pi^-$ decays was obtained by counting all simulated mesons and normalizing this number to the branching ratio value.

and

$$\varepsilon_{reco} = \frac{N^{VDS+Patt}_{K^0_s\to\pi^+\pi^-}}{N^{ref}_{K^0_s\to\pi^+\pi^-}} \tag{A.8}$$

Here, the number of reconstructed K^0_s in VDS, $N^{VDS}_{K^0_s\to\pi^+\pi^-}$, and in the pattern tracker, $N^{Patt}_{K^0_s\to\pi^+\pi^-}$. The efficiency of matching two reconstructed segments of the pattern tracker and the VDS is defined as follows:

$$\varepsilon_{match} = \frac{\varepsilon_{reco}}{\varepsilon^{VDS}_{reco}\cdot\varepsilon^{Patt}_{reco}} \tag{A.9}$$

The selection efficiency is:

$$\varepsilon_{sel} = \frac{N^{obs}_{mc}}{N^{ref}_{K^0_s\to\pi^+\pi^-}} \tag{A.10}$$

Here N^{obs}_{mc} is the numner of observed K^0_s.

Table A.6: *Efficiencies related to the reconstruction of K^0_s meson obtained for $i2$ and $i1$ wires ("realistic" scenario).*

efficiencies, %	Inner II (Carbon)	Inner I (Titanium)
ε^{geo}	10.6 ± 0.3	10.3 ± 0.3
ε^{VDS}_{reco}	92.9 ± 2.7	92.1 ± 3.7
$\varepsilon^{Patt}_{reco}$	89.3 ± 2.6	89.0 ± 3.6
ε_{reco}	66.0 ± 2.1	64.1 ± 2.9
ε_{match}	79.5 ± 4.1	78.3 ± 5.7
ε_{sel}	49.3 ± 2.7	55.6 ± 4.0
ε_{tot}	3.4 ± 0.3	3.7 ± 0.3

Table A.7: *Efficiencies related to the reconstruction of K^0_s meson obtained for $i2$ and $i1$ wires ("optimistic" scenario).*

efficiencies, %	Inner II (Carbon)	Inner I (Titanium)
ε^{geo}	10.7 ± 0.4	10.3 ± 0.3
ε^{VDS}_{reco}	93.2 ± 5.0	92.0 ± 3.7
$\varepsilon^{Patt}_{reco}$	90.9 ± 5.0	92.6 ± 3.7
ε_{reco}	67.6 ± 4.0	67.9 ± 3.0
ε_{match}	79.8 ± 7.7	79.7 ± 5.7
ε_{sel}	49.2 ± 5.0	58.1 ± 4.5
ε_{tot}	3.5 ± 0.4	4.1 ± 0.4

The total efficiency to detect the $K_s^0 \to \pi^+\pi^-$ decay is defined as follows:

$$\varepsilon_{tot} = \varepsilon_{geo} \cdot \varepsilon_{reco} \cdot \varepsilon_{sel} \tag{A.11}$$

The efficiencies obtained with 50330 events [4] (carbon) and 21120 events (titanium) are shown in table A.6. As can be seen in Fig. A.15, there is a good agreement between simulated and reconstructed momenta of pion tracks when the kaons are reconstructed in both the VDS and the pattern tracker. The agreement is less good, especially for low momenta ($<$ 5 GeV), when only the VDS or the pattern tracks information is used (Fig. A.16,A.17). It is interesting to note that almost all such events with large momentum difference belong to positive pion tracks when the K_s^0 is reconstructed in the pattern tracker and almost all these tracks have reconstructed momenta smaller than 1 GeV (Fig. A.16, upper plots). The fraction of such events is about 10%. No difference between π^+ and π^- is observed when the K_s^0 is reconstructed in the VDS alone.

The corresponding efficiencies obtained with the "optimistic" scenario are slightly higher (Table A.7). However, the results are compatible within the errors. As shown in Fig. A.18-A.20, similar conclusion can be drawn. Fig. 21-28 show the geometrical acceptance and the reconstruction efficiency of the kaon as a function of the scaling variable, x_F, the pseudorapidity, η, transverse momentum, p_T, and momentum, p, of the particle.

It is also observed that the wrong charge assignment is quite significant when the decay is reconstructed in the VDS, whereas it is small for K_s^0 reconstructed in the pattern tracker and completely negligible when the decay is detected in both subsystems. The related numbers are presented in Table A.8.

Table A.8: *Wrong charge assignment ratio in $K_s^0 \to \pi^+\pi^-$ decay.*

wire	Inner II (Carbon wire)		Inner I (titanium wire)	
scenario	"realistic"	"optimistic"	"realistic"	"optimistic"
VDS	14.54 %	12.92 %	14.47 %	12.21 %
OTR/ITR	1.23 %	0.76 %	1.21 %	1.42 %
VDS-OTR/ITR	0.06 %	-	-	-

[4] In the case of running "optimistic" scenario for carbon material only 14190 Monte Carlo simulated events have been used.

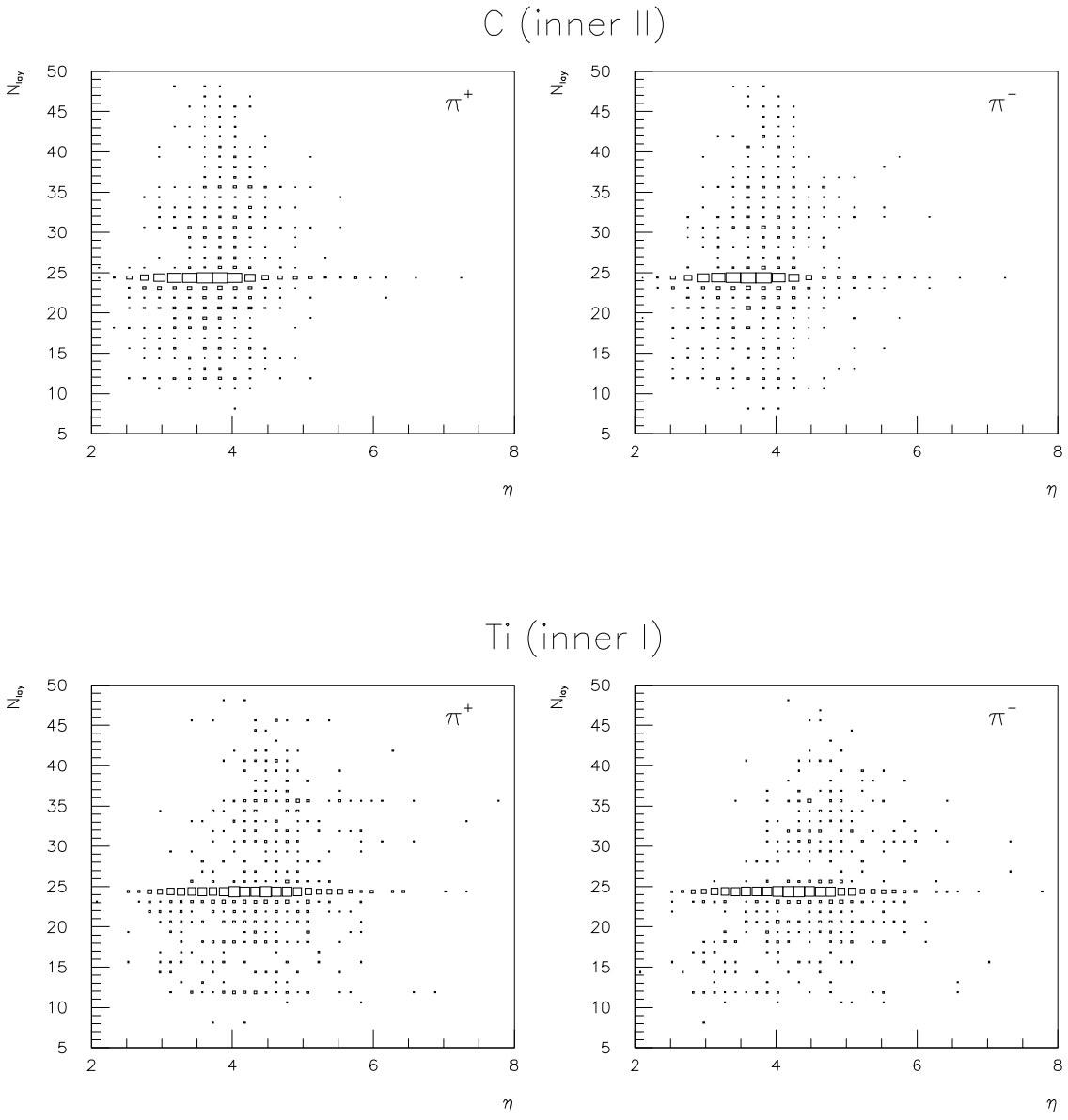

Figure A.13: *Number of layers, N_{lay}, crossed by a track in the pattern region of the tracking system versus pseudorapidity, η, of simulated K_s^0 meson. The plots are shown for the reference K_s^0 tracks.*

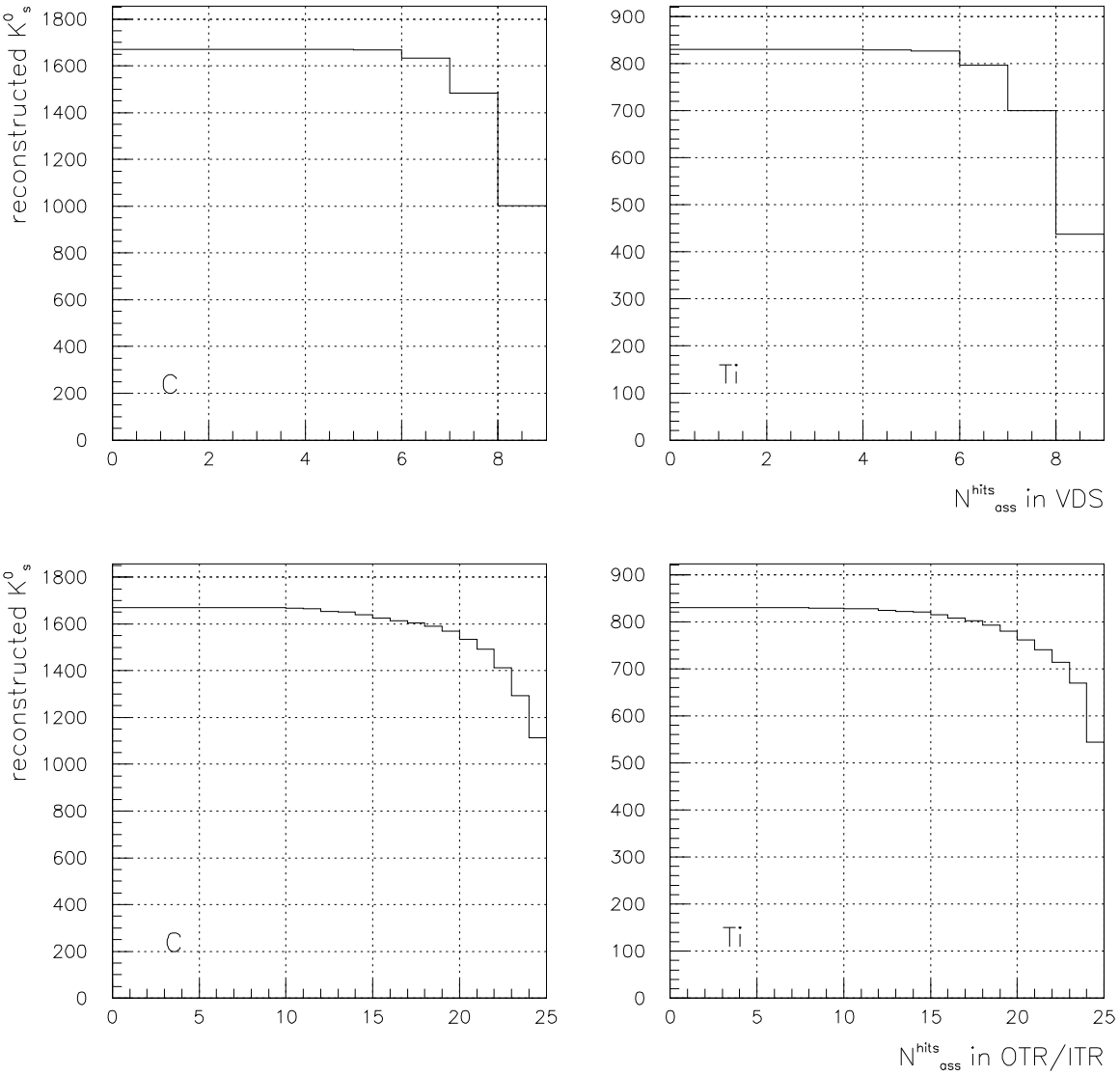

Figure A.14: *Number of reconstructed $K_s^0 \to \pi^+\pi^-$ decays as a function of associated hits in VDS (up) and the pattern tracker (down) for carbon (C) and titanium (Ti) targets. The plots were obtained with the "realistic" scenario (Eq.(A.1)).*

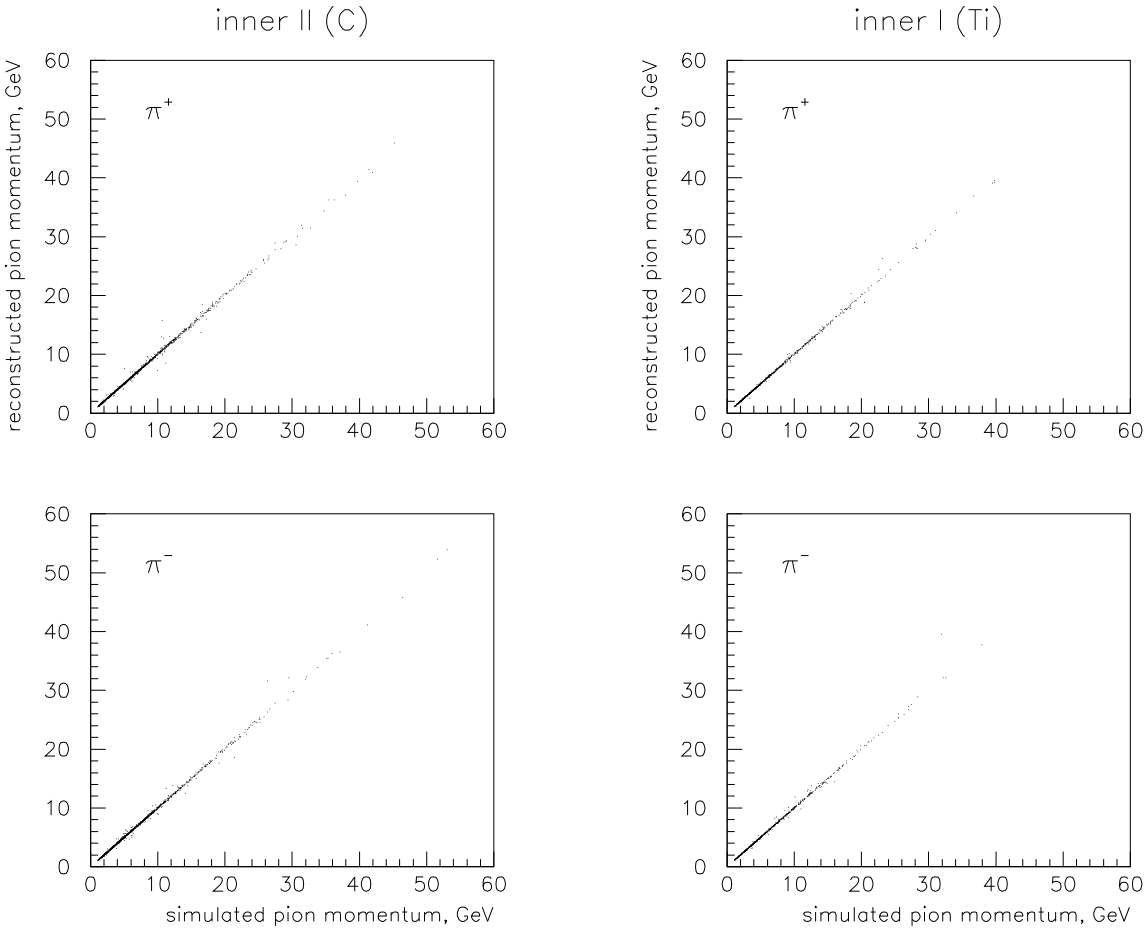

Figure A.15: *Momentum of simulated pions from the $K_s^0 \to \pi^+\pi^-$ versus momentum of reconstructed tracks assigned to the pions. The K_s^0 is reconstructed. The plots were obtained with the "realistic" scenario (Eq.(A.1)).*

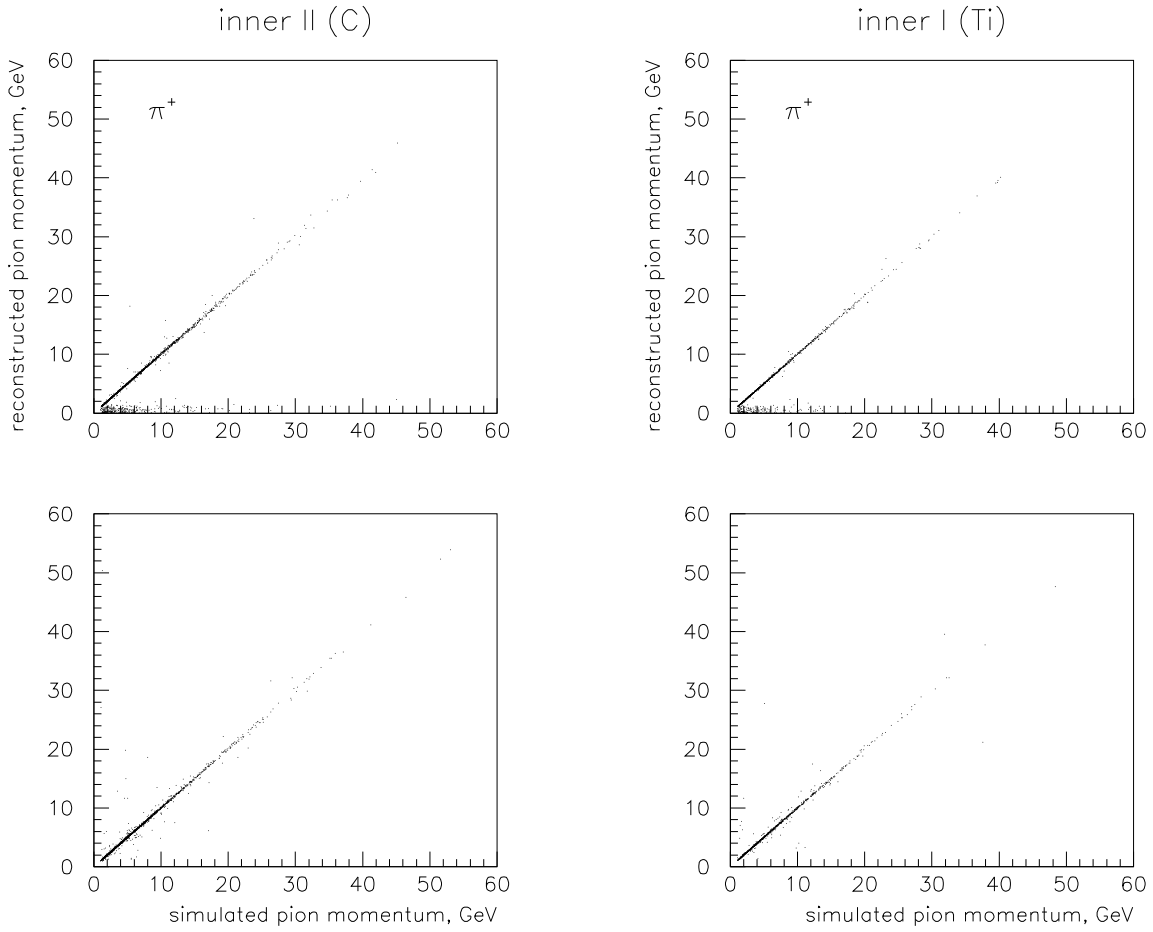

Figure A.16: *Momentum of simulated pions from the $K^0_s \to \pi^+\pi^-$ versus momentum of reconstructed tracks assigned to the pions. The K^0_s is reconstructed in the pattern tracker. The plots were obtained with the "realistic" scenario (Eq.(A.1)).*

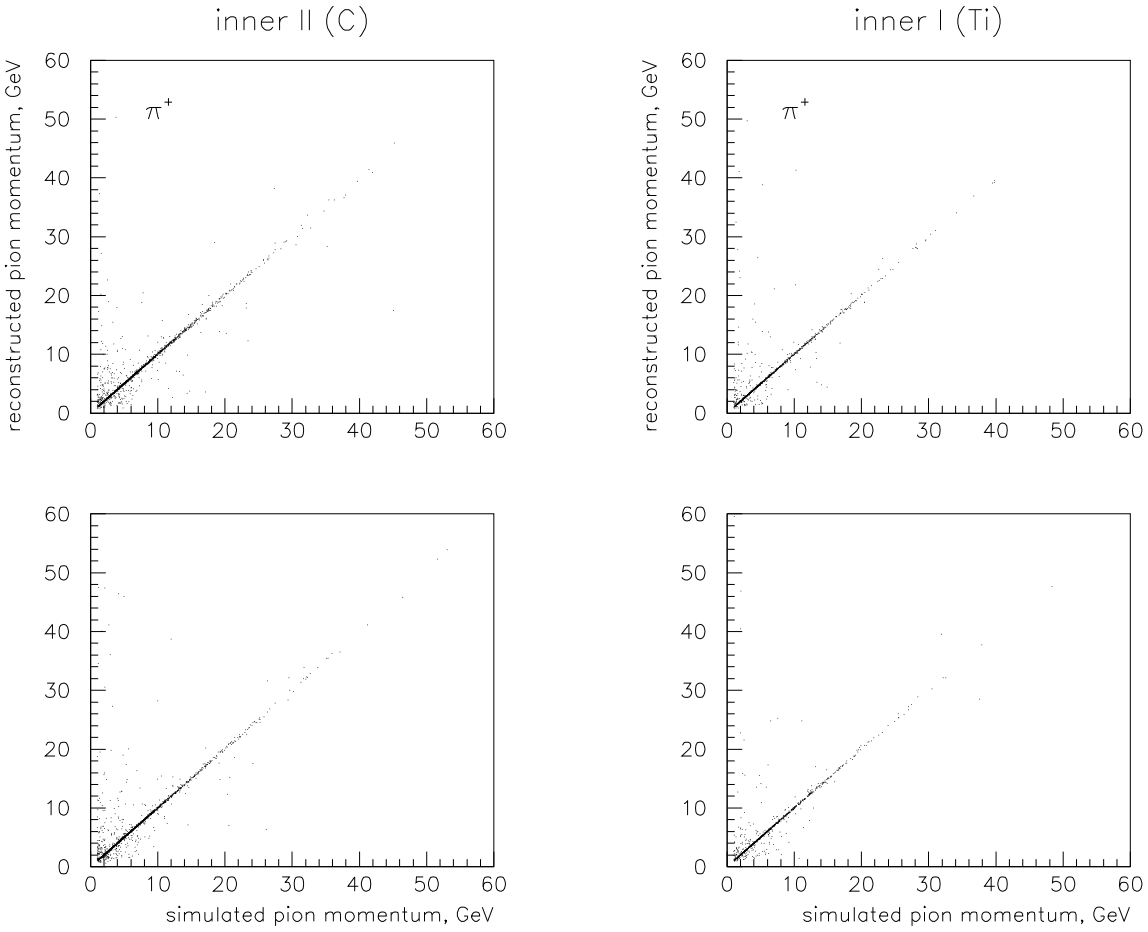

Figure A.17: *Momentum of simulated pions from the $K_s^0 \to \pi^+\pi^-$ versus momentum of reconstructed tracks assigned to the pions. The K_s^0 is reconstructed in the VDS. The plots were obtained with the "realistic" scenario (Eq.(A.1)).*

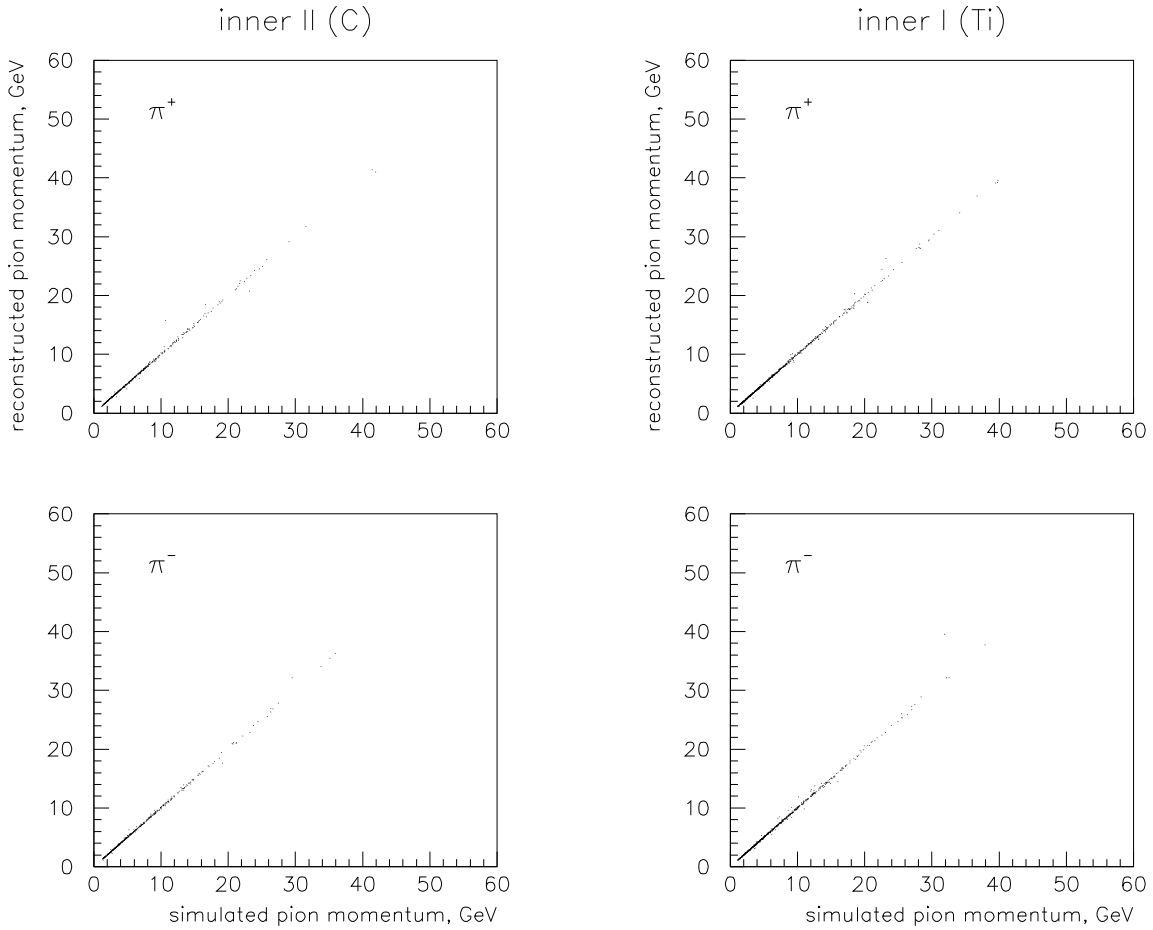

Figure A.18: A.2)). *Momentum of simulated pions from the $K_s^0 \to \pi^+\pi^-$ versus momentum of reconstructed tracks assigned to the pions. The K_s^0 is reconstructed. The plots were obtained with the "optimistic" scenario (Eq.(*

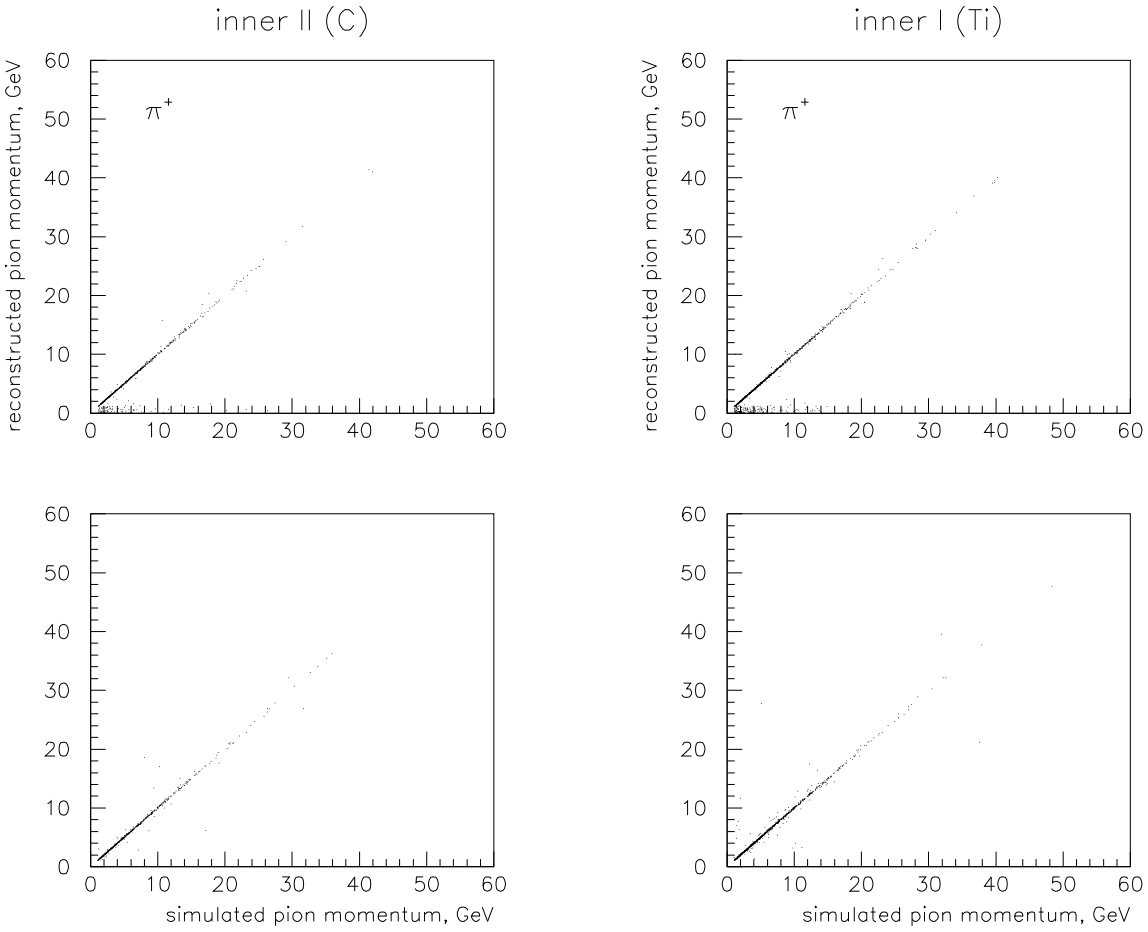

Figure A.19: *Momentum of simulated pions from the $K_s^0 \to \pi^+\pi^-$ versus momentum of reconstructed tracks assigned to the pions. The K_s^0 is reconstructed in the pattern tracker. The plots were obtained with the "optimistic" scenario (Eq.(A.2)).*

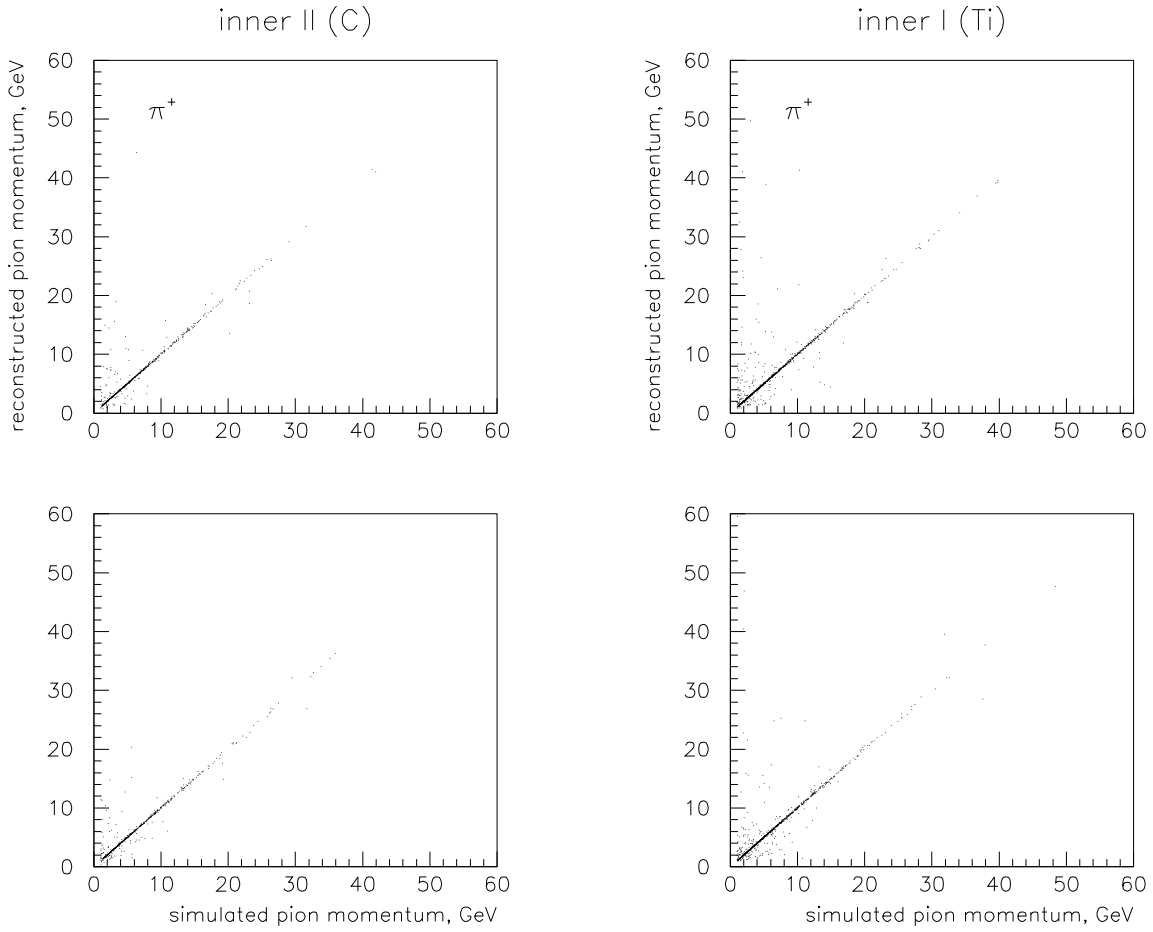

Figure A.20: *Momentum of simulated pions from the $K^0_s \to \pi^+\pi^-$ versus momentum of reconstructed tracks assigned to the pions. The K^0_s is reconstructed in the VDS. The plots were obtained with the "optimistic" scenario (Eq.(A.2)).*

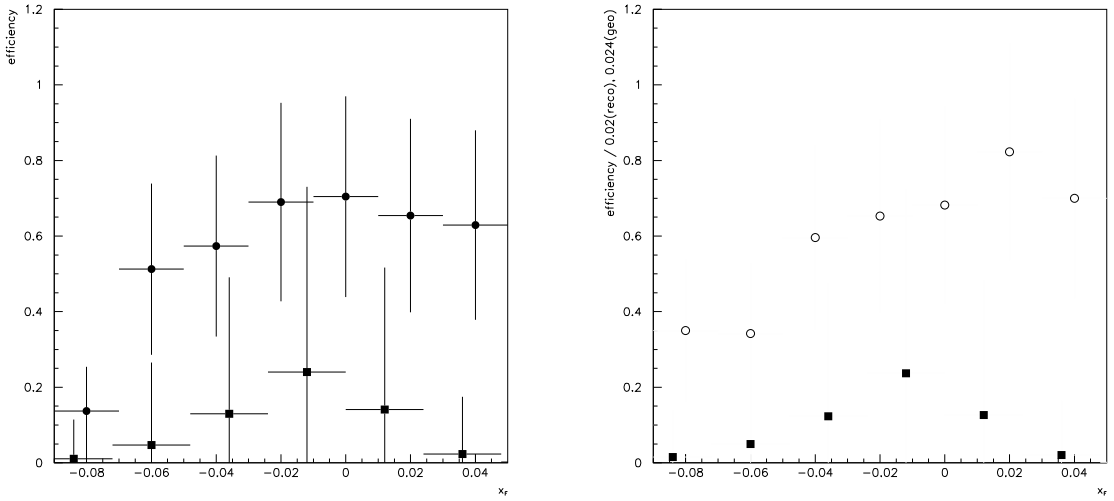

Figure A.21: *Geometrical acceptance (square marker) and reconstruction efficiency (circle marker) as a function of Feynman x_F of K^0_s, for carbon target $i2$ (left) and titanium target $i1$ (right). The plots were obtained with the "realistic" scenario (Eq.(A.1)). The uncertainties, that are not shown explicitly in left plot, are of the same order as those shown in right plot.*

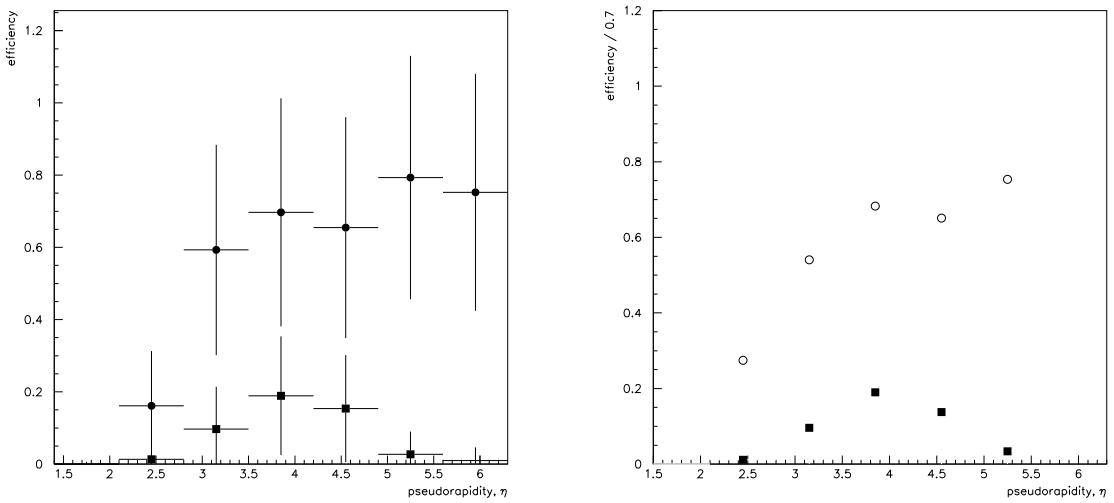

Figure A.22: *Geometrical acceptance (square marker) and reconstruction efficiency (circle marker) as a function of the pseudorapidity η of K^0_s, calculated in the lab frame for carbon target $i2$ (left) and titanium target $i1$ (right). The plots were obtained with the "realistic" scenario (Eq.(A.1)). The uncertainties, that are not shown explicitly in left plot, are of the same order as those shown in right plot.*

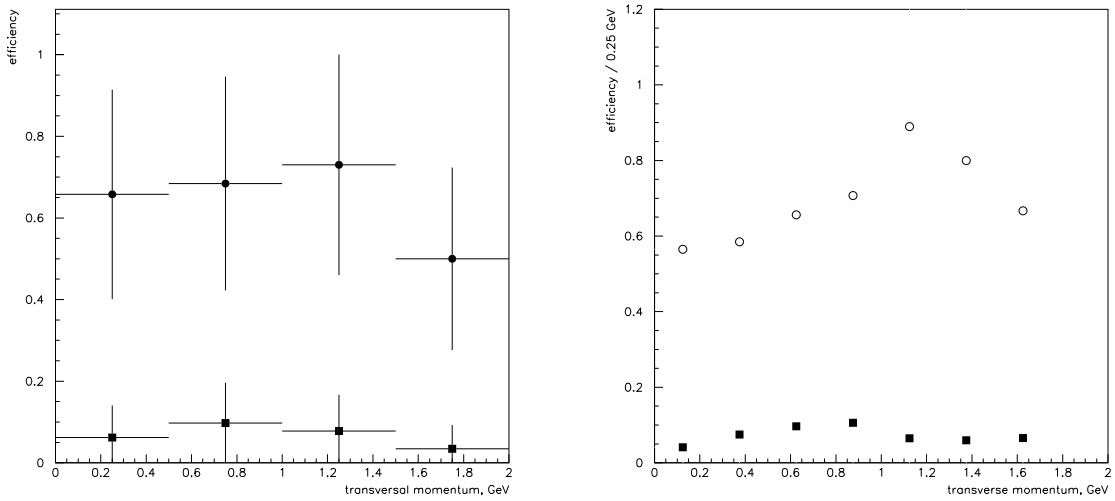

Figure A.23: *Geometrical acceptance (square marker) and reconstruction efficiency (circle marker) as a function of the transverse momentum p_T of K_s^0, for carbon target $i2$ (left) and titanium target $i1$ (right). The plots were obtained with the "realistic" scenario (Eq.(A.1)). The uncertainties, that are not shown explicitly in left plot, are of the same order as those shown in right plot.*

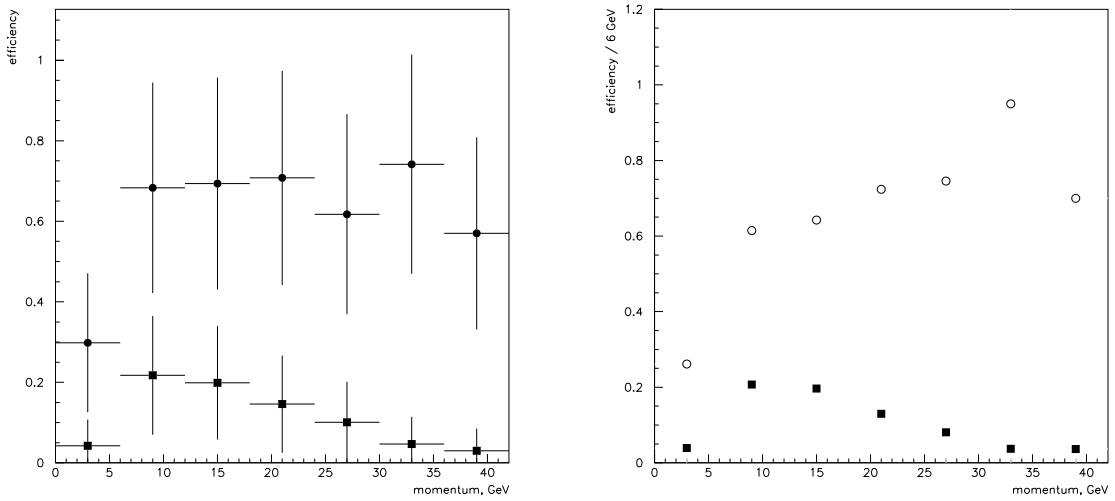

Figure A.24: *Geometrical acceptance (square marker) and reconstruction efficiency (circle marker) as a function of the kaon momentum p, for carbon target $i2$ (left) and titanium target $i1$ (right). The plots were obtained with the "realistic" scenario (Eq.(A.1)). The uncertainties, that are not shown explicitly, are of the same order as those presented for "realistic" scenario.*

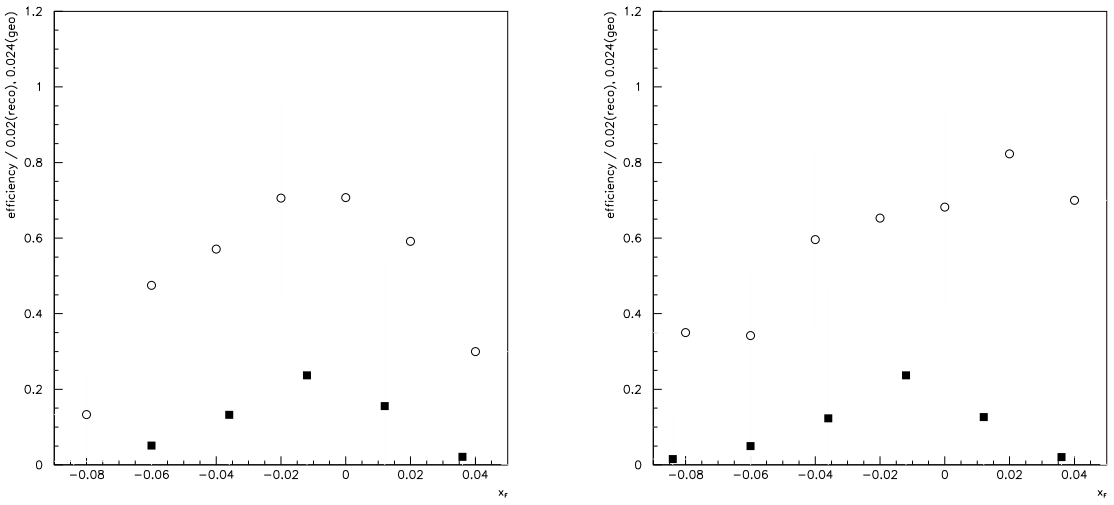

Figure A.25: *Geometrical acceptance (square marker) and reconstruction efficiency (circle marker) as a function of Feynman x_F of K_s^0, for carbon target $i2$ (left) and titanium target $i1$ (right). The plots were obtained with the "optimistic" scenario (Eq.(A.2)). The uncertainties, that are not shown explicitly, are of the same order as those presented for "realistic" scenario (Fig. A.21).*

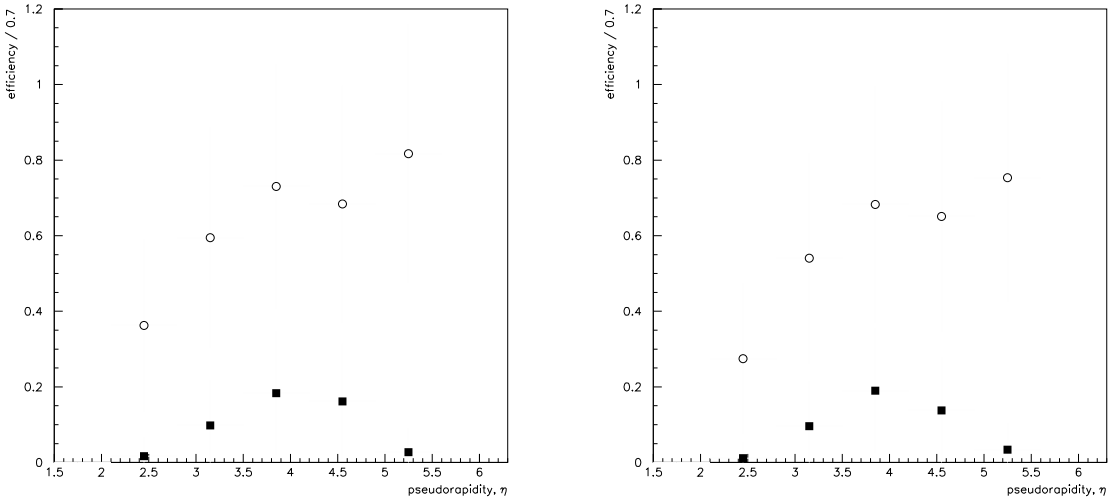

Figure A.26: *Geometrical acceptance (square marker) and reconstruction efficiency (circle marker) as a function of the pseudorapidity η of K_s^0, calculated in the lab frame for carbon target $i2$ (left) and titanium target $i1$ (right). The plots were obtained with the "optimistic" scenario (Eq.(A.2)). The uncertainties, that are not shown explicitly, are of the same order as those presented for "realistic" scenario (Fig. A.22).*

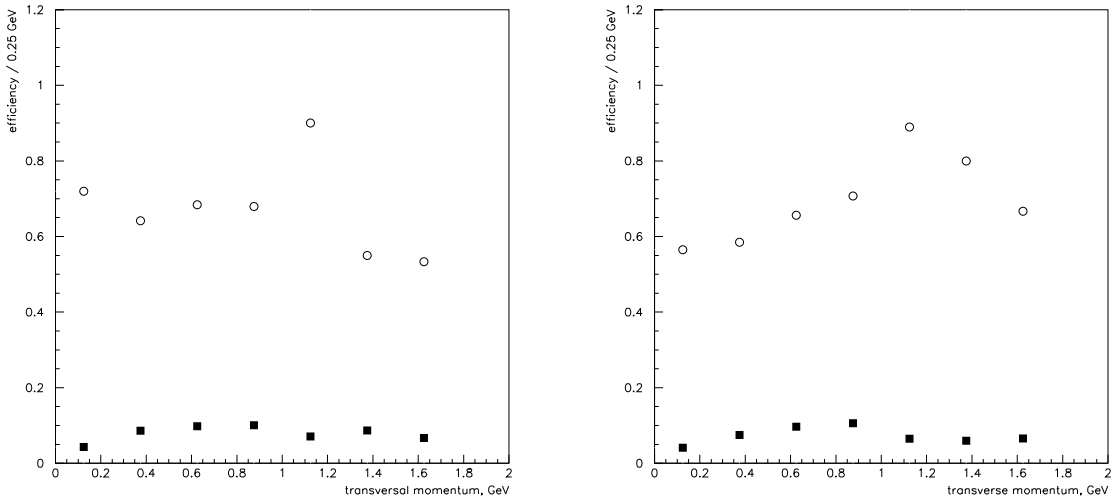

Figure A.27: *Geometrical acceptance (square marker) and reconstruction efficiency (circle marker) as a function of the transverse momentum p_T of K^0_s, for carbon target $i2$ (left) and titanium target $i1$ (right). The plots were obtained with the "optimistic" scenario (Eq.(A.2)). The uncertainties, that are not shown explicitly, are of the same order as those presented for "realistic" scenario (Fig. A.23).*

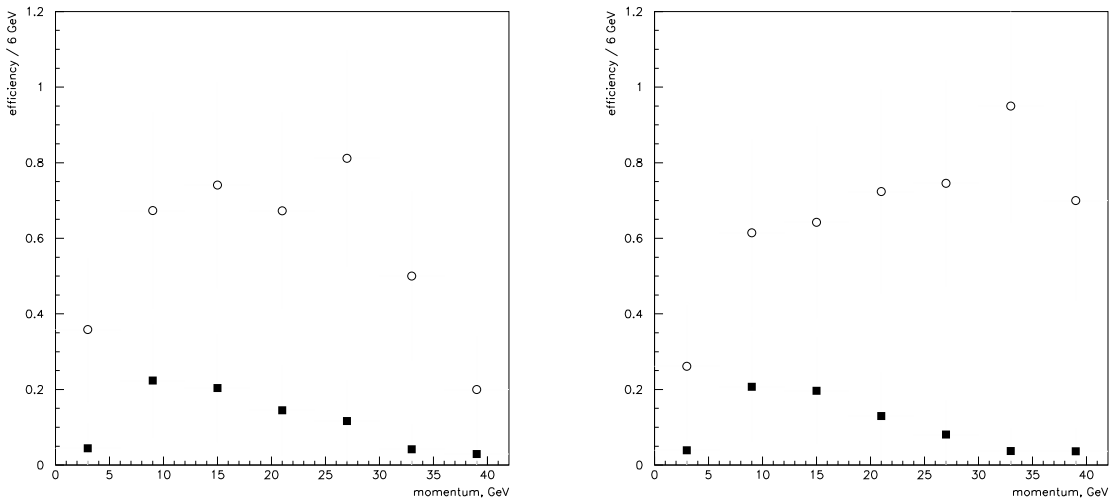

Figure A.28: *Geometrical acceptance (square marker) and reconstruction efficiency (circle marker) as a function of the kaon momentum p, for carbon target $i2$ (left) and titanium target $i1$ (right). The plots were obtained with the "optimistic" scenario (Eq.(A.2)). The uncertainties, that are not shown explicitly, are of the same order as those presented for "realistic" scenario (Fig. A.24).*

A.6 Cross-section evaluation

Using the efficiencies determined above it is possible to evaluate the $K^0/\bar{K}^0$ production cross-section in proton nucleus interactions at ~ 41.6 GeV CM energy. The cross-section is determined as follows:

$$\sigma = \frac{N^{obs}}{\varepsilon_{tot} \cdot Br} \cdot \frac{1}{L} \tag{A.12}$$

Here N^{obs} is the measured number of K^0_s; Br is the branching ratio of the $K^0_s \to \pi^+\pi^-$ decay channel ($Br = 0.6861 \pm 0.0028$); ε_{tot} is the total efficiency for the detection of this channel (Eq.(A.11); L is the integrated luminosity (taken from [108]). The results are presented in Table A.9.

Table A.9: *Measured $K^0/\bar{K}^0$ cross-section in interval of* $0.12 < x_F < 0$

target	runs	L, $(mb \cdot nucl.)^{-1}$	N^{obs}	σ, $mb \cdot nucl.$ "realistic"	σ, $mb \cdot nucl.$ "optimistic"
C	14577	1093 ± 38	2256 ± 67	88 ± 9	85 ± 11
Ti	14551, 15553	308 ± 10	2015 ± 67	261 ± 23	233 ± 23

The raw x_F and p_T spectra recorded by HERA-B in April 2000 are shown in Fig. A.29. To obtain them the invariant mass spectra (from carbon and titanium wire) were divided into p_T and x_F bins. Each bin then undergoes the fit for the kaon peak as for the entire signal (as described in section 1). The width of the standard bins is 0.2 GeV for p_T and 0.02 for x_F.

Fig. A.30,A.31 show the p_T and x_F spectra of the K^0_s particle corrected by geometrical acceptance, reconstruction and selection efficiencies[5]. The fit of the x_F spectra are made using the function

$$\frac{dN}{dx_F} = A(1 - |x_F|)^n \tag{A.13}$$

The resulting values of the fit parameter n are listed in Table A.10.

To find the differential p_T spectrum each bin was calculated using the formula:

$$\frac{dN}{dp^2_{t\,i}} = \frac{N^i_{K^0_s}}{N_0 \cdot p^i_T} \tag{A.14}$$

N_0 is a normalization factor chosen to be $N_0 = 2 \cdot N^{obs}$, where N^{obs} is the number of observed neutral kaons; $N^i_{K^0_s}$ is the acceptance-corrected number of observed neutral kaons per bin (Fig.A.30) and p^i_T is the average transverse momentum for bin i. Figure A.32 shows dN/dp^2_t as a function of the transverse momentum for both target materials.

[5] obtained with the "realistic" scenario (Eq.(A.1)

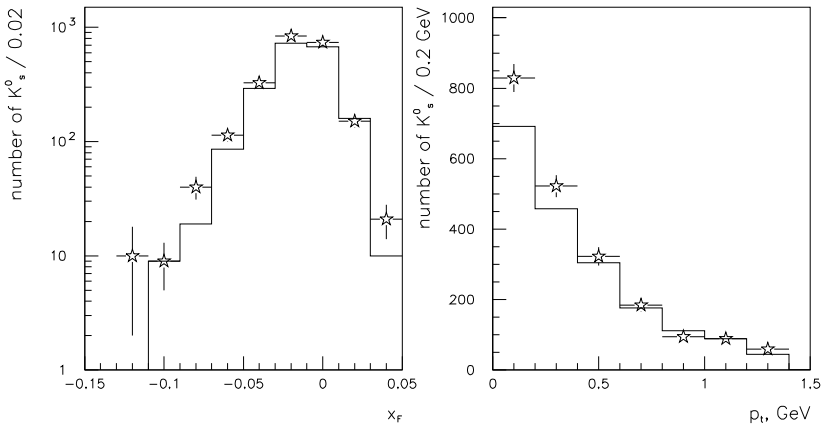

Figure A.29: *Raw x_F and p_T spectra of the K^0_s meson recorded by HERA-B in April 2000. Histogram show spectra obtained on titanium wire, while markers show spectra obtained on carbon wire.*

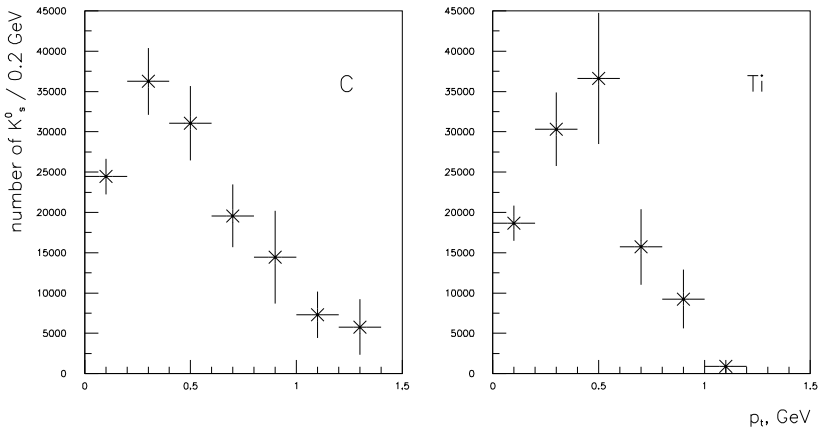

Figure A.30: *The acceptance-corrected p_T spectrum of the K^0_s meson. The errors are statistical.*

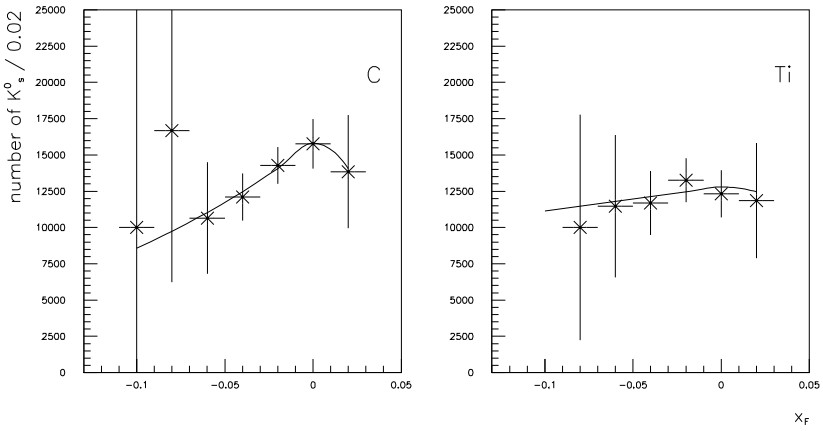

Figure A.31: *The acceptance-corrected x_F spectrum of the K^0_s meson. The errors are statistical. The fit is made using the parametrization of Eq.(A.13).*

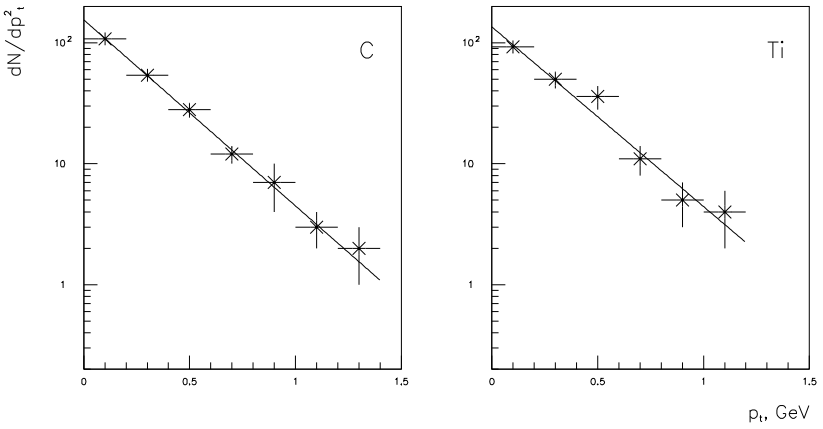

Figure A.32: *Differential cross-section for $K^0/\bar{K}^0$ production versus transverse momentum measured at HERA-B for carbon (C) and titanium (Ti) targets. The fit is made using the parametrization of Eq.(A.15). The y axes are in arbitrary units.*

The calculated values and statistical errors[6] are shown along with a fit to the function

$$\frac{dN}{dp_t^2} = Ae^{-Bp_T} \tag{A.15}$$

The resulting values of fit parameter B are listed in Table A.10.

Table A.10: *Results of fits to dN/dx_F and dN/dp_T^2.*

	n	$B,\ GeV^-2$
Carbon	5.8 ± 3.6	3.5 ± 0.2
Titanium	1.3 ± 4.1	3.4 ± 0.3

A.7 Conclusions

Base of on the studies performed, one can conclude that the amount of ghosts in $K^0_s \to \pi^+\pi^-$ decay is about 10 (18) % for carbon (titanium) target. In both cases the problem decreases quite significantly with the application of selection cuts. The large reduction of ghost tracks due to the standard procedure of clone removal indicate a close connection between the problem of ghosts and multiple track reconstruction. In addition, it was found that this procedure of removing large amount of background events reduces also the signal by about 12%.

The estimated reconstruction efficiency is 66 % and 64 % for carbon and titanium, respectively. The K^0_s reconstruction efficiency in the VDS is estimated to be of order 93 (92) %. The corresponding values for pattern tracker are about 89 % for both targets. The loss due to the inefficiency of the matching between the VDS and the pattern tracker is estimated to be 21 % amd 22 %, respectively. In terms of efficiency, the results obtained from different detector scenarios are compatible within the statistical errors. The comparison of the efficiencies obtained from different detector simulation scenarios show some difference in their values. This difference in compatible within the errors. The evaluated production cross-section of $K^0/\bar{K}^0$ is about 88 (261) $mb \cdot nucleus$, respectively for carbon and titanium.

Acknowledgments

I would like to thank Farid Ould-Saada for valuable discussions and suggestions. I also would like to thank Ulrich Uwer and Federico Sanchez for their help during my stay at DESY.

The K^0_s analysis of 2002 data, presented in this appendix, was accomplished by spring 2002. The $K^0/\bar{K}^0$ cross-section estimated for proton-carbon and proton-titanium interactions (see Table A.9) were in accord with the corresponding numbers available at that time from a V^0 analysis [108], which resulted later in a publication [109].

[6]Errors were calculated for $N^i_{K^0_s}$

Appendix B

$R_{\chi c}$ differential distributions

In this appendix we provide details concerning x_F differential spectra of R_{χ_c}, presented in chapter 6, section 6.3.

To obtain the differential x_F spectra of R_{χ_c} we divide the $\mu^+\mu^-$ invariant mass distribution into x_F bins of size 0.06 (Table B.1), after the standard J/Ψ selection (chapter 4, subsection 4.3.2 and Table 5.3). Each bin then undergoes the fit for the J/Ψ signal (Fig. B.1(e,f)). In the fit we use a Gaussian to describe the signal and an exponential or a polynomial for background parametrization. Subsequently, the search for an isolated photon is performed for each bin of x_F. This is followed by the determination of the ΔM distributions in ranges of x_F (Fig. B.1(a-d)). The χ_c signals are then extracted from a fit to ΔM (chapter 5, subsection 5.3.5). In the fit to ΔM we fix the width of the χ_c peak to 38 MeV/c^2, in order to compensate for limited statistics and inaccuracies in the background description for marginal x_F bins.

The resulting numbers are presented in Tables B.2-B.3, B.4-B.5 and B.6-B.7 for carbon, tungsten and combined data sets, respectively. Each of two tables contains:

- Numbers related to the evaluation of R_{χ_c},
- and the parameters of the fits to ΔM and J/Ψ mass distributions.

Figure B.1 sows, as an example, ΔM and J/Ψ mass distributions related to the extraction of the R_{χ_c} ratio for the range $-0.06 \leq x_F < 0.00$.

Table B.1: $x_F^{J/\Psi}$ *bin numbering.*

Number	Bin
1	$-0.30 \leq x_F < -0.24$
2	$-0.24 \leq x_F < -0.18$
3	$-0.18 \leq x_F < -0.12$
4	$-0.12 \leq x_F < -0.06$
5	$-0.06 \leq x_F < 0.00$
6	$0.00 \leq x_F < 0.06$
7	$0.06 \leq x_F < 0.12$

Table B.2: *R_{χ_c} divided into $x_F^{J/\Psi}$ bins for carbon data. The numbers of χ_c, N_{χ_c}, and J/Ψ, $N_{J/\Psi}$, events, measured in proton-carbon interactions are presented. The simulated χ_c signal, $N_{\chi_c}^{MC}$, and number of J/Ψ, $N_{J/\Psi}^{\chi_c}$, stemming from χ_c radiative decays are also given along with the photon detection efficiency, ε_γ.*

	Data			Monte Carlo		
Bin	R_{χ_c}, %	N_{χ_c}	$N_{J/\Psi}$	$N_{\chi_c}^{MC}$	$N_{J/\Psi}^{\chi_c}$	ε_γ
1	–	–	555 ± 30	–	39 ± 6	–
2	–	–	2865 ± 67	–	175 ± 14	–
3	12.1 ± 4.3	529 ± 144	10800 ± 128	251 ± 58	622 ± 25	40.3 ± 9.4
4	12.0 ± 3.1	1180 ± 225	24170 ± 189	542 ± 91	1330 ± 37	40.8 ± 6.9
5	19.7 ± 4.4	1753 ± 223	28490 ± 202	528 ± 94	1692 ± 41	31.2 ± 5.6
6	21.2 ± 4.9	985 ± 122	12760 ± 129	294 ± 56	809 ± 29	36.3 ± 7.1
7	11.4 ± 5.5	93 ± 34	1306 ± 40	57 ± 16	91 ± 10	62.2 ± 19.3

Table B.3: *R_{χ_c} divided into $x_F^{J/\Psi}$ bins for carbon data. Parameters of the fits to ΔM: χ^2 per degree of freedom and the position of the χ_c peak for data, $\langle \Delta M \rangle_{\chi_c}$, and Monte Carlo, $\langle \Delta M \rangle_{\chi_c}^{MC}$. The position, $\langle M \rangle_{J/\Psi}$, and width, $\sigma_{M_{J/\Psi}}$, of J/Ψ measured in data are also presented.*

	Data				Monte Carlo	
Bin	$(\chi^2/n.d.f.)_{\chi_c}$	$\langle \Delta M \rangle_{\chi_c}$	$\sigma_{M_{J/\Psi}}$	$\langle M \rangle_{J/\Psi}$	$(\chi^2/n.d.f.)_{\chi_c}^{MC}$	$\langle \Delta M \rangle_{\chi_c}^{MC}$
1	–	–	41.0 ± 2.0	3.107 ± 0.002		–
2	–	–	41.1 ± 0.7	3.103 ± 0.001		–
3	100.2/84	439 ± 14	43.8 ± 0.1	3.098 ± 0.001	55.9/83	442 ± 9
4	99.2/85	430 ± 7	44.4 ± 0.1	3.092 ± 0.001	57.4/85	434 ± 6
5	82.9/85	436 ± 3	44.7 ± 0.2	3.091 ± 0.001	83.7/85	443 ± 6
6	85.3/86	423 ± 5	44.4 ± 0.2	3.092 ± 0.001	92.3/85	441 ± 8
7	108.5/85.	402 ± 14	45.6 ± 0.4	3.086 ± 0.001	88.2/85	431 ± 17

Table B.4: *R_{χ_c} divided into $x_F^{J/\Psi}$ bins for tungsten data. The numbers of χ_c, N_{χ_c}, and J/Ψ, $N_{J/\Psi}$, events, measured in proton-tungsten interactions are presented. The simulated χ_c signal, $N_{\chi_c}^{MC}$, and number of J/Ψ, $N_{J/\Psi}^{\chi_c}$, stemming from χ_c radiative decays are also given along with the photon detection efficiency, ε_γ.*

	Data			Data		
Bin	R_{χ_c}, %	N_{χ_c}	$N_{J/\Psi}$	$N_{\chi_c}^{MC}$	$N_{J/\Psi}^{\chi_c}$	ε_γ, %
1	–	54 ± 21	310 ± 23	–	48 ± 7	–
2	32.0 ± 22.2	116 ± 50	1293 ± 62	54 ± 29	192 ± 14	28.1 ± 15.4
3	7.5 ± 5.1	170 ± 108	5127 ± 98	269 ± 62	621 ± 26	43.4 ± 10.0
4	13.0 ± 5.7	480 ± 172	12200 ± 144	372 ± 93	1234 ± 36	30.1 ± 7.6
5	18.5 ± 6.0	728 ± 164	14080 ± 157	391 ± 90	1401 ± 37	27.9 ± 6.4
6	24.8 ± 9.8	430 ± 95	6686 ± 95	168 ± 54	647 ± 25	25.9 ± 8.5
7	–	–	688 ± 31	–	72 ± 9	–

Table B.5: *R_{χ_c} divided into $x_F^{J/\Psi}$ bins for tungsten data. Parameters of the fits to ΔM: χ^2 per degree of freedom and the position of the χ_c peak for data, $\langle \Delta M \rangle_{\chi_c}$, and Monte Carlo, $\langle \Delta M \rangle_{\chi_c}^{MC}$. The position, $\langle M \rangle_{J/\Psi}$, and width, $\sigma_{M_{J/\Psi}}$, of J/Ψ measured in data are also presented.*

	Data				Monte Carlo	
Bin	$(\chi^2/n.d.f.)_{\chi_c}$	$\langle \Delta M \rangle_{\chi_c}$	$\sigma_{M_{J/\Psi}}$	$\langle M \rangle_{J/\Psi}$	$(\chi^2/n.d.f.)_{\chi_c}^{MC}$	$\langle \Delta M \rangle_{\chi_c}^{MC}$
1	105.1/79	417 ± 28	48.9 ± 1.0	3.105 ± 0.004		–
2	81.0/83	403 ± 9	44.77 ± 0.02	3.103 ± 0.001	49.5/83	450 ± 20
3	81.9/84	408 ± 19	43.3 ± 0.5	3.096 ± 0.001	77.2/83	434 ± 10
4	133.185	428 ± 13	46.2 ± 0.1	3.092 ± 0.001	60.9/85	450 ± 9
5	60.7/86	425 ± 8	46.4 ± 0.4	3.092 ± 0.001	53.6/85	454 ± 7
6	102.2/85	431 ± 8	45.8 ± 0.1	3.092 ± 0.001	53.9/86	455 ± 6
7	–	–	41.3 ± 1.8	3.091 ± 0.002	–	–

Table B.6: *R_{χ_c} divided into $x_F^{J/\Psi}$ bins for combined data. The numbers of χ_c, N_{χ_c}, and J/Ψ, $N_{J/\Psi}$, events, measured in pC, pW and pTi interactions are presented. The simulated χ_c signal, $N_{\chi_c}^{MC}$, and number of J/Ψ, $N_{J/\Psi}^{\chi_c}$, stemming from χ_c radiative decays are also given along with the photon detection efficiency, ε_γ.*

	Data			Monte Carlo		
Bin	R_{χ_c}, %	N_{χ_c}	$N_{J/\Psi}$	$N_{\chi_c}^{MC}$	$N_{J/\Psi}^{\chi_c}$	ε_γ, %
1	33.8 ± 20.6	63 ± 35	897 ± 40	18 ± 4*	87 ± 9	20.7 ± 5.1
2	11.4 ± 8.3	138 ± 85	4415 ± 87	101 ± 40	367 ± 19	27.5 ± 11.0
3	9.3 ± 3.1	638 ± 186	16850 ± 164	507 ± 85	1245 ± 35	40.7 ± 6.9
4	12.8 ± 2.9	1701 ± 291	38480 ± 244	884 ± 131	2564 ± 51	34.5 ± 5.1
5	18.8 ± 3.5	2441 ± 283	45060 ± 279	893 ± 130	3095 ± 56	28.8 ± 4.2
6	23.6 ± 5.0	1466 ± 160	20490 ± 165	442 ± 79	1459 ± 38	30.3 ± 5.5
7	8.0 ± 4.8	82 ± 43	2097 ± 52	81 ± 22	165 ± 13	49.1 ± 14.0

* Matched signal

Table B.7: *R_{χ_c} divided into $x_F^{J/\Psi}$ bins for combined data. Parameters of the fits to ΔM: χ^2 per degree of freedom and the position of the χ_c peak for data, $\langle \Delta M \rangle_{\chi_c}$, and Monte Carlo, $\langle \Delta M \rangle_{\chi_c}^{MC}$. The position, $\langle M \rangle_{J/\Psi}$, and width, $\sigma_{M_{J/\Psi}}$, of J/Ψ measured in data are also presented.*

	Data				Monte Carlo	
Bin	$(\chi^2/n.d.f.)_{\chi_c}$	$\langle \Delta M \rangle_{\chi_c}$	$\sigma_{M_{J/\Psi}}$	$\langle M \rangle_{J/\Psi}$	$(\chi^2/n.d.f.)_{\chi_c}^{MC}$	$\langle \Delta M \rangle_{\chi_c}^{MC}$
1	70.0/82	436 ± 24	43.0 ± 1.7	3.105 ± 0.002	–	–
2	82.5/83	409 ± 28	42.3 ± 0.7	3.103 ± 0.001	50.9/83	430 ± 18
3	88.1/84	426 ± 12	43.5 ± 0.1	3.097 ± 0.001	60.2/83	439 ± 7
4	111.2/85	427 ± 4	44.96 ± 0.03	3.092 ± 0.001	49.9/85	440 ± 5
5	73.7/86	433 ± 4	45.3 ± 0.3	3.091 ± 0.001	77.1/85	449 ± 5
6	99.0/86	428 ± 4	44.8 ± 0.2	3.092 ± 0.001	85.2/86	447 ± 7
7	73.4/85	413 ± 19	44.3 ± 0.6	3.088 ± 0.001	54.8/86	433 ± 13

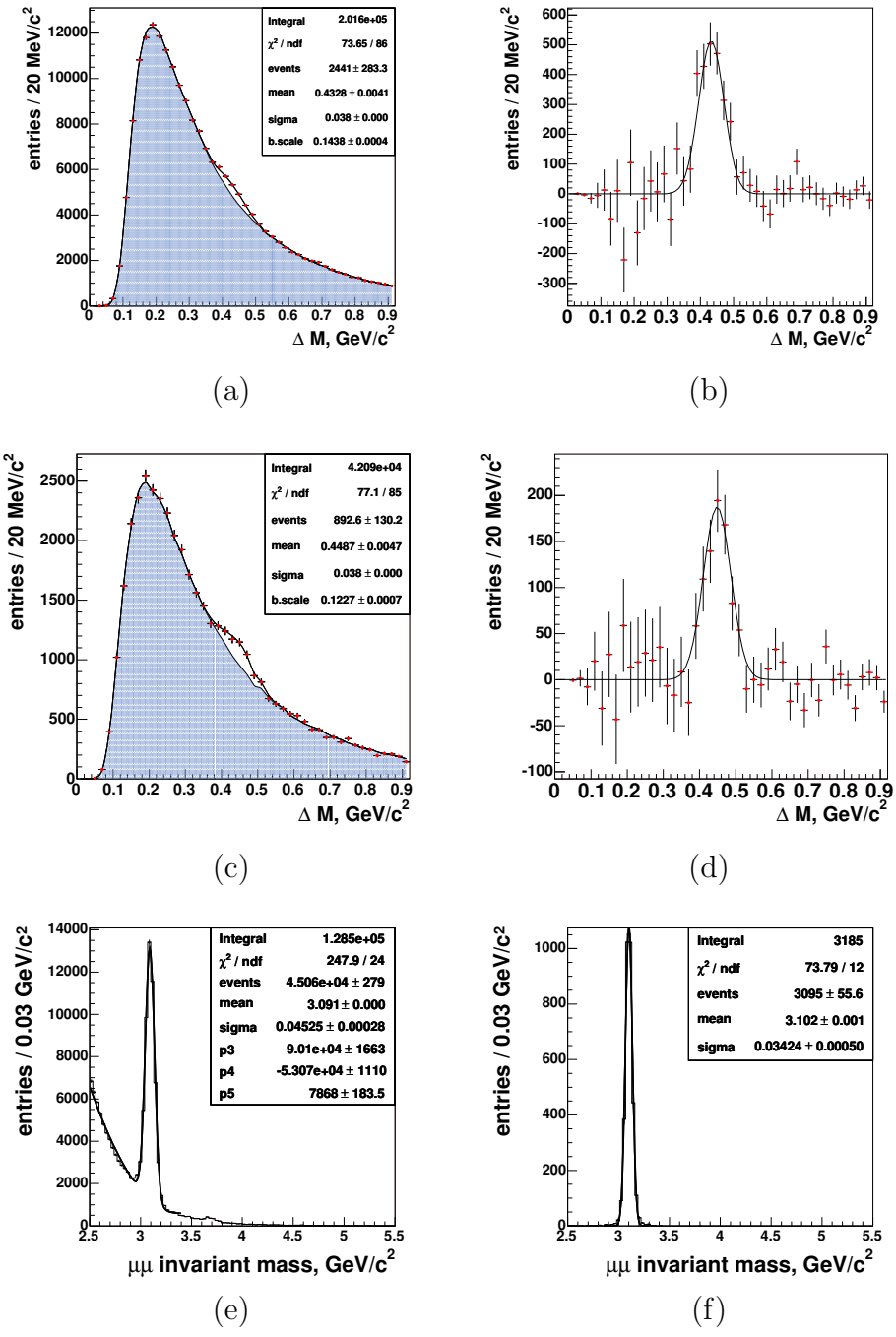

Figure B.1: *Combined data set. (a) The ΔM distribution for combined data (C,W,Ti). The presented fit is performed by using the parametrization (5.34). The fit parameters, events, mean, sigma and b.scale, shown in the plot, correspond to the number of χ_c events, $N^{i2}_{\chi_c}$, position of the signal, $\langle \Delta M \rangle^{i2}_{\chi_c}$, its width, $\sigma^{i2}_{\Delta M_{\chi_c}}$, and the normalization of the background, respectively. The filled histogram represents the combinatorial background estimated by event mixing. (b) The background subtracted signal is shown. Solid line correspond to a Gaussian from the fit to the ΔM. (c,d) the same as (a,b) but for Monte Carlo simulations. (e) J/Ψ signal for data is shown in plot (e), whereas for simulations - in plot (f). The distributions presented correspond to $-0.06 \leq x_F^{J/\Psi} < -0$ range.*

Appendix C

Study of systematical uncertainties

In this appendix, we present details concerning the evaluation of the systematical error imposed by the criteria used to select photons. The summary of the selection criteria is given in Table 5.3.

The evaluation is done by studying the behavior of R_{χ_c} with respect to cuts on cluster energy, cluster transverse energy, number of cells building the cluster, exclusion of the innermost par of the calorimeter, π^0 photons rejection and J/Ψ mass cut. In addition, we check the behavior of the photon detection efficiency, ε_γ, and the ratio between reconstructed χ_c and J/Ψ events, $N_{\chi_c}/N_{J/\Psi}$.

For the energy cut we examine the variation of R_{χ_c} in the range between $E_{cl} > 2\ GeV$ and $E_{cl} > 4\ GeV$ cuts. To cut outside the specified range, results in large systematics deviations. A cut below $2\ GeV$ would result in background dominating the signal, whereas cuts above $4\ GeV$ would make the background peak under the signal, which would drastically increase uncertainties related to the signal extraction. The resulting plots are shown in Fig. C.1.

For the E_T^{cl} cut we examine the variation of R_{χ_c} in the range up to the cut $E_T^{cl} > 200\ MeV$. To cut further the specified range, would result in background peaking under the signal, which would minimize our chances to obtain a reliable signal. The resulting plots are shown in Fig. C.2.

In order to prove that the cut on the number of cluster cells, N_{cells}, has no influence on R_{χ_c}, we estimate the ratio using $N_{cells} > 0, 1, 3, 4$ cuts in addition to the value used in the analysis ($N_{cells} > 2$). The corresponding distributions are shown in Fig. C.3.

The cut that rejects π^0 photons is studied by varying the size of $\gamma\gamma$ invariant mass window which defines π^0 photons, i.e. from $3\sigma_{M_{\pi^0}}$ to $5\sigma_{M_{\pi^0}}$ as indicated in Fig. C.4.

The effect of the exclusion of the ECAL innermost part, $x_{cl}^2/4 + y_{cl}^2 > r^2$, was examined by varying the value of r^2 in the range up to 736 cm^2, as presented in Fig. C.5.

Finally, we check the requirement of J/Ψ mass is the search for isolated photon: $|M_{J/\Psi} - 3.093| < K$. For that, we vary the cut in the range from $K = 132\ MeV/c^2 \approx 3\sigma_{M_{J/\Psi}}$ to $K = 60\ MeV/c^2 \approx 1.3\sigma_{M_{J/\Psi}}$. The variation of K from $3\sigma_{M_{J/\Psi}}$ to $1.7\sigma_{M_{J/\Psi}}$ result in a flat behavior of R_{χ_c}. Any further cut, results in a systematical underestimation of the R_{χ_c} ratio, as indicated in Fig. C.6.

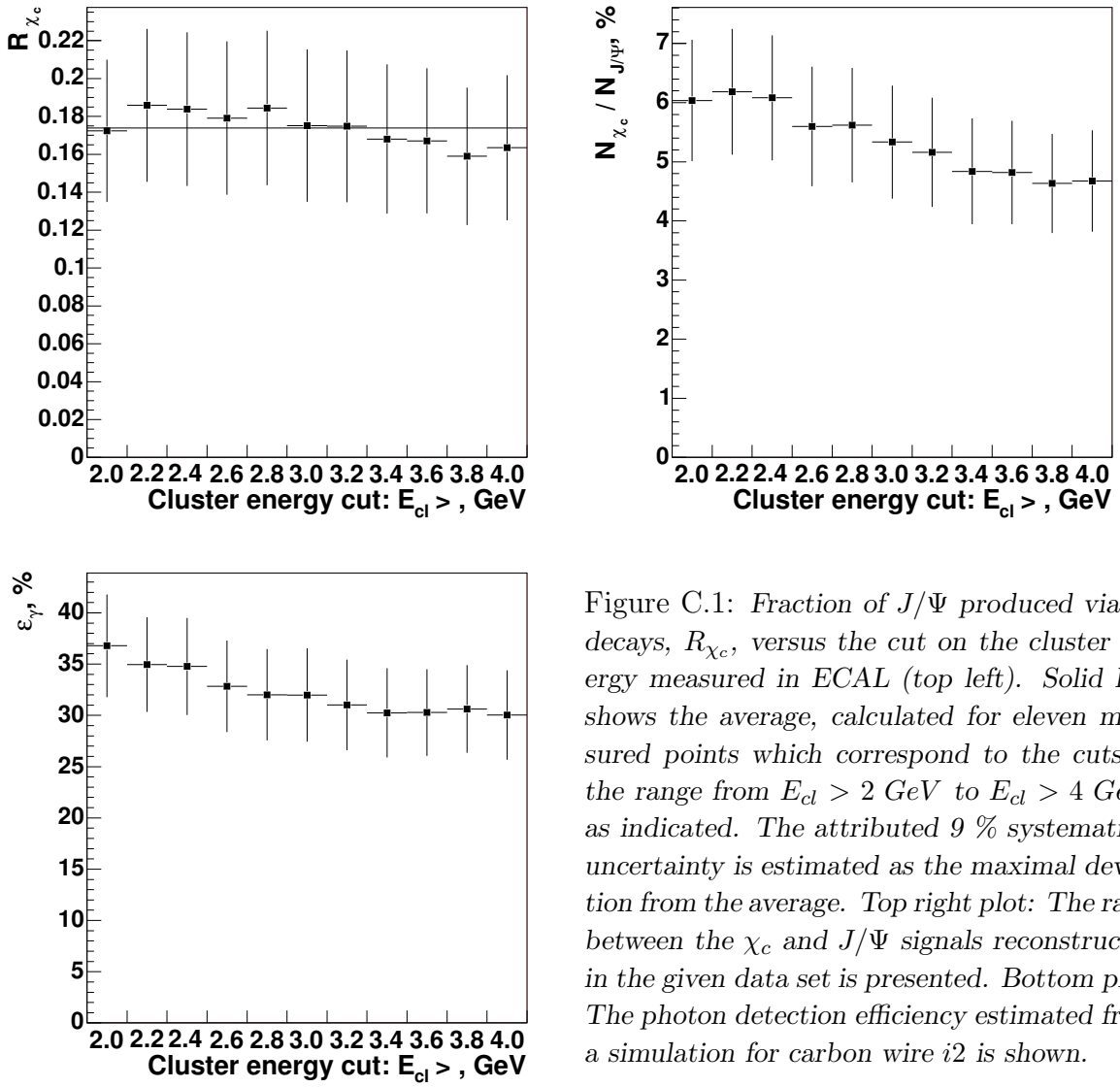

Figure C.1: *Fraction of J/Ψ produced via χ_c decays, R_{χ_c}, versus the cut on the cluster energy measured in ECAL (top left). Solid line shows the average, calculated for eleven measured points which correspond to the cuts in the range from $E_{cl} > 2\ GeV$ to $E_{cl} > 4\ GeV$, as indicated. The attributed 9 % systematical uncertainty is estimated as the maximal deviation from the average. Top right plot: The ratio between the χ_c and J/Ψ signals reconstructed in the given data set is presented. Bottom plot: The photon detection efficiency estimated from a simulation for carbon wire $i2$ is shown.*

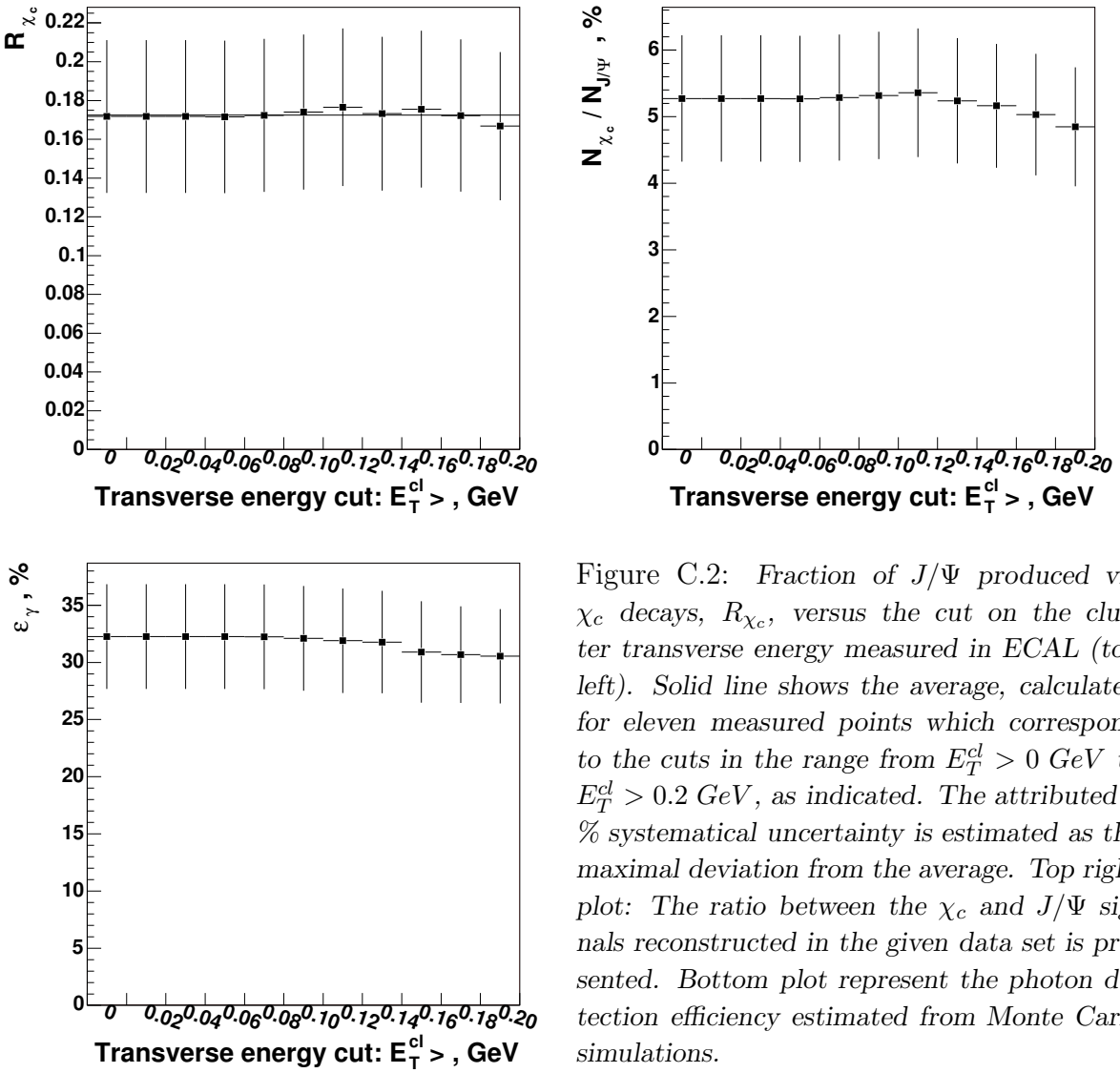

Figure C.2: *Fraction of J/Ψ produced via χ_c decays, R_{χ_c}, versus the cut on the cluster transverse energy measured in ECAL (top left). Solid line shows the average, calculated for eleven measured points which correspond to the cuts in the range from $E_T^{cl} > 0$ GeV to $E_T^{cl} > 0.2$ GeV, as indicated. The attributed 3 % systematical uncertainty is estimated as the maximal deviation from the average. Top right plot: The ratio between the χ_c and J/Ψ signals reconstructed in the given data set is presented. Bottom plot represent the photon detection efficiency estimated from Monte Carlo simulations.*

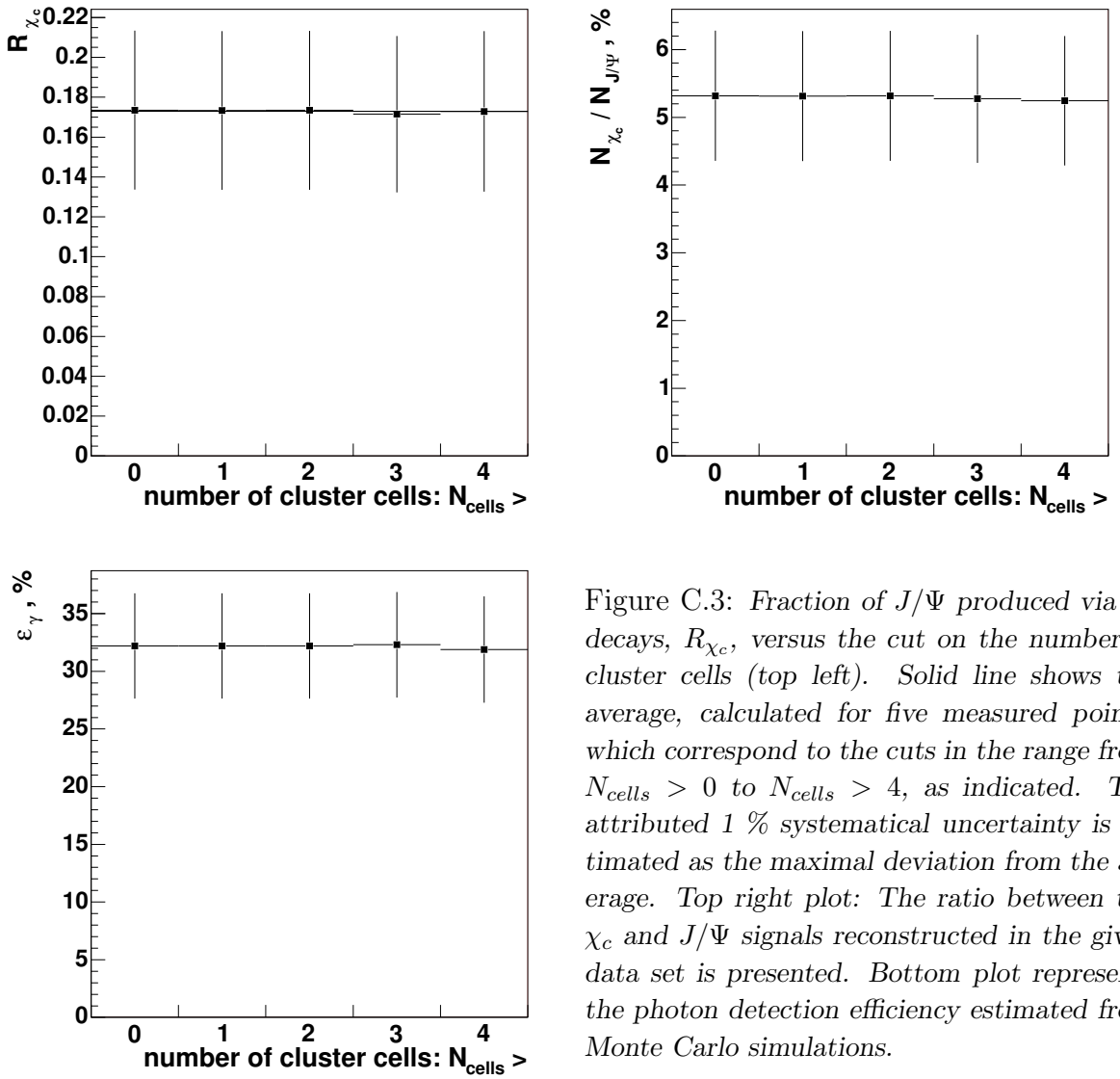

Figure C.3: *Fraction of J/Ψ produced via χ_c decays, R_{χ_c}, versus the cut on the number of cluster cells (top left). Solid line shows the average, calculated for five measured points. which correspond to the cuts in the range from $N_{cells} > 0$ to $N_{cells} > 4$, as indicated. The attributed 1 % systematical uncertainty is estimated as the maximal deviation from the average. Top right plot: The ratio between the χ_c and J/Ψ signals reconstructed in the given data set is presented. Bottom plot represents the photon detection efficiency estimated from Monte Carlo simulations.*

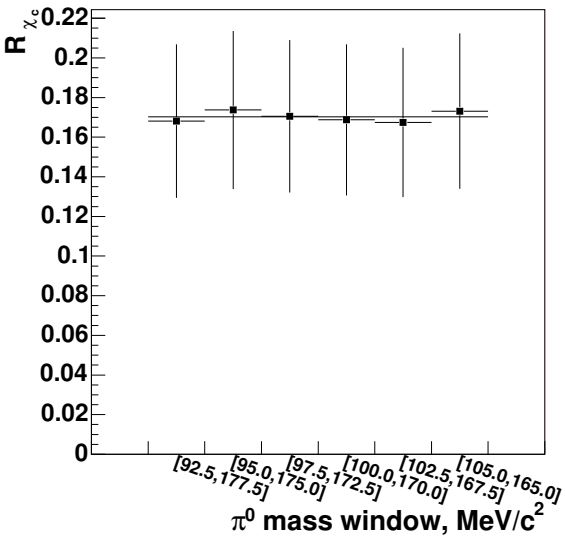

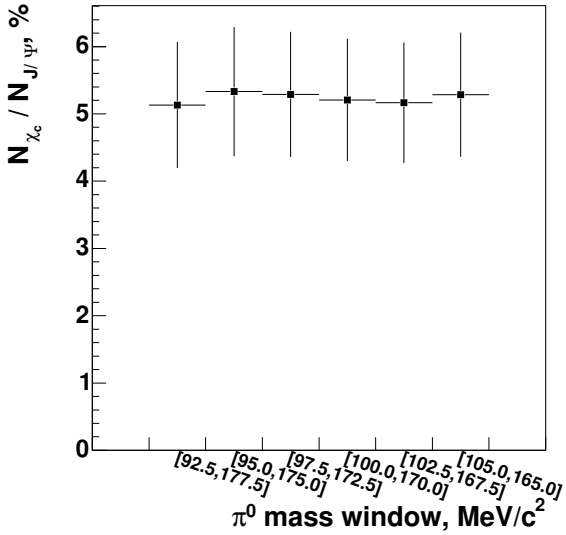

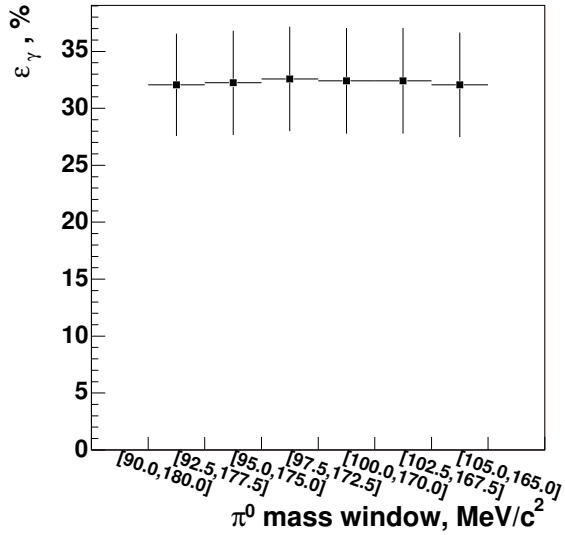

Figure C.4: *Fraction of J/Ψ produced via χ_c decays, R_{χ_c}, versus the π^0 exclusion cut (top left). In the plot, the horizontal axis represent the $\gamma\gamma$ invariant mass window, which defines "π^0 events". Solid line shows the average, calculated for six measured points. The attributed 2 % systematical uncertainty is estimated as the maximal deviation from the average. Top right plot: The ratio between the χ_c and J/Ψ signals reconstructed in the given data set is presented. Bottom plot represents the photon detection efficiency estimated from Monte Carlo simulations.*

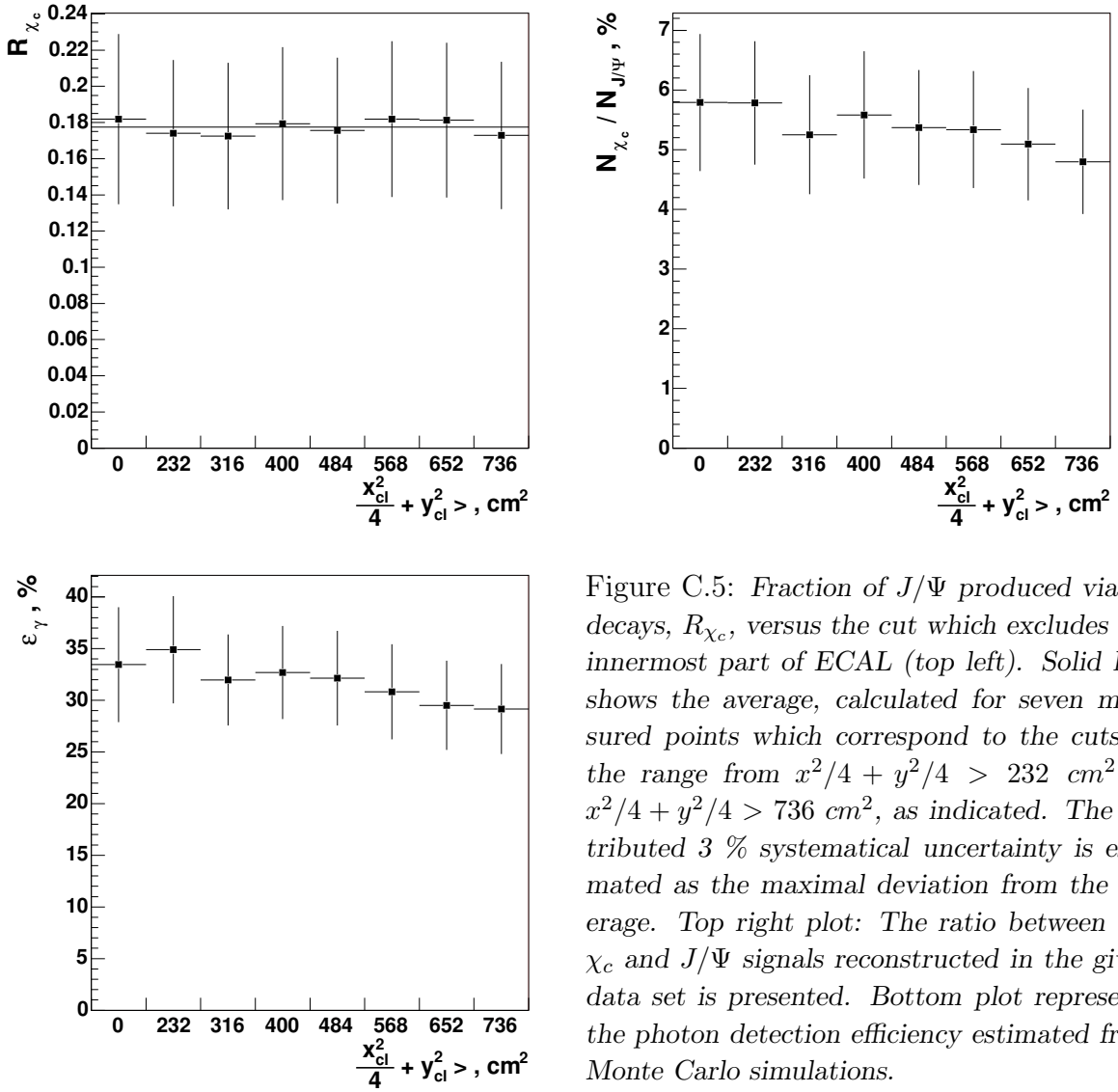

Figure C.5: *Fraction of J/Ψ produced via χ_c decays, R_{χ_c}, versus the cut which excludes the innermost part of ECAL (top left). Solid line shows the average, calculated for seven measured points which correspond to the cuts in the range from $x^2/4 + y^2/4 > 232$ cm^2 to $x^2/4 + y^2/4 > 736$ cm^2, as indicated. The attributed 3 % systematical uncertainty is estimated as the maximal deviation from the average. Top right plot: The ratio between the χ_c and J/Ψ signals reconstructed in the given data set is presented. Bottom plot represents the photon detection efficiency estimated from Monte Carlo simulations.*

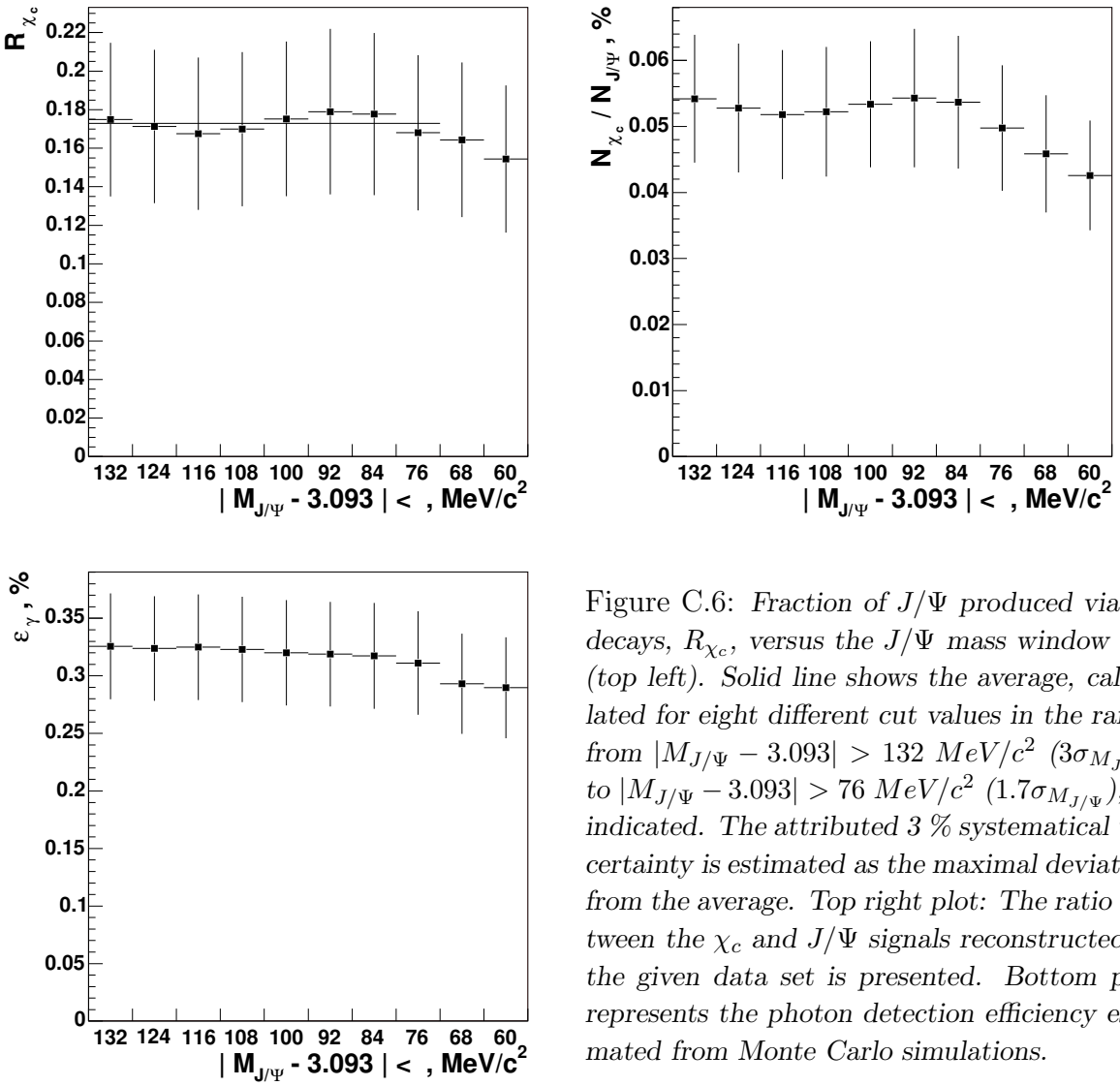

Figure C.6: *Fraction of J/Ψ produced via χ_c decays, R_{χ_c}, versus the J/Ψ mass window cut (top left). Solid line shows the average, calculated for eight different cut values in the range from $|M_{J/\Psi} - 3.093| > 132\ MeV/c^2$ ($3\sigma_{M_{J/\Psi}}$) to $|M_{J/\Psi} - 3.093| > 76\ MeV/c^2$ ($1.7\sigma_{M_{J/\Psi}}$), as indicated. The attributed 3 % systematical uncertainty is estimated as the maximal deviation from the average. Top right plot: The ratio between the χ_c and J/Ψ signals reconstructed in the given data set is presented. Bottom plot represents the photon detection efficiency estimated from Monte Carlo simulations.*

Bibliography

[1] J. J. Aubert et al., *Experimental Observation of a Heavy Particle J.* Phys. Rev. Lett. 33, (1974) 1404-1406

[2] J. -E. Augustin et al., *Discovery of a Narrow Resonance in e^+e^- Annihilation.* Phys. Rev. Lett. 33, (1974) 1406-1408

[3] T.Matsui and H.Satz, *J/Ψ suppression by quark-gluon plasma formation.* Phys. Lett. B 178, (1986) 416

[4] R. Baier, R. Rueckl, *Hadronic production of J/Ψ and Υ : Transverse momentum distributions.* Phys. Lett. B102 (1981)364; Z. Phys. C19 (1983) 251

[5] G.T. Bodwin, E. Braaten, G.P. Lepage, *Rigorous QCD analysis of inclusive annihilation and production of heavy quarkonium.* Phys. Rev. D51 (1995) 1125, P. Cho, A. Leibovich, *Color-octet quarkonia production. II.* Phys. Rev. D53 (1996) 6203

[6] M. Beneke and I. Z. Rothstein, *Hadroproduction of quarkonium in fixed-target experiments.* Phys. Rev. D 54, (1996) 2005;

[7] M. Vanttinen et al., *Hadroproduction and polarization of charmonium.* Phys. Rev. D 51, 3332 (1995).

[8] R. Gavai et al. *Quarkonium production in hadronic collisions.* Int. J. Mod. Phys. A10 (1995) 3043-3070; hep-ph/9502270

[9] M.Krämer, *Quarkonium Production at High-Energy Colliders.* Prog.Part.Nucl.Phys. 47 (2001) 141-201

[10] T.Lohse et al, *HERA-B - An Experiment to Study CP Violation in the B System Using an Internal Target at the HERA Proton Ring* 1994 (http://www-hera-b.de/general/publications/proposal/)

[11] D.A. Bauer et al. (E610 Collaboration), *Differences between proton- and π^--induced production of the charmonium χ states.* Phys. Rev. Lett. 54 (1985) 753; T. Alexopoulos et al. (E771 Collaboration), *Hadroproduction of the χ_1 and χ_2 states of charmonium in 800-GeV/c proton-silicon interactions.* Phys. Rev. D 62, 032006 (2000).

[12] L.Antoniazzi et al., (E705 Collaboration) *Production of χ charmonium via 300-GeV/c pion and proton interactions on a lithium target*, Phys. Rev. D49 (1994) 543

[13] S. Frixione, F. Maltoni et al., *Heavy flavor production and fragmentation* , J.Phys.G: Nucl.Part.Phys.27(2001)1111-1157; F.Maltoni, *Quarkonium Decays and Production in NRQCD*, Invited talk presented at 5th Workshop on QCD, Villefranche-sur-Mer, France 3-7 January 2000

[14] S. Ahmed et al. (SNO Collaboration), *Measurement of the Total Active ^8B Solar Neutrino Flux at the Sudbury Neutrino Observatory with Enhanced Neutral Current Sensitivity.* Phys. Rev. Lett. 92 (2004) 181301; K. Eguchi et al. (KamLAND Collaboration), *First Results from KamLAND: Evidence for Reactor Antineutrino Disappearance.* Phys. Rev. Lett. 90, (2003) 021802

[15] T.Nakano et al., *Evidence for a Narrow $S = +1$ Baryon Resonance in Photoproduction from the Neutron.* Phys.Rev.Lett 91, 012002-1, (2003)

[16] C Alt et al. *Observation of an Exotic S=-2, Q=-2 Baryon resonance in Proton-Proton Collisions at the CERN SPS* 2003 hep-ex/0310014.

[17] S.-K. Choi et al. (Belle Collaboration), *Observation of a Narrow Charmonium like State in Exclusive $B^{\pm} \to K^{\pm}\pi^{+}\pi^{-}J/\Psi$ Decays.* Phys. Rev. Lett. 91, (2003) 262001

[18] D. Acosta et al. (CDF II Collaboration), *Observation of the Narrow State $X(3872) \to J/Psi\pi^{+}\pi^{-}$ in $\bar{p}p$ Collisions at $\sqrt{s} = 1.96\ TeV$.*, Phys. Rev. Lett. 93, (2004) 072001

[19] C.Edwards et al., *Observation an an $\eta_c^{'}$ Candidate State with Mass 3592 ± 5 MeV.* Phys.Rev.Lett 48, (1982)70-73

[20] S.Eidelman et al., *Review of Particle Physics*, Phys.Lett. B592, (2004) 1

[21] L.Antoniazzi et al., *Search for hidden charm states decaying into J/Ψ or Ψ' plus pions.* Phys.Rew., D50, (1994) 4258-4264; T.A.Armstrong et al., *Observation of the $^1P_1$ state of charmonium.* Phys.Rev.Lett 69, (1992)2337-2340; C.Baglin et al., *Search for the $^1P_1$ charmonium state in $p\bar{p}$ annihilations at the CERN intersecting storage rings.* Phys.Lett B171, (1986) 135-141

[22] E.Eichten et al., *Spectrum of Charmed Quark-Antiquark Bound States.* Phys.Rev.Lett. 34(1975) 369-372

[23] W.Buchmueller, S.H.H.Tye, *Quarkonia and quantum chromodynamics.* Phys.Rew D24 (1981) 132-156

[24] R.Feynman, *Very High-Energy Collisions of Hadrons.* Phys.Rev.Lett. 23 (1969) 1415

[25] S.Flemming et al, *Power Counting and Effective Filed Theory for Charmonium.* Phys.Rev. D 64 (2001) 036002; M.Beneke, *Non-relativistic effective theory for quarkonium production in hadron collisions.* hep-ph/9703429

[26] V.N.Gribov and L.N.Lipatov, Yad. Fiz. 15, 1218(1972); G.Altareli and G.Parisi Nucl.Phys.B126,298(1977); Y.L.Dokshitzer Sov.Phys.JETP 46,641(1977)

[27] E. Berger, D. Jones, *Inelastic photoproduction of J/Ψ and Υ by gluons.* Phys.Rev. D 23 (1981) 1521

[28] G.A. Schuler, *Production of heavy quarks and heavy quarkonia.* Z. Phys., C 71 (1996) 317-328

[29] D. Kharzeev and H. Satz, *Charmonium composition and nuclear suppression*, Phys. Lett. B 336 (1996) 316-322

[30] F.Abe et al., *J/Ψ and $\Psi(2S)$ Production in p anti-p Collisions at $\sqrt{s}$ = 1.8 TeV* . Phys. Rev. Lett. 79, 572 (1997).

[31] R.Vogt, *J/Ψ production and suppression*, Phys.Rep. 310 (1999) 197-260

[32] R.Vogt, *Are the J/Ψ and χ_c A Dependencies the same?* hep-ph/0107045 (2001);

[33] M.C.Abreu et al., *Evidence for deconfinement of quarks and gluons from the J/Ψ suppression pattern measured in Pb-Pb collisions at the CERN-SPS* . Phys. Lett. B477, (2000) 28

[34] F.Abe et al., *Production of J/Ψ Mesons from χ_c Meson Decays in $p\bar{p}$ Collisions at sqrts = 1.8 TeV* . Phys.Rev.Lett. 79 (1997) 578

[35] S.Todorova-Nova, *(Some of) Recent $\gamma\gamma$ measurements from LEP.* hep-ph/0112050; G.Alexader et al., *Observation of Υ production in hadronic Z^0 decays.* Phys.Lett. B 370 (1996) 185

[36] B.Aubert et al. (BABAR Collaboration), *Measurement of J/Ψ production in Continuum e^+e^- Annihilations near $\sqrt{s}$ = 10.6 GeV.* Phys.Rev.Lett 87 (2001) 162002

[37] K.Abe et al., *Observation of Double $c\bar{c}$ Production in e^+e^- Annihilation at $\sqrt{s} \sim 10.6\ GeV$*, hep-ex/0205104

[38] P.Cho and A,Leibovich, *Color-singlet Ψ_Q production at e^+e^- colliders.* Phys.Rev. D54(1996) 6690

[39] P.Merkel, *Diffractive Heavy Vector Meson Production at HERA.* Nucl.Phys.Proc.Suppl. 79 (1999) 371

[40] A.Meyer, DESY-THESIS-1998-012; S.Mohrdieck, DESY-THESIS-2000-059

[41] T.Affolder et al, *Measurement of J/Ψ and $\Psi(2S)$ polarization in pp-bar Collisions at $\sqrt{s}$ = 1.8 TeV.* Phys. Rev. Lett. 85 (2000) 2886

[42] C.Biino et al., *J/Ψ longitudinal polarization from πN interactions.* Phys.Rev, Lett, 58 (1987) 2523

[43] J.G.Heinrich et al., *Higher-twist effect in the reaction* $\pi^- N \to \mu^+\mu^- X$ *at 253 GeV/c.* Phys.Rev. D44 (1991) 1909

[44] A.Gribushin et al., *Production of* J/Ψ *mesons in pBe collisions at 530 and 800 GeV/c.* Phys.Rev,D62, (2000) 012001

[45] C.Akerlof et al., Ψ *production in* $\bar{p}N$ *and* $\pi^- N$ *interactions at 125 GeV/c and a determination of gluon structure functions of the* $\bar{p}$ *and the* π^-. Phys.Rev. D48 (1993) 5067

[46] E.Braaten et al, *Polarization of prompt* J/Ψ *at the Fermilab Tevatron.* Phys.Rev. D 62 (2000) 094005

[47] T.Alexopoulos et al., *Differential cross-section of* J/Ψ *and* Ψ' *in 800 GeV/c p-Si interactions.* Phys.Rev. D55 (1997) 3927

[48] T.-H.Chang, *Angular distribution of* J/Ψ *decays in the di-muon channel in 800 GeV* $p - Cu$ *collisions*, hep-ex/0012034

[49] A.G. Clark et al. (ISR Collaboration), Nucl. Phys. B142 (1978) 29; D.A. Bauer et al. (E610 Collaboration), Phys. Rev. Lett. 54 (1985) 753; L. Antoniazzi et al. (E705 Collaboration), Phys. Rev. Lett. 70 (1993) 383; T. Alexopoulos et al. (E771 collaboration), Phys. Rev. D62 (2000) 032006

[50] F. Binon et al. (IHEP140 Collaboration), Nucl. Phys. B239 (1984) 311; Y. Lemoigne et al. (WA11 collaboration), Phys. Lett. B113 (1982) 509; D.A. Bauer et al. (E610 collaboration), Phys. Rev. Lett. 54 (1985) 753; T.B.W. Kirk et al. (E673 collaboration), Phys. Rev. Lett. 42 (1979) 619; S.R. Hahn et al. (E369 collaboration), Phys Rev. D30 (1984) 671; L. Antoniazzi et al. (E705 collaboration), Phys. Rev. Lett. 70 (1993) 383; V. Koreshev et al. (E672/E706 collaboration), Phys. Rev. Lett 77 (1996) 4294

[51] I.Abt et al., J/Ψ *Production via* χ_c *Decays in 920 GeV pA Interactions* , Phys.Lett.B561(2003)61-72

[52] Y. Lemoigne et al. (WA11 Collaboration), *Measurement of hadronic production of the* χ_1^{++}*(3507) and the* χ_2^{++}*(3553) through their radiative decay to* J/Ψ. Phys. Lett. 113 B, 509 (1982); S. R. Hahn et al. (E369 Collaboration), *Hadronic production of charmonium in 225-GeV/c* $\pi^- Be$ *interactions.* Phys. Rev. D 30, 671 (1984); V. Koreshev et al. (E672 Collaboration/E706 Collaboration), *Production of Charmonium States in* $pi^- Be$ *Collisions at 515 GeV/c.* Phys. Rev.Lett. 77, 4294 (1996);

[53] K.Abe et al. (Belle Collaboration), *Production of Prompt Charmonia in* $e^- e^-$ *Annihilation at* $\sqrt{s} \approx 10.6 GeV$ Phys.Rev.Lett 88 (2002) 052001;

[54] R.Barate et al. (NA14 Collaboration), *Measurement of* J/Ψ *and* Ψ' *real photoproduction on* $^6 Li$ *at mean energy of 90 GeV.* Z.Phys. C33 (1987) 505

[55] HERA-B Collaboration *HERA-B Report on Status and Prospects October 2000.* DESY-PRC-00-04; DESY-PRC-94-02

[56] K. Ehret et al., *Commissioning of the HERA-B internal target: using the HERA proton ring as a B-factory.* Nucl.Instrum.Meth.A446:190-198,2000

[57] S.Masciocchi, *MC-Data Comparison. i2 2002.* HERA-B $b\bar{b}$ Analysis Meeting, 28.01.2004

[58] K.T.Knoepfle, Nucl. Intr. Meth. A368(1995)192-198; C.Bauer et al., Nucl.Instr.Meth. A418(1998)65-79; C.Bauer et al., Nucl.Instr.Meth. A447(2000)61-68; C.Bauer et al., Nucl.Instr.Meth. A453(2000)103-108; C.Bauer et al., Nucl.Instr.Meth. A501(2003)39-48

[59] W.Gradl, *The Inner Tracker of HERA-B.* Nucl.Instr.Meth.A461(2001)80-81

[60] Y.Gourbunov, *Coll. Meeting, May 12-16th, 2003, ITR Performance for Analysis.* HERA-B-03-027

[61] A.Lanyov, Modular OTR geometry description in ARTE, HERA-B-97-259 (1997)

[62] H. Kapitza, *Coll. Meeting, May 12-16th, 2003,OTR 2002/2003 Performance.* HERA-B-03-028

[63] G.Avoni et. al., *The electromagnetic calorimeter of the HERA-B experiment.* Nucl.Intrum.Meth.A461(2001)332

[64] A.Zoccoli, Nucl.Instr.Meth.A446(2000)246-252; O.Igonkina, *Online pi0 calibration of ECAL.* HERA-B-00-103

[65] S.Shuvalov, *Coll. Meeting, May 12-16th, 2003, Electromagnetic Calorimeter performance review.* HERA-B-03-31 (2003)

[66] V.Eiges et al, *The MUON detector at the HERA-B experiment*, Nucl.Instrum.Meth.A461(2001)104-106

[67] Y.Zaitsev, *Coll. Meeting, May 12-16th, 2003, Outline Occupancies Efficiencies and Masks.* HERA-B-03-32 (2003)

[68] S. Korpar for the HERA-B RICH Collaboration Nucl.Instrum.Meth.A502:41-45(2003); M. Staric for the HERA-B RICH Collaboration, Nucl.Instrum.Meth.A502:289-293(2003); R. Eckmann, D. Dujmic, R.F. Schwitters *THE PERFORMANCE OF THE HERA-B RICH.* Nucl.Instrum.Meth.A461:563-564(2001)

[69] B.A.Pedersen, *Beauty production at HERA-B*, DESY PhD thesis, 2002

[70] V.Balagura, *Coll. Meeting, May 12-16th, 2003, FLT Efficiency Maps.* HERA-B-03-035 (2003)

[71] M.Dam et al., *The Second Level Trigger Algorithm* HERA-B-03-021

[72] T.Nunez, *Coll. Meeting, May 12-16th, 2003, SLT Status and Studies.* HERA-B-03-036 (2003)

[73] M.Dam et al., *HERA-B Data Acquisition System*, HERA-B-03-063

[74] J. M. Hernndez et al., *Offline mass data processing using online computing resources at HERA-B*, Nucl.Instrum.Meth.A502(2003)471-474

[75] H.Albrecht et al., *ARTE (Analysis and Reconstruction Tool).* HERA-B-95-065

[76] T.Sjöstrand, *High-Energy physics event generation with PYTHIA 5.7 and JETSET 7.4.*, Comp.Phys.Comm.82(1994)74; T.Sjöstrand, *PYTHIA 5.7 and JETSET 7.4 Physics and Manual*, hep-pj/9508391

[77] H.Pi. Comp.Phys.Comm. 71 (1992) 173

[78] J.Ivarsson, *PYTHIA and FRITIOF: Event Generators for HERA-B*, HERA-B-99-067

[79] *GEANT - Detector description and simulation tool.* CERN Program Library W5013 (1993)

[80] M.H.Schub et al.,*Measurement of J/Ψ and Ψ' production in 800 GeV/c proton-gold collisions.* Phys.Rev.D.52 (1995) 1307

[81] M.Braeuer, *Coll. Meeting, Sept. 16-20, 2002, Data quality.* HERAB-02-085

[82] K.Ehret et al., *Observation of coasting beam at the HERA proton ring.* Nucl.Instrum.Meth.A456(2001)206-216

[83] D.Emaliyanov et al., *GROVER*, http://www-hera-b.desy.de/subgroup/software/arte/grover/grover.html

[84] A.Spiridonov HERA-B-04-016; *Details of Jpsi(mumu) mass resolution and tests on repro 5* Charmonium working group Meeting January 29th, 2004

[85] A.Gorisek et al., *Status report of global alignment of HERA-B.* HERA-B-02-032

[86] A.Belkov, B.Fominykh, *Study of Muon misidentification in the HERA-B experiment.* HERA-B-02-036

[87] I. Gorbounov, *Do we have a Ghost Problem in $J/\Psi \to \mu^+\mu^-$ Decays?* HERA-B-01-143

[88] J.Carvalho *Cross-Section compilation for the measurement of the luminosity at HERA-B* HERA-B-01-144

[89] HERA-B Collaboration, *Measurement of the $b\bar{b}$ production cross-section at HERA-B with the 2000 data sample.* HERA-B-02-005

[90] D.Dujmic, *Open Charm Production at HERA-B.* DESY PhD thesis, December 2001.

[91] HERA-B Collaboration, Measurement of the b anti-b production cross-setion in 920-GeV fixed target proton nucleus collisions. Eur.Phys.J.C26:345-355,2003

[92] P.L.McGaughey et al., *Cross section for the production of high-mass muon pairs from 800 GeV proton bombardment of ^2H.* Phys.Rev.D50 (1994) 3038-3045; Errartum: Phys.Rev.D60 (1999) 119903

[93] U.Huesemannm *Prospects of Drell-Yan Physics with the HERA-B Detector.*DESY-THESIS-2001-019 (2001)

[94] M.J.Leitch et al. (E866/NuSea Collaboration), *Measurement of Differences between J/Ψ and Ψ' Suppression in p-A Collisions.* Phys.Rev. Lett. 84 (2000) 3256

[95] M.Villa, *Coll. Meeting/Copenhagen, June 19-22, 2001, Electron Identification and Backgrounds to Electrons.* HERA-B-01-093 (2001)

[96] M.Villa, *Progress Report on the ECAL Reconstruction Software.* HERA-B-97-135 (1997)

[97] O.Igonkina et al., *ECAL Performances for J/psi Reconstruction.* HERA-B-97-150 (1997)

[98] B.Bobchenko, *The Electromagnetic Calorimeter of the HERA-B experiment.* Proceedings of the XI International Conference on Calorimetry in High Energy Physics, March 29-April 2, 2004, Perugia, Italy. To be published by World Scientific

[99] O.Igonkina, *Determination of the fraction of J/psi produced via radiative decays of Xc.* HERA-B-02-028 (2002)

[100] D.L'hôte, *About resonance signal extraction from multiparticle data: combinatorics and event mixing methods.* Nucl.Instr.Meth. A337 (1994) 544

[101] A.Lanyov, *Systematic Effects in $\chi_c \to J/\Psi\gamma$ Background From Event Mixing Method and Their Corrections in Data.* HERA-B-04-013

[102] C.Casso et al., *Review of Particle Physics.* Eur.Phys.J., C15, (2000) 1

[103] O. Igonkina, *Implementation of CSM and NRQCD for the simulation of charmonium production in PYTHIA.* HERA-B-01-067

[104] A.Spiridonov, *Momentum and Angular Resolutions in the HERA-B Detector.* HERA-B-02-069

[105] R.Mankel, Recommendations for Evaluating the Performance of HERA-B Reconstruction Modules, HERA-B-99-063 (1999)

[106] T. Affolder et al., *Production of χ_{c1} and χ_{c2} in p anti-p Collisions at $\sqrt{s} = 1.8TeV$* , Phys. Rev. Lett. 86(2001) 3963-3968

[107] F. Yuan, K.-T. Chao, *χ_c production at the Fermilab Tevatron.*, Phys.Lett.B500(2001)99-104

[108] M.Zavertiaev (HERA-B Collaboration), *V^0 inclusive production cross sections.* Technical HERA-B note in preparation (2002); J. Carvalho, *Status of the Luminosity Determination at HERA-B.* Coll. Meeting, Jan. 21-25, 2002, HERA-B-02-017

[109] HERA-B Collaboration *Inclusive V^0 production cross-section from 920-GeV fixed target proton-nucleus collisions.* Eur. Phys. J. C29 (2003) 181-190 (hep-ex/0212040)